frontiers

RESEARCH TOPICS

ENGINEERING APPROACHES TO STUDY CARDIOVASCULAR PHYSIOLOGY: MODELING, ESTIMATION, AND SIGNAL PROCESSING

Hosted by
Riccardo Barbieri and Zhe Chen

frontiers in PHYSIOLOGY

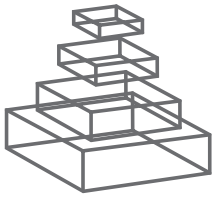

frontiers

Cover image provided by Ibbl sarl, Lausanne CH

ISSN 1664-8714
ISBN 978-2-88919-079-9
DOI 10.3389/978-2-88919-079-9

ABOUT FRONTIERS

Frontiers is more than just an open-access publisher of scholarly articles: it is a pioneering approach to the world of academia, radically improving the way scholarly research is managed. The grand vision of Frontiers is a world where all people have an equal opportunity to seek, share and generate knowledge. Frontiers provides immediate and permanent online open access to all its publications, but this alone is not enough to realize our grand goals.

FRONTIERS JOURNAL SERIES

The Frontiers Journal Series is a multi-tier and interdisciplinary set of open-access, online journals, promising a paradigm shift from the current review, selection and dissemination processes in academic publishing.
All Frontiers journals are driven by researchers for researchers; therefore, they constitute a service to the scholarly community. At the same time, the Frontiers Journal Series operates on a revolutionary invention, the tiered publishing system, initially addressing specific communities of scholars, and gradually climbing up to broader public understanding, thus serving the interests of the lay society, too.

DEDICATION TO QUALITY

Each Frontiers article is a landmark of the highest quality, thanks to genuinely collaborative interactions between authors and review editors, who include some of the world's best academicians. Research must be certified by peers before entering a stream of knowledge that may eventually reach the public - and shape society; therefore, Frontiers only applies the most rigorous and unbiased reviews.
Frontiers revolutionizes research publishing by freely delivering the most outstanding research, evaluated with no bias from both the academic and social point of view.
By applying the most advanced information technologies, Frontiers is catapulting scholarly publishing into a new generation.

WHAT ARE FRONTIERS RESEARCH TOPICS?

Frontiers Research Topics are very popular trademarks of the Frontiers Journals Series: they are collections of at least ten articles, all centered on a particular subject. With their unique mix of varied contributions from Original Research to Review Articles, Frontiers Research Topics unify the most influential researchers, the latest key findings and historical advances in a hot research area!
Find out more on how to host your own Frontiers Research Topic or contribute to one as an author by contacting the Frontiers Editorial Office: researchtopics@frontiersin.org

ENGINEERING APPROACHES TO STUDY CARDIOVASCULAR PHYSIOLOGY: MODELING, ESTIMATION, AND SIGNAL PROCESSING

Hosted By:
Riccardo Barbieri, Massachusetts Institute of Technology, USA
Zhe Chen, Massachusetts Institute of Technology, USA

With cardiovascular diseases being one of the main causes of death in the world, quantitative modeling, assessment and monitoring of the cardiovascular control system plays a critical role in bringing important breakthroughs to cardiovascular care. Quantification of cardiovascular physiology and its control dynamics from physiological recordings and by use of mathematical models and algorithms has been proved to be of important value in understanding the causes of cardiovascular diseases and assisting the prognostic or diagnostic process. Nowadays, development of new recording technologies (e.g., electrophysiology, imaging, ultrasound, etc) has enabled us to improve and expand acquisition of a wide spectrum of physiological measures related to cardiovascular control. An emerging challenge is to process and interpret such increasing amount of information by using state-of-the-art approaches in systems modeling, estimation and control, and signal processing, which would lead to further insightful scientific findings. In particular, multi-disciplinary engineering-empowered approaches of studying cardiovascular systems would greatly deepen our understanding of cardiovascular functions (e.g., heart rate variability, baroreflex sensitivity) and autonomic control, as it would also improve the knowledge about heart pathology, cardiovascular rehabilitation and therapy. Meanwhile, developing cardiovascular biomedical devices or heart-machine interface for either clinical monitoring or rehabilitation purpose is of greater and greater interest for both scientific advancement and potential medical benefits.

This Research Topic will bring together established experts whose areas of research cover a wide range of studies and applications. Contributions include but are not limited to state-of-the-art modeling methodologies, algorithmic development in signal processing and estimation, as well as applications in cardiovascular rehabilitation, and clinical monitoring. The Research Topic will consider both invited reviews and original research.

Table of Contents

frontiers in
PHYSIOLOGY

EDITORIAL
published: 05 November 2012
doi: 10.3389/fphys.2012.00425

Editorial: engineering approaches to study cardiovascular physiology: modeling, estimation, and signal processing

***Zhe Chen*[1,2]* *and Riccardo Barbieri*[1,2]**

[1] *Neuroscience Statistics Research Lab, Department of Anesthesia Critical Care and Pain Medicine, Massachusetts General Hospital, Harvard Medical School, Boston, MA, USA*
[2] *Department of Brain and Cognitive Sciences, Massachusetts Institute of Technology, Cambridge, MA, USA*
**Correspondence: zhechen@mit.edu*

Edited by:
Raimond L. Winslow, The Johns Hopkins University, USA

Reviewed by:
Raimond L. Winslow, The Johns Hopkins University, USA

With cardiovascular diseases being among the main causes of death in the world, quantitative modeling, assessment and monitoring of cardiovascular dynamics, and functioning play a critical role in bringing important breakthroughs to cardiovascular care. Quantification of cardiovascular physiology and its control mechanisms from physiological recordings, by use of mathematical models and algorithms, has been proved to be of important value in understanding the causes of cardiovascular diseases and assisting the diagnostic and prognostic process. This E-Book is derived from the *Frontiers in Computational Physiology and Medicine* Research Topic entitled "Engineering Approaches to Study Cardiovascular Physiology: Modeling, Estimation and Signal Processing." Its goal is to bring established experts together in order to present a sample of state-of-the-art studies in cardiovascular physiology, and to give a general idea of the very different approaches that can be adopted to answer the research challenges posed by the varied, complex nature of the cardiovascular system. This book presents 10 contributions, in the form of review and original research articles.

There are two review articles. The first review article by Chen et al. (2012) presents a unified point process probabilistic framework to assess heart beat dynamics and autonomic cardiovascular control. Using clinical recordings of healthy subjects during Propofol anesthesia, the authors demonstrate the effectiveness of their approach by applying the proposed paradigm to estimate instantaneous heart rate (HR), heart rate variability (HRV), respiratory sinus arrhythmia (RSA) and baroreflex sensitivity (BRS). The second review article, contributed by Zhang et al. (2011), provides a comprehensive overview of tube-load model parameter estimation for monitoring arterial hemodynamics. The authors discuss the motivation, assumption and validity of the proposed tube-load model, and summarize various estimation techniques and their experimental results, as well as potential applications.

The remaining eight original research articles can be mainly classified into two categories. The two articles from the first category emphasize modeling and estimation methods. In particular, the paper "Modeling the autonomic and metabolic effects of obstructive sleep apnea: a simulation study" by Cheng and Khoo (2012), combines computational modeling and simulations to study the autonomic and metabolic effects of obstructive sleep apnea (OSA). The second paper, "Estimation of cardiac output and peripheral resistance using square-wave-approximated aortic flow signal" by Fazeli and Hahn (2012), presents a model-based approach to estimate cardiac output (CO) and total peripheral resistance (TPR), and validates the proposed approach via *in vivo* experimental data from animal subjects.

The six articles in the second category focus on application of signal processing techniques and statistical tools to analyze cardiovascular or physiological signals in practical applications. the paper "Modulation of the sympatho-vagal balance during sleep: frequency domain study of heart rate variability and respiration" by Cabiddu et al. (2012), uses spectral and cross-spectral analysis of heartbeat and respiration signals to assess autonomic cardiac regulation and cardiopulmonary coupling variations during different sleep stages in healthy subjects. the paper "increased non-gaussianity of heart rate variability predicts cardiac mortality after an acute myocardial infarction" by Hayano et al. (2011) uses a new non-gaussian index to assess the HRV of cardiac mortality using 670 post-acute myocardial infarction (AMI) patients. the paper "non-gaussianity of low frequency heart rate variability and sympathetic activation: lack of increases in multiple system atrophy and parkinson disease" by Kiyono et al. (2012), applies a non-gaussian index to assess HRV in patients with multiple system atrophy (MSA) and parkinson diseases and reports the relation between the non-gaussian intermittency of the heartbeat and increased sympathetic activity. The paper "Information domain approach to the investigation of cardio-vascular, cardiopulmonary, and vasculo-pulmonary causal couplings" by Faes et al. (2011), proposes an information domain approach to evaluate nonlinear causality among heartbeat, arterial pressure, and respiration measures during tilt testing and paced breathing protocols. The paper "integrated central-autonomic multifractal complexity in the heart rate variability of healthy humans" by Lin and Sharif (2012), uses a relative multifractal complexity measure to assess HRV in healthy humans and discusses the related implications in central autonomic interactions. Lastly, the paper "Time scales of autonomic information flow in near-term fetal sheep" by Frasch et al. (2012), analyzes the autonomic information flow (AIF) with kullback–leibler entropy in fetal sheep as a function of vagal and sympathetic modulation of fetal HRV during atropine and propranolol blockade.

In summary, this Research Topic attempts to give a general panorama of the possible state-of-the-art modeling methodologies, practical tools in signal processing and estimation, as well as several important clinical applications, which can altogether help deepen our understanding about heart physiology and pathology and further lead to new scientific findings. We hope that the readership of *Frontiers* will appreciate this collected volume and enjoy reading the presented contributions. Finally, we are grateful to all contributed authors, reviewers, and editorial staffs who had all put tremendous effort to make this E-Book a reality.

REFERENCES

Cabiddu, R., Cerutti, S., Viardot, G., Werner, S., and Bianchi, A. M. (2012). Modulation of the sympatho-vagal balance during sleep: frequency domain study of heart rate variability and respiration. *Front. Physio*. 3:45. doi: 10.3389/fphys.2012.00045

Chen, Z., Purdon, P. L., Brown, E. N., and Barbieri, R. (2012). A unified point process probabilistic framework to assess heartbeat dynamics and autonomic cardiovascular control. *Front. Physio.* 3:4. doi: 10.3389/fphys.2012.00004

Cheng, L., and Khoo, M. C. K. (2012). Modeling the autonomic and metabolic effects of obstructive sleep apnea: a simulation study. *Front. Physio.* 2:111. doi: 10.3389/fphys.2011.00111

Faes, L., Nollo, G., and Porta, A. (2011). Information domain approach to the investigation of cardio-vascular, cardio-pulmonary, and vasculo-pulmonary causal couplings. *Front. Physio.* 2:80. doi: 10.3389/fphys.2011.00080

Fazeli, N., and Hahn, J.-O. (2012). Estimation of cardiac output and peripheral resistance using square-wave-approximated aortic flow signal. *Front. Physio.* 3:298. doi: 10.3389/fphys.2012.00298

Frasch, M. G., Frank, B., Last, M., and Müller, T. (2012). Time scales of autonomic information flow in near-term fetal sheep. *Front. Physio.* 3:378. doi: 10.3389/fphys.2012.00378

Hayano, J., Kiyono, K., Struzik, Z. R., Yamamoto, Y., Watanabe, E., Stein, P. K., et al. (2011). Increased non-gaussianity of heart rate variability predicts cardiac mortality after an acute myocardial infarction. *Front. Physio.* 2:65. doi: 10.3389/fphys.2011.00065

Kiyono, K., Hayano, J., Kwak, S., Watanabe, E., and Yamamoto, Y. (2012). Non-Gaussianity of low frequency heart rate variability and sympathetic activation: lack of increases in multiple system atrophy and Parkinson disease. *Front. Physio.* 3:34. doi: 10.3389/fphys.2012.00034

Lin, D. C., and Sharif, A. (2012). Integrated central-autonomic multifractal complexity in the heart rate variability of healthy humans. *Front. Physio.* 2:123. doi: 10.3389/fphys.2011.00123

Zhang, G., Hahn, J., and Mukkamala, R. (2011). Tube-load model parameter estimation for monitoring arterial hemodynamics. *Front. Physio.* 2:72. doi: 10.3389/fphys.2011.00072

Received: 25 September 2012; accepted: 18 October 2012; published online: 05 November 2012.

*Citation: Chen Z and Barbieri R (2012) Editorial: engineering approaches to study cardiovascular physiology: modeling, estimation, and signal processing. Front. Physio. **3**:425. doi: 10.3389/fphys.2012.00425*

This article was submitted to Frontiers in Computational Physiology and Medicine, a specialty of Frontiers in Physiology.

frontiers in
PHYSIOLOGY

REVIEW ARTICLE
published: 01 February 2012
doi: 10.3389/fphys.2012.00004

A unified point process probabilistic framework to assess heartbeat dynamics and autonomic cardiovascular control

Zhe Chen[1,2]*, Patrick L. Purdon[1,2], Emery N. Brown [1,2,3] and Riccardo Barbieri [1,2]

[1] *Neuroscience Statistics Research Lab, Massachusetts General Hospital, Harvard Medical School, Boston, MA, USA*
[2] *Department of Brain and Cognitive Sciences, Massachusetts Institute of Technology, Cambridge, MA, USA*
[3] *Harvard-MIT Division of Health Science and Technology, Massachusetts Institute of Technology, Cambridge, MA, USA*

Edited by:
John Jeremy Rice, Functional Genomics and Systems Biology, USA

Reviewed by:
Lilianne Rivka Mujica-Parodi, State University of New York at Stony Brook, USA
Ioannis Pavlidis, University of Houston, USA

***Correspondence:**
Zhe Chen, Neuroscience Statistics Research Lab, Massachusetts General Hospital, Harvard Medical School, Boston, MA 02114, USA.
e-mail: zhechen@mit.edu

In recent years, time-varying inhomogeneous point process models have been introduced for assessment of instantaneous heartbeat dynamics as well as specific cardiovascular control mechanisms and hemodynamics. Assessment of the model's statistics is established through the Wiener-Volterra theory and a multivariate autoregressive (AR) structure. A variety of instantaneous cardiovascular metrics, such as heart rate (HR), heart rate variability (HRV), respiratory sinus arrhythmia (RSA), and baroreceptor-cardiac reflex (baroreflex) sensitivity (BRS), are derived within a parametric framework and instantaneously updated with adaptive and local maximum likelihood estimation algorithms. Inclusion of second-order non-linearities, with subsequent bispectral quantification in the frequency domain, further allows for definition of instantaneous metrics of non-linearity. We here present a comprehensive review of the devised methods as applied to experimental recordings from healthy subjects during propofol anesthesia. Collective results reveal interesting dynamic trends across the different pharmacological interventions operated within each anesthesia session, confirming the ability of the algorithm to track important changes in cardiorespiratory elicited interactions, and pointing at our mathematical approach as a promising monitoring tool for an accurate, non-invasive assessment in clinical practice. We also discuss the limitations and other alternative modeling strategies of our point process approach.

Keywords: autonomic cardiovascular control, heart rate variability, baroreflex sensitivity, respiratory sinus arrhythmia, point process, Wiener-Volterra expansion, general anesthesia

1. INTRODUCTION

Modeling physiological systems by control systems theory, advanced signal processing, and parametric modeling and estimation approaches has been of focal importance in biomedical engineering (Khoo, 1999; Marmarelis, 2004; Xiao et al., 2005; Porta et al., 2009). Modeling autonomic cardiovascular control using mathematical approaches helps in the understanding and assessment of autonomic cardiovascular functions in healthy or pathological subjects (Task Force, 1996; Berntson et al., 1997; Parati et al., 2001; Stauss, 2003; Eckberg, 2008). Continuous quantification of heartbeat dynamics, as well as their interactions with other cardiovascular measures, have also been subject of important studies in the past decades (Baselli et al., 1988; Saul and Cohen, 1994; Chon et al., 1996; Barbieri et al., 2001; Porta et al., 2002). Non-linear system identification methods have also been applied to heartbeat interval analysis (Christini et al., 1995; Chon et al., 1996; Zou et al., 2003; Zhang et al., 2004; Xiao et al., 2005; Wang et al., 2007). Examples of higher order characterization for cardiovascular signals include non-linear autoregressive (AR) models, Volterra-Wiener series expansion, and Volterra-Laguerre models (Korenberg, 1991; Marmarelis, 1993; Akay, 2000). Several authors have demonstrated the feasibility and validity of non-linear autoregressive models, suggesting that heart rate dynamics studies should put greater emphasis on non-linear analysis (Christini et al., 1995; Chon et al., 1996; Zhang et al., 2004; Jo et al., 2007). However, the wide majority of these studies use either beat series (tachograms) unevenly distributed in time, or they interpolate these series with filters not supported by an underlying model of heartbeat generation.

More recently, advanced statistical methods have been developed for modeling the heartbeat dynamics, treating the heartbeats, detected from continuous electrocardiogram (ECG) recordings, as discrete events that can be described as a stochastic point process (Barbieri et al., 2005; Barbieri and Brown, 2006; Chen et al., 2009a, 2010a). Several probability density functions (e.g., the inverse Gaussian, Gaussian, lognormal, or gamma distribution) have been considered to model the probability of having a beat at each moment in time given the previous observations (Chen et al., 2008). An important result of our recent studies pointed at the inverse Gaussian model (here considered in the methods) as the best probability structure to explain heartbeat generation (Ross, 1997; Barbieri et al., 2005; Chen et al., 2009a), where the expected heartbeat interval (the distributions mean) is modulated by previous inter-beat intervals and other physiological covariates of interest, such as respiration and arterial blood pressure (ABP).

In this tutorial paper, in light of the Wiener-Volterra theory, we present a comprehensive point process framework to model linear and non-linear interactions between the heartbeat intervals, respiration, and arterial blood pressure. The point process framework provides a coherent way to assess the important cardiovascular

functions by instantaneous quantitative indices, such as heart rate variability (HRV), respiratory sinus arrhythmia (RSA), and baroreflex sensitivity (BRS). These indices of interest can be estimated recursively based on online estimation approaches, such as adaptive filtering and local maximum likelihood estimation (Barbieri et al., 2005; Barbieri and Brown, 2006). The adaptive estimation, combined with the point process framework, provides a more accurate estimate in a finer timescale than conventional window-based adaptive filtering methods, such as the recursive least squares (RLS) filter (Haykin, 2001). Of note, we have also further extended the point process approach to consider the non-linear nature of heartbeat dynamics (Chen et al., 2010a).

Assessing and monitoring informative physiological indices is an important goal in both clinical practice and laboratory research. To provide an exemplary application, we employ the proposed point process methods to analyze experimental recordings from healthy subjects during administration of propofol to induce controlled states of general anesthesia (Purdon et al., 2009). To this extent, as reviewed in this article, our recent investigations have reported promising results in monitoring cardiovascular regulation under induction of anesthesia (Chen et al., 2009b, 2010b, 2011a).

2. OVERVIEW OF THE POINT PROCESS FRAMEWORK

In computerized cardiology, various types of data such as the ECG, ABP (e.g., measured by invasive arterial line catheters or non-invasive finger cuffs), and respiratory effort (RP, e.g., measured by plethysmography or by piezoelectric respiratory belt transducers) are recorded, digitized, and saved to a computer to be available for off-line analysis. A specific goal in analyzing these data is to discover and quantify the statistical dependence between the physiological measurements, and consequently extract informative physiological indices from the data. A direct approach computes empirical statistics (e.g., mean and variance, spectral content, or degree of non-linearity) without making any assumption on how the observed quantities are motivated by the physiology. Conversely, a model-based approach relies on mathematical formulations to define either a mechanistic or a statistical model to explain the observed data. Despite the simplification, the model attempts to describe the generative mechanism of the physiological measurements, and therefore it is critical for further data simulation and interpretation. Being defined by unknown parameters, identification of the model also requires a statistical approach to estimate optimal sets of parameters that best fit the observed physiological dynamics (Xiao et al., 2005). Typically, modeling the complex nature of the data (e.g., non-linearity) would further call for more complex model structures. Model selection or model assessment can be evaluated by some established goodness-of-fit statistics.

Here we propose a unified point process statistical framework to model the physiological measurements commonly acquired in computerized cardiology. In statistics, a point process is a type of random process for which any one realization consists of a set of isolated points either in time or space (Daley and Vere-Jones, 2007). Point processes are frequently used to model random events in time or space (from simple scenarios like the arrival of a customer to a counter, to very complex phenomena such as neuronal spiking activity). In our specific case, heartbeat events detected from the ECG waveforms can be also viewed as a point process, and the generative mechanism of the beat-to-beat intervals can be described by a parametric probability distribution. To model the heartbeat dynamics and cardiovascular/cardio respiratory interactions, we will make some assumptions and simplifications about the data generative mechanisms, while facilitating the ease for data interpretation.

Our paradigm can be outlined in three separate phases (see the flowchart in **Figure 1**): acquisition and preprocessing (Phase I) where the raw physiological measurements are processed to obtain proper input variables to the models, modeling and goodness-of-fit assessment (Phase II) where a chosen number of models are tested and optimal parameters are estimated to best fit the observed input dynamics, and monitoring (Phase III) where a proper combination of the estimated parameters can be manipulated to define instantaneous indices directly related to specific cardiovascular control mechanisms. Mathematical and technical details of Phase II and Phase III will be described in the next section.

3. METHODS AND DATA

3.1. PROBABILITY MODELS FOR THE HEARTBEAT INTERVAL

Given a set of R-wave events $\{u_j\}_{j=1}^{J}$ detected from the recorded ECG waveform, let $RR_j = u_j - u_{j-1} > 0$ denote the jth R-R interval. By treating the R-waves as discrete events, we may develop a probabilistic point process model in the continuous-time domain. Assuming history dependence, the waiting time $t - u_j$ (as a continuous random variable, where $t > u_j$) until the next R-wave event can be modeled by an inverse Gaussian model (Barbieri et al., 2005; Barbieri and Brown, 2006; Chen et al., 2009a)

$$p(t) = \left(\frac{\theta}{2\pi t^3}\right)^{\frac{1}{2}} \exp\left(-\frac{\theta\left(t - u_j - \mu_{\mathrm{RR}}(t)\right)^2}{2\left(t - u_j\right)\mu_{\mathrm{RR}}^2(t)}\right), \tag{1}$$

where u_j denotes the previous R-wave event occurred before time t, $\theta > 0$ denotes the shape parameter (which might also be time-varying), and $\mu_{\mathrm{RR}}(t)$ denotes the instantaneous R-R mean parameter. The use of an inverse Gaussian distribution to characterize the R-R intervals' occurrences is further motivated by a physiological integrate-and-fire model of heartbeat generation: in fact, if the rise of the membrane potential to a threshold initiating the cardiac contraction is modeled as a Gaussian random-walk with drift, then the probability density of the times between threshold crossings (the R-R intervals) is indeed the inverse Gaussian distribution (Barbieri et al., 2005).

Note that when the mean $\mu_{\mathrm{RR}}(t)$ is much greater than the variance, the inverse Gaussian distribution can be well approximated by a Gaussian distribution with an identical mean and a variance equal to $\mu_{\mathrm{RR}}^3(t)/\theta$. However, the inverse Gaussian distribution is more robust since it can better model the outliers due to its long tail behavior. In our earlier investigation (Chen et al., 2008, 2009a), we have compared heartbeat interval fitting point process models using different probability distributions, and found that the inverse Gaussian model achieved the overall best fitting results. In practice, we can always conduct an empirical model fit analysis (e.g., data histogram, the Q-Q plot, and the Kolmogorov-Smirnov plot) for the raw R-R intervals, testing the appropriateness of the inverse Gaussian model (Chen et al., 2011a).

In point process theory, the inter-event probability $p(t)$ is related to the conditional intensity function (CIF) $\lambda(t)$ by a one-to-one transformation (Brown et al., 2003)

$$\lambda(t) = \frac{p(t)}{1 - \int_{u_j}^{t} p(\tau)\mathrm{d}\tau}. \quad (2)$$

The estimated CIF can be used to evaluate the goodness-of-fit of the probabilistic heartbeat interval model.

3.2. INSTANTANEOUS INDICES OF HR AND HRV

Heart rate (HR) is defined as the reciprocal of the R-R intervals. For time t measured in seconds, the new variable $r = c(t - u_j)^{-1}$ (where $c = 60$ s/min is a constant) can be defined in beats per minute (bpm). By virtue of the *change-of-variables* formula, from equation (1) the HR probability $p(r) = p(c(t - u_j)^{-1})$ is given by $p(r) = |\mathrm{d}t/\mathrm{d}r|p(t)$, and the mean and the SD of HR r can be derived (Barbieri et al., 2005)

$$\mu_{\mathrm{HR}} = \tilde{\mu}^{-1} + \tilde{\theta}^{-1}, \quad (3)$$

$$\sigma_{\mathrm{HR}} = \sqrt{\left(2\tilde{\mu} + \tilde{\theta}\right)/\tilde{\mu}\,\tilde{\theta}^2}, \quad (4)$$

where $\tilde{\mu} = c^{-1}\mu_{\mathrm{RR}}$ and $\tilde{\theta} = c^{-1}\theta$. Essentially, the instantaneous indices of HR and HRV are characterized by the mean μ_{HR} and SD σ_{HR}, respectively. In a non-stationary environment, where the probability distribution of HR is possibly slowly changing over time, we aim to dynamically estimate the instantaneous mean $\mu_{\mathrm{RR}}(t)$ and instantaneous shape parameter θ_t in equation (1) so that the evolution of the probability density $p(r)$ can be tracked in an online fashion.

In **Table 1**, several potential probabilistic heartbeat interval models are listed, along with the derived probabilistic HR models (Chen et al., 2008, 2009a). For all probabilistic HR models, μ_{HR} and σ_{HR} can be either analytically derived or numerically evaluated. This provides a mathematically rigorous definition of instantaneous indices of HR and HRV, which sidesteps some of the difficulties in defining HR and HRV based on the series of heartbeat intervals unevenly distributed in time.

3.3. AUTONOMIC CARDIOVASCULAR CONTROL AND MODELING HEARTBEAT DYNAMICS

In line with a control systems engineering approach, short term autonomic cardiovascular control can be modeled as a closed-loop system that involves blood pressure (BP) and respiratory (RP) measures as the two major variables that influence heartbeat dynamics (Baselli et al., 1988; De Boer et al., 1995; Barbieri et al., 2001). The closed-loop system can be illustrated by the simplified diagram shown in **Figure 2**. In the feedforward pathway (RR → BP), the R-R intervals influence the forthcoming BP measure as defined by the H_{12} transfer function (either in the time or frequency domains), including the effects of heart contractility and vasculature tone on arterial pressure. In the feedback pathway (BP → RR), the autonomic nervous system modulates the beat-to-beat interval through a feedback control mechanism mediated by

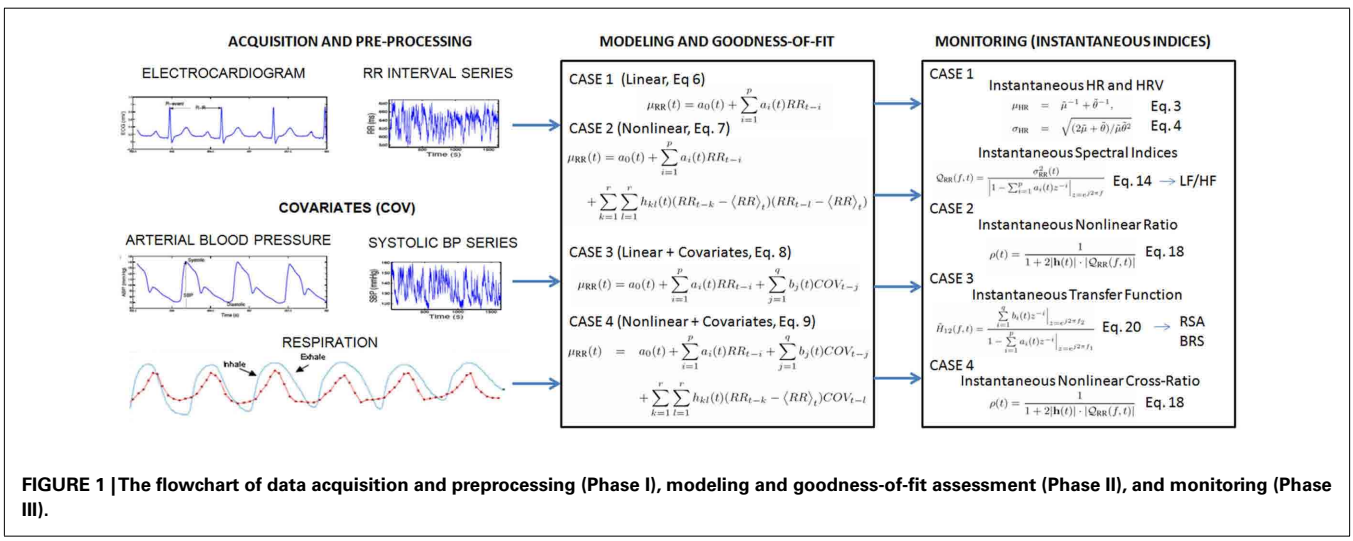

FIGURE 1 | The flowchart of data acquisition and preprocessing (Phase I), modeling and goodness-of-fit assessment (Phase II), and monitoring (Phase III).

Table 1 | List of four two-parameter parametric probabilistic models for the heartbeat R-R interval and heart rate (HR).

	R-R interval model $p(t\|\theta_1, \theta_2)$	$\mathbb{E}(t)$	$\mathrm{Var}(t)$	HR model $p(r\|\theta_1, \theta_2)$	Note: $c = 60$ s/min
Gaussian	$\frac{1}{\sqrt{2\pi\theta_2}}\exp(-\frac{(t-\theta_1)^2}{2\theta_2})$	θ_1	θ_2	$\frac{c}{\sqrt{2\pi\theta_2 r^2}}\exp(-\frac{(cr^{-1}-\theta_1)^2}{2\theta_2})$	
invGaussian	$(\frac{\theta_2}{2\pi t^3})^{\frac{1}{2}}\exp(-\frac{\theta_2(t-\theta_1)^2}{2\theta_1^2 t})$	θ_1	θ_1^3/θ_2	$(\frac{\theta_2^*}{2\pi r})^{\frac{1}{2}}\exp(-\frac{\theta_2^*(1-\theta_1^* r)^2}{2\theta_1^{*2} r})$	$\theta_1^* = \theta_1/c, \theta_2^* = \theta_2/c$
Lognormal	$\frac{1}{\sqrt{2\pi\theta_2 t}}\exp(-\frac{(\log(t)-\theta_1)^2}{2\theta_2})$	$e^{\theta_1+\theta_2/2}$	$e^{2\theta_1+\theta_2}(e^{\theta_2}-1)$	$\frac{1}{\sqrt{2\pi\theta_2 r}}\exp(-\frac{(\log(cr^{-1})-\theta_1)^2}{2\theta_2})$	
Gamma	$\frac{\theta_2^{\theta_1}}{\Gamma(t\theta_1^{-1})}\exp(-\theta_2 t)$	θ_1/θ_2	θ_1/θ_2^2	$\frac{\theta_2^{*\theta_1}}{\Gamma(\theta_1)r^{\theta_1+1}}\exp(-\frac{\theta_2^*/r}{2\theta_2})$	$\theta_2^* = c\theta_2$

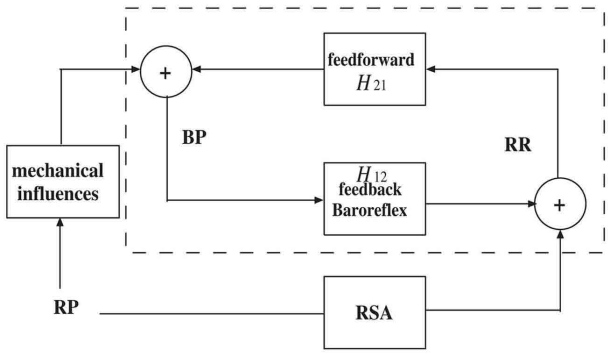

FIGURE 2 | A simplified diagram of the cardiovascular closed-loop model. The beat-to-beat R-R interval is modulated by blood pressure (BP) through the feedback baroreflex loop. The dashed box represents a closed-loop baroreceptor-cardiac reflex (baroreflex) model. Outside the dashed box, the respiratory (RP) input also modulates RR through respiratory sinus arrhythmia (RSA) and modulates BP through mechanical influences.

the baroreceptors, where the H_{21} transfer function includes both baroreflex and autonomic control to the heart. In a second feedback pathway (RP → RR), the changes in lung volume modulates the beat-to-beat interval. The cardiovascular functions associated with these two feedback influences, baroreflex sensitivity (BRS) and respiratory sinus arrhythmia (RSA), operate within specific frequency bands.

A common methodological approach to characterize a physiological system is through system identification (Nikias and Petropulu, 1993; Marmarelis, 2004; Xiao et al., 2005). In general, let us consider a causal, continuous-time non-linear mapping F between an output variable $y(t)$ and two input variables $x(t)$ and $u(t)$. Expanding the Wiener-Volterra series of function F (up to the second-order) with respect to inputs $x(t)$ and $u(t)$ yields (Schetzen, 1980)

$$\begin{aligned} y(t) &= F(x(t), u(t)) \\ &= \int_0^t a(\tau)\, x(t-\tau)\, \mathrm{d}\tau + \int_0^t b(\tau)\, u(t-\tau)\, \mathrm{d}\tau \\ &\quad + \int_0^t \int_0^t h_1(\tau_1, \tau_2)\, x(t-\tau_1)\, u(t-\tau_2)\, \mathrm{d}\tau_1 \mathrm{d}\tau_2 \\ &\quad + \int_0^t \int_0^t h_2(\tau_1, \tau_2)\, x(t-\tau_1)\, x(t-\tau_2)\, \mathrm{d}\tau_1 \mathrm{d}\tau_2 \\ &\quad + \int_0^t \int_0^t h_3(\tau_1, \tau_2)\, u(t-\tau_1)\, u(t-\tau_2)\, \mathrm{d}\tau_1 \mathrm{d}\tau_2 \end{aligned} \tag{5}$$

where $F(\cdot): \mathbb{R}^2 \mapsto \mathbb{R}$ is a non-linear function, and $a(\cdot)$, $b(\cdot)$, $h_1(\cdot,\cdot)$, $h_2(\cdot,\cdot)$, and $h_3(\cdot,\cdot)$ are Volterra kernels with appropriate orders. In our cardiovascular system identification case, $y(t)$ represents the expected heartbeat interval $\mu_{\mathrm{RR}}(t)$, $x(t)$ represents the previous R-R intervals, $u(t)$ represents the vector of covariates (COV) such as BP or RP, and the continuous-time integral (convolution) is approximated by afinite and discrete summation. The first and second-order Volterra kernels will be replaced by discrete filter coefficients.

We consider four individual cases of discrete-time Volterra series expansion, which lead to different formulations to model the heartbeat interval mean μ_{RR} in equation (1).

- Dropping all of second-order terms as well as the COV terms in the Volterra series expansion (5), we obtain a univariate (noise-free) AR model

$$\mu_{\mathrm{RR}}(t) = a_0(t) + \sum_{i=1}^{p} a_i(t)\, RR_{t-i} \tag{6}$$

  where the a_0 term is incorporated to compensate the non-zero mean of the R-R intervals.
- Dropping the COV terms in the Volterra series expansion (5), we obtain

$$\begin{aligned} \mu_{\mathrm{RR}}(t) &= a_0(t) + \sum_{i=1}^{p} a_i(t)\, RR_{t-i} \\ &\quad + \sum_{k=1}^{r} \sum_{l=1}^{r} h_{kl}(t) \left(RR_{t-k} - \langle RR \rangle_t\right) \left(RR_{t-l} - \langle RR \rangle_t\right) \end{aligned} \tag{7}$$

  where $\langle RR \rangle_t = 1/\ell \sum_{k=1}^{\ell} RR_{t-k}$ $(\ell = max\{p, r\})$ denotes the local mean of the past ℓ R-R intervals.
- Dropping all of second-order terms in the Volterra series expansion (5), we obtain a bivariate discrete-time linear system

$$\mu_{\mathrm{RR}}(t) = a_0(t) + \sum_{i=1}^{p} a_i(t)\, RR_{t-i} + \sum_{j=1}^{q} b_j(t)\, COV_{t-j} \tag{8}$$

  where the first two terms represent a linear autoregressive (AR) model of the past R-R intervals, and COV_{t-j} denotes the previous jth covariate value prior to time t. Note that the COV observations will be preprocessed to have zero mean (since the DC component is of minimal importance to model the oscillation). Equation (8) can also be viewed as a linear (noise-free) autoregressive moving average (ARMA) model (Lu et al., 2001). Also note that here we have used RR_{t-i} instead of $\mu_{\mathrm{RR}}(t-i)$ as regressors since this would require a higher order p due to the long-range dependence of $\mu_{\mathrm{RR}}(t-i)$ under a very small timescale. Due to the absence of driving noise, Equation (8) can also be viewed as an ARX model, where the COV term serves as the exogenous input.
- Dropping the last two quadratic terms in the Volterra series expansion (5), we obtain

$$\begin{aligned} \mu_{\mathrm{RR}}(t) &= a_0(t) + \sum_{i=1}^{p} a_i(t)\, RR_{t-i} + \sum_{j=1}^{q} b_j(t)\, COV_{t-j} \\ &\quad + \sum_{k=1}^{r} \sum_{l=1}^{r} h_{kl}(t) \left(RR_{t-k} - \langle RR \rangle_t\right) COV_{t-l} \end{aligned} \tag{9}$$

  Equation (9) can be viewed as a bivariate bilinear system (Tsoulkas et al., 2001), which can also be viewed as a (noise-free) non-linear ARMA or non-linear ARX model (Lu et al., 2001).

3.4. ONLINE ESTIMATION: ADAPTIVE POINT PROCESS FILTERING AND LOCAL LIKELIHOOD ESTIMATION

Since our earliest point process cardiovascular characterizations (Barbieri et al., 2005; Barbieri and Brown, 2006), in order to optimize the estimation of the model parameters, we have developed two model fitting algorithms: the adaptive point process filtering method (based on recursive *adaptive filtering*, and the local maximum likelihood (based on *local likelihood estimation* using a moving window). These two online estimation methods enable us to update the parameters of the heartbeat probability model at each moment in time in order to continuously track the non-stationary nature of the observations.

In the adaptive filtering method, let $\boldsymbol{\xi} = [\{a_i\}_{i=0}^{p}, \{b_j\}_{j=1}^{q}, \{h_{kl}\}, \theta]^T$ denote the vector that contains all unknown parameters in the heartbeat interval probability model. Let the continuous-time interval be binned with a constant bin size Δ. A state-space formulation of the discrete-time (indexed by k) point process filtering algorithm is described here (Brown et al., 1998; Eden et al., 2004; Barbieri and Brown, 2006)

$$\begin{aligned}
\boldsymbol{\xi}_{k|k-1} &= \boldsymbol{\xi}_{k-1|k-1} \\
\boldsymbol{P}_{k|k-1} &= \boldsymbol{P}_{k-1|k-1} + \boldsymbol{W} \\
\boldsymbol{\xi}_{k|k} &= \boldsymbol{\xi}_{k|k-1} + \boldsymbol{P}_{k|k-1}\left(\nabla \log \lambda_k\right)\left[n_k - \lambda_k \Delta\right] \\
\boldsymbol{P}_{k|k} &= \left[\boldsymbol{P}_{k|k-1}^{-1} + \nabla\lambda_k \nabla\lambda_k^T \frac{\Delta}{\lambda_k} - \nabla^2 \log \lambda_k \left[n_k - \lambda_k \Delta\right]\right]^{-1}
\end{aligned}$$

where $\boldsymbol{P}$ and $\boldsymbol{W}$ denote the parameter and noise covariance matrices, respectively; and Δ denotes the time bin size. The choice of bin size reflects the timescale of estimation interest, we typically use $\Delta = 5$ ms. Diagonal noise covariance matrix $\boldsymbol{W}$, which determines the level of parameter fluctuation at the timescale of Δ, can be either initialized empirically from the random-walk theory,[1] or estimated from the expectation-maximization (EM) algorithm (Smith and Brown, 2003). In our experiments, a typical value of noise variance value for the AR parameter is $10^{-6} \sim 10^{-7}$, and the typical noise variance value for the shape parameter is $10^{-3} \sim 10^{-4}$. The sensitivity analysis of the noise variance will be illustrated and discussed in the result section.

Symbols $\nabla\lambda_k = \partial\lambda_k/\partial\boldsymbol{\xi}_k$ and $\nabla^2\lambda_k = \frac{\partial^2\lambda_k}{\partial\boldsymbol{\xi}_k \partial\boldsymbol{\xi}_k^T}$ denote the first- and second-order partial derivatives of the CIF with respect to $\boldsymbol{\xi}$ at time $t = k\Delta$, respectively. The indicator variable $n_k = 1$ if a heartbeat occurs in the time interval $((k-1)\Delta, k\Delta]$ and 0 otherwise. The point process filtering equations can be viewed as a point process analog of the Kalman filtering equations in the presence of continuous-valued observations (Eden et al., 2004). Given a predicted (*a priori*) estimate $\boldsymbol{\xi}_{k|k-1}$, the innovations $[n_k - \lambda_k\Delta]$ is weighted by $\boldsymbol{P}_{k|k-1}(\nabla\log\lambda_k)$ (viewed as an adaptation gain) to further produce the filtered (*a posteriori*) estimate $\boldsymbol{\xi}_{k|k}$. Since the innovations term is likely to be non-zero in the absence of a beat, the parameters are always updated at each time step k. The *a posteriori* error covariance $\boldsymbol{P}_{k|k}$ is derived based on a Gaussian approximation of the log-posterior (Eden et al., 2004). We always use the *a posteriori* estimate to the HR, HRV, and other statistics. The time-varying CIF λ_k is also numerically computed from equation (2) using the *a posteriori* estimate.

In the local likelihood estimation method (Loader, 1999), we can define the log-likelihood given an observation window $(t-l, t]$ consisting of n heartbeat events $\{t - l < u_1 < u_2 < \ldots < u_n \leq t\}$ as (Loader, 1999; Barbieri and Brown, 2006; Kodituwakku et al., 2012)

$$\begin{aligned}
\log p\left(u_{t-l:t}\right) = &\sum_{j=2}^{n} w\left(t - u_j\right) \log p\left(u_j - u_{j-1}\right) \\
&+ w\left(t - u_n\right) \log \int_{t-u_n}^{\infty} p\left(v\right) \mathrm{d}v
\end{aligned} \tag{10}$$

where $w(t-u_j) = \alpha^{t-u_j}$ $(0 < \alpha < 1)$ is a weighting function for the local likelihood estimation. The weighting time constant α governs the degree of influence of a previous event observation u_j on the local likelihood at time t. The second term of equation (10) represents the log-likelihood of the partially observed interval since the last observed beat u_n (right censoring). The local log-likelihood (10) can be optimized using a Newton-Raphson method to obtain a local maximum likelihood estimate of $\boldsymbol{\xi}$ (Loader, 1999).

The above estimation methods are by no means the only options. Other alternative methods can be considered. For instance, particle filtering is known to have a better tracking performance for non-linear dynamics at the cost of increasing memory and computational complexity (Brockwell et al., 2004; Ergun et al., 2007). In addition, instead of the Gaussian approximation, other types of approximation approaches may also be employed to obtain a more accurate point process filtering algorithm (Koyama et al., 2009, 2010).

3.5. FREQUENCY ANALYSIS

3.5.1. Estimating the frequency response at the feedback pathway (baroreflex or RSA)

Assuming a linear relation between the input and output of interest, we can estimate the transfer function (based on the Laplace transform) and the associated frequency response between the input and output variables (Saul et al., 1991; Pinna and Maestri, 2001; Xiao et al., 2005; Pinna, 2007).

In light of equation (8), the frequency response for the baroreflex (BP → RR) or RSA (RP → RR) is computed as (Chen et al., 2009a, 2011a)

$$H_{12}\left(f, t\right) = \frac{\sum_{i=1}^{q} b_i\left(t\right) z^{-i}\big|_{z=e^{j2\pi f_2}}}{1 - \sum_{i=1}^{p} a_i\left(t\right) z^{-i}\big|_{z=e^{j2\pi f_1}}}, \tag{11}$$

where f_1 and f_2 denote the rate (beat/s) for the R-R and COV-COV intervals, respectively; here we assume $f_1 \approx f_2 \equiv f$ (we typically assume that the heartbeat period is about the same as the BP-event period, while the RP measurement can be resampled or interpolated at the beat time). The order of the AR model also determines the number of poles, or oscillations, in the frequency range. Modifying the AR coefficients is equivalent to changing the positions

[1] According to the Gaussian random-walk theory, the variance or the translational squared distance of one random variable in one dimension within a time period is linearly proportional to the associated diagonal entry of $\boldsymbol{W}$ and the total time traveled.

of the poles and reshaping the frequency response curve. With the time-varying AR coefficients $\{a_i(t)\}$ and $\{b_j(t)\}$ estimated from the point process filter, we can evaluate the dynamic frequency response of (11) at different ranges (LF, 0.04–0.15 Hz; HF, 0.15-min $\{0.5, 0.5/RR\}$ Hz, where $0.5/RR$ denotes the Nyquist sampling frequency).

In the case where COV is BP, the frequency-dependent baroreflex gain or BRS, characterized by $|H_{12}(f)|$, represents the frequency-dependent modulation effect of BP on the heartbeat, mediated by the neural autonomic reflex. In the case where COV is RP, $|H_{12}(f)|$ represents the frequency-dependent RSA gain.

3.5.2. Estimating the frequency response at the feedforward pathway

In the feedforward (RR → BP) pathway of **Figure 2**, the frequency response allows us to evaluate the impact of the heartbeat durations on the hemodynamics. In light of AR modeling in the feedback pathway, we can also model BP with a bivariate linear AR model

$$BP_k = c_0(k) + \sum_{i=1}^{p} c_i(k)\, BP_{k-i} + \sum_{i=1}^{p} d_i(k)\, \mu_{RR}(k-i), \quad (12)$$

where $\mu_{RR}(k-i)$ represents the estimated instantaneous R-R mean value at the time bin when BP-events occur. The coefficients $\{c_i(k)\}_{i=0}^{p}$ and $\{d_i(k)\}_{i=1}^{p}$ are dynamically tracked by a RLS filter. Unlike the point process filter, the update occurs only at the occurrence time of BP-events, although it is important to highlight that the point process framework allows for these innovations to be associated with the evolution of the heartbeat dynamics at the exact time when the hemodynamic changes occur, without having to wait for the next heartbeat to be observed. Similarly, the frequency response of the RR → BP pathway can be estimated as

$$H_{21}(f) = \frac{\sum_{i=1}^{p} d_i(k)\, z^{-i}\big|_{z=e^{j2\pi f}}}{1 - \sum_{i=1}^{p} c_i(k)\, z^{-i}\big|_{z=e^{j2\pi f}}}, \quad (13)$$

where f denotes the sampling rate (beat/s) for BP-BP intervals. Likewise, we can estimate the dynamic gain and phase of $H_{21}(f)$ at each single BP-event (whereas during between-events period, the coefficient estimates remain unchanged).

3.5.3. Estimating the dynamic R-R spectrum

Let $\mathcal{Q}_{RR}(f)$ denote the power spectrum of the R-R series. In the case of equation (6), $\mathcal{Q}_{RR}(f)$ is estimated by

$$\mathcal{Q}_{RR}(f,t) = \frac{\sigma^2_{RR}(t)}{\left|1 - \sum_{i=1}^{p} a_i(t)\, z^{-i}\right|_{z=e^{j2\pi f}}}. \quad (14)$$

In the case of equation (8), $\mathcal{Q}_{RR}(f)$ can be estimated by

$$\mathcal{Q}_{RR}(f,t) \approx \frac{\sigma^2_{RR}(t)}{\left|1 - \sum_{i=1}^{p} a_i(t)\, z^{-i}\right|_{z=e^{j2\pi f}}} + \frac{\left|\sum_{i=1}^{q} b_i(t)\, z^{-i}\right| \sigma^2_{BP}(t)}{\left|1 - \sum_{i=1}^{p} a_i(t)\, z^{-i}\right|_{z=e^{j2\pi f}}}. \quad (15)$$

From $\mathcal{Q}_{RR}$ we can also compute the time-varying LF/HF power ratio. Note that we have assumed that the variance $\sigma^2_{BP}(t)$ (estimated from the feedforward pathway) remains unchanged between two consecutive systolic BP values.

3.5.4. Estimating the dynamic coherence

In order to estimate the cross-spectrum in the context of a closed-loop system, we assume that the noise variance and the non-linear interactions in the feedforward and feedback loops are sufficiently small. From equation (11), we can estimate the cross-spectrum (between BP and RR) in the feedback loop as $\mathcal{C}_{uy}(f) \approx H_{12}(f)\mathcal{Q}_{BP}(f)$. As the coefficients $\{a_i(t)\}$ and $\{b_j(t)\}$ are iteratively updated in time, the point process filter produces an instantaneous estimate of BRS as well as the cross-spectrum. Similarly, from equation (13) we can estimate the cross-spectrum in the feedforward pathway: $\mathcal{C}_{yu}(f) \approx H_{21}(f)\mathcal{Q}_{RR}(f)$.

Furthermore, the instantaneous normalized cross-spectrum (i.e., coherence) can be computed as

$$\begin{aligned} \mathrm{Coh}(f,t) &= \frac{|\mathcal{C}_{uy}(f,t)|}{\sqrt{|\mathcal{Q}_{BP}(f,t)| \cdot |\mathcal{Q}_{RR}(f,t)|}} \\ &= \frac{\sqrt{|\mathcal{C}_{uy}(f,t)| \cdot |\mathcal{C}_{yu}(f,t)|}}{\sqrt{|\mathcal{Q}_{BP}(f,t)| \cdot |\mathcal{Q}_{RR}(f,t)|}} \\ &= \sqrt{|H_{12}(f,t)\, H_{21}(f,t)|}, \end{aligned} \quad (16)$$

where $|\cdot|$ denotes the modulus of a complex variable. The second equality in equation (16) holds due to the fact that $\mathcal{C}_{yu}(f) = \mathcal{C}^*_{uy}(f) = H_{12}(-f)\mathcal{Q}_{BP}(f)$, where *denotes the Hermitian operator (note that $|\mathcal{C}_{yu}| = |\mathcal{C}_{uy}|$ and has anti-phase against each other). The third equality indicates that the time-varying coherence function can be expressed by the multiplication of two (feedback and feedforward) time-varying transfer functions (Zhao et al., 2005), computed from equations (11 and 13), respectively.

The time-varying closed-loop coherence function $\mathrm{Coh}(f,t)$ can be computed at very fine timescales by using two adaptive filters (i.e., the point process filter at the feedback pathway, and the RLS filter at the feedforward pathway) either synchronously or asynchronously, several studies have examined its properties (e.g., stability, numerical bound) in detail (Porta et al., 2002; Zhao et al., 2005, 2007).

3.6. NON-LINEARITY ASSESSMENT

Heartbeat dynamics are well known to be non-linear (Christini et al., 1995; Chon et al., 1996, 1997; Zhang et al., 2004; Chen et al., 2010a). In the literature, various non-linear indices such as the Lyapunov exponent, the fractal exponent, or the approximate entropy, have been proposed to characterize the non-linear behavior of the underlying physiological system (Peng et al., 1995; Ivanov et al., 1999; Akay, 2000; Teich et al., 2001; Costa et al., 2002; Struzik et al., 2004; Voss et al., 2009). It has been suggested that such non-linearity indices might provide informative indicators for diagnosing cardiovascular diseases (Poon and Merill, 1997; Goldberger et al., 2002; Tulppo et al., 2005; Atyabi et al., 2006).

Motivated by the importance of quantifying the contribution of non-linearity to HRV and the heartbeat dynamics, we have proposed a quantitative index based on the *spectrum-bispectrum ratio* (Chen et al., 2010a, 2011a)

$$\text{Ratio} = \frac{\text{(cross) spectrum}}{\text{(cross) spectrum} + \text{(cross) bispectrum}}, \tag{17}$$

The nominator of equation (17) corresponds to the R-R spectrum (or cross-spectrum between RR and COV in the presence of covariate), whereas the denominator corresponds to the sum of the R-R spectrum and R-R bispectrum (or cross-spectrum and cross-bispectrum in the presence of covariate). The above-defined ratio is frequency-dependent, and it is dimensionless and bounded between 0 and 1.

In both cases, the instantaneous ratio is derived as (see Chen et al., 2010a, 2011a) for assumptions and details)

$$\rho(t) = \frac{1}{1 + 2\left|\mathbf{h}(t)\right| \cdot \left|\mathcal{Q}_{\text{RR}}(f,t)\right|}, \tag{18}$$

where $|\mathbf{h}(t)| = \sqrt{\sum_k \sum_l h_{kl}^2(t)}$. The spectrum norm defines the area integrated over the frequency range under the spectral density curve. When the non-linear or bilinear interaction is small, the coefficients $\{h_{kl}\}$ are small, and the ratio is close to 1.

3.7. MODELING NON-STATIONARY WITH THE ARIMA MODEL

In time series modeling, it is common to "detrend" a time series by taking differences if the series exhibits undesired non-stationary features. The autoregressive integrated moving average (ARIMA) process may provide a suitable framework to achieve such a goal (Vu, 2007). Simply, the original time series is applied by a difference operator (one or more times) until the non-stationary trends are not observed in the ultimate series. This is essentially equivalent to applying a high-pass filter to get rid of the slow oscillation. Non-stationary trends are often observed in the epochs of experimental recordings of R-R intervals and/or other physiological measures, especially during the periods of intervention by external factors (e.g., drug administration, ventilation).

Motivated by this idea, we define the "increment of R-R series" $\{\delta RR_{t-i}\} \equiv \{RR_{t-i} - RR_{t-i-1}\}$ and the "increment of COV series" $\{\delta COV_{t-i}\} \equiv \{COV_{t-i} - COV_{t-i-1}\}$, and model the instantaneous heartbeat interval mean by the following new equation (Chen et al., 2010b)

$$\mu_{\text{RR}}(t) = RR_{t-1} + \sum_{i=1}^{p} a_i(t)\,\delta RR_{t-i} + \sum_{i=1}^{q} b_i(t)\,\delta COV_{t-i}. \tag{19}$$

The new series $\{\delta RR_{t-i}\}$ and $\{\delta COV_{t-i}\}$ have zero mean and are combined within a new (noise-free) AR model in parallel with equation (8). Note that the $a_0(t)$ term in equation (8) has been replaced by RR_{t-1} in equation (19).

From equation (19), we can compute the *differential frequency response* between δRR and δCOV

$$\tilde{H}_{12}(f,t) = \frac{\sum_{i=1}^{q} b_i(t)\, z^{-i}\big|_{z=e^{j2\pi f_2}}}{1 - \sum_{i=1}^{p} a_i(t)\, z^{-i}\big|_{z=e^{j2\pi f_1}}}, \tag{20}$$

When using BP as covariate, we call $|\tilde{H}_{12}|$ as the *differential BRS*; when using RP as covariate, $|\tilde{H}_{12}|$ is referred to as the *differential RSA*. Rearranging the terms $\{a_i(t)\}$ and $\{b_j(t)\}$ in equation (19) and applying the frequency analysis further yields the frequency response (in the conventional sense)

$$H_{12}(f,t) = \frac{\begin{array}{l} b_1(t)\, z^{-1} + b_q(t)\, z^{-q} \\ \quad + \sum_{i=2}^{q-1} (b_i(t) - b_{i-1}(t))\, z^{-i}\big|_{z=e^{j2\pi f_2}} \end{array}}{\begin{array}{l} 1 - (1 + a_1(t))\, z^{-1} - a_p(t)\, z^{-p} \\ \quad - \sum_{i=2}^{p-1} (a_i(t) - a_{i-1}(t))\, z^{-i}\big|_{z=e^{j2\pi f_1}} \end{array}},$$

Note: It shall be pointed out that, due to the absence of the driven noise (equations 6–9, and 19), the terms AR, ARMA, ARX, or ARIMA models defined in this paper do not coincide with an AR-type model in the traditional sense. These models can be viewed as distinctive AR-type models with vanishing noise variance. In other words, as the uncertainty is embedded in the probability structure, we did not consider the noise component in modeling the mean.

3.8. MODEL ORDER SELECTION AND GOODNESS-OF-FIT TESTS

Once a model is selected, we would need to predetermine the model order $\{p, q\}$ of equations (6–9) in the selected Volterra series expansion. In general, the need of a tradeoff between model complexity and goodness-of-fit arises when a point process model is considered. In practice, the order of the model may be determined based on the *Akaike information criterion* (AIC; by pre-fitting a subset of the data using either the point process filter or the local likelihood method (Loader, 1999; Barbieri et al., 2005) as well as the *Kolmogorov-Smirnov* (KS) statistic (Brown et al., 2003) in the *post hoc* analysis. For different values p and q, we can compare the AIC and choose the parameter setup with the minimum AIC value. Let $\mathcal{L}$ designate the log-likelihood value obtained from the pre-fitted data, the AIC is defined as

$$\text{AIC} = -2\mathcal{L} + 2dim(\boldsymbol{\xi}) \tag{21}$$

where $dim(\boldsymbol{\xi})$ denotes the dimensionality of unknown parameter vector $\boldsymbol{\xi}$ used in the probability model of the heartbeat interval. In the presence of a non-linear or bilinear AR model, once the order is determined, the initial Volterra coefficients will be estimated by a least squares method (Westwick and Kearney, 2003). Specifically, the coefficients $\{a_i\}$ are optimized by solving a Yule-Walker equation for the linear part using the first few hundreds sample points, and the coefficients $\{h_{ij}\}$ are estimated by fitting the residual error via least squares. For the non-linear and bilinear models (equations 7 and 9), we use a sequential estimation instead of a joint estimation procedure for fitting the Volterra coefficients, since we prefer to preserve the interpretation of the linear AR coefficients. A joint estimation procedure is possible based on orthogonal

projection, cross-correlation, or least squares (Marmarelis, 1993; Westwick and Kearney, 2003), although such method may destroy the structure described by the linear AR coefficients.

The goodness-of-fit of the point process model is based on the KS test (Brown et al., 2003). Given a point process specified by J discrete events: $0 < u_1 < \ldots < u_J < T$, the random variables $z_j = \int_{u_{j-1}}^{u_j} \lambda(\tau)d\tau$ are defined for $j = 1, 2, \ldots, J-1$. If the model is correct, then the variables $v_j = 1 - \exp(-z_j)$ are independent, uniformly distributed within the interval $[0, 1]$, and the variables $g_j = \Phi^{-1}(v_j)$ (where $\Phi(\cdot)$ denotes the cumulative distribution function (cdf) of the standard Gaussian distribution) are sampled from an independent standard Gaussian distribution. To conduct the KS test, the v_js are sorted from smallest to largest, and plotted against the cdf of the uniform density defined as $(j - 0.5)/J$. If the model is correct, the points should lie on the 45° line. The 95% confidence interval lines are defined as $y = x \pm \frac{1.36}{(J-1)^{1/2}}$. The KS distance, defined as the maximum distance between the KS plot and the 45° line, is also used to measure lack-of-fit between the model and the data. The autocorrelation function of the g_js: $\mathrm{ACF}(m) = \frac{1}{J-m}\sum_{j=1}^{J-m} g_j g_{j+m}$, can also be computed. If the g_j s are independent, $\mathrm{ACF}(m)$ shall be small for any lag m, which is within the 95% confidence interval $\frac{1.96}{(J-1)^{1/2}}$ around 0.

3.9. EXPERIMENTAL PROTOCOL AND DATA

A total of 15 healthy volunteer subjects (mean age 24 ± 4), gave written consent to participate in this study approved by the Massachusetts General Hospital (MGH) Department of Anesthesia and Critical Clinical Practices Committee, the MGH Human Research Committee and the MGH General Clinical Research Center. Subjects were evaluated with a detailed review of his/her medical history, physical examination, electrocardiogram, chest X-ray, a urine drug test, hearing test, and for female subjects, a pregnancy test. Any subject whose medical evaluation did not allow him or her to be classified as American Society of Anesthesiologists (ASA) Physical Status I was excluded from the study. Other exclusion criteria included neurological abnormalities, hearing impairment, and use of either prescribed or recreational psychoactive drugs. Intravenous and arterial lines were placed in each subject. Propofol was infused intravenously using a previously validated computer controlled delivery system running STANPUMP (a computer controlled delivery system; Shafer et al., 1988) connected to a Harvard 22 syringe pump (Harvard Apparatus, Holliston, MA), using the well-established pharmacokinetic and pharmacodynamic models (Schnider et al., 1998, 1999). In Subject 1, five effect-site target concentrations (0.0, 1.0, 2.0, 3.0, and 4.0 μg/ml) were each maintained for about 15 min respectively, where concentration level 0 corresponds to the conscious and wakefulness baseline. In the remainder of subjects, an additional effect-site target concentration of 5.0 μg/ml was administered. Capnography, pulse oximetry, ECG, and arterial blood pressure were monitored continuously by an anesthesiologist team throughout the study. Bag-mask ventilation with 30% oxygen was administered as needed in the event of propofol-induced apnea. Because propofol is a potent peripheral vasodilator, phenylephrine was administered intravenously to maintain mean arterial blood pressure (ABP) within 20% of the baseline value. ECG and ABP were recorded at a sampling rate of 1 kHz using a PowerLab ML795 data acquisition system (ADInstruments, Inc., Colorado Springs, CO). Four recordings (Subjects #6, 11, 12, 14) were excluded for analysis either because the subjects fell asleep during the experimental behavioral protocol or because of poor quality of the data recordings.

4. RESULTS

Applications of the proposed point process framework to the experimental data led to instantaneous assessment of HRV, RSA, BRS, and of non-linearity of heartbeat dynamics in healthy subjects under progressive stages of propofol anesthesia (Chen et al., 2009b, 2010b, 2011a). All instantaneous indices are estimated to accommodate the non-stationary nature of the experimental recordings. Overall, our observations have revealed interesting dynamic trends across the experiment for individual subjects. Due to the tutorial nature of the current article, only three subjects (Subjects 5, 9, 15) are portrayed here for illustration purpose, detailed group comparison statistics can be found in (Chen et al., 2011a). The inverse Gaussian point process model for heartbeat intervals is considered in all the examples reported here, and all instantaneous indices are estimated using a point process filter with $\Delta = 5$ ms temporal resolution.

4.1. TRACKING EXAMPLES AND ESTIMATED INDEX STATISTICS

Figure 3 shows results from a subject (Subject 15) transitioning from level 0 to level 3 (several time intervals are replaced by shaded areas to appropriately portray all transitions of interest in one panel). In this subject, HRV, RSA, and BRS progressively decrease with increasing propofol administration, accompanied by a relevant increase in linear cardiorespiratory coupling as a result of dispensation of the first propofol bolus. Two sharp drops in BRS (within the LF range) are also observed at the level $0 \rightarrow 1$ and $1 \rightarrow 2$ transitions upon increasing the target drug concentration level. Meanwhile, RSA (within the HF range) also drops accordingly. Interestingly, the ratio ρ (computed with RP as COV) increases from level 0 to level 1 and then remains steady, suggesting that the non-linearity at the HF range slightly decreases with propofol administration. **Table 2** shows a summary of the averaged statistics of the estimated instantaneous indices of interest within levels 1–3 as compared with baseline (level 0).

In a second example, **Figure 4** shows a different subject (Subject 9) where, after the initial propofol administration, phenylephrine is administered to compensate a critical drop in blood pressure, followed by artificial ventilation. In this case, a sharp decrease in RSA is observed with anesthetic intervention, respiratory coupling is then partly restored, but systolic BP progressively decreases to critical levels, possibly due to baroreflex failure. After phenylephrine is administered ($\sim$2960 s), BRS and systolic BP slightly recover, but fail to go back to baseline levels. During the period of apnea, artificial ventilation reflects in RSA variability and acts to restore HRV (as seen by the increase in σ_{HR}), only partly succeeding in raising BP levels via the feedforward pathway. **Table 2** shows a summary of the averaged statistics of the estimated instantaneous indices for levels 1–3 as compared with the baseline (level 0), accompanied by a portrayal of the instantaneous dynamics observed within each level for the considered indices (**Figure 5**), confirming the progressive decrease in HRV, RSA, and BRS, as

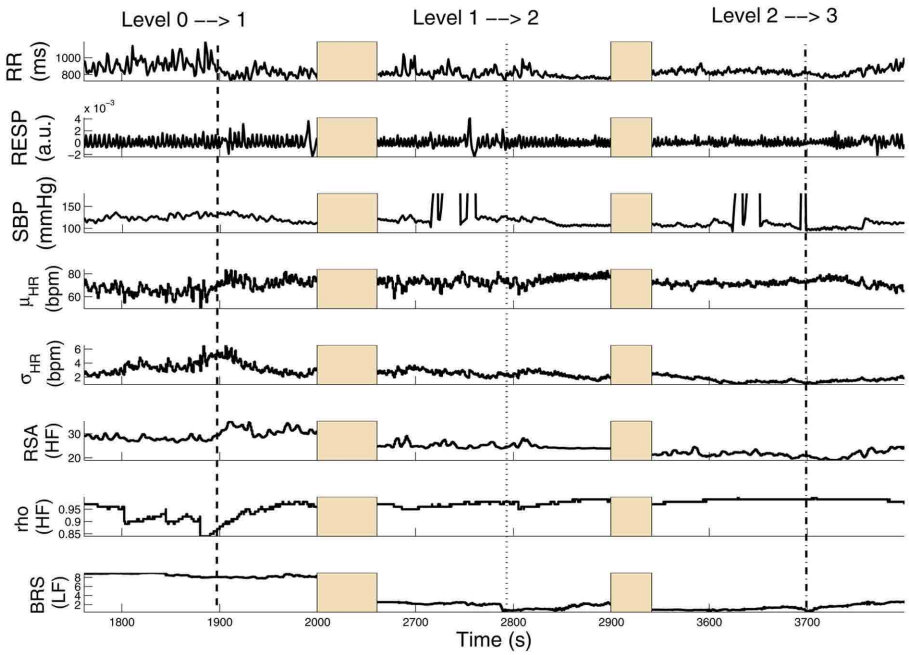

FIGURE 3 | Tracking results of various instantaneous indices for Subject 15. Three transient periods (level 0 → 1, level 1 → 2, level 2 → 3) are shown (Chen et al. (2011b), Proceedings of EMBC. Reprinted with permission, Copyright ©2011 IEEE).

Table 2 | Averaged statistics of the estimated instantaneous indices in the general anesthesia protocol (level 0–3 for two selected subjects).

	μ_{HR} (bpm)	σ_{HR} (bpm)	RSA (a.u.)	ρ	BRS (mmHg/ms)
SUBJECT 15					
Level 0	66.8 ± 4.5	4.41 ± 0.88	39.0 ± 2.9	0.89 ± 0.03	6.16 ± 2.96
Level 1	75.1 ± 3.0*	2.09 ± 0.48*	15.2 ± 0.5*	0.97 ± 0.01*	3.34 ± 0.41
Level 2	74.7 ± 2.9*	1.72 ± 0.43*	11.1 ± 0.5*	0.98 ± 0.01*	2.91 ± 0.62*
Level 3	61.8 ± 5.2	3.82 ± 0.83	8.7 ± 1.5*	0.82 ± 0.07	10.07 ± 0.65*
SUBJECT 9					
Level 0	61.2 ± 5.8	3.19 ± 0.92	20.8 ± 1.7	0.88 ± 0.05	8.55 ± 3.24
Level 1	61.8 ± 2.7	2.25 ± 0.42	34.7 ± 1.5*	0.95 ± 0.01*	7.33 ± 1.26*
Level 2	64.3 ± 4.1	2.65 ± 1.01	21.6 ± 4.2	0.97 ± 0.01*	3.77 ± 0.64*
Level 3	67.1 ± 2.5*	1.94 ± 0.67	16.1 ± 0.85*	0.85 ± 0.06	3.28 ± 0.42*

The ρ index here was computed based on the respiratory measure as covariate. RSA and ρ are computed in the HF range (0.15-min {0.5, 0.5/RR} Hz), while BRS is computed in the LF range (0.04–0.15 Hz). RSA has an arbitrary unit since the recorded respiratory signal was non-calibrated. ∗Significant $p < 0.05$ by pairwise rank-sum test (compared to level 0).

well as the linear cardiorespiratory coupling increase in the first two levels of propofol anesthesia.

In addition, for pairwise comparison we also compute the mean statistic (averaged over time in each epoch) of all instantaneous indices during level 0 and level 1 drug concentrations for all 11 subjects. **Figure 6** show the scatter plots for the mean HR, HRV, and BRS (LF range) values. More details can also be found in (Chen et al., 2011a).

4.2. EXAMPLE OF APPLYING THE ARIMA MODEL

Next, we illustrate how the use of ARIMA modeling (Section 3.7) can improve identification in the presence of highly non-stationary scenarios. The left panels of **Figure 7** show the raw R-R interval series and systolic BP series are shown. In the considered subject (Subject 5), the systolic BP series has a decreasing trend (dropping from around 160–130 mmHg) within about 150 s, showing a high degree of non-stationarity (with a decreasing mean statistic along time). In contrast, the first-order difference series δRR and δSBP are stationary and have steady zero mean along time. As expected, modeling the mean heartbeat interval using equation (19) is more desirable than using equation (8). To verify our hypothesis, we have used the same model order ($p = q = 8$) for these two equations, and applied the point process model to fit the observed R-R and systolic BP series. The goodness-of-fit

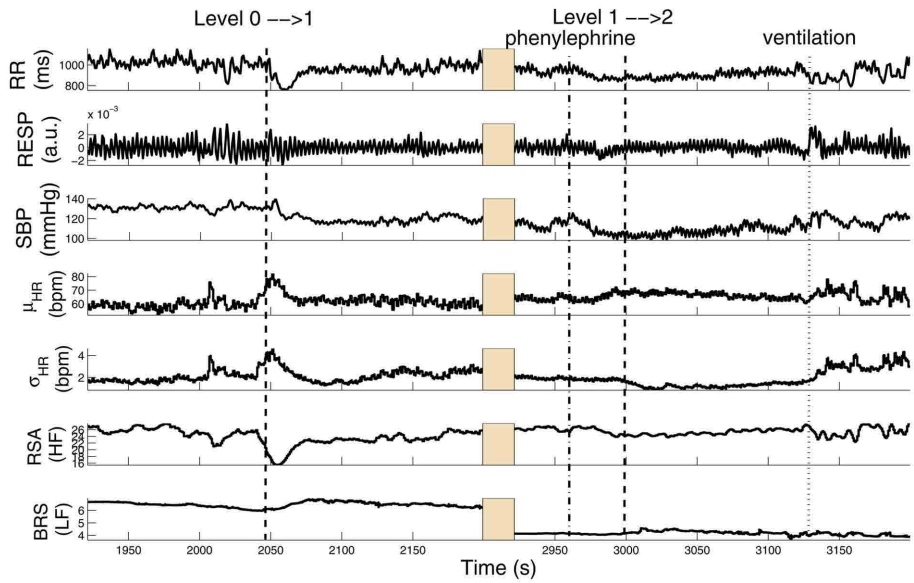

FIGURE 4 | Tracking results of various instantaneous indices for Subject 9. The two dashed lines (∼2010 and ∼3000 s) mark the drug concentration level 0 → 1 (i.e., propofol administration onset time) and level 1 → 2, respectively. The dotted dashed line (∼2960 s) marks the time when phenylephrine was administered; and the dotted line (∼3125 s) marks the time of hand ventilation (Chen et al. (2011b), Proceedings of EMBC. Reprinted with permission, Copyright ©2011 IEEE).

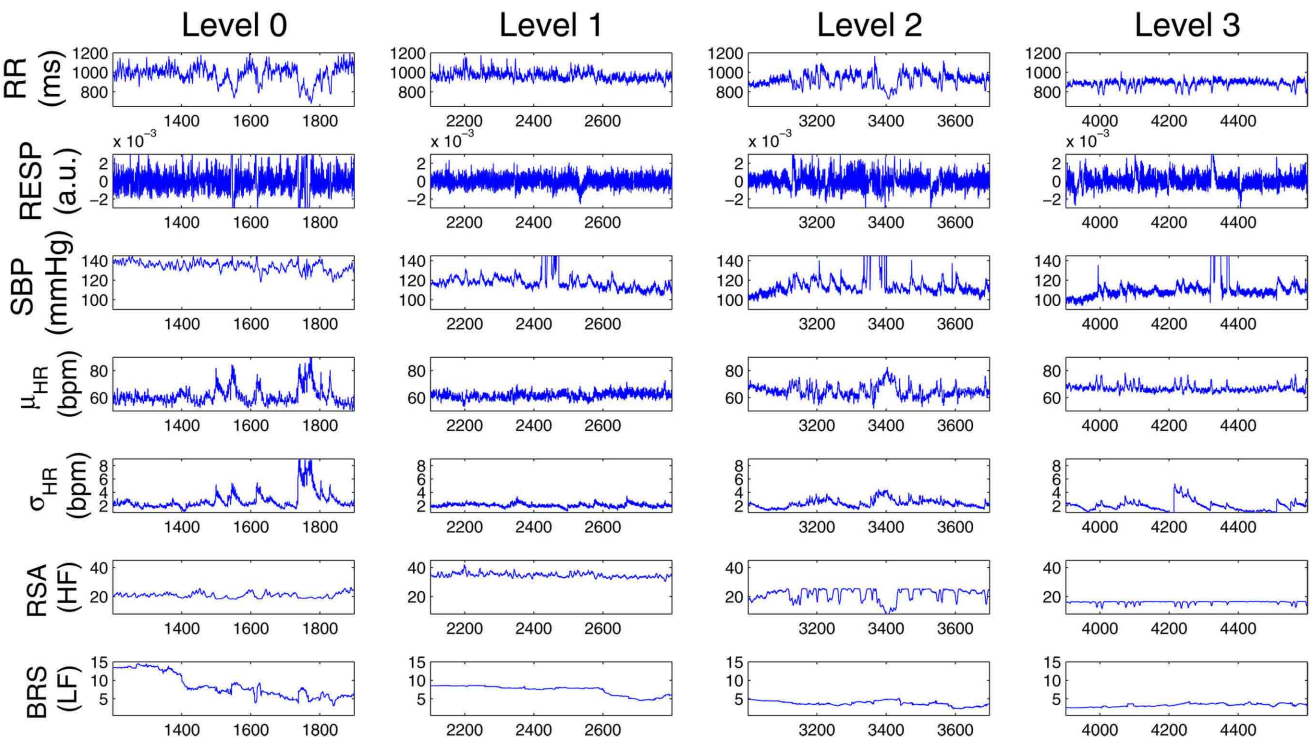

FIGURE 5 | Comparison of the estimated instantaneous indices from four drug concentration levels (0–3) for Subject 9. Note that at each row, the vertical axes at all four panels have the same scale.

assessment shows that the ARIMA modeling improves the model fit with decreasing KS distance (from 0.0893 to 0.0513) in the KS test. **Figure 8** shows the KS plot (including the KS statistic comparison) and the autocorrelation plot based on the ARIMA modeling.

The fact that the curves fall within the 95% confidence intervals in both the KS and the autocorrelation plots indicates a good model description of the point process heartbeat events.

4.3. SENSITIVITY ANALYSIS

Finally, we perform sensitivity analysis to test the robustness of the proposed point process approach and the choice of parameters. Two issues are examined here. One is the choice of probability distribution (the inverse Gaussian against the Gaussian distribution) used for the R-R intervals. The other is the choice of the parameters used in the model and the point process filter.

To illustrate the first issue, we select the raw R-R intervals from one epoch at the level 0 drug concentration. Under the same point process framework, we fit the data with both the inverse Gaussian and Gaussian distributions for the inter-event intervals. Upon fitting the data, we compare their corresponding KS statistics. From the empirical data histogram (**Figure 9A**), it can be noticed that the distribution of the R-R intervals is asymmetric and slightly skewed (with a longer tail at the high value range). The Q-Q plot analysis also confirms that the inverse Gaussian distribution provides a better fit for the data (**Figures 9C,D**). As expected, the final KS statistic improves by using the inverse Gaussian (KS distance: 0.0562) rather than the Gaussian distribution (KS distance: 0.0719).In this case, although the fitted results from two models are very similar, only the inverse Gaussian model passes the KS test, i.e., its KS plot completely falls within the 95% confidence interval (**Figure 9E**).

To illustrate the second issue of parameter estimation, the AR-type model parameters are initialized based on a subset of the same data used in **Figure 9A** at the start of the recordings. The data sample size used for initialization varies between 100, 200, and 300 (the time duration varies depending on the HR). The noise covariance matrix $\boldsymbol{W}$ in the filtering equation determines the level of parameter fluctuation at the every time step of $\Delta = 5$ ms. For simplicity, we select different scale levels for the elements of $\boldsymbol{W}$ related to the AR parameters, on the order of 10^{-6}, 10^{-7}, and 10^{-8}. Using the inverse Gaussian model, we compare the fitting KS statistic values under various parameter initialization setups and show the comparative result in **Figure 9F**. As seen, under a wide range of parameter choices, the fitted results are rather robust. The robustness of the performance can be ascribed to the flexibility of the random-walk model and to the fact that the tracking performance is insensitive to the *exact* value of the noise covariance matrix. Nevertheless, too large error covariance values will induce instability in the filtering operation, and cause unsatisfactory tracking performances. Finding an optimal range of the noise covariance matrix often involves a trial-and-error process based on a subset of the available recordings.

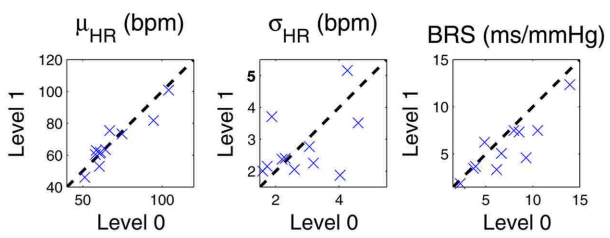

FIGURE 6 | Scatter plots of the mean statistic (averaged over time in each epoch) of instantaneous HR, HRV, and BRS (LF range) indices during level 0 and level 1 drug concentrations for all 11 subjects. The dashed diagonal indicates a 45° line.

5. DISCUSSION

Dynamic assessment of cardiovascular control is of fundamental importance to monitor physiological states that may change dramatically in very short time intervals. We have devised a unified point process probabilistic framework to assess heartbeat dynamics and autonomic cardiovascular control by using the heartbeat interval occurrences extracted from ECG recordings, together with other cardiovascular measures such as ABP and

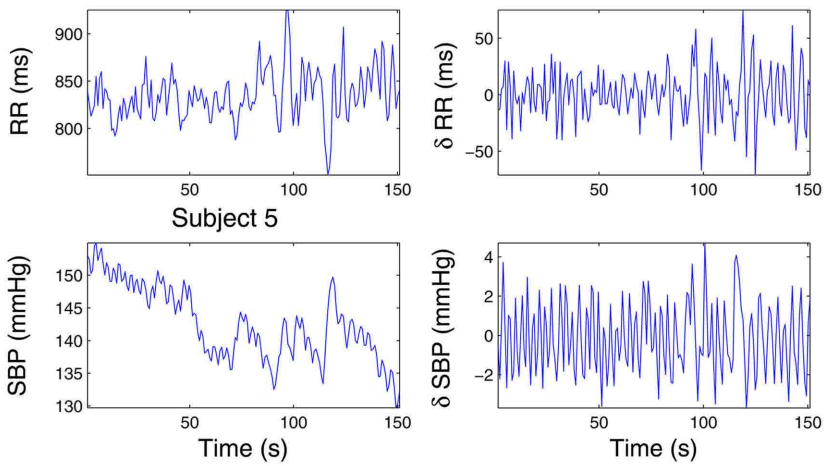

FIGURE 7 | Experimental R-R interval series and systolic BP (SBP) series (left panels) from one recording epochs during level 1 propofol concentration. Their corresponding incremental series are also shown at the right panels. The raw SBP series has a decreasing trend (Chen et al. (2010b), Proceedings of EMBC. Reprinted with permission, Copyright ©2010 IEEE).

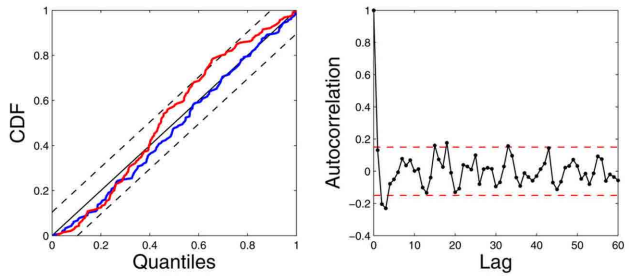

FIGURE 8 | The estimated instantaneous indices from the data of Subject 5 (level 1 epoch) and the associated KS plot (left) and the autocorrelation plot (right). The KS statistic is improved from 0.0893 (standard model, red curve) to 0.0513 (ARIMA model, blue curve; Chen et al. (2010b), Proceedings of EMBC. Reprinted with permission, Copyright ©2010 IEEE).

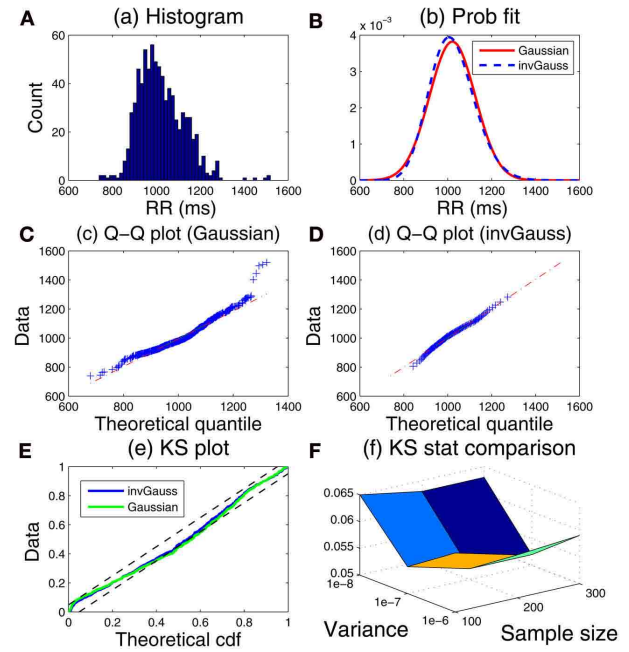

FIGURE 9 | (A) Histogram of the R-R intervals from one selected epoch. **(B)** Maximum-likelihood-fitted Gaussian and inverse Gaussian distributions for the R-R intervals. **(C,D)** Q-Q plots for the Gaussian and inverse Gaussian distribution, respectively. **(E)** Comparative KS plots of point process model assessment using the inverse Gaussian and Gaussian distributions. **(F)** Comparison of KS statistics with different parameter initialization setups.

respiration. The proposed point process framework enables us to estimate instantaneous heartbeat dynamics (HR and HRV) as well as other cardiovascular functions (BRS and RSA) at fine temporal resolution. The Wiener-Volterra series expansion allows to model the instantaneous heartbeat interval based on the previously observed R-R intervals and selected cardiovascular covariates. The online estimation (adaptive point process filter or local likelihood method) allows us to track the fast transient dynamics of the indices. Currently, the model parameters are initialized based on small subset of recordings, and then allowed to be adapted based on an online estimation method. In the presence of high non-stationarity (e.g., baseline shift due to drugs or other effects), special attention is required in both modeling (such as using the ARIMA model) and parameter initialization (such as reinitializing the parameters based on observed informative markers).

Some limitations of our approach are worth mentioning. Currently, we are using the inverse Gaussian distribution for modeling the random heartbeat intervals. The inverse Gaussian distribution is a good candidate since it is more robust in modeling outliers due to its long-tailed behavior. However, just like many asymmetric long-tailed distributions (e.g., lognormal), the inverse Gaussian distribution can only capture outliers in the high value range (i.e., the long tail lies in the high percentile of the distribution). Therefore, it is insufficient to characterize potential outliers in the low-value range (i.e., outliers' values smaller than the mean statistic). Another limitation of the current approach is that we have not separated the influences of blood pressure from that of respiration on HRV, which could produce some estimation bias for both BRS and RSA due to simplification of our model. How to integrate these physiological covariates all together still remains the subject of future investigation. One possibility is to consider a trivariate model. Another possibility is to incorporate a continuous-valued latent input that modulates $\mu_{RR}(t)$ within the point process model, and might account for the non-modeled physiological effect; in the maximum likelihood framework, for example, the latent variable can be inferred using an EM algorithm (Smith and Brown, 2003).

In applying the proposed point process framework to physiological data under a general anesthesia protocol, our outcomes have revealed important dynamics involved with procedures of induction of anesthesia. The study of transient periods due to pharmacological and physical intervention has demonstrated the capacity of the point process filter to quickly capture fast physiological changes within the cardiovascular system. For example, significant sudden variations in the instantaneous BRS in coincidence with interventional maneuvers suggests that baroreflex responses are supposedly triggered by sharp disturbances affecting the control system, whereas the clear reduction of BRS in correspondence to increasing induction of anesthesia might suggest that baroreflex responses are reset with propofol to control HR at a lower BP, and that BRS further decreases after administration as a result. The shift in the HR/BP set point may also reflect the propofol's systemic vasodilatory effect, whereas baroreflex impairment is most likely the result of disruption of cardiac control within the central nervous system. The instantaneous indices associated with respiration further suggest that RSA gradually decreases from baseline after administration of propofol anesthesia, that RSA is generally suppressed by phenylephrine, and that the linear interactions within cardiorespiratory control remain stable or increase (Chen et al., 2009b). Specifically, RSA is likely to be mediated by withdrawal of vagal efferent activity resulting from either baroreflex response to spontaneous BP fluctuations, or respiratory gating of central arterial baroreceptor and chemoreceptor afferent inputs. From baseline to Level 1 we also observed an increase of non-linearity in the bilinear interactions between RR and systolic BP, accompanied by a significant decrease in linear coherence between these two series (Chen et al., 2011a). This seems to indicate that the nonlinear component of the heartbeat dynamics during anesthesia is mainly generated from the cardiovascular (baroreflex) loop, with a

more stable linear interaction maintained within cardiorespiratory coupling. It is also possible that the respiratory system indirectly influences HR by modulating the baroreceptor and chemoreceptor input to cardiac vagal neurons although, as in every cardiovascular system identification study, it is difficult to disentangle the separate influence of BP from the influence of respiration on HRV.

In light of these promising results, future directions of our research are aimed at further development and integration of a set of algorithms to preprocess the recorded signals prior to application of the modeling framework, to perform a robust and automated classification and correction of ECG-derived heartbeats, and to achieve an automatic determination procedure for tuning and initialization of the model parameters, with the final goal to devise a monitoring tool for real-time cardiovascular assessment.

CONCLUSION

In conclusion, we have appraised a comprehensive point process probabilistic framework to simultaneously assess linear and nonlinear indices of HRV, together with important cardiovascular functions of interest. To date, the proposed point process framework has been successfully applied to a wide range of experimental protocols (Barbieri et al., 2005; Barbieri and Brown, 2006; Chen et al., 2009a, 2010a, 2011a; Kodituwakku et al., 2012). Although all of data analyses have been done in off-line laboratory settings, all of the developed statistical models pose a solid basis for devising a real-time quantitative tool to bestow vital indicators for ambulatory monitoring in clinical practice. Particularly in general anesthesia settings, the proposed instantaneous indices may provide a valuable quantitative assessment of the interaction between heartbeat dynamics and hemodynamics during general anesthesia, and they could be monitored intraoperatively in order to improve drug administration and reduce side-effects of anesthetic drugs.

ACKNOWLEDGMENTS

The authors thank L. Citi, K. Habeeb, G. Harrell, R. Merhar, E. T. Pierce, A. Salazar, C. Tavares, and J. Walsh (Massachusetts General Hospital) for assistance with data collection and interpretation. Preliminary results of this article have been presented in *Proc. IEEE EMBC*'10, Buenos Aires, and *Proc. IEEE EMBC*'11, Boston, MA. The work was supported in part by NIH Grants R01-HL084502 (Riccardo Barbieri), DP1-OD003646 (Emery N. Brown), K25-NS05758 (Patrick L. Purdon), DP2-OD006454 (Patrick L. Purdon), as well as a CRC UL1 grant RR025758.

REFERENCES

Akay, M. (2000). *Nonlinear Biomedical Signal Processing*: *Dynamic Analysis and Modeling*, Vol. 2. New York: Wiley-IEEE Press.

Atyabi, F., Livari, M. A., Kaviani, K., and Tabar, M. R. R. (2006). Two statistical methods for resolving healthy individuals and those with congestive heart failure based on extended self-similarity and a recursive method. *J. Biol. Phys.* 32, 489–495.

Barbieri, R., and Brown, E. N. (2006). Analysis of heart beat dynamics by point process adaptive filtering. *IEEE Trans. Biomed. Eng.* 53, 4–12.

Barbieri, R., Matten, E. C., Alabi, A. A., and Brown, E. N. (2005). A point-process model of human heartbeat intervals: new definitions of heart rate and heart rate variability. *Am. J. Physiol. Heart Circ. Physiol.* 288, 424–435.

Barbieri, R., Parati, G., and Saul, J. P. (2001). Closed- versus open-loop assessment of heart rate baroreflex. *IEEE Eng. Med. Biol. Mag.* 20, 33–42.

Baselli, G., Cerutti, S., Civardi, S., Malliani, A., and Pagani, M. (1988). Cardiovascular variability signals: towards the identification of a closed-loop model of the neural control mechanisms. *IEEE Trans. Biomed. Eng.* 35, 1033–1046.

Berntson, G. G., Bigger, J. T., Eckberg, D. L., Grossman, P., Kaufmann, P. G., Malik, M., Nagaraja, H. N., Porges, S. W., Saul, J. P., Stone, P. H., and van der Molen, M. W. (1997). Heart rate variability: origins, methods, and interpretive caveats. *Psychophysiology* 34, 623–648.

Brockwell, A. E., Rojas, A., and Kass, R. E. (2004). Recursive Bayesian decoding of motor cortical signals by particle filtering. *J. Neurophysiol.* 91, 1899–1907.

Brown, E. N., Barbieri, R., Eden, U. T., and Frank, L. M. (2003). "Likelihood methods for neural data analysis," in *Computational Neuroscience: A Comprehensive Approach*, ed. J. Feng (London: CRC Press), 253–286.

Brown, E. N., Frank, L. M., Tang, D., Quirk, M. C., and Wilson, M. A. (1998). A statistical paradigm for neural spike train decoding applied to position prediction from ensemble firing patterns of rat hippocampal place cells. *J. Neurosci.* 18, 7411–7425.

Chen, Z., Brown, E. N., and Barbieri, R. (2008). "A study of probabilistic models for characterizing human heart beat dynamics in autonomic blockade control," in *Proc. ICASSP'08*, Las Vegas, NV, 481–484.

Chen, Z., Brown, E. N., and Barbieri, R. (2009a). Assessment of autonomic control and respiratory sinus arrhythmia using point process models of human heart beat dynamics. *IEEE Trans. Biomed. Eng.* 56, 1791–1802.

Chen, Z., Purdon, P. L., Pierce, E. T., Harrell, G., Walsh, J., Salazar, A. F., Tavares, C. L., Brown, E. N., and Barbieri, R. (2009b). "Linear and nonlinear quantification of respiratory sinus arrhythmia during propofol general anesthesia," in *Proceedings of IEEE 31st Annual Conference Engineering in Medicine and Biology (EMBC'09)*, Minneapolis, MN, 5336–5339.

Chen, Z., Brown, E. N., and Barbieri, R. (2010a). Characterizing nonlinear heartbeat dynamics within a point process framework. *IEEE Trans. Biomed. Eng.* 57, 1335–1347.

Chen, Z., Purdon, P. L., Brown, E. N., and Barbieri, R. (2010b). "A differential autoregressive modeling approach within a point process framework for non-stationary heartbeat intervals analysis," in *Proceedings of IEEE 32nd Annual Conference Engineering in Medicine and Biology (EMBC'10)*, Buenos Aires, 3567–3570.

Chen, Z., Purdon, P. L., Pierce, E. T., Harrell, G., Walsh, J., Brown, E. N., and Barbieri, R. (2011a). Dynamic assessment of baroreflex control of heart rate during induction of propofol anesthesia using a point process method. *Ann. Biomed. Eng.* 39, 260–276.

Chen, Z., Citi, L., Purdon, P. L., Brown, E. N., and Barbieri, R. (2011b). "Instantaneous assessment of autonomic cardiovascular control during general anesthesia," in *Proceedings of IEEE 33rd Annual Conference Engineering in Medicine and Biology (EMBC'11)*, Boston, MA, 8444–8447.

Chon, K. H., Mukkamala, R., Toska, K., Mullen, T. J., Armoundas, A. A., and Cohen, R. J. (1997). Linear and nonlinear system identification of autonomic heart-rate modulation. *IEEE Eng. Med. Biol. Mag.* 16, 96–105.

Chon, K. H., Mullen, T. J., and Cohen, R. J. (1996). A dual-input nonlinear system analysis of autonomic modulation of heart rate. *IEEE Trans. Biomed. Eng.* 43, 530–540.

Christini, D. J., Bennett, F. M., Lutchen, K. R., Ahmed, H. M., Hausdofi, J. M., and Oriol, N. (1995). Application of linear and nonlinear time series modeling to heart rate dynamics analysis. *IEEE Trans. Biomed. Eng.* 42, 411–415.

Costa, M., Goldberger, A. L., and Peng, C.-K. (2002). Multiscale entropy analysis of complex physiologic time series. *Phys. Rev. Lett.* 89, 068102.

Daley, D. J., and Vere-Jones, D. (2007). *An Introduction to the Theory of Point Processes*, Vol. 1, 2. New York: Springer.

De Boer, R. W., Karemaker, J. M., and Strackee, J. (1995). Relationships between short-term blood-pressure fluctuations and heart-rate variability in resting subjects: a spectral analysis approach. *Med. Biol. Eng. Comput.* 23, 352–358.

Eckberg, D. L. (2008). Arterial baroreflexes and cardiovascular modeling. *Cardiovasc. Eng.* 8, 5–13.

Eden, U. T., Frank, L. M., Solo, V., and Brown, E. N. (2004). Dynamic analyses of neural encoding by point process adaptive filtering. *Neural Comput.* 16, 971–998.

Ergun, A., Barbieri, R., Eden, U. T., Wilson, M. A., and Brown, E. N. (2007). Construction of point process adaptive filter algorithms for neural systems using sequential Monte Carlo methods. *IEEE Trans. Biomed. Eng.* 54, 419–428.

Goldberger, A. L., Peng, C.-K., and Lipsitz, L. A. (2002). What is physiologic complexity and how does it change with aging and disease? *Neurobiol. Aging* 23, 23–26.

Haykin, S. (2001). *Adaptive Filter Theory,* 4th Edn. Upper Saddle River, NJ: Prentice Hall.

Ivanov, P. C., Amaral, L. A., Goldberger, A. L., Havlin, S., Rosenblum, M. G., Struzik, Z. R., and Stanley, H. E. (1999). Multifractality in human heartbeat dynamics. *Nature* 399, 461–465.

Jo, J. A., Blasi, A., Valladares, E. M., Juarez, R., Baydur, A., and Khoo, M. C. K. (2007). A nonlinear model of cardiac autonomic control in obstructive sleep apnea syndrome. *Ann. Biomed. Eng.* 35, 1425–1443.

Khoo, M. C. K. (1999). *Physiological Control Systems: Analysis, Simulation, and Estimation.* New York: Wiley-IEEE Press.

Kodituwakku, S., Lazar, S. W., Indic, P., Chen, Z., Brown, E. N., and Barbieri, R. (2012). Point process time-frequency analysis of dynamic breathing patterns during meditation practice. *Med. Biol. Eng. Comput.* (in press).

Korenberg, M. J. (1991). Parallel cascade identification and kernel estimation for nonlinear systems. *Ann. Biomed. Eng.* 19, 429–455.

Koyama, S., Castellanos Pérez-Bolde, L., Shalizi, C. R., and Kass, R. E. (2010). Approximate methods for state-space models. *J. Am. Stat. Assoc.* 105, 170–180.

Koyama, S., Eden, U. T., Brown, E. N., and Kass, R. E. (2009). Bayesian decoding of neural spike trains. *Ann. Inst. Stat. Math.* 62, 37–59.

Loader, C. (1999). *Local Regression and Likelihood.* New York: Springer.

Lu, S., Ju, K. H., and Chon, K. H. (2001). A new algorithm for linear and nonlinear ARMA model parameter estimation using affine geometry. *IEEE Trans. Biomed. Eng.* 48, 1116–1124.

Marmarelis, P. Z. (1993). Identification of nonlinear biological systems using Laguerre expansions of kernels. *Ann. Biomed. Eng.* 21, 573–589.

Marmarelis, V. Z. (2004). *Nonlinear Dynamic Modeling of Physiological Systems.* New York: Wiley.

Nikias, C., and Petropulu, A. P. (1993). *Higher Order Spectra Analysis: A Non-Linear Signal Processing Framework.* Englewood Cliffs, NJ: Prentice Hall.

Parati, G., DiRienzo, M., and Mancia, G. (2001). Dynamic modulation of baroreflex sensitivity in health and disease. *Ann. N. Y. Acad. Sci.* 940, 469–487.

Peng, C. K., Havlin, S., Stanley, H. E., and Goldberger, A. L. (1995). Quantification of scaling exponents and crossover phenomena in nonstationary heartbeat time series. *Chaos* 5, 82–87.

Pinna, G. D. (2007). Assessing baroreflex sensitivity by the transfer function method: what are we really measuring? *J. Appl. Physiol.* 102, 1310–1311.

Pinna, G. D., and Maestri, R. (2001). New criteria for estimating baroreflex sensitivity using the transfer function method. *J. Med. Biol. Eng. Comput.* 40, 79–84.

Poon, C.-S., and Merill, C. K. (1997). Decrease of cardiac chaos in congestive heart failure. *Nature* 389, 492–495.

Porta, A., Aletti, F., Vallais, F., and Baselli, G. (2009). Multimodal signal processing for the analysis of cardiovascular variability. *Philos. Trans. R. Soc. Lond. A* 367, 391–409.

Porta, A., Furlan, R., Rimoldi, O., Pagani, M., Malliani, A., and van de Borne, P. (2002). Quantifying the strength of linear causal coupling in closed loop interacting cardiovascular variability signals. *Biol. Cybern.* 86, 241–251.

Purdon, P. L., Pierce, E. T., Bonmassar, G., Walsh, J., Harrell, P. G., Kwo, J., Deschler, D., Barlow, M., Merhar, R. C., Lamus, C., Mullaly, C. M., Sullivan, M., Maginnis, S., Skoniecki, D., Higgins, H. A., and Brown, E. N. (2009). Simultaneous electroencephalography and functional magnetic resonance imaging of general anesthesia. *Ann. N. Y. Acad. Sci.* 1157, 61–70.

Ross, S. M. (1997). *Introduction to Probability Models*, 6th Edn. San Diego, CA: Academic Press.

Saul, J. P., Berger, R. D., Albrecht, P., Stein, S. P., Chen, M. H., and Cohen, R. J. (1991). Transfer function analysis of the circulation: unique insights into cardiovascular regulation. *Am. J. Physiol. Heart Circ. Physiol.* 261, H1231–H1245.

Saul, J. P., and Cohen, R. J. (1994). "Respiratory sinus arrhythmia," in *Vagal Control of the Heart: Experimental Basis and Clinical Implications*, eds M. N. Levy and P. J. Schwartz (Armonk, NY: Futura Publishing Inc.), 511–536.

Schetzen, M. (1980). *The Volterra and Wiener Theories of Nonlinear Systems.* New York: Wiley.

Schnider, T. W., Minto, C. F., Gambus, P. L., Andresen, C., Goodale, D. B., Shafer, S. L., and Youngs, E. J. (1998). The influence of method of administration and covariates on the pharmacokinetics of propofol in adult volunteers. *Anesthesiology* 88, 1170–1182.

Schnider, T. W., Minto, C. F., Shafer, S. L., Gambus, P. L., Andresen, C., Goodale, D. B., and Youngs, E. J. (1999). The influence of age on propofol pharmacodynamics. *Anesthesiology* 90, 67–72.

Shafer, A., Doze, V. A., Shafer, S. L., and White, P. F. (1988). Pharmacokinetics and pharmacodynamics of propofol infusions during general anesthesia. *Anesthesiology* 69, 348–356.

Smith, A. C., and Brown, E. N. (2003). Estimating a state-space model from point process observations. *Neural Comput.* 15, 965–991.

Stauss, H. M. (2003). Heart rate variability. *Am. J. Physiol. Regul. Integr. Comp. Physiol.* 285, R927–R931.

Struzik, Z. R., Hayano, J., Sakata, S., Kwak, S., and Yamamoto, Y. (2004). 1/f scaling in heart rate requires antagonistic autonomic control. *Phys. Rev. E Stat. Nonlin. Soft Matter Phys.* 70, 050901.

Task Force. (1996). Task Force of the European Society of Cardiology, and the North American Society of Pacing, and Electrophysiology. Heart rate variability. *Circulation* 93, 1043–1065.

Teich, M. C., Lowen, S. B., Jost, B. M., Vibe-Rheymer, K., and Heneghan, C. (2001). "Heart rate variability: measures and models," in *Nonlinear Biomedical Signal Processing*, Vol. 2, *Dynamic Analysis and Modeling*, ed. M. Akay (New York: Wiley-IEEE), 159–212.

Tsoulkas, V., Koukoulas, P., and Kalouptsidis, N. (2001). Identification of input output bilinear systems using cumulants. *IEEE Trans. Signal Process.* 49, 2753–2761.

Tulppo, M. P., Kiviniemi, A. M., Hautala, A. J., Kallio, M., Seppanen, T., Makikallio, T. H., and Huikuri, H. V. (2005). Physiological background of the loss of fractal heart rate dynamics. *Circulation* 112, 314–319.

Voss, A., Schulz, S., Schroeder, R., Baumert, M., and Caminal, P. (2009). Methods derived from nonlinear dynamics for analysing heart rate variability. *Philos. Trans. R. Soc. Lond. A* 367, 277–296.

Vu, K. M. (2007). The ARIMA and VARIMA Time Series: Their Modelings, Analyses and Applications. AuLac Technologies, Inc. Available at: http://www.chegg.com/textbooks/arima-and-varima-time-series-their-modelings-analyses-and-applications-1st-edition-9780978399610-0978399617

Wang, H., Ju, K., and Chon, K. H. (2007). Closed-loop nonlinear system identification via the vector optimal parameter search algorithm: application to heart rate baroreflex control. *Med. Eng. Phys.* 29, 505–515.

Westwick, D. T., and Kearney, R. E. (2003). "Explicit least-squares methods," in *Identification of Nonlinear Physiological Systems*, Chap. 7 (New York: Wiley), 169–206.

Xiao, X., Mullen, T. J., and Mukkamala, R. (2005). System identification: a multi-signal approach for probing neural cardiovascular regulation. *Physiol. Meas.* 26, R41–R71.

Zhang, Y., Wang, H., Ju, K. H., Jan, K.-M., and Chon, K. H. (2004). Nonlinear analysis of separate contributions of autonomous nervous systems to heart rate variability using principal dynamic modes. *IEEE Trans. Biomed. Eng.* 26, 255–262.

Zhao, H., Cupples, W. A., Ju, K., and Chon, K. H. (2007). Time-varying causal coherence function and its application to renal blood pressure and blood flow data. *IEEE Trans. Biomed. Eng.* 54, 2142–2150.

Zhao, H., Lu, S., Zou, R., Ju, K., and Chon, K. H. (2005). Estimation of time-varying coherence function using time-varying transfer functions. *Ann. Biomed. Eng.* 33, 1582–1594.

Zou, R., Wang, H., and Chon, K. H. (2003). A robust time-varying identification algorithm using basis functions. *Ann. Biomed. Eng.* 31, 840–853.

Conflict of Interest Statement: The authors declare that the research was conducted in the absence of any commercial or financial relationships that could be construed as a potential conflict of interest.

Received: 31 August 2011; accepted: 06 January 2012; published online: 01 February 2012.

Citation: Chen Z, Purdon PL, Brown EN and Barbieri R (2012) A unified point process probabilistic framework to assess heartbeat dynamics and autonomic cardiovascular control. Front. Physio. ***3****:4. doi: 10.3389/fphys.2012.00004*

This article was submitted to Frontiers in Computational Physiology and Medicine, a specialty of Frontiers in Physiology.

frontiers in
PHYSIOLOGY

REVIEW ARTICLE
published: 01 November 2011
doi: 10.3389/fphys.2011.00072

Tube-load model parameter estimation for monitoring arterial hemodynamics

Guanqun Zhang[1], Jin-Oh Hahn[2] and Ramakrishna Mukkamala[1]*

[1] *Department of Electrical and Computer Engineering, Michigan State University, East Lansing, MI, USA*
[2] *Department of Mechanical Engineering, University of Alberta, Edmonton, AB, Canada*

Edited by:
Riccardo Barbieri, Massachusetts Institute of Technology, USA

Reviewed by:
Amina Eladdadi, The College of Saint Rose, USA
Zhe Chen, Massachusetts Institute of Technology, USA

***Correspondence:**
Ramakrishna Mukkamala, Department of Electrical and Computer Engineering, Michigan State University, 2120 Engineering Building, East Lansing, MI 48824–1266, USA.
e-mail: rama@egr.msu.edu

A useful model of the arterial system is the uniform, lossless tube with parametric load. This tube-load model is able to account for wave propagation and reflection (unlike lumped-parameter models such as the Windkessel) while being defined by only a few parameters (unlike comprehensive distributed-parameter models). As a result, the parameters may be readily estimated by accurate fitting of the model to available arterial pressure and flow waveforms so as to permit improved monitoring of arterial hemodynamics. In this paper, we review tube-load model parameter estimation techniques that have appeared in the literature for monitoring wave reflection, large artery compliance, pulse transit time, and central aortic pressure. We begin by motivating the use of the tube-load model for parameter estimation. We then describe the tube-load model, its assumptions and validity, and approaches for estimating its parameters. We next summarize the various techniques and their experimental results while highlighting their advantages over conventional techniques. We conclude the review by suggesting future research directions and describing potential applications.

Keywords: arterial compliance, blood pressure and flow waveforms, central pressure, hemodynamic monitoring, pulse wave velocity, tube-load model, transfer function, wave reflection

INTRODUCTION

Mathematical modeling of arterial hemodynamics has been long-standing. Two basic modeling approaches have been employed: forward modeling and inverse modeling. Forward modeling concerns building a model based on physical principles to predict data (i.e., estimating data from physical models with known parameters). This approach is useful for testing our understanding of the physiology underlying arterial hemodynamics. On the other hand, inverse modeling concerns building a model from observed data (e.g., estimating model parameters by fitting measured waveforms). Although less developed than its forward modeling counterpart, this approach is becoming more and more important by virtue of its ability to permit individualized monitoring of arterial hemodynamics.

The available models may be divided into two classes: lumped-parameter models and distributed-parameter models. The most popular lumped-parameter model is the "Windkessel" model proposed by Frank (Sagawa et al., 1990). It analogizes the arterial system as a capacitor connected in parallel with a resistor. The capacitor represents the large artery compliance, whereas the resistor represents the total peripheral resistance. This two-parameter Windkessel model can be extended to include additional circuit elements in order to improve accuracy (Stergiopulos et al., 1999). Because Windkessel models are so simple, they are highly suitable for parameter estimation purposes. That is, Windkessel models are characterized by only a few parameters, which can be readily estimated from the limited arterial waveforms typically available in practice. However, lumped-parameter models assume infinite pulse wave velocity and therefore cannot reproduce wave propagation and reflection phenomena that are essential in shaping these waveforms.

By contrast, distributed-parameter models can reproduce wave propagation and reflection phenomena through finite pulse wave velocity. Most often, distributed-parameter models represent the arterial system using a one-dimensional simplification of the Navier–Stokes equation. These models usually account for both geometrical and mechanical properties of the arteries explicitly as model parameters. Detailed distributed-parameter models have been built that account for multi-level branching, elastic and geometric tapering, and arterial terminations (Raines et al., 1974; Avolio, 1980; Zagzoule and Marc-Vergnes, 1986; Wan et al., 2002; Sherwin et al., 2003; Azer and Peskin, 2007; Huberts et al., 2009). These comprehensive models can provide great accuracy. However, the models cannot be readily applied for parameter estimation purposes, because they are characterized by an excessive number of model parameters that makes it virtually impossible to obtain unique parameter estimates from limited arterial waveforms.

Less accurate, yet mathematically tractable, distributed-parameter models have also been developed. These models usually consist of multiple tubes with terminal loads in parallel. Often times, the model comprises two such tubes and loads ("T-tube" model). The tube represents the wave propagation path in the large conduit arteries, whereas the load signifies the wave reflection site (e.g., arterial bed distal to a peripheral artery). The tube can be elastically and/or geometrically tapered or uniform as well as lossy (i.e., exhibits energy dissipation) or lossless, while the load can be non-parametric (i.e., characterized without a model structure

through a generic frequency response) or parametric. It turns out that the simplest of these models, the uniform, lossless tube with parametric load, is almost as accurate as the most complicated of the models. Indeed, this model, which will henceforth be referred to simply as the tube-load model, is often able to fit arterial pressure and flow waveforms remarkably well despite being characterized by only a few parameters. Consequently, the tube-load model carries advantages of both Windkessel and comprehensive distributed-parameter models and therefore permits an attractive platform for improved monitoring of arterial hemodynamics.

In this paper, we review tube-load model parameter estimation techniques that have appeared in the literature for monitoring wave reflection, large artery compliance, pulse transit time, and central aortic pressure. We first provide a detailed explanation of the tube-load model and the estimation of its parameters. We then describe the various techniques and their experimental results while highlighting their advantages over conventional techniques. **Table 1** provides a summary of the techniques. We conclude the review by suggesting future research directions and describing potential applications.

TUBE-LOAD MODEL AND PARAMETER ESTIMATION

MODEL DESCRIPTION

Figure 1A illustrates the tube-load model. This model represents the arterial system as a parallel connection of m uniform, lossless tubes with parametric loads. The meaning of the tubes and loads depend on perspective. From the perspective of the central (ascending) aorta, a tube represents the wave propagation path through a segment of the aorta, whereas the load represents an effective reflection site due to the entire arterial network distal to the segment. For example, for the T-tube model in which m is equal to two, the two effective reflection sites correspond to the head-end and body-end arterial beds. The flow through the body-end tube represents the descending aortic flow, whereas the flow through the head-end tube represents the difference between central and descending aortic flows. From the perspective of a peripheral artery, on the other hand, a tube represents the wave propagation path from the central aorta to the peripheral artery, whereas the load represents the reflection site due to the arterial bed distal to the peripheral artery. In this case, m is equal to the number of peripheral arteries. The flow at the proximal end of

Table 1 | Summary of available tube-load model parameter estimation techniques for monitoring arterial hemodynamics.

Monitored variable	References	Tube type	Load type	Parameter estimation	Advantages over previous techniques
Wave reflection	Burattini and Campbell (1989)	T-tube	Type II	Central aortic pressure waveform fitted in response to central aortic flow waveform	Validated forward and backward waves Arterial flow waveform and external perturbations not required
	Burattini et al. (1991)	T-tube	Type II	Central and descending aortic flow waveforms fitted in response to central aortic pressure waveform	Accuracy via use of all waveform frequencies
	Swamy et al. (2010)	1 tube	Type III	Different combinations of central and femoral arterial pressure waveforms fitted to each other	Detailed aspects of wave reflection phenomena revealed
Large artery compliance	Campbell et al. (1990)	T-tube	Type II	Central aortic pressure waveform fitted in response to central aortic flow waveform Central aortic flow waveform fitted in response to central aortic pressure waveform Central and descending aortic flow waveforms fitted in response to central aortic pressure waveform	External perturbation not required
	Burattini and Campbell (1993)	T-tube	Type I Type II Type III	Central and descending aortic flow waveforms fitted in response to central aortic pressure waveform	Accuracy by accounting for wave reflection
	Shroff et al. (1995)	T-tube	Type II	Central and descending aortic flow waveforms fitted in response to central aortic pressure waveform	
Pulse transit time	Xu et al. (2010), Zhang et al. (2011)	1 tube	Type I	Central aortic pressure waveform fitted in response to femoral arterial pressure waveform	True pulse transit time in the absence of wave reflection revealed Robustness to waveform artifact
	Hahn et al. (2010)	T-tube	Type II	Femoral arterial pressure waveform fitted in response to radial arterial pressure waveform (or vice versa)	Central aortic waveform not required
Central aortic pressure	Hahn et al. (2009a)	T-tube	Type II	Femoral arterial pressure waveform fitted in response to radial arterial pressure waveform (or vice versa)	Accuracy by adapting to the inter-subject and temporal variability of the arterial tree
	Swamy et al. (2009)	1 tube	Type I	Femoral arterial flow waveform fitted to zero during diastole in response to femoral arterial pressure waveform	
	Hahn et al. (2008)	1 tube	Type II	Derivative of central aortic pressure waveform fitted to zero in response to derivative of radial arterial pressure waveform at high sampling rate	

a tube is not measurable. It represents the component of central aortic flow that reaches a peripheral artery. However, the sum of the flows at the proximal end of all tubes corresponds to the total central aortic flow.

The ith tube is of length d_i and has constant characteristic impedance $Z_{ci} =, \sqrt{l_i/c_i}$, where l_i and c_i are the large artery inertance and compliance, respectively. Pressure and flow waves propagate with constant time delay $T_i = \sqrt{l_i \cdot c_i}$ from one end of the tube to the other. Note that this time delay corresponds to pulse transit time and that its governing equation arises from the Bramwell–Hill equation (Bramwell, 1922). The mean value of the waves is constant throughout the tube.

The ith load has frequency-dependent impedance $Z_{Li}(j\omega)$, where j is the imaginary number and ω is the frequency, that is characterized by a pole–zero structure. **Figure 1B** shows three types of commonly used loads along with the specific form of their $Z_{Li}(j\omega)$. The Type I and Type II loads are three-parameter Windkessel models. These models account for the resistance R and compliance C of the effective load or peripheral resistance and compliance (depending on perspective) while matching the tube impedance at infinite frequency per arterial input impedance studies (Noordergraaf, 1978; Nichols and O'Rourke, 2005). The Type III load is a generic pole–zero model. A principal advantage of this type of model is that it allows a flexible system order rather than being fixed to first-order as with its Type I and Type II counterparts. The disadvantage is that it has no physiologic meaning. As a result, its coefficients are neither dependent on each other nor constrained as they are with the Type I and Type II loads. For any load, the wave reflection coefficient at the ith load is given by the following relationship involving tube and load impedances:

$$\Gamma_i(j\omega) = \frac{Z_{Li}(j\omega) - Z_{ci}}{Z_{Li}(j\omega) + Z_{ci}}. \quad (1)$$

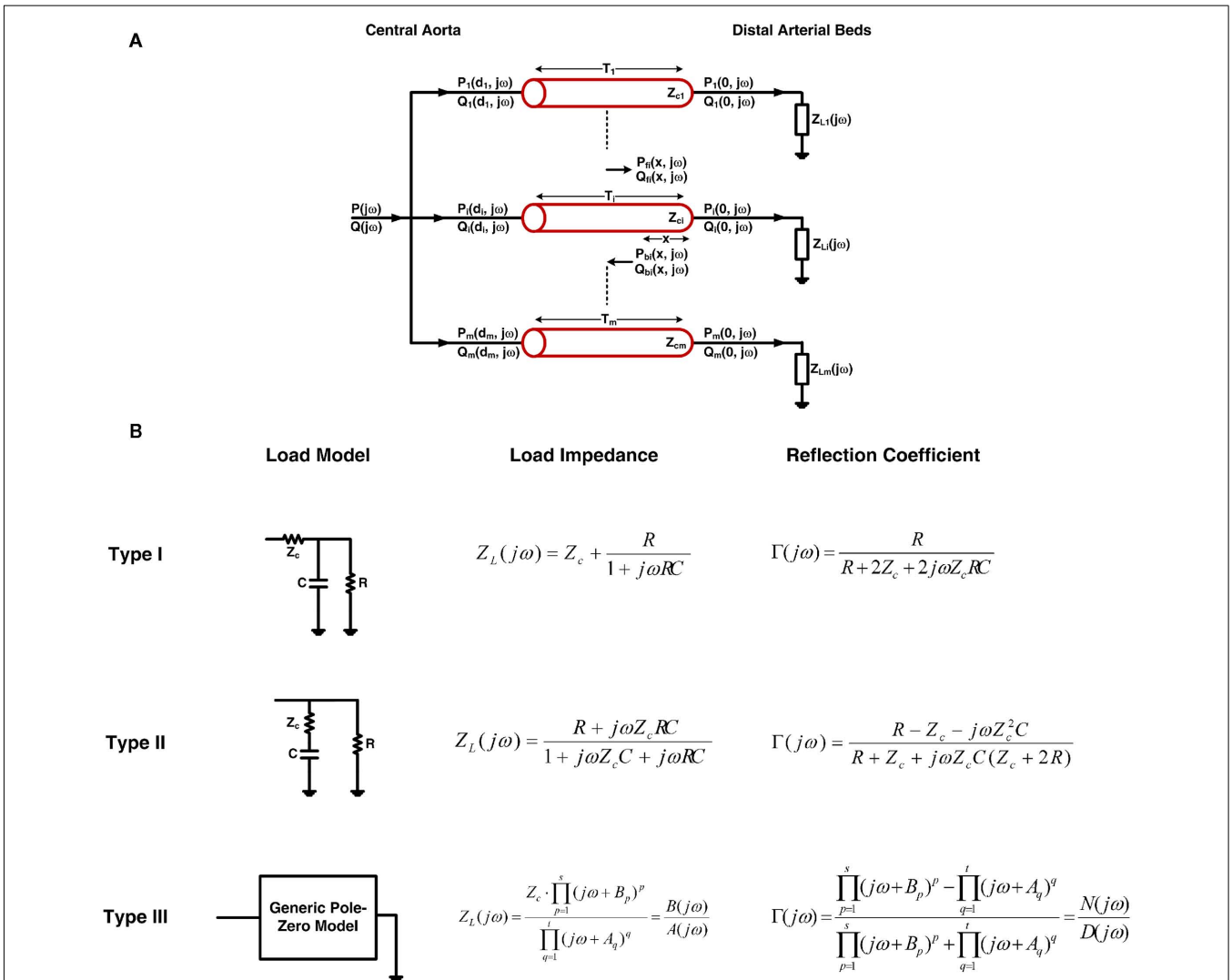

FIGURE 1 | (A) The tube-load model with arbitrary load. **(B)** Three types of commonly used loads along with their corresponding impedances and reflection coefficients. See text for complete model details.

Qualitatively, pressure and flow waves propagate in the forward direction (proximal to distal tube ends) along a tube without distortion and are proportional to each other. These waves are reflected in the opposite direction at the load due to the impedance mismatch [$Z_{ci} \neq Z_{Li}(j\omega)$]. The resulting backward pressure and flow waves likewise propagate along the tube without distortion and are proportional to each other but have opposite sign. The actual arterial pressure and flow waveforms at any point on the tube then arise as the sum of the forward and backward propagating waves shifted in time to account for their wave propagation time to the point of interest.

Quantitatively, pressure and flow waves on a tube are related through its characteristic impedance as follows:

$$Q_{fi}\left(x,\, j\omega\right) = \frac{P_{fi}\left(x,\, j\omega\right)}{Z_{ci}},\; Q_{bi}\left(x,\, j\omega\right) = -\frac{P_{bi}\left(x,\, j\omega\right)}{Z_{ci}}. \tag{2}$$

Here, $P_{fi}(x, j\omega)$ and $P_{bi}(x, j\omega)$ are forward and backward propagating pressure waves in the frequency-domain at a point x on the ith tube, and $Q_{fi}(x, j\omega)$ and $Q_{bi}(x, j\omega)$ are the corresponding flow waves at the same point. Note that the forward waves actually represent the sum of all waves propagating from the proximal to distal tube ends (i.e., the incident wave from the heart and the backward waves re-reflected at the heart), while the backward waves may be interpreted analogously. Also, note that $x = 0$ and $x = d_i$ correspond to the distal and proximal ends of the tube, respectively.

The forward and backward waves at a distal tube end are related to each other through the wave reflection coefficient as follows:

$$P_{bi}\left(0,\, j\omega\right) = \Gamma_i\left(j\omega\right) \cdot P_{fi}\left(0,\, j\omega\right). \tag{3}$$

The forward and backward waves at any point on a tube may be expressed in terms of the corresponding waves at the distal tube end as follows:

$$\begin{aligned} P_{fi}\left(x,\, j\omega\right) &= P_{fi}\left(0,\, j\omega\right) e^{j\omega T_i \cdot x/d_i} \\ P_{bi}\left(x,\, j\omega\right) &= P_{bi}\left(0,\, j\omega\right) e^{-j\omega T_i \cdot x/d_i}, \end{aligned} \tag{4}$$

where the exponential term is the frequency-domain time shifting operator.

By combining Eqs 2–4, the actual arterial pressure and flow waveforms at any point on a tube may then be expressed in terms of the forward and backward waves as follows:

$$\begin{aligned} P_i\left(x,\, j\omega\right) &= P_{fi}\left(x,\, j\omega\right) + P_{bi}\left(x,\, j\omega\right) \\ &= P_{fi}\left(0,\, j\omega\right) \cdot \left[e^{j\omega T_i \cdot x/d_i} + \Gamma_i\left(j\omega\right) e^{-j\omega T_i \cdot x/d_i}\right] \\ Q_i\left(x,\, j\omega\right) &= Q_{fi}\left(x,\, j\omega\right) + Q_{bi}\left(x,\, j\omega\right) \\ &= \frac{P_{fi}\left(0,\, j\omega\right)}{Z_{ci}} \cdot \left[e^{j\omega T_i \cdot x/d_i} - \Gamma_i\left(j\omega\right) e^{-j\omega T_i \cdot x/d_i}\right], \end{aligned} \tag{5}$$

where $P_i(x, j\omega)$ and $Q_i(x, j\omega)$ are the arterial pressure and flow waveforms in the frequency-domain at point x on the ith tube.

Due to the parallel connection of the model, the central aortic pressure waveform is identical to the arterial pressure waveforms at each proximal tube end, whereas the central aortic flow waveform is the sum of all flow waveforms at the proximal tube ends as follows:

$$\begin{aligned} P\left(j\omega\right) &= P_i\left(d_i, j\omega\right) = P_{fi}\left(0,\, j\omega\right)\left[e^{j\omega T_i} + \Gamma_i\left(j\omega\right) e^{-j\omega T_i}\right] \\ Q\left(j\omega\right) &= \sum\nolimits_{i=1}^{m} Q_i\left(d_i, j\omega\right) \\ &= \sum\nolimits_{i=1}^{m} \left\{\frac{P_{fi}\left(0,\, j\omega\right)}{Z_{ci}} \cdot \left[e^{j\omega T_i} + \Gamma_i\left(j\omega\right) e^{-j\omega T_i}\right]\right\}, \end{aligned} \tag{6}$$

where $P(j\omega)$ and $Q(j\omega)$ are the central aortic pressure and flow waveforms in the frequency-domain.

Finally, Eqs 5 and 6 may be given explicitly in terms of the tube-load model parameters by substituting a $\Gamma(j\omega)$ from **Figure 1B** into these equations.

ASSUMPTIONS AND VALIDITY

Assumptions of the tube-load model include: (a) wave propagation without energy loss in large conduit arteries, (b) a load characterized by a few parameters, and (c) non-interacting reflections occurring at distal sites only by virtue of neglecting elastic and geometric tapering and multi-level branching. Assumption (a) is quite valid. Friction in the large conduit arteries is indeed negligible, because resistance is inversely proportional to the fourth power of the vessel radius. Pressure loss in the descending aorta, for example, has been shown to be trivial (Burattini and Campbell, 2000). Assumption (b) is justifiable based on empirical data. That is, while the actual load is certainly complicated with many parameters needed for its representation, the arterial input impedance computed with the tube-load model has been shown to match that determined with standard non-parametric Fourier analysis (Burattini and Campbell, 1989, 1993). Note, however, that an even simpler purely real load may not be supported by empirical data (Burattini and Campbell, 2000). Assumption (c) is the least tenable but can be defended to some extent. The arterial terminations do often constitute the dominant reflection sites for two reasons. First, they pose the greatest impedance mismatch, as the radius of the arterioles is much smaller than that of proximal arteries (Pappano et al., 2007). Second, vessel tapering tends to be offset by vessel branching in the forward direction so as to achieve relative impedance matching (Noordergraaf, 1978). In addition, the tube-load model has been shown to fit experimental waveforms almost as well as an exponentially tapered version of the model (Fogliardi et al., 1997). On the other hand, backward waves should experience strong re-reflections as they return to the heart due to necessarily significant impedance mismatches in the backward direction (Noordergraaf, 1978). Further, the multiple reflected waves that return from distal sites actually interact in the aorta due to multi-level branching.

In short, the tube-load model has a physiologic foundation but does ignore aspects of actual arterial hemodynamics. Despite its simplicity, it is able to fit experimental arterial pressure and flow waveforms remarkably well. **Figure 2** illustrates major waveform phenomena that the model can predict. This ability to fit experimental data provides further validation of the tube-load model and suggests that it may be phenomenological in addition to physiological.

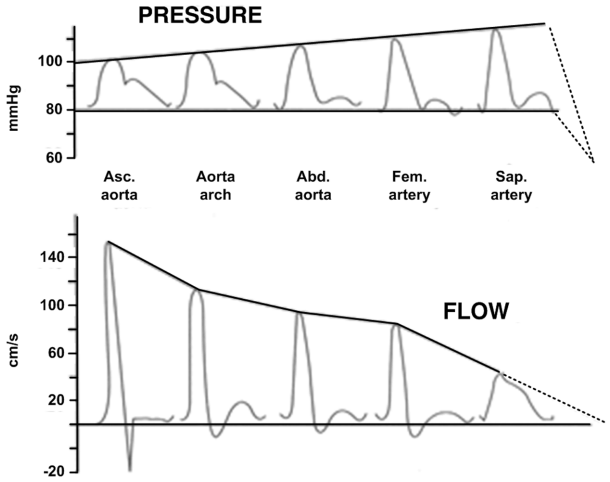

FIGURE 2 | Experimental arterial pressure and flow waveforms with increasing distance from the heart. Reproduced from Nichols and O'Rourke (2005).

PARAMETER ESTIMATION

Most often, estimating the tube-load model parameters is accomplished by casting the governing equations into a transfer function. The transfer function relating a pair of arterial pressure and/or flow waveforms at any points on a tube may be obtained based on Eq. 5. For example, using the T-tube model with Type II load, the transfer function relating the central aortic pressure waveform to the central aortic flow waveform is given as follows:

$$\begin{aligned} Q_i\left(d_i,\, j\omega\right) &= H_i\left(j\omega\right)\cdot P\left(j\omega\right) \\ &= \frac{1}{Z_{ci}}\frac{e^{j\omega T_i}-\Gamma_i\left(j\omega\right)e^{-j\omega T_i}}{\left[e^{j\omega T_i}+\Gamma_i\left(j\omega\right)e^{-j\omega T_i}\right]}\cdot P\left(j\omega\right) \\ &= \frac{1}{Z_{ci}}\frac{\begin{array}{c}\left[\left(R_i+Z_{ci}\right)e^{j\omega T_i}-\left(R_i-Z_{ci}\right)e^{-j\omega T_i}\right] \\ +j\omega C_iZ_{ci}\left[\left(2R_i+Z_{ci}\right)e^{j\omega T_i}+Z_{ci}e^{-j\omega T_i}\right]\end{array}}{\begin{array}{c}\left[\left(R_i+Z_{ci}\right)e^{j\omega T_i}+\left(R_i-Z_{ci}\right)e^{-j\omega T_i}\right] \\ +j\omega C_iZ_{ci}\left[\left(2R_i+Z_{ci}\right)e^{j\omega T_i}-Z_{ci}e^{-j\omega T_i}\right]\end{array}}\cdot P\left(j\omega\right) \end{aligned}$$

$i = 1$ or 2. (7a)

$$Q\left(j\omega\right) = \left[H_1\left(j\omega\right)+H_2\left(j\omega\right)\right]\cdot P\left(j\omega\right). \quad (7b)$$

As another example, using the Type I load, the transfer function relating the central aortic pressure waveform to a peripheral arterial pressure waveform is given as follows:

$$\begin{aligned} P_i\left(0,\, j\omega\right) &= \frac{1+\Gamma_i\left(j\omega\right)}{e^{j\omega T_i}+\Gamma_i\left(j\omega\right)e^{-j\omega T_i}}\cdot P\left(j\omega\right) \\ &= \frac{j\omega+\frac{1}{R_iC_i}+\frac{1}{Z_{ci}C_i}}{\left(j\omega+\frac{1}{R_iC_i}+\frac{1}{2Z_{ci}C_i}\right)e^{j\omega T_i}+\frac{1}{2Z_{ci}C_i}e^{-j\omega T_i}}\cdot P\left(j\omega\right). \end{aligned} \quad (8)$$

The former transfer function is defined by the eight unknown parameters of the T-tube model. However, while the latter transfer function includes all four unknown model parameters of a single tube and load, only three aggregate parameters are actually observable (T_i, R_iC_i and $Z_{ci}C_i$). Thus, all four parameters cannot be estimated, but identification of the transfer function is simplified to a three-parameter problem.

Estimation of the observable model parameters is accomplished in two steps. First, arterial pressure and flow waveforms corresponding to the input and output of the transfer function of interest are measured. Then, the parameters are estimated by finding the transfer function, which when applied to the measured input, optimally fits the measured output. Alternatively, in some instances, the parameters of the transfer function may be optimally estimated using *a priori* physiologic knowledge (see Pulse Transit Time Monitoring and Central Aortic Pressure Monitoring). The advantage of this alternative is to reduce the burden on the required waveform measurements. In either case, parameter estimation is usually performed in the time-domain by converting the transfer function into a recursive difference equation, and the optimality is typically established in the least squares sense.

The step of estimating the tube-load model parameters is actually quite challenging. First, the transfer functions are not simply linear in distinct parameters. For example, as can be ascertained from Eqs 7 and 8, the transfer functions are non-linear in the T_i (pulse transit time) parameter. Second, the parameter values have numerical constraints. For instance, the characteristic impedance should be smaller than the peripheral resistance, and all parameters must be positive and not exceed physiologic bounds. For these two reasons, straightforward parameter estimation techniques with analytical solutions are generally not applicable. The parameters are instead typically estimated via numerical search in which the needed global optimum cannot be guaranteed. Use of brute-force methods that search over a discretized grid in multi-dimensional parameter space increases the likelihood of identifying the global optimum at the expense of substantial computational time. On the other hand, use of available local search methods such as the steepest descent method, conjugate gradient method, Newton's method and its Levenberg–Marquardt modification, and simplex method (possibly with penalty factors for keeping the parameters within physiologic bounds; Ljung, 1999) require little computational time, but the global optimum is seldom found without an initial guess that resides near the global optimum. This problem is often mitigated by employing multiple, initial guesses and then choosing the solution that represents the optimum amongst the multiple solutions of the local search method. However, the computational time will obviously increase with the number of initial guesses. Another practical issue is that the upper physiologic bounds on the parameters are often unclear. However, the challenge of parameter estimation can be alleviated to some degree by direct measurement of one or more parameters, especially pulse transit time and load resistance (Campbell et al., 1990; Burattini and Campbell, 1993; Hahn et al., 2009a; Swamy et al., 2009). Despite these challenges, asymptotic variance analysis has shown that the confidence intervals on the parameters estimates can be tight (Hahn et al., 2009a).

WAVE REFLECTION MONITORING

SIGNIFICANCE

The magnitude and timing of the backward wave relative to the forward wave in the central aorta can materially impact cardiac afterload and myocardial perfusion. For example, a significant reflected wave returning early from distal sites to the aorta during systole can impede stroke volume, whereas such a wave arriving later during diastole can augment myocardial perfusion. It would therefore be useful to be able to precisely monitor wave reflection.

PREVIOUS TECHNIQUES

Several techniques are available to separate arterial pressure and flow waveforms into their forward and backward wave components. The most popular of these techniques (Westerhof et al., 1972) models the proximal aorta as a short, uniform, lossless tube. The tube characteristic impedance is then estimated from measured central aortic pressure and flow waveforms as the average magnitude of the high frequency arterial input impedance. Finally, the forward and backward pressure waves in the tube are calculated from the central aortic pressure and flow waveforms and the characteristic impedance by adding pressure waves and subtracting flow waves (i.e., solution of two equations with two unknowns that arise from Eqs 2 and 5).

A couple of techniques are also available to calculate forward and backward waves from arterial pressure waveforms alone. The most interesting of these techniques (Newman et al., 1979) measures an arterial pressure waveform before and after complete occlusion of a distal artery. The backward pressure wave is then determined as half of the waveform obtained after the occlusion. Finally, the forward pressure wave is determined by subtracting this backward wave from the waveform obtained before the occlusion.

While these techniques have shed light on wave reflection phenomena, they have several disadvantages. First, it is generally difficult to validate the calculated waves against reference measurements. Indeed, to our knowledge, the techniques have yet to be validated in this way. Second, these techniques require either an arterial flow waveform, which is more difficult to measure than arterial pressure waveforms, or an experimental perturbation and are therefore not convenient to implement. Third, the estimation of characteristic impedance can be problematic. For example, the waveforms usually lack sufficient high frequency content. Finally, detailed aspects of wave reflection phenomena such as the location of the effective reflection sites cannot be ascertained with these techniques.

TUBE-LOAD MODEL PARAMETER ESTIMATION TECHNIQUES

Wave reflection can be readily monitored using tube-load model parameter estimation techniques. Once the model parameters are estimated from measured waveforms, the forward and backward waves can be determined. In particular, based on Eq. 5, the forward wave can be calculated from the parameter estimates and measured waveforms using standard deconvolution methods (Proakis and Manolakis, 2007). Then, according to Eq. 3, the backward wave can be computed from the forward wave and parameter estimates via convolution. Because these techniques are based on a model of the arterial system, they are able to overcome the disadvantages of the previous techniques enumerated above. First, the calculated waves can be validated in terms of their ability to predict a reference arterial pressure or flow waveform not utilized for parameter estimation (by adding or subtracting the waves after time shifting to account for the wave propagation time to the reference measurement site). Second, the waves can be calculated from only arterial pressure waveforms obtained without any external perturbation. Third, the model parameters can be estimated more accurately by the analysis of all waveform frequencies. Finally, the model parameters reveal detailed aspects of wave reflection phenomena. These advantages come at the cost of using a model that is not entirely correct (see Tube-Load Model and Parameter Estimation).

Burattini and Campbell (1989) calculated forward and backward waves from central aortic pressure and flow waveforms, validated the waves, and estimated the locations of the effective reflection sites. The authors specifically utilized the T-tube model with Type II load. They determined the load resistance parameters from measured total peripheral resistance and an assumed ratio of the head-end to body-end arterial flows. Then, based on Eq. 7b, they estimated the remaining six parameters by fitting the central aortic pressure waveform in response to the central aortic flow waveform. The waveform fitting was always satisfactory. From the model parameter estimates and Eq. 7a, they also predicted the descending aortic flow waveform. This prediction is equivalent to subtracting the calculated forward and backward waves at the proximal end of the body-end tube. **Figure 3** illustrates that the predicted waveform corresponded quite well to the measured descending aortic flow waveform. The authors analyzed the validated forward and backward waves. A prominent oscillation observed in the central aortic pressure waveform during diastole was caused by reflection from the body-end. Based on phase velocity estimated with the descending aortic flow waveform, the effective body-end reflection site is located at abdominal aorta. Finally, the effective head-end reflection site is closer to the heart and responsible for reflection during late systole. Later, these authors (Burattini and Campbell, 1993) would confirm that the abdominal aorta represents the effective body-end reflection site using similar techniques and further validate the

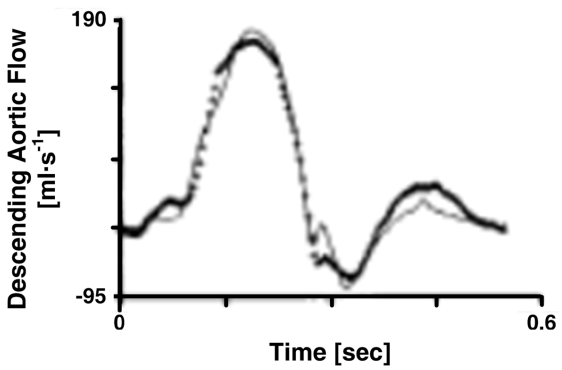

FIGURE 3 | Descending aortic flow waveforms measured (line with crosses) and predicted (solid line) from central aortic pressure and flow waveforms. Adapted from Burattini and Campbell (1989).

waves via prediction of the waveform at this site (see Large Artery Compliance Monitoring).

Burattini et al. (1991) calculated forward and backward waves to investigate the existence of two distinct reflection sites. The authors specifically used the T-tube model with Type II load and measured the load resistance parameters. Based on Eq. 7a, they estimated the remaining six model parameters by fitting the central and descending aortic flow waveforms in response to the central aortic pressure waveform. Three waveforms were used in accordance with an earlier study by the authors (Campbell et al., 1990; see Large Artery Compliance Monitoring). They analyzed the forward and backward waves when a diastolic oscillation was present and absent in the central aortic pressure waveform. Two effective reflection sites could explain either case. When the diastolic oscillation was present, both reflection sites were needed to fit the oscillation. When this oscillation was absent, the backward waves from the head-end and body-end either canceled each other out or superimposed on each other to appear as a single backward wave. In this case, one tube and load sufficed in fitting the central aortic pressure waveform. **Figure 4** illustrates the forward and backward waves calculated during both cases. In short, there are two reflection sites, but they can sometimes appear as one to the heart.

Swamy et al. (2010) calculated forward and backward waves from just two arterial pressure waveforms and validated the resulting waves during diverse hemodynamic interventions. The authors specifically employed a single tube with Type III load to relate central aortic and femoral arterial pressure waveforms and used the foot-to-foot detection technique to estimate the pulse transit time parameter (see Pulse Transit Time Monitoring). They re-cast Eq. 5 with Type III load to the following form:

$$\underbrace{P_i\left(0,\, j\omega\right) e^{j\omega T_i} - P\left(j\omega\right)}_{Y(j\omega)} = \Gamma_i\left(j\omega\right) \cdot \underbrace{P\left(j\omega\right) - P_i\left(0,\, j\omega\right) e^{-j\omega T_i}}_{X(j\omega)}$$

$$D_i\left(j\omega\right) \cdot Y\left(j\omega\right) = N_i\left(j\omega\right) \cdot X\left(j\omega\right). \tag{9}$$

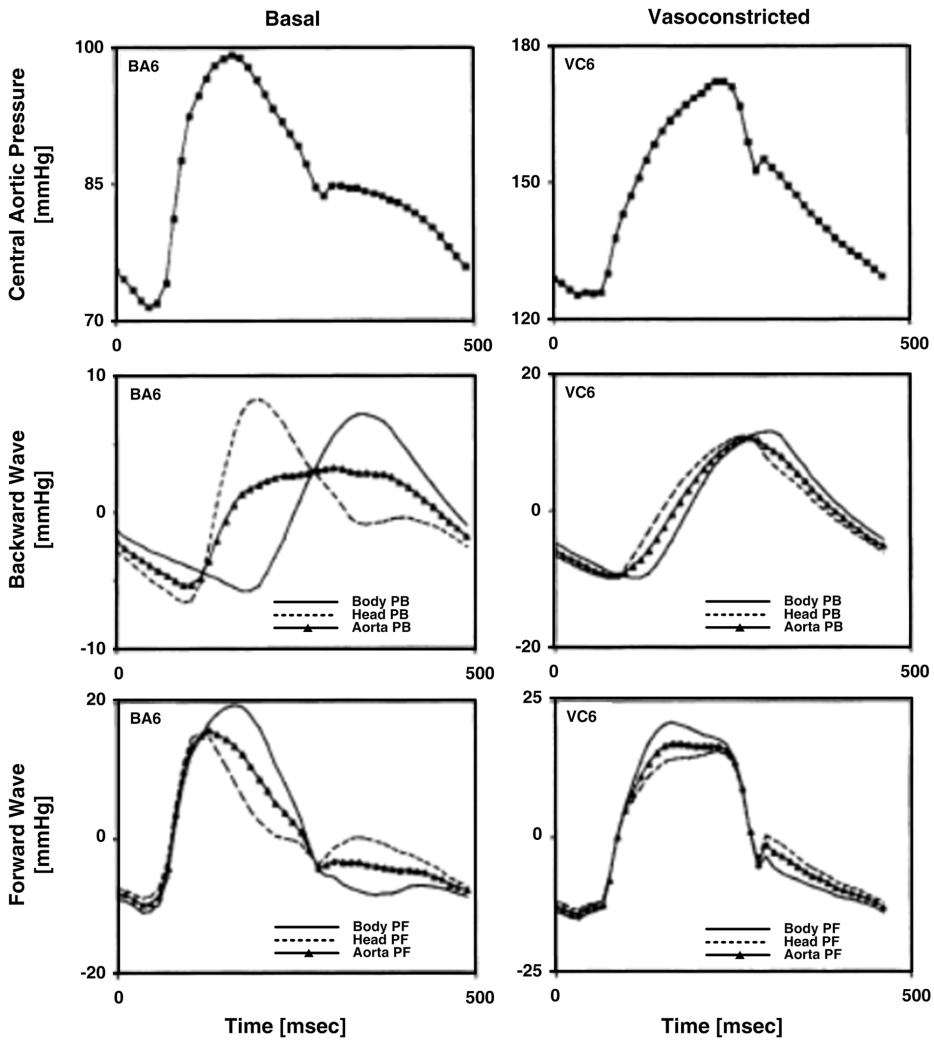

FIGURE 4 | Measured central aortic pressure waveforms and forward and backward pressure waves in the central aorta (PF and PB) calculated from central aortic pressure and flow and descending aortic flow waveforms. Adapted from Burattini et al. (1991).

The waveforms $X(j\omega)$ and $Y(j\omega)$ can be easily constructed from the measured waveforms. Given these constructed waveforms, Eq. 9 may be regarded as linear in distinct parameters for one-step ahead fitting (i.e., fitting the output in response to the past values of the input and output rather than fitting the entire output in response to the input as described in Tube-Load Model and Parameter Estimation). They therefore employed standard autoregressive exogenous input identification (Ljung, 1999) to analytically estimate the parameters as well as to determine the order of the wave reflection coefficient and thus the load (see **Figure 1B**). Rather than using standard deconvolution to calculate two versions of the forward wave from Eq. 5 and each arterial pressure waveform, they computed a single, optimal forward wave from both waveforms using multi-channel linear least squares deconvolution (Abed-Meraim et al., 1997). From the calculated forward and backward waves, the authors predicted the abdominal aortic pressure and femoral arterial flow waveforms (wherein the appropriate time shift was established by again using the foot-to-foot detection technique to estimate the pulse transit time between the corresponding measured waveform and the femoral arterial pressure waveform). **Figures 5A,B** illustrate that the predicted waveforms agreed well with the corresponding measured waveforms. As further validation, **Figure 5C** shows that the magnitude of the backward wave relative to the forward wave correctly increased during vasoconstriction and decreased during vasodilation. Finally, the estimated load order was second-order on average. This finding indicates that the first-order Types I and II loads are reasonable choices.

LARGE ARTERY COMPLIANCE MONITORING

SIGNIFICANCE

Large artery compliance characterizes arterial stiffness. The decline in this parameter is a major part of the degenerative changes that occur in aging and arterial disease (Haynes et al., 1979; Benetos et al., 1993; Van Bortel and Spek, 1998; Lévy, 2001). Indeed, in hypertension, the age-matched increase in pulse pressure is mainly due to a decrease in large artery compliance caused in part by intrinsic alteration of the arterial wall (London et al., 1989; Reneman and Hoeks, 1995). Thus, large artery compliance is of great clinical value. For example, it has been shown to be able to sensitively discriminate the severity of coronary artery disease (Waddell et al., 2001), and early recognition of abnormal compliance may favor patients at risk for arterial disease (Glasser et al., 1998). In addition, the ability to monitor large artery compliance is important for advancing the understanding of its role in pathophysiology.

PREVIOUS TECHNIQUES

The gold standard technique for monitoring large artery compliance is to measure aortic volume (or cross-sectional area) and pressure during an external perturbation (e.g., vena cava balloon occlusion) and then determine the slope of the line that best relates the resulting changes in volume to pressure. However, this technique is difficult to implement. More convenient techniques are available in which large artery compliance is estimated from arterial pressure and flow waveforms without the need for any external perturbation. The simplest of these techniques is the ratio of the stroke volume to pulse pressure (Hamilton and Remington, 1947). Another popular technique is the diastolic decay time method in which the *RC* time constant of the Windkessel model is estimated from an arterial pressure waveform during diastole and then divided by the ratio of the average arterial pressure to cardiac output (Sagawa et al., 1990). However, these waveform analysis techniques are subject to limited reliability, because they neglect wave reflection phenomena.

TUBE-LOAD MODEL PARAMETER ESTIMATION TECHNIQUES

Large artery compliance can also be monitored from pressure and flow waveforms using tube-load model parameter estimation techniques. These techniques specifically calculate large artery compliance by dividing the estimated pulse transit time parameter ($T_i = \sqrt{l_i \cdot c_i}$) by the estimated characteristic impedance parameter ($Z_{ci} = \sqrt{l_i / c_i}$). Their obvious advantage over the previous waveform analysis techniques is taking wave reflection into account.

Campbell et al. (1990) compared large artery compliance and other parameter estimates of different waveform analysis techniques during three vasoactive states. The authors specifically used the T-tube model with Type II load and measured the load resistance parameters. Based on Eq. 7, they estimated the remaining six model parameters by fitting (a) the central aortic pressure waveform in response to the central aortic flow waveform, (b) the central aortic flow waveform in response to the central aortic pressure waveform, and (c) the central and descending aortic flow waveforms in response to the central aortic pressure waveform. In all cases, the model was able to fit the waveforms well. **Figure 6A** illustrates an example of the waveform fitting. However, tight confidence intervals on the parameter estimates were only obtained when all three waveforms were analyzed. They justified this finding by arguing that the descending aortic flow waveform carries additional information revealing distinct reflection characteristics associated with the body-end arterial system and thus advocated the use of three waveforms for estimating the T-tube model. Further, the resulting large artery compliance estimates (and other parameter estimates) were consistent with known physiology. That is, the body-end compliance was greater than the head-end compliance. Indeed, the body-end consists of the most compliant arterial vessels (e.g., thoracic aorta) and has a greater vascular network. In addition, both compliances decreased with vasoconstriction and increased with vasodilation, as expected. Finally, **Figure 6B** shows that the sum of the two compliances was consistently smaller than that estimated with the Windkessel model during the three vasoactive states. Thus, accounting for wave reflection does make a difference in estimating large artery compliance.

Burattini and Campbell (1993) validated the large artery compliance estimates against gold standard reference measurements. The authors specifically estimated the parameters of the T-tube model with all three load types by fitting the central and descending aortic flow waveforms in response to the central aortic pressure waveform as per Campbell et al. (1990). They then used pulse wave velocity measurements via the foot-to-foot detection technique (see Pulse Transit Time Monitoring) to conclude that the distal end of the body-end tube corresponds to the abdominal

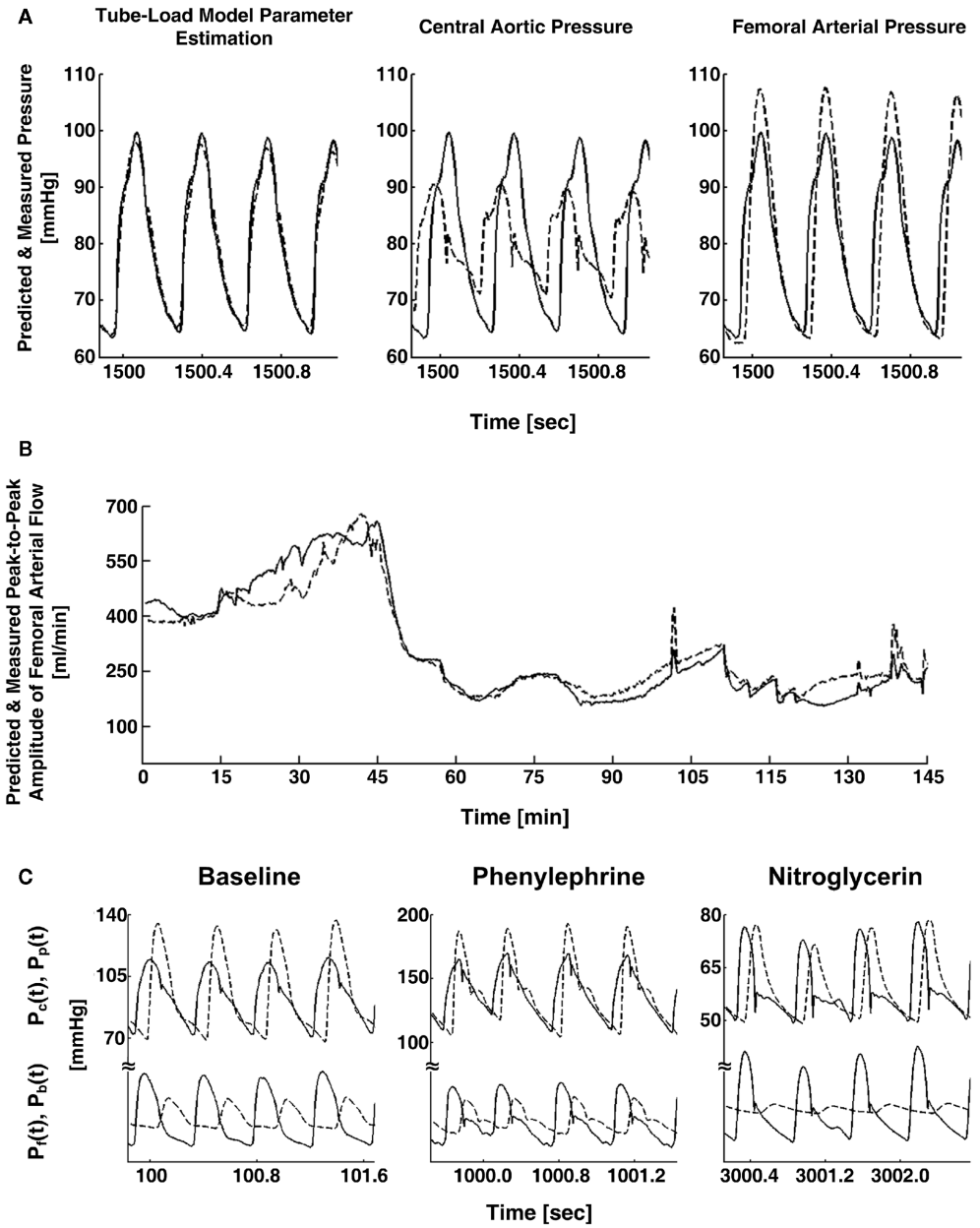

FIGURE 5 | (A) Abdominal aortic pressure waveforms measured (solid) and predicted (dash) from central aortic and femoral arterial pressure waveforms (left) and the raw central aortic and femoral arterial pressure waveforms (center and right). **(B)** Femoral arterial flow measured (solid) and predicted (dash; after a single calibration) from central aortic and femoral arterial pressure waveforms during several interventions. **(C)** Measured central aortic [$P_c(t)$, solid] and femoral arterial [$P_p(t)$, dash] pressure waveforms (upper) and forward [$P_f(t)$, solid] and backward [$P_b(t)$, dash] waves in the central aorta (lower) calculated from the measured waveforms. Adapted from Swamy et al. (2010).

aorta. The estimated compliance of the body-end tube was very close to the reference measurements obtained from the aortic arch to the abdominal aorta ($123 \pm 20 \times 10^{-6}\,\mathrm{g}^{-1}\,\mathrm{cm}^{-4}\,\mathrm{s}^2$ versus $119 \pm 10 \times 10^{-6}\,\mathrm{g}^{-1}\,\mathrm{cm}^{-4}\,\mathrm{s}^2$). On the other hand, they did not find physiologic meaning in the compliance estimates of the load model and therefore advocated the use of the Type III load. The authors also validated the model as a whole by predicting the abdominal aortic pressure waveform from the model parameter estimates and Eq. 8 for the body-end tube and load (see Wave Reflection Monitoring). The predicted waveform was in good agreement with the pressure waveform measured at the abdominal aorta.

Shroff et al. (1995) investigated the ability of the model parameter estimates to track changes during local as well as global interventions, with emphasis on arterial compliance. The authors employed the same parameter estimation technique as Campbell

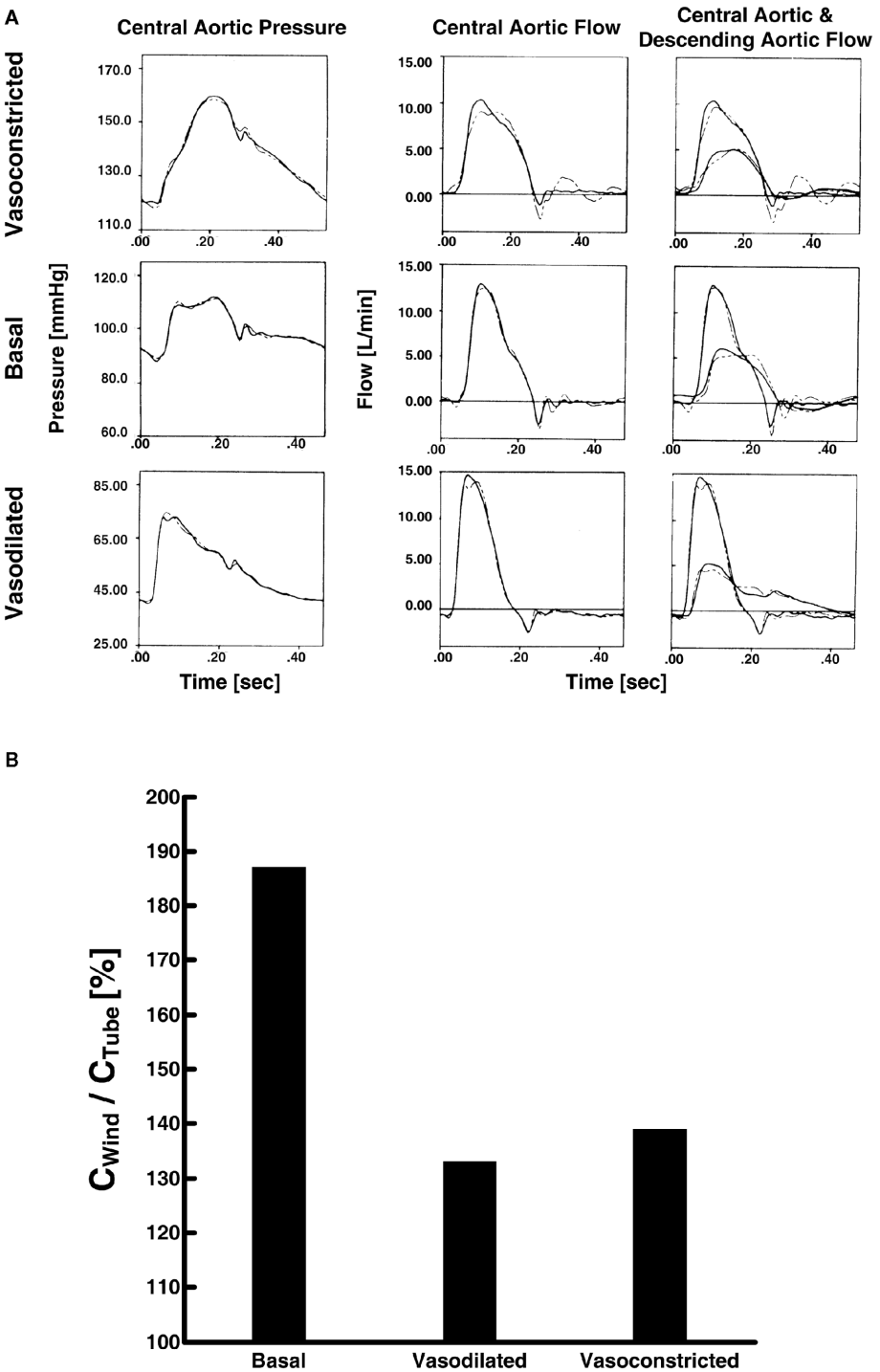

FIGURE 6 | (A) Measured central aortic pressure and flow and descending aortic flow waveforms (solid) and waveforms fitted (dash) using the first two waveforms only (left and center) and all three waveforms (right). Adapted from Campbell et al. (1990). **(B)** Ratio of large artery compliance estimates via Windkessel model (C_{Wind}) and tube-load model (C_{Tube}; Campbell et al., 1990).

et al. (1990). For a local intervention, they inflated a balloon in the iliac artery. The body-end tube compliance and all of the head-end model parameters were not affected by this intervention, whereas the compliance and resistances of the body-end load were significantly altered. **Figure 7** illustrates these physiologically consistent results. For global interventions, they administered a vasoconstrictor and vasodilator. The compliances and other model parameters changed in the expected direction in response to these

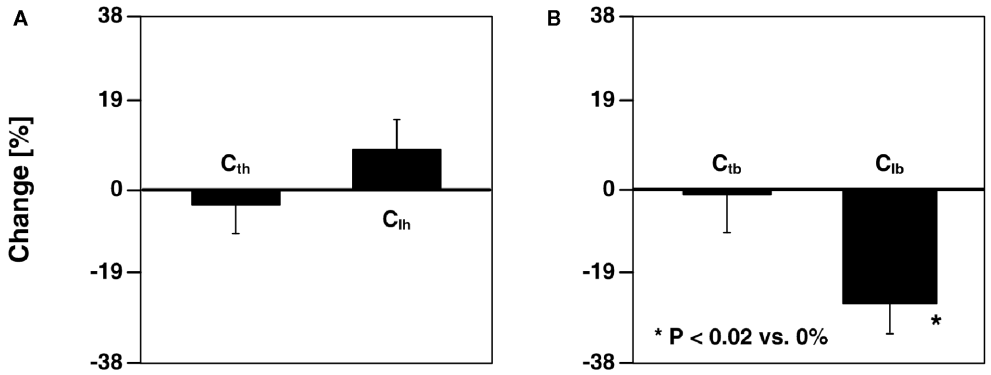

FIGURE 7 | Percent changes in (A) head-end tube and load compliances (C_{th} and C_{lh}) and (B) body-end tube and load compliances (C_{tb} and C_{lb}) estimated from central aortic pressure and flow and descending aortic flow waveforms after inflation of a balloon in the left external iliac artery. Adapted from Shroff et al. (1995).

interventions similar to Campbell et al. (1990). However, one notable difference was that the head-end tube compliance did not change during vasodilation.

PULSE TRANSIT TIME MONITORING

SIGNIFICANCE

As indicated above, pulse transit time varies with the square root of large artery compliance. Indeed, pulse transit time, in the form of pulse wave velocity, is now the most popular index of arterial stiffness for two reasons. First, it is an independent predictor of all-cause mortality and cardiovascular events in hypertensive and other patients (Mancia et al., 2007). Second, it can be estimated from only arterial pressure waveforms, whereas direct estimation of large artery compliance requires more difficult arterial flow waveform measurements.

PREVIOUS TECHNIQUES

Conventionally, pulse transit time is estimated by measuring central and peripheral arterial pressure waveforms with non-invasive transducers and then detecting the foot-to-foot time delay between the waveforms. The premise of this foot-to-foot detection technique is that interference from the backward wave is negligible during late diastole and early systole when the waveform feet occur. However, wave reflection interference may not always be trivial at the waveform feet. For example, at low heart rate, the backward wave adds constructively to the forward wave. Thus, in this condition, the technique can grossly underestimate pulse transit time. Just as important, the technique is not robust to artifact often present in the non-invasive waveforms (Solà et al., 2010). These two disadvantages of the foot-to-foot detection technique prevent pulse transit time from realizing its potential clinical value. Moreover, in contrast to peripheral arterial pressure waveforms, central arterial pressure waveforms are actually not easy to measure (Chen et al., 1997). As a result, pulse transit time is not widely used in clinical practice (Mancia et al., 2007).

Several other techniques are available for estimating pulse transit time/pulse wave velocity. However, for the most part, these techniques have not revealed any practical advantage over the foot-to-foot detection technique. As a relevant example, techniques have been conceived for estimating the true pulse transit time (i.e., the pulse transit time in the absence of wave reflection) via a tube model with a non-parametric load (see Milnor, 1989 and references therein). However, these techniques are inconvenient in that they necessitate three or more waveforms for measurement.

TUBE-LOAD MODEL PARAMETER ESTIMATION TECHNIQUES

Monitoring pulse transit time with tube-load model parameter estimation techniques potentially has significant advantages over the previous techniques. Since the model includes the true pulse transit time as an explicit parameter and characterizes the load with only a few parameters, these techniques can yield an artifact-robust estimate of the pulse transit time in the absence of wave reflection from only central and peripheral arterial pressure waveforms or even a pulse transit time estimate from just two peripheral arterial pressure waveforms.

Xu et al. (2010) and Zhang et al. (2011) estimated pulse transit time from central and peripheral arterial pressure waveforms during cardiac pacing and various other hemodynamic interventions. The authors specifically employed a single tube with Type I load. Based on Eq. 8, they estimated the true pulse transit time and the other two observable parameters by fitting the central aortic pressure waveform in response to a femoral arterial pressure waveform. Since the entire waveforms, rather than just their feet, were analyzed, they claimed that these pulse transit time estimates would be more robust to artifact in addition to reflecting the pulse transit time in the absence of wave reflection. To support this claim, the authors compared the tube-load model parameter estimation technique to the foot-to-foot detection technique in terms of the ability of their pulse transit time estimates to track changes in arterial pressure, a major, acute determinant of aortic stiffness with an inverse relationship to arterial compliance. The tube-load model parameter estimation technique showed tighter correlation between the pulse transit time estimates and arterial pressure than the foot-to-foot detection technique, especially during low signal-to-noise and low heart rate conditions. **Figure 8** illustrates that the tube-load model parameter estimation technique revealed strong, negative correlation at low heart rates, whereas the conventional technique showed non-physiologic, positive correlation indicative

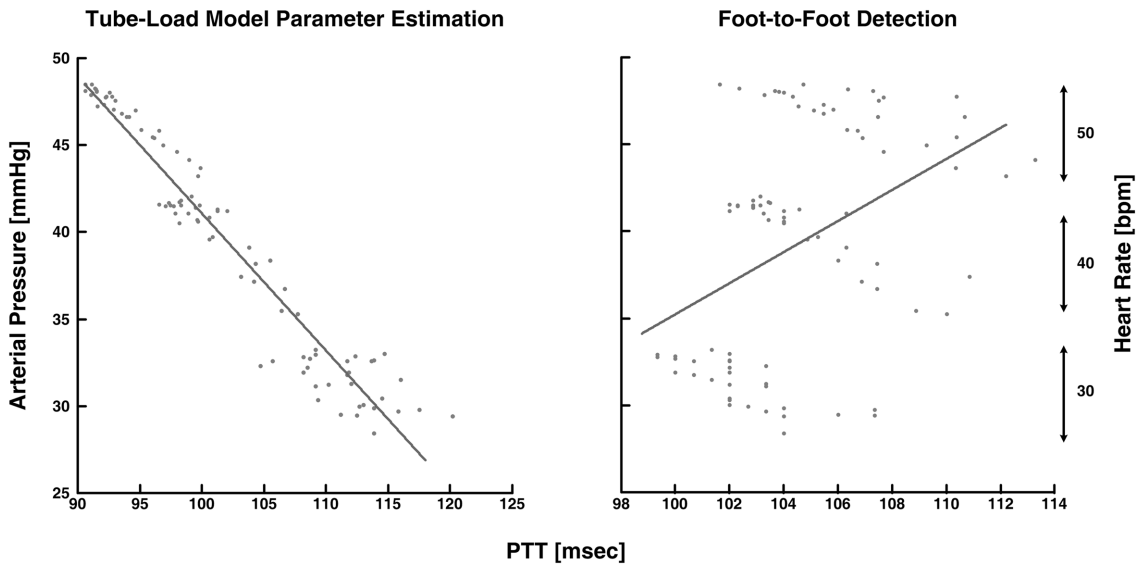

FIGURE 8 | Measured arterial pressure versus pulse transit time (PTT) estimated from central aortic and femoral arterial pressure waveforms. Adapted from Zhang et al. (2011).

of increasing underestimation of pulse transit time with decreasing heart rate.

Hahn et al. (2010) estimated pulse transit time from two diametric peripheral arterial pressure waveforms measured at the radial and femoral arteries. The authors specifically employed a T-tube model with Type II load. To estimate the model parameters without using the central aortic pressure waveform, they assumed that the head-end and body-end effective reflection sites correspond to the arterial beds distal to the radial and femoral arteries, respectively. They used Eq. 8 to define the transfer functions relating the central aortic pressure waveform to the radial and femoral arterial pressure waveforms as follows:

$$\begin{aligned} &P\left(j\omega\right) \\ &= \frac{\left[\left(R_1 + Z_{c1}\right) e^{j\omega T_1} + \left(R_1 - Z_{c1}\right) e^{-j\omega T_1}\right] + j\omega C_1 Z_{c1}\left[\left(2R_1 + Z_{c1}\right) e^{j\omega T_1} - Z_{c1} e^{-j\omega T_1}\right]}{2R_1\left(1 + j\omega Z_{c1} C_1\right)} \cdot P_1\left(0,\, j\omega\right) \\ &= \frac{\left[\left(R_2 + Z_{c2}\right) e^{j\omega T_2} + \left(R_2 + Z_{c2}\right) e^{-j\omega T_2}\right] + j\omega C_2 Z_{c2}\left[\left(2R_2 + Z_{c2}\right) e^{j\omega T_2} - Z_{c2} e^{-j\omega T_2}\right]}{2R_2\left(1 + j\omega Z_{c2} C_2\right)} \cdot P_2\left(0,\, j\omega\right), \end{aligned} \tag{10}$$

where the subscripts 1 and 2 denote the radial and femoral arteries, respectively. The authors were then able to estimate the true pulse transit time parameters and the other four observable parameters by fitting the femoral arterial pressure waveform in response to the radial arterial pressure waveform (or vice versa) via the second equality in Eq. 10. To facilitate the parameter estimation, they constrained the pulse transit times so that their difference is equal to the foot-to-foot time delay between the radial and femoral arterial pressure waveforms. It is important to note that Eq. 10 may only be used to estimate the model parameters, if the transfer functions on the left- and right-hand sides of Eq. 10 do not share any poles or zeros (i.e., the coprime condition Doyle et al., 2009). That is, common poles and/or zeros would cancel each other out, and the associated parameters would become unobservable in Eq. 10. In addition to the coprime condition, the authors showed in earlier work (Hahn et al., 2009a) that additional conditions must be met in order to uniquely estimate the parameters in Eq. 10. They further showed that these conditions can be fulfilled by appropriate choice of the peripheral arterial measurement sites and sampling frequency. The estimated pulse transit time was highly correlated with the foot-to-foot time delay between the central aortic (end of aortic arch) and peripheral arterial pressure waveforms. **Figure 9** shows the estimates (after an initial calibration with the foot-to-foot time delay) versus the foot-to-foot time delays.

CENTRAL AORTIC PRESSURE MONITORING

SIGNIFICANCE

Systolic and diastolic pressures measured specifically in the central aorta truly reflect cardiac afterload and myocardial perfusion. Further, pressure exerted on the central (elastic) arteries, as opposed to the peripheral arteries, is a major determinant of the degenerative changes that occur in hypertension and aging (Agabiti-Rosei et al., 2007). Because of its greater physiologic relevance, central arterial pressure can provide superior clinical value. Indeed, central arterial pressure, but not peripheral arterial pressure, has been shown to be an independent predictor of morality and/or cardiovascular events in geriatric patients (Pini et al., 2008), end-stage renal disease patients (Safar et al., 2002), and coronary artery disease patients (Jankowski et al., 2008). Moreover, compared to peripheral arterial pressure, central arterial pressure has been shown to correlate more strongly with age (Choi et al., 2010) and better discriminate the severity of coronary artery disease (Waddell et al., 2001). However, peripheral arterial pressure waveforms can

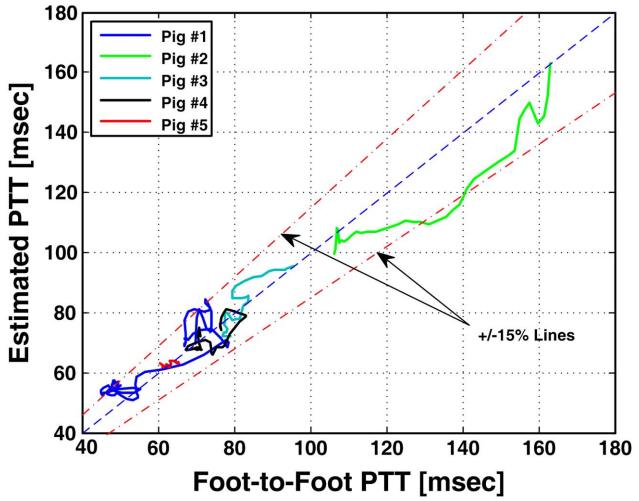

FIGURE 9 | Pulse transit time estimated from radial and femoral arterial pressure waveforms (after a single calibration) versus PTT estimated from aortic and peripheral arterial pressure waveforms via foot-to-foot detection. Adapted from Hahn et al. (2010).

be measured more easily and safely and are therefore typically measured in practice. Thus, it would be of great value to be able to monitor central aortic pressure from peripheral arterial pressure.

PREVIOUS TECHNIQUES

Several generalized transfer function techniques are available for deriving the central aortic pressure waveform from a peripheral arterial pressure waveform (Karamanoglu et al., 1993; Chen et al., 1997; Fetics et al., 1999; Söderström et al., 2002; Hope et al., 2003). These techniques involve creating an average black-box (rather than physiology-based) transfer function using central aortic and peripheral arterial pressure waveform measurements from a group of subjects and then applying this transfer function to the peripheral arterial pressure waveform of a new subject to predict the central aortic pressure waveform. The techniques therefore do not adapt to the inter-subject and temporal variability of the arterial tree due to, for example, age-related large artery compliance differences and neuro-humoral modulation of peripheral resistance, and consequently may be prone to serious error.

To improve accuracy, a technique to adapt the transfer function to arterial parameters has become available more recently (Sugimachi et al., 2001). This technique defines the transfer function in terms of the tube-load model parameters (i.e., inverse of Eq. 8). The pulse transit time parameter is then measured for each subject using a non-invasive measurement of any waveform indicative of the timing of the central arterial pulse. However, similar to generalized transfer function techniques, this technique uses population averages for the remaining observable parameters and is therefore only mildly adaptive.

TUBE-LOAD MODEL PARAMETER ESTIMATION TECHNIQUES

The central aortic pressure waveform can also be monitored from peripheral arterial pressure waveforms using tube-load model parameter estimation techniques. These techniques estimate all observable transfer function model parameters by exploiting *a priori* physiologic knowledge. Thus, the resulting transfer functions are fully adaptive by virtue of continually re-estimating the model parameters for each subject.

Hahn et al. (2009a) derived the central aortic pressure waveform from radial and femoral arterial pressure waveforms. The authors specifically employed a T-tube model with Type II load, as opposed to a black-box model (Swamy et al., 2007; Swamy and Mukkamala, 2008). They estimated the model parameters based on Eq. 10 in accordance with their parallel work (see Pulse Transit Time Monitoring). Then, they derived the central aortic pressure waveform by deconvolving the peripheral arterial pressure waveforms from the resulting transfer functions in Eq. 10 using a filtering technique they developed for stable deconvolution of signals in multi-channel coprime systems. In addition to the central aortic pressure waveform, the authors used the model parameter estimates to derive the central aortic flow waveform. **Figure 10A** shows a block diagram of their derivation of the central aortic pressure and flow waveforms. They specifically used the six estimated parameters and the *RC* time constant, as determined from the peripheral arterial pressure waveforms during diastole, to determine all but one of the parameters of the transfer function in Eq. 7b. They were then able to apply this transfer function to the derived central aortic pressure waveform to estimate the contour of the central aortic flow waveform (i.e., without absolute gain factor). Finally, the authors developed a metric that correlates with the quality of the estimated T-tube model parameters. The metric is defined as the distance between the heart rate frequency and the frequency at which the transfer function of the body-end tube model in Eq. 10 achieves its first maximum modulus. The rationale is that the fidelity of the parameter estimates depends on how well the arterial pressure waveforms (with maximum energy located at the heart rate frequency) excites the arterial tree at the first maximum modulus frequency (where the T-tube model is highly sensitive to all of the observable model parameters). **Figure 10B** illustrates that the derived central aortic pressure and flow waveforms (the latter after an initial calibration) agreed well with the corresponding measured waveforms.

Swamy et al. (2009) derived the central aortic pressure waveform from a single peripheral arterial pressure waveform during diverse hemodynamic interventions. The authors specifically employed a single tube with essentially Type I load to relate a peripheral arterial pressure waveform to the central aortic pressure waveform through the inverse of Eq. 8. They then estimated all three observable parameters by exploiting pre-knowledge that central aortic flow is negligible during diastole. More specifically, using Eq. 5, they first defined the transfer function relating the peripheral arterial pressure waveform to the central aortic flow waveform component to the peripheral artery in terms of the same unknown model parameters as follows:

$$Q_i\left(d_i, j\omega\right) = \frac{1}{Z_{ci}} \frac{\left(j\omega + \frac{1}{R_i C_i} + \frac{1}{2Z_{ci}C_i}\right) e^{j\omega T_i} - \frac{1}{2Z_{ci}C_i} e^{-j\omega T_i}}{j\omega + \frac{1}{R_i C_i} + \frac{1}{Z_{ci}C_i}} \cdot P_i\left(0, j\omega\right). \quad (11)$$

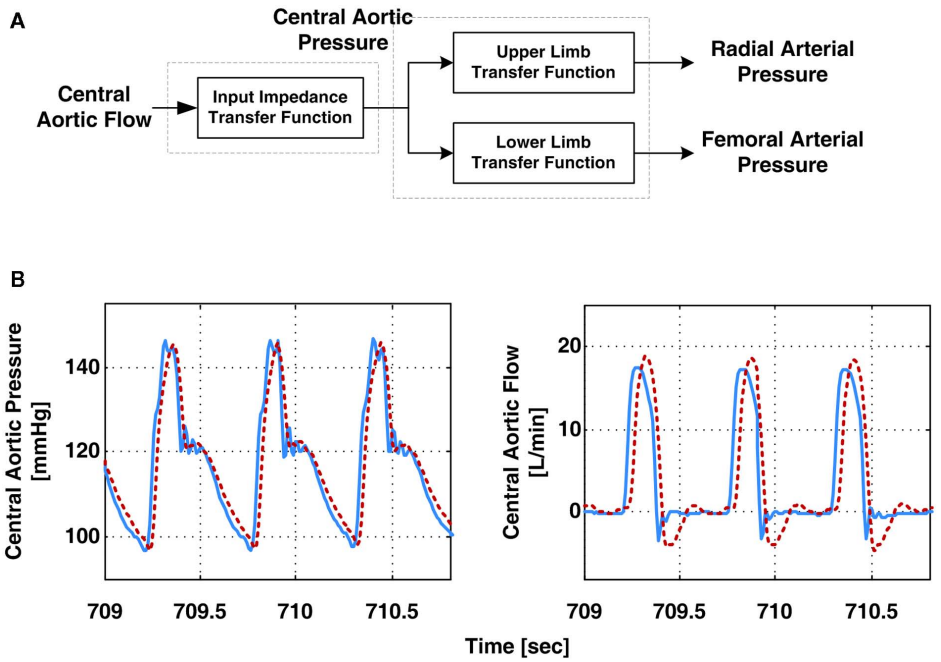

FIGURE 10 | (A) Block diagram of derivation of the aortic pressure and central aortic flow waveforms from radial and femoral arterial pressure waveforms. **(B)** Measured (solid) and derived (dash) waveforms. Adapted from Hahn et al. (2009a).

They then estimated the common parameters by fitting the central aortic flow waveform component to zero during diastole (as estimated via heart rate Malik, 1996) in response to a femoral arterial pressure waveform. To facilitate the parameter estimation, they likewise obtained an initial pulse transit time parameter estimate using a one-time, non-invasive measurement of a central arterial waveform. Finally, they inserted the parameter estimates into the inverse of Eq. 8 and applied this transfer function to the femoral arterial pressure waveform to derive the central aortic pressure waveform. The derived waveforms corresponded with reference central aortic pressure waveforms significantly better than those waveforms derived with the previous techniques, even though these techniques had the unfair advantage of being developed with a subset of the reference waveforms. **Figure 11** illustrates examples of the derived and measured pressure waveforms during three different interventions.

Hahn et al. (2008) derived the central aortic pressure waveform from a single peripheral arterial pressure waveform at the head-end circulation (e.g., radial or finger artery) without requiring a pulse transit time measurement. The authors specifically employed a single tube with Type II load to relate the two waveforms through the inverse of Eq. 8 with Type II load. First, they utilized the physiologic knowledge that the rate of change of the central aortic pressure waveform is smaller than that of the peripheral arterial pressure waveform. Thus, there exists a (sufficiently high) sampling frequency for which the rate of change of only the former waveform can be approximated as zero. By selecting this sampling frequency, the following equation results:

$$\begin{aligned}&\left\{\left[(R+Z)\,e^{j\omega T}+(R-Z)\,e^{-j\omega T}\right]\right.\\&\left.\quad+j\omega CZ\left[(2R+Z)\,e^{j\omega T}-Ze^{-j\omega T}\right]\right\}\cdot j\omega P\left(0,\,j\omega\right)\\&=\left[2R\left(1+j\omega ZC\right)\right]\cdot j\omega P\left(j\omega\right)\approx 0\end{aligned}\tag{12}$$

For a set of candidate pulse transit times, they were able to estimate the other two observable parameters by fitting the right-hand side of this equation to zero in response to the time derivative of the peripheral arterial pressure waveform. Second, to estimate the pulse transit time, they applied a feature extraction technique to the peripheral arterial pressure waveform. More specifically, they utilized the physiologic knowledge that, at the central aorta, the backward pressure wave from the head-end circulation will be positioned between the forward systolic wave and the backward pressure wave from the body-end circulation, which manifests itself as the secondary diastolic peak in the forward wave. They claimed that the forward systolic wave plus the head-end and body-end backward waves superposed in this way minimizes the sharpness of the central aortic pressure waveform (measured in terms of the second derivative norm of the waveform). Indeed, for small pulse transit time values corresponding to peripheral arterial pressure waveforms, strong superposition of forward systolic and head-end backward waves occurs, which yields a high systolic pressure that increases the sharpness of the waveform. On the other hand, for very large pulse transit time values that are not physiologically relevant, strong superposition of forward systolic and body-end backward waves occurs, which essentially yield a non-physiologic central aortic pressure waveform with a diastolic

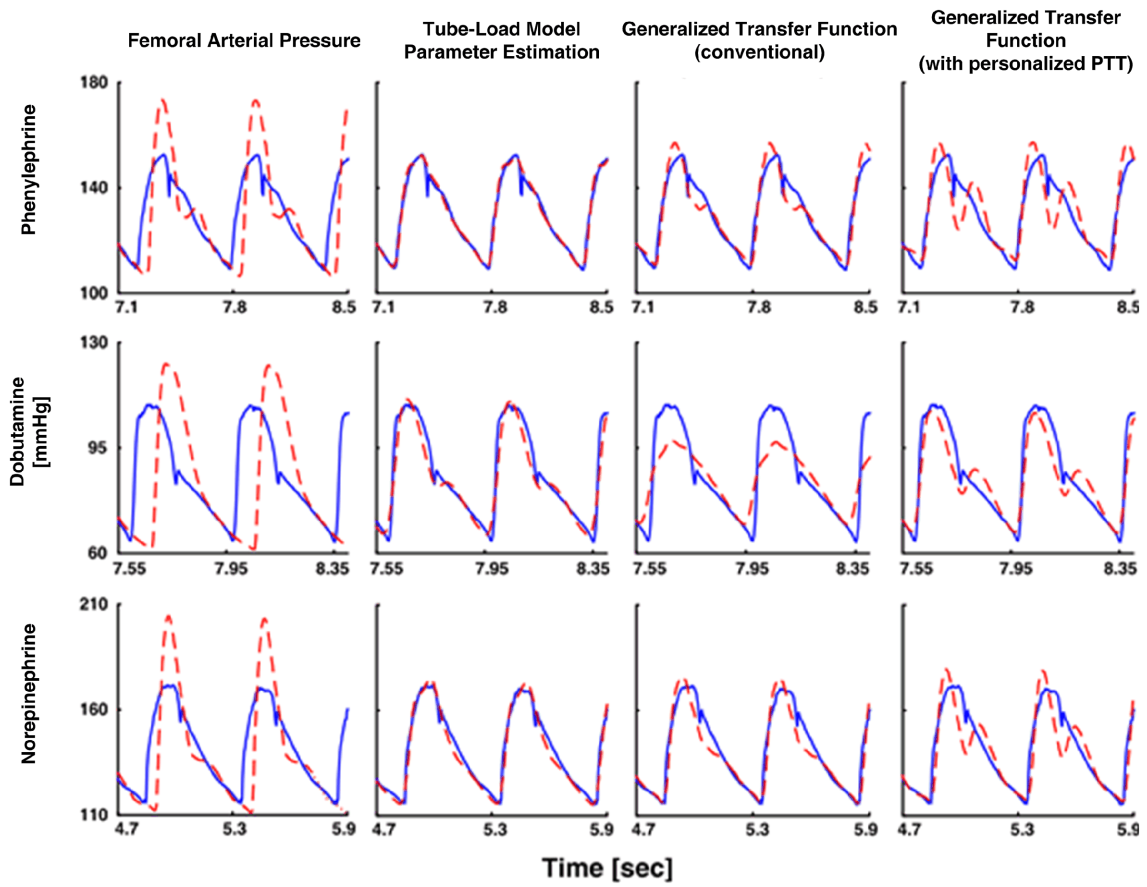

FIGURE 11 | Central aortic pressure waveforms measured (solid) and derived from a femoral arterial pressure waveform (dash). Adapted from Swamy et al. (2009).

peak larger than its systolic counterpart. For each of the candidate pulse transit time values, they inserted the three-parameter estimates into the inverse of Eq. 8 with Type II load and applied this transfer function to derive the candidate central aortic pressure waveform. They then calculated its second derivative norm. The central aortic pressure waveform was selected as the one with minimum sharpness among all candidate waveforms. **Figure 12** shows exemplary results of the derived central aortic pressure waveforms in comparison with measured central aortic and radial arterial pressure waveforms.

CONCLUSION

SUMMARY

The tube-load model of the arterial system represents an excellent balance between accuracy and simplicity. That is, this model can account for wave propagation and reflection phenomena (unlike lumped-parameter models models) while being characterized by only a few parameters that can be readily estimated from the limited arterial pressure and/or flow waveforms typically available in practice (unlike comprehensive distributed-parameter models). As a result, tube-load model parameter estimation represents an attractive platform for improved monitoring of arterial hemodynamics. A number of tube-load model parameter estimation techniques have appeared in the literature for monitoring wave reflection, large artery compliance, pulse transit time, and central aortic pressure. These techniques can offer significant advantages over previous waveform analysis techniques for monitoring these quantities. Indeed, they (a) have yielded important insights into the nature of wave reflections; (b) can allow for more convenient monitoring of wave reflection and pulse transit time; and (c) can permit more accurate monitoring of large artery compliance, pulse transit time, and central aortic pressure. A notable hallmark of the techniques is that their validation against reference measurements.

FUTURE DIRECTIONS

Although significant progress has been made in the area of tube-load model parameter estimation, there are still quite a few opportunities for future investigation. First, since peripheral arterial pressure waveforms are most easily measured, the application of tube-load model parameter estimation to these waveforms deserves further attention. The development of techniques for specifically estimating pulse transit time and central aortic flow from just a single peripheral arterial pressure waveform would be of tremendous clinical value. Second, the methods for parameter estimation require significant improvement. In particular, the development of efficient methods for honing in on the global

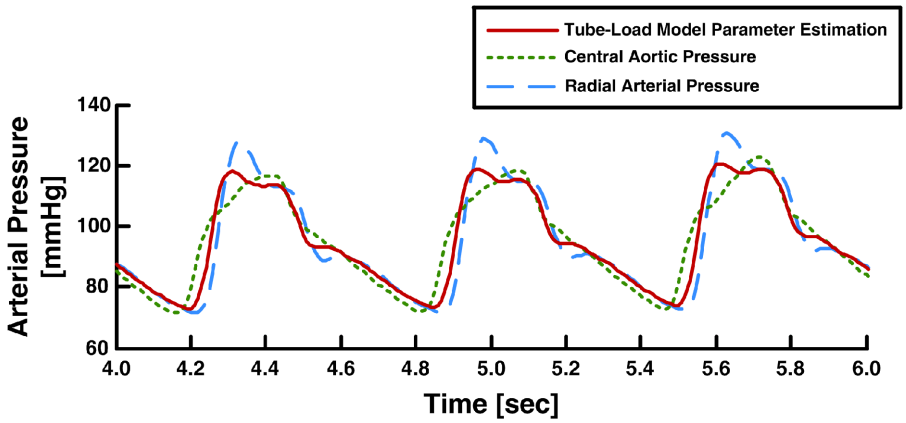

FIGURE 12 | Measured aortic and radial arterial pressure waveforms and aortic pressure waveform derived from the radial arterial pressure waveform. Adapted from Hahn et al. (2008).

optimum and useful physiologic bounds on the parameters would constitute a major contribution. Some combination of brute-force and local search methods may represent a good starting point. Third, investigation of the added value in using higher order loads that account for peripheral inertance for example would also be worthwhile. Finally and most importantly, continued validation of the techniques is necessary. The techniques have only been validated as applied to invasive waveforms from animals up to now. Therefore, validation in humans and as applied to non-invasive waveforms is a must (see, e.g., Hahn et al., 2009b). It would also be important to validate the pulse transit time estimates against gold standard measurements of large artery compliance and determine whether the techniques are applicable to waveforms measured at any peripheral arterial site or just certain sites.

POTENTIAL APPLICATIONS

With further investigation, tube-load model parameter estimation techniques have several potential applications. That is, the techniques for monitoring wave reflection and large artery compliance could be applied to invasive arterial pressure and flow waveforms from animal models to advance the understanding of arterial hemodynamics in health and disease. In addition, the techniques, especially for monitoring central aortic pressure, could be conveniently employed in critically ill patients with peripheral arterial catheters already in place for more precise titration of therapy (Chen et al., 1997). Finally, and most importantly, the techniques for monitoring pulse transit time and central aortic pressure in particular could be applied to non-invasive arterial pressure waveforms obtained with applanation tonometry or finger-cuff photoplethysmography to improve the management of hypertensive and other outpatients as suggested by clinical guidelines (Mancia et al., 2007).

ACKNOWLEDGMENTS

This work was supported in part by the National Science Foundation CAREER Grant 0643477, an award from the American Heart Association, and the Natural Sciences and Engineering Research Council of Canada.

REFERENCES

Abed-Meraim, K., Qiu, W., and Hua, Y. (1997). Blind system identification. *Proc. IEEE* 85, 1310–1322.

Agabiti-Rosei, E., Mancia, G., O'Rourke, M. F., Roman, M. J., Safar, M. E., Smulyan, H., Wang, J.-G., Wilkinson, I. B., Williams, B., and Vlachopoulos, C. (2007). Central blood pressure measurements and antihypertensive therapy: a consensus document. *Hypertension* 50, 154–160.

Avolio, A. P. (1980). Multi-branched model of the human arterial system. *Med. Biol. Eng. Comput.* 18, 709–718.

Azer, K., and Peskin, C. S. (2007). A one-dimensional model of blood flow in arteries with friction and convection based on the Womersley velocity profile. *Cardiovasc. Eng.* 7, 51–73.

Benetos, A., Laurent, S., Hoeks, A. P., Boutouyrie, P. H., and Safar, M. E. (1993). Arterial alterations with aging and high blood pressure. A noninvasive study of carotid and femoral arteries. *Arterioscler. Thromb.* 13, 90–97.

Bramwell, J. C. (1922). The velocity of the pulse wave in man. *Proc. R. Soc. Lond. B Biol. Sci.* 93, 298–306.

Burattini, R., and Campbell, K. B. (1989). Modified asymmetric T-tube model to infer arterial wave reflection at the aortic root. *IEEE Biomed. Eng.* 36, 805–814.

Burattini, R., and Campbell, K. B. (1993). Effective distributed compliance of the canine descending aorta estimated by modified T-tube model. *Am. J. Physiol.* 264, 1977–1987.

Burattini, R., and Campbell, K. B. (2000). Physiological relevance of uniform elastic tube-models to infer descending aortic wave reflection: a problem of identifiability. *Ann. Biomed. Eng.* 28, 512–523.

Burattini, R., Knowlen, G. G., and Campbell, K. B. (1991). Two arterial effective reflecting sites may appear as one to the heart. *Circ. Res.* 68, 85–99.

Campbell, K. B., Burattini, R., Bell, D. L., Kirkpatrick, R. D., and Knowlen, G. G. (1990). Time-domain formulation of asymmetric T-tube model of arterial system. *Am. J. Physiol.* 258, 1761–1774.

Chen, C. H., Nevo, E., Fetics, B., Pak, P. H., Yin, F. C., Maughan, W. L., and Kass, D. A. (1997). Estimation of central aortic pressure waveform by mathematical transformation of radial tonometry pressure. Validation of generalized transfer function. *Circulation* 95, 1827–1836.

Choi, C. U., Kim, E. J., Kim, S. H., Shin, S. Y., Choi, U.-J., Kim, J. W., Lim, H. E., Rha, S. W., Park, C. G., Seo, H. S., and Oh, D. J. (2010). Differing effects of aging on central and peripheral blood pressures and pulse wave velocity: a direct intra-arterial study. *J. Hypertens.* 28, 1252–1260.

Doyle, J., Francis, B., and Tannenbaum, A. (2009). *Feedback Control Theory*. New York, NY: Macmillan Publishing Company.

Fetics, B., Nevo, E., Chen, C. H., and Kass, D. A. (1999). Parametric model derivation of transfer function for noninvasive estimation of aortic pressure by radial tonometry. *IEEE Biomed. Eng.* 46, 698–706.

Fogliardi, R., Burattini, R., and Campbell, K. B. (1997). Identification and physiological relevance of an exponentially tapered tube model of canine descending aortic circulation. *Med. Eng. Phys.* 19, 201–211.

Glasser, S. P., Arnett, D. K., McVeigh, G. E., Finkelstein, S. M., Bank, A. K., Morgan, D. J., and Cohn, J. N. (1998). The importance of arterial compliance in cardiovascular drug therapy. *J. Clin. Pharmacol.* 38, 202–212.

Hahn, J.-O., Asada, H. H., Reisner, A. T., and Jaffer, F. A. (2008). "A new approach to reconstruction of central aortic blood pressure using adaptive transfer function," in *30th Annual International Conference of the IEEE Engineering in Medicine and Biology Society*, Vancouver, 813–816.

Hahn, J.-O., Reisner, A. T., and Asada, H. H. (2009a). Blind identification of two-channel IIR systems with application to central cardiovascular monitoring. *J. Dyn. Syst. Meas. Control* 131, 051009.

Hahn, J.-O., Reisner, A. T., and Harry Asada, H. (2009b). Modeling and 2-sensor blind identification of human cardiovascular system. *Control Eng. Pract.* 17, 1318–1328.

Hahn, J.-O., Reisner, A. T., and Asada, H. H. (2010). Estimation of pulse transit time using two diametric blood pressure waveform measurements. *Med. Eng. Phys.* 32, 753–759.

Hamilton, W. F., and Remington, J. W. (1947). The measurement of the stroke volume from the pressure pulse. *Am. J. Physiol.* 148, 14–24.

Haynes, R. B., Taylor, D. W., and Sackett, D. L. (1979). "Determinants of compliance: the disease and the mechanics of treatment," in *Compliance in Health Care*, eds R. B. Haynes, D. W. Taylor, and D. L. Sackett (Baltimore, MD: The Johns Hopkins University Press), 49–62.

Hope, S. A., Tay, D. B., Meredith, I. T., and Cameron, J. D. (2003). Use of arterial transfer functions for the derivation of aortic waveform characteristics. *J. Hypertens.* 21, 1299–1305.

Huberts, W., Bosboom, E. M. H., and van de Vosse, F. N. (2009). A lumped model for blood flow and pressure in the systemic arteries based on an approximate velocity profile function. *Math. Biosci. Eng.* 6, 27–40.

Jankowski, P., Kawecka-Jaszcz, K., Czarnecka, D., Brzozowska-Kiszka, M., Styczkiewicz, K., Loster, M., Kloch-Badelek, M., Wilinski, J., Curylo, A. M., Dudek, D., and Aortic Blood Pressure and Survival Study Group. (2008). Pulsatile but not steady component of blood pressure predicts cardiovascular events in coronary patients. *Hypertension* 51, 848–855.

Karamanoglu, M., O'Rourke, M. F., Avolio, A. P., and Kelly, R. P. (1993). An analysis of the relationship between central aortic and peripheral upper limb pressure waves in man. *Eur. Heart J.* 14, 160–167.

Lévy, B. I. (2001). Artery changes with aging: degeneration or adaptation? *Dialog. Cardiovasc. Med.* 6, 104–111.

Ljung, L. (1999). *System Identification: Theory for the User*, 2nd Edn. Upper Saddle River, NJ: Prentice Hall.

London, G. M., Marchais, S. J., and Safar, M. E. (1989). Arterial compliance in hypertension. *J. Hum. Hypertens.* 3(Suppl. 1), 53–56.

Malik, M. (1996). If Dr. Bazett had had a computer. *Pacing Clin. Electrophysiol.* 19, 1635–1639.

Mancia, G., De Backer, G., Dominiczak, A., Cifkova, R., Fagard, R., Germano, G., Grassi, G., Heagerty, A. M., Kjeldsen, S. E., Laurent, S., Narkiewicz, K., Ruilope, L., Rynkiewicz, A., Schmieder, R. E., Boudier, H. A., Zanchetti, A., Vahanian, A., Camm, J., De Caterina, R., Dean, V., Dickstein, K., Filippatos, G., Funck-Brentano, C., Hellemans, I., Kristensen, S. D., McGregor, K., Sechtem, U., Silber, S., Tendera, M., Widimsky, P., Zamorano, J. L., Erdine, S., Kiowski, W., Agabiti-Rosei, E., Ambrosioni, E., Lindholm, L. H., Viigimaa, M., Adamopoulos, S., Agabiti-Rosei, E., Ambrosioni, E., Bertomeu, V., Clement, D., Erdine, S., Farsang, C., Gaita, D., Lip, G., Mallion, J. M., Manolis, A. J., Nilsson, P. M., O'Brien, E., Ponikowski, P., Redon, J., Ruschitzka, F., Tamargo, J., van Zwieten, P., Waeber, B., Williams, B., Management of Arterial Hypertension of the European Society of Hypertension, and European Society of Cardiology. (2007). 2007 guidelines for the management of arterial hypertension: the task force for the management of arterial hypertension of the European Society of Hypertension (ESH) and of the European Society of Cardiology (ESC). *J. Hypertens.* 25, 1105–1187.

Milnor, W. (1989). *Hemodynamics*, 2nd Edn. Baltimore, MD: Williams and Wilkins.

Newman, D. L., Greenwald, S. E., and Bowden, N. L. (1979). An in vivo study of the total occlusion method for the analysis of forward and backward pressure waves. *Cardiovasc. Res.* 13, 595–600.

Nichols, W. W., and O'Rourke, M. F. (2005). *McDonald's Blood Flow in Arteries: Theoretical, Experimental and Clinical Principles*, 5th Edn. New York, NY: Oxford University Press.

Noordergraaf, A. (1978). *Circulatory System Dynamics.* New York, NY: Academic Press.

Pappano, A. J., Wier, W. G., Nelson, M. T., and Levy, M. N. (2007). *Cardiovascular Physiology*, 9th Edn. Philadelphia, PA: Mosby Elsevier.

Pini, R., Cavallini, M. C., Palmieri, V., Marchionni, N., Di Bari, M., Devereux, R. B., Masotti, G., and Roman, M. J. (2008). Central but not brachial blood pressure predicts cardiovascular events in an unselected geriatric population: the ICARe Dicomano study. *J. Am. Coll. Cardiol.* 51, 2432–2439.

Proakis, J. G., and Manolakis, D. K. (2007). *Digital Signal Processing*, 4th Edn. Upper Saddle River, NJ: Prentice Hall.

Raines, J. K., Jaffrin, M. Y., and Shapiro, A. H. (1974). A computer simulation of arterial dynamics in the human leg. *J. Biomech.* 7, 77–91.

Reneman, R. S., and Hoeks, A. P. (1995). Arterial distensibility and compliance in hypertension. *Neth. J. Med.* 47, 152–161.

Safar, M. E., Blacher, J., Pannier, B., Guerin, A. P., Marchais, S. J., Guyonvarc'h, P.-M., and London, G. M. (2002). Central pulse pressure and mortality in end-stage renal disease. *Hypertension* 39, 735–738.

Sagawa, K., Lie, R. K., and Schaefer, J. (1990). Translation of Otto Frank's paper "Die Grundform des Arteriellen Pulses" Zeitschriftfür Biologie. *J. Mol. Cell. Cardiol.* 22, 253–254.

Sherwin, S. J., Franke, V., Peiró, J., and Parker, K. (2003). One-dimensional modelling of a vascular network in space-time variables. *J. Eng. Math.* 47, 217–250.

Shroff, S. G., Berger, D. S., Korcarz, C., Lang, R. M., Marcus, R. H., and Miller, D. E. (1995). Physiological relevance of T-tube model parameters with emphasis on arterial compliances. *Am. J. Physiol.* 269, 365–374.

Söderström, S., Nyberg, G., O'Rourke, M. F., Sellgren, J., and Pontén, J. (2002). Can a clinically useful aortic pressure wave be derived from a radial pressure wave? *Br. J. Anaesth.* 88, 481–488.

Solà, J. M., Rimoldi, S. F., and Allemann, Y. (2010). "Ambulatory monitoring of the cardiovascular system: the role of pulse wave velocity," in *New Developments in Biomedical Engineering*, ed. D. Campolo (Rijeka, Croatia: InTech), 391–424.

Stergiopulos, N., Westerhof, B. E., and Westerhof, N. (1999). Total arterial inertance as the fourth element of the windkessel model. *Am. J. Physiol.* 276, 81–88.

Sugimachi, M., Shishido, T., Miyatake, K., and Sunagawa, K. (2001). A new model-based method of reconstructing central aortic pressure from peripheral arterial pressure. *Jpn. J. Physiol.* 51, 217–222.

Swamy, G., Ling, Q., Li, T., and Mukkamala, R. (2007). Blind identification of the aortic pressure waveform from multiple peripheral artery pressure waveforms. *Am. J. Physiol. Heart Circ. Physiol.* 292, 2257–2264.

Swamy, G., and Mukkamala, R. (2008). Estimation of the aortic pressure waveform and beat-to-beat relative cardiac output changes from multiple peripheral artery pressure waveforms. *IEEE Biomed. Eng.* 55, 1521–1529.

Swamy, G., Olivier, N. B., and Mukkamala, R. (2010). Calculation of forward and backward arterial waves by analysis of two pressure waveforms. *IEEE Biomed. Eng.* 57, 2833–2839.

Swamy, G., Xu, D., Olivier, N. B., and Mukkamala, R. (2009). An adaptive transfer function for deriving the aortic pressure waveform from a peripheral artery pressure waveform. *Am. J. Physiol. Heart Circ. Physiol.* 297, 1956–1963.

Van Bortel, L. M., and Spek, J. J. (1998). Influence of aging on arterial compliance. *J. Hum. Hypertens.* 12, 583–586.

Waddell, T. K., Dart, A. M., Medley, T. L., Cameron, J. D., and Kingwell, B. A. (2001). Carotid pressure is a better predictor of coronary artery disease severity than brachial pressure. *Hypertension* 38, 927–931.

Wan, J., Steele, B., Spicer, S. A., Strohband, S., Feijóo, G. R., Hughes, T. J. R., and Taylor, C. A. (2002). A one-dimensional finite element method for simulation-based medical planning for cardiovascular disease. *Comput. Methods Biomed.* 5, 195–206.

Westerhof, N., Sipkema, P., van den Bos, G. C., and Elzinga, G. (1972). Forward and backward waves in the arterial system. *Cardiovasc. Res.* 6, 648–656.

Xu, D., Zhang, G., Olivier, N. B., and Mukkamala, R. (2010). "Monitoring aortic stiffness in the presence of measurement artifact based on an arterial tube model," in *32nd Annual International Conference of the IEEE Engineering in Medicine and Biology Society*, Buenos Aires, 3453–3456.

Zagzoule, M., and Marc-Vergnes, J. P. (1986). A global mathematical model of the cerebral circulation in man. *J. Biomech.* 19, 1015–1022.

Zhang, G., Gao, M., and Mukkamala, R. (2011). "Robust, beat-to-beat estimation of the true pulse transit time from central and peripheral blood pressure or flow waveforms using an arterial tube-load model," in *33rd Annual International Conference of the IEEE Engineering in Medicine and Biology Society*, Boston, MA.

Conflict of Interest Statement: The authors declare that the research was conducted in the absence of any commercial or financial relationships that could be construed as a potential conflict of interest.

Received: 01 August 2011; accepted: 30 September 2011; published online: 01 November 2011.

Citation: Zhang G, Hahn J-O and Mukkamala R (2011) Tube-load model parameter estimation for monitoring arterial hemodynamics. Front. Physio. ***2****:72. doi: 10.3389/fphys.2011.00072*

This article was submitted to Frontiers in Computational Physiology and Medicine, a specialty of Frontiers in Physiology.

frontiers in
PHYSIOLOGY

ORIGINAL RESEARCH ARTICLE
published: 04 January 2012
doi: 10.3389/fphys.2011.00111

Modeling the autonomic and metabolic effects of obstructive sleep apnea: a simulation study

Limei Cheng and Michael C. K. Khoo*

Biomedical Engineering Department, University of Southern California, Los Angeles, CA, USA

Edited by:
Zhe Chen, Massachusetts Institute of Technology, USA

Reviewed by:
Luca Citi, Harvard Medical School, USA
Premananda Indic, University of Massachusetts Medical School, USA
Sandun Kodituwakku, Australian National University, Australia

****Correspondence:***
Michael C. K. Khoo, Biomedical Engineering Department, University of Southern California, DRB-140, University Park, Los Angeles, CA 90089-1111, USA.
e-mail: khoo@bmsr.usc.edu

Long-term exposure to intermittent hypoxia and sleep fragmentation introduced by recurring obstructive sleep apnea (OSA) has been linked to subsequent cardiovascular disease and Type 2 diabetes. The underlying mechanisms remain unclear, but impairment of the normal interactions among the systems that regulate autonomic and metabolic function is likely involved. We have extended an existing integrative model of respiratory, cardiovascular, and sleep–wake state control, to incorporate a sub-model of glucose–insulin–fatty acid regulation. This computational model is capable of simulating the complex dynamics of cardiorespiratory control, chemoreflex and state-related control of breath-to-breath ventilation, state-related and chemoreflex control of upper airway potency, respiratory and circulatory mechanics, as well as the metabolic control of glucose–insulin dynamics and its interactions with the autonomic control. The interactions between autonomic and metabolic control include the circadian regulation of epinephrine secretion, epinephrine regulation on dynamic fluctuations in glucose and free-fatty acid in plasma, metabolic coupling among tissues and organs provided by insulin and epinephrine, as well as the effect of insulin on peripheral vascular sympathetic activity. These model simulations provide insight into the relative importance of the various mechanisms that determine the acute and chronic physiological effects of sleep-disordered breathing. The model can also be used to investigate the effects of a variety of interventions, such as different glucose clamps, the intravenous glucose tolerance test, and the application of continuous positive airway pressure on OSA subjects. As such, this model provides the foundation on which future efforts to simulate disease progression and the long-term effects of pharmacological intervention can be based.

Keywords: physiological model simulation, obstructive sleep apnea, sleep regulation, metabolic function, autonomic–metabolic interactions, computational modeling, integrative modeling, metabolism

INTRODUCTION

The current obesity epidemic is contributing to the increasing prevalence of the "metabolic syndrome," the clustering of symptoms that include insulin resistance, hypertension, and dyslipidemia (Reilly and Rader, 2003). The components of metabolic syndrome individually or collectively constitute high-risk factors for cardiovascular disease and Type 2 diabetes. Since obstructive sleep apnea (OSA) commonly occurs among obese individuals, there is a growing recognition of the possibility that OSA may constitute an independent risk factor for the metabolic syndrome (Tasali and Ip, 2008). Indeed, OSA has been found to be strongly associated with insulin resistance (Punjabi et al., 2002), Type 2 diabetes (Chasens, 2007), as well as hypertension and various kinds of cardiovascular disease (Reaven, 1980). The causal pathways that link OSA to hypertension and insulin resistance remain unclear. However, it has been demonstrated that exposure to intermittent hypoxia (IH) in humans can lead to prolonged elevation of muscle sympathetic nerve activity following termination of the chemical stimulation (Xie et al., 2000). As well, in an elegant canine model, artificially induced periodic airway obstruction during sleep led to sustained elevation of daytime blood pressure after several weeks of nocturnal exposure (Brooks et al., 1997). Thus, a plausible scenario is that the sympathetic overactivity resulting from OSA leads to increased catecholamine release, which produces hyperglycemia and, in turn, hyperinsulinemia, which promotes insulin resistance. Increased sympathetic activity is also known to stimulate lipolysis from adipose tissue and thus contribute to the elevation of circulating free-fatty acids (FFAs; Bamshad et al., 1998). Increased FFAs impair net glucose uptake by the tissues, contributing further to the hyperglycemia and hyperinsulinemia (Roy and Parker, 2006). Since hyperinsulinemia stimulates sympathetic activity, a vicious cycle could well develop that leads to worsening autonomic function and insulin resistance.

As mentioned in our previous work (Cheng et al., 2010), many simulation models of cardiovascular and respiratory systems have been developed since 1950s and some models were designed for special disorders in cardiorespiratory physiology but very few were involved in the interactions between these systems and none of them have studied the interactions of cardiorespiratory response with sleep. Also, over the past several decades, a large number of mathematical models of glucose and insulin

dynamics have appeared in the literature. Most of the earlier models were aimed at gaining a better understanding of glucose–insulin dynamics during diagnostic tests (Himsworth and Ker, 1939; Steele, 1959; Bolie, 1961; Ackerman et al., 1965; Andres et al., 1966; DeFronzo et al., 1979). The models employed primarily for purposes of parameter estimation have generally been simple in terms of the small number of free parameters, such as Bergman's minimal model (Bergman et al., 1979) and Turner's homeostatic model assessment (HOMA, Turner et al., 1979). However, there are also many models that have more complex structures, such as those used for quantifying β-cell mass, glucose disappearance, β-cell glucose sensitivity, and insulin secretion and resistance (Srinivasan et al., 1970; Sherwin et al., 1974; Insel et al., 1975; Howard et al., 1984; Berger and Rodbard, 1989; Bergman, 1989; Berman et al., 1993; Genter et al., 1998; Bergman et al., 2006). Some of these models have been designed to account for glucose–insulin dynamics observed in subjects with Type 1 diabetes (Skowronski et al., 1991; Parker et al., 1999; Porksen et al., 2002). Other models also incorporate the dynamics of fatty acids (Skowronski et al., 1991; Nolan et al., 2006; Hucking et al., 2007). Most of these models are useful in providing better insight into metabolic regulation and for developing therapeutic approaches to Type 1 and Type 2 diabetes, but none have taken into account the potential mechanisms with which autonomic dysfunction may contribute to metabolic dysfunction and vice versa. To date, we know of no other modeling study that has linked cardiovascular autonomic and respiratory control with metabolic control, especially in the context of sleep-disordered breathing.

As a first exploration of the hypothesis that the sympathetic nervous system may be the crucial factor that lies at the center of the causal pathways that link OSA to hypertension and metabolic dysfunction, we extended our existing integrative model of respiratory, cardiovascular, and sleep regulation (Cheng et al., 2010) to incorporate a sub-model of metabolic function, capable of simulating the dynamics of glucose–insulin, and FFA dynamics in wakefulness and sleep. The extended model includes features such as the circadian regulation of sympathetic nervous activity and epinephrine secretion, and the effects of epinephrine on the dynamic fluctuations of glucose and FFA in plasma. The extended model also incorporates the effect of hyperinsulinemia on the peripheral sympathetic nervous system.

MATERIALS AND METHODS

Our existing comprehensive model of sleep-cardiorespiratory control, heretofore referred to as "PNEUMA," includes the autonomic control of the cardiovascular system, chemoreflex and state-related control of breath-to-breath ventilation, state-related and chemoreflex control of upper airway potency, as well as respiratory and circulatory mechanics. It provides realistic predictions of the physiological responses under a wide variety of conditions, including the day-to-day sleep–wake cycle, hypoxia-induced periodic breathing, Cheyne–Stokes respiration in chronic heart failure, and OSA. It can be used to investigate the effects of virtual experiments and interventions such as isocapnic and hypercapnic and/or hypoxic gas administration, the Valsalva and Mueller maneuvers, and the application of continuous positive airway pressure (CPAP) on OSA patients. A detailed account of "PNEUMA" is given in Cheng et al. (2010).

To better understand the causal link between OSA and insulin resistance, it is necessary to extend "PNEUMA" to include a metabolic model of glucose and insulin that involves with energy metabolism and its interaction with the autonomic function. One of the most widely used and validated models of glucose and insulin dynamics is the three compartment minimal model method by Bergman et al. (1981), which is commonly used to estimate insulin sensitivity from an intravenous glucose tolerance test (IVGTT). The model is "minimal" in the sense that it is sufficiently complex enough to characterize the key features of the dynamic interaction between glucose and insulin, and yet simple enough to be fully estimated from blood measurements of insulin and glucose in individual subjects. It provides a sufficient level of complexity for characterizing glucose and insulin dynamics in our large-scale model with minimum numbers of model parameters, while the other metabolic models are either too simple or too complex. FFA provides about 90% of the muscle energy at rest and FFA has been shown to play an important role in glucose and insulin dynamics in last three decades (Randle et al., 1988; Rebrin et al., 1995). However, the metabolic regulation of FFA and its incorporation with glucose and insulin has been largely ignored by others. The extended minimal model (Roy and Parker, 2006) takes into account the contribution of FFA metabolism and its interaction with glucose and insulin, thereby allowing the synthesis "lipid-based" metabolic models with meals. For this reason, we have based our metabolic regulation sub-model on the Roy–Parker extended minimal model. Furthermore, it is known that sympathetic activation affects glucose and FFA metabolism. In this model, we postulate that sympathetic activity directly affects plasma epinephrine levels, and that epinephrine modulates glucose and FFA metabolism via mechanisms modeled by Kim et al. (2006).

The model of glucose dynamics employed here is a modified version of the minimal model by Bergman et al. (1981). Plasma glucose disappearance occurs in the peripheral tissues by oxidation and in the liver mainly by glycogenesis. The dynamics of glucose metabolism is given by Eq. 1, where $G(t)$ is the plasma glucose concentration, $X(t)$ is "remote" insulin action that accelerates glucose utilization in the peripheral tissues and liver and inhibits hepatic glucose production, $Z(t)$ is the plasma FFA concentration and is described in the FFA dynamics section, subscript "b" stands for basal level, $u_{2\text{int}}(t)$ is the internal glucose flux rate, $u_{2\text{ext}}(t)$ is the glucose external input rate that could be food intake or external infusion rate of glucose, and Vol_G is the glucose distribution space.

$$\frac{dG(t)}{dt} = -p_1 G(t) + p_1 G_b - p_4 X(t) G(t) + p_4 X_b G_b + p_6 Z(t) G(t) - p_6 Z_b G_b + \frac{k_{\text{EG}} u_{2\,\text{int}}(t) + u_{2\text{ext}}(t)}{\text{Vol}_G} \quad (1)$$

Plasma insulin dynamics is described using a two-compartment model with three first-order functions given by Eqs 2–4 below, where $I(t)$ is the plasma insulin concentration, $X(t)$ is time-course of insulin action which presents a receptor for insulin in periphery, $Y(t)$ is added in the extended minimal model to represent

the insulin in peripheral tissues that promotes FFA storage and inhibits FFA release from adipose tissue into the circulations, G_h is the threshold glucose concentration, T_{Di} is the variable time delay, and $u_1(t)$ is the external input rate for the insulin model.

$$\frac{dI(t)}{dt} = \gamma\left(G\left(t - T_{\mathrm{Di}}\right) - G_h\right)t - n\left(I(t) - I_b\right) + p_5 u_1(t) \quad (2)$$

$$\frac{dX(t)}{dt} = -p_2\left(X(t) - X_b\right) + p_3\left(I(t) - I_b\right) \quad (3)$$

$$\frac{dY(t)}{dt} = -p_{F2}\left(Y(t) - Y_b\right) + p_{F3}\left(I(t) - I_b\right) \quad (4)$$

Although FFA metabolism accounts for most of the energy production in the body at rest, the role of FFA has been overlooked in most models of glucose–insulin regulation. To incorporate the contribution of FFA in metabolic control, we employed the model introduced by Roy and Parker (2006). A schematic diagram of the dynamics of FFA and the interactions among glucose, insulin, and FFA is displayed in **Figure 1**; the model is characterized by Eqs 5–7 below, where $F(t)$ is the FFA concentration in plasma, $Z(t)$ is the additional first-order filter, acting as the remote plasma FFA concentration that promotes the glucose uptake, subscript b represents basal level in the plasma, $u_{3\mathrm{int}}(t)$ is the internal FFA flux rate, and $u_{3\mathrm{ext}}(t)$ is the external FFA uptake rate. **Table 1** provides a detailed listing of all model parameters and their values.

$$\frac{dF(t)}{dt} = -p_7 F(t) + p_7 F_b - p_8 Y(t)F(t) + p_8 Y_b F_b + p_9^G G(t)F(t) - p_9^G G_b F_b + \frac{k_{\mathrm{EF}} u_{3\,\mathrm{int}}(t) + u_{3\mathrm{ext}}(t)}{\mathrm{Vol}_F} \quad (5)$$

$$\frac{dZ(t)}{dt} = -k_2\left(Z(t) - Z_b\right) + k_1\left(F(t) - F_b\right) \quad (6)$$

where

$$p_9^G = 0.00021e^{-0.0055G} \quad (7)$$

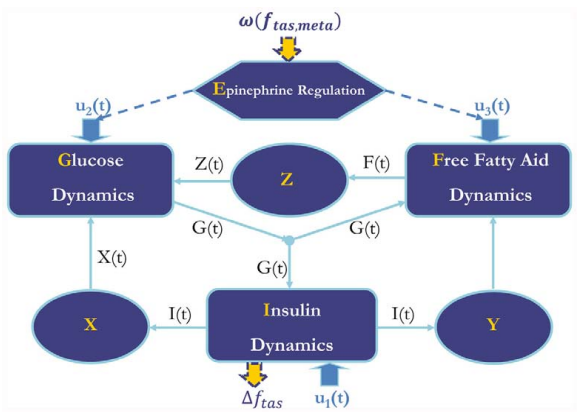

FIGURE 1 | Diagram of metabolic model with epinephrine regulation. X, remote insulin level; Y, remote insulin promotes FFA production and utilization; Z, remote FFA level. Δf_{tas}, feedback from metabolic system to autonomic control; $\omega(f_{\mathrm{tas,meta}})$, effect of efferent sympathetic activity and circadian process on metabolic system. $u_1(t)$, $u_2(t)$, and $u_3(t)$: inputs for insulin, glucose, and FFA dynamics, respectively.

The model allows for insulin to be introduced intravenously into the system (as external input rate $u_1(t)$ in **Figure 1**) for simulation of IVGTT and hyperinsulinemic interventions. Glucose can be introduced intravenously into the system for simulation of hyperglycemia, euglycemia, and hypoglycemia in the form of external infusion rate $u_{2\mathrm{ext}}(t)$. Another external source of glucose is in the form of dietary glucose intake rate $[u_{2\mathrm{ext}}(t)]$; in this case, we assume periodic pulses that represent three meals which occur at regular times each day.

In the extended model, we assume that the peripheral sympathetic activity and state index generated by PNEUMA affects epinephrine dynamics, which in turn influences the neuroendocrine inputs to the heart, skeletal muscle, and pancreas (**Figure 1**). "Feedback" from the metabolic sub-model to the autonomic part of PNEUMA is represented by the stimulatory effect of insulin on alpha-sympathetic activity (ANS Control block on **Figure 2**). The metabolic fluxes for glucose and FFA in heart, skeletal muscle, gastrointestinal tract, adipose tissue, and other tissues (including kidney) are modulated by epinephrine and given in the form displayed as Eq. 8, which is derived from the multi-scale model of Kim et al. (2006). The flux i in tissue/organ x is mathematically characterized as the following flux rates:

$$V_{x,i} = V_{x,i}^o\left(1.0 + \lambda_{x,i}^E \frac{(\Delta \cdot \mathrm{E}(t) - \mathrm{E}(0))^2}{\alpha_{x,i}^{\mathrm{E}} + (\Delta \cdot \mathrm{E}(t) - \mathrm{E}(0))^2}\right) \quad (8)$$

where subscript x = "heart," "muscle," "gastrointestinal tract," "adipose tissue," or "other tissues"; subscript i = "glucose" (assuming the metabolic pathway: GLC ← → G6P ← GLY) or "FFA" (assuming the metabolic pathway: TGL ← → FFA → ACoA).

For the heart, there are both glucose fluxes and FFA fluxes from epinephrine regulation which provide inputs to glucose dynamics and FFA dynamics in the whole metabolic control system; for muscle, there are both glucose fluxes and FFA fluxes from epinephrine regulation; and for the gastrointestinal tract, there is only FFA flux involved. The internal input rates for glucose and FFA kinetics are the sum of metabolic flux rates given by epinephrine regulation as Eqs 9A and 9B, respectively. The arterial epinephrine concentration is a static function of alpha-sympathetic activity given by Eq. 10.

$$u_{2\,\mathrm{int}}(t) = \sum_x V_{x,i}(t) \quad (9a)$$

$$u_{3\,\mathrm{int}}(t) = \sum_x V_{x,i}(t) \quad (9b)$$

$$E(t) = E(0) + E_b \cdot \omega\left(f_{\mathrm{tas,meta}}\right) \cdot \left[1.0 - exp\left(-t/\tau_E\right)\right] \quad (10)$$

Figure 3 shows the results of a simulation in which the extension to PNEUMA is run on a stand-alone basis (prior to being linked with the rest of PNEUMA). Here, epinephrine regulation is driven by the function $\omega(\alpha_{\mathrm{symp}})$ which represents the time-course of relative sympathetic activity over the circadian period of 24 h. $\omega(\alpha_{\mathrm{symp}})$ is assumed to remain at a constant level of zero over

Table 1 | Simulation parameters and initial conditions in metabolic model and its link with autonomic control.

Parameter	Definition	Values	Units	Source
INTERLINK BETWEEN METABOLIC MODEL AND AUTONOMIC CONTROL				
$K_{Ce,0}$	Gain for basal level of epinephrine in plasma	9	Dimension-less	Model
b_{REM}	Gain for REM sleep effect from autonomic control on epinephrine regulations	0.4	Dimension-less	Model
a_w	Parameter from autonomic control on epinephrine regulations	0.6	Dimension-less	Model
$f_{tas,0}$	Basal firing rate of sympathetic activity	2.1	1/s	Cheng et al. (2010)
K_{as}	Gain of metabolic feedback to change of sympathetic activities	2	Dimension-less	Model
$f_{tas,I0}$	Parameter of metabolic feedback to change of sympathetic activities	1	Dimension-less	Model
$K_{isc,I}$	Parameter of metabolic feedback to change of sympathetic activities	20	Dimension-less	Model
τ_I	Time constant of metabolic feedback to change of sympathetic activities	30	Minute	Model
PLASMA GLUCOSE DYNAMICS				
P_1	Utilization rate for plasma glucose concentration	0.068	1/min	Roy and Parker (2006)
P_4	Utilization rate for plasma glucose concentration under the influence of remote insulin	1.3	mL/min/μU	Roy and Parker (2006)
P_6	Production rate for remote plasma glucose concentration that promotes FFA	0.00006	L/min/μmol	Roy and Parker (2006)
G_b	Basal level of plasma glucose concentration	124.8	mg/dL	Roy and Parker (2006)
Vol_G	Glucose distribution space	117	dL	Roy and Parker (2006)
K_{EG}	Gain from epinephrine to glucose uptake	0.04	Dimension-less	Model
PLASMA INSULIN DYNAMICS				
n	Utilization rate for plasma insulin concentration	0.142	1/min	Roy and Parker (2006)
P_5	Factor for insulin inputs	0.000568	1/mL	Roy and Parker (2006)
I_b	Basal level of plasma insulin concentration	16.6	μU/mL	Model
P_3	Production rate for remote insulin concentration	0.000012	1/min	Roy and Parker (2006)
γ	Insulin sensitivity factor	0.038	μU/mL/min^2/mg/dL	Toffolo et al. (1980)
T_{Di}	Variable time delay	5 ± 3	s	Model
G_h	Threshold of plasma glucose concentration	125	mg/dL	Roy and Parker (2006)
P_2	Utilization rate for remote insulin concentration	0.037	1/min	Roy and Parker (2006)
P_{F2}	Utilization rate for remote insulin concentration that promotes FFA	0.17	1/min	Roy and Parker (2006)
P_{F3}	Production rate for remote insulin concentration that promotes FFA	0.00001	1/min	Roy and Parker (2006)
X_b	Basal level of remote plasma insulin concentration	0.08125	μU/mL	Model
Y_b	Basal level of remote plasma insulin concentration that promotes FFA production	0.008125	μU/mL	Model
PLASMA FREE-FATTY ACID DYNAMICS				
P_7	Utilization rate for plasma FFA concentration	0.03	1/min	Roy and Parker (2006)
P_8	Utilization rate for remote plasma insulin involved FFA concentration	4.5	mL/min/μU	Roy and Parker (2006)
F_b	Basal level of plasma FFA concentration	380	μmol/L	Roy and Parker (2006)
Z_b	Basal level of remote plasma FFA concentration	190	μmol/L	Roy and Parker (2006)
k_2	Utilization rate for remote FFA concentration	0.03	1/min	Roy and Parker (2006)
k_1	Production rate for remote FFA concentration	0.02	1/min	Roy and Parker (2006)
Vol_F	FFA distribution space	11.7	L	Roy and Parker (2006)
K_{EF}	Gain from epinephrine to FFA uptake	0.01	Dimension-less	Model
EPINEPHRINE REGULATION				
E_b	Basal level of epinephrine concentration in plasma	198	pM	Kim et al. (2006)
τ_E	Time constant for epinephrine regulation	30	min	Kim et al. (2006)
Δ	Epinephrine regulation factor for metabolic fluxes	1e6	Dimension-less	Model
$V_{0\_GLC\_Heart}$	Maximum rate coefficient in heart	88	μmol/min	Kim et al. (2006)
$\lambda_{E\_GLC\_Heart}$	Epinephrine regulated flux parameter in heart	3	Dimension-less	Kim et al. (2006)
$\alpha_{E\_GLC\_Heart}$	Epinephrine regulated flux parameter in heart	1000	pM	Kim et al. (2006)
$V_{0\_GLY\_Heart}$	Maximum rate coefficient in heart	320	μmol/min	Kim et al. (2006)
$\lambda_{E\_GLY\_Heart}$	Epinephrine regulated flux parameter in heart	0	Dimension-less	Kim et al. (2006)

(Continued)

Table 1 | Continued

Parameter	Definition	Values	Units	Source
$\alpha_{E\_GLY\_Heart}$	Epinephrine regulated flux parameter in heart	0	pM	Kim et al. (2006)
$V_{0\_FFA\_Heart}$	Maximum rate coefficient in heart	280	μmol/min	Kim et al. (2006)
$\lambda_{E\_FFA\_Heart}$	Epinephrine regulated flux parameter in heart	2	Dimension-less	Kim et al. (2006)
$\alpha_{E\_FFA\_Heart}$	Epinephrine regulated flux parameter in heart	447.2	pM	Kim et al. (2006)
$V_{0\_TGL\_Heart}$	Maximum rate coefficient in heart	8	μmol/min	Kim et al. (2006)
$\lambda_{E\_TGL\_Heart}$	Epinephrine regulated flux parameter in heart	0.5	Dimension-less	Kim et al. (2006)
$\alpha_{E\_TGL\_Heart}$	Epinephrine regulated flux parameter in heart	1000	pM	Kim et al. (2006)
$V_{0\_GLC\_Muscle}$	Maximum rate coefficient in muscle	398	μmol/min	Kim et al. (2006)
$\lambda_{E\_GLC\_Muscle}$	Epinephrine regulated flux parameter in muscle	18	Dimension-less	Kim et al. (2006)
$\alpha_{E\_GLC\_Muscle}$	Epinephrine regulated flux parameter in muscle	1000	pM	Kim et al. (2006)
$V_{0\_GLY\_Muscle}$	Maximum rate coefficient in muscle	1000	μmol/min	Kim et al. (2006)
$\lambda_{E\_GLY\_Muscle}$	Epinephrine regulated flux parameter in muscle	0.3	Dimension-less	Kim et al. (2006)
$\alpha_{E\_GLY\_Muscle}$	Epinephrine regulated flux parameter in muscle	10	pM	Kim et al. (2006)
$V_{0\_FFA\_Muscle}$	Maximum rate coefficient in muscle	701	μmol/min	Kim et al. (2006)
$\lambda_{E\_FFA\_Muscle}$	Epinephrine regulated flux parameter in muscle	9	Dimension-less	Kim et al. (2006)
$\alpha_{E\_FFA\_Muscle}$	Epinephrine regulated flux parameter in muscle	447.2	pM	Kim et al. (2006)
$V_{0\_PYR\_Muscle}$	Maximum rate coefficient in muscle	80	μmol/min	Kim et al. (2006)
$\lambda_{E\_PYR\_Muscle}$	Epinephrine regulated flux parameter in muscle	2	Dimension-less	Kim et al. (2006)
$\alpha_{E\_PYR\_Muscle}$	Epinephrine regulated flux parameter in muscle	1000	pM	Kim et al. (2006)
$V_{0\_TGL\_Muscle}$	Maximum rate coefficient in muscle	260	μmol/min	Kim et al. (2006)
$\lambda_{E\_TGL\_Muscle}$	Epinephrine regulated flux parameter in muscle	2.5	Dimension-less	Kim et al. (2006)
$\alpha_{E\_TGL\_Muscle}$	Epinephrine regulated flux parameter in muscle	1000	pM	Kim et al. (2006)
$V_{0\_TGL\_GI}$	Maximum rate coefficient in GI tract	80	μmol/min	Kim et al. (2006)
$\lambda_{E\_TGL\_GI}$	Epinephrine regulated flux parameter in GI tract	2	Dimension-less	Kim et al. (2006)
$\alpha_{E\_TGL\_GI}$	Epinephrine regulated flux parameter in GI tract	1000	pM	Kim et al. (2006)
$V_{0\_TGL\_adipose}$	Maximum rate coefficient in adipose	190	μmol/min	Kim et al. (2006)
$\lambda_{E\_TGL\_adipose}$	Epinephrine regulated flux parameter in adipose	2	Dimension-less	Kim et al. (2006)
$\alpha_{E\_TGL\_adipose}$	Epinephrine regulated flux parameter in adipose	1000	pM	Kim et al. (2006)

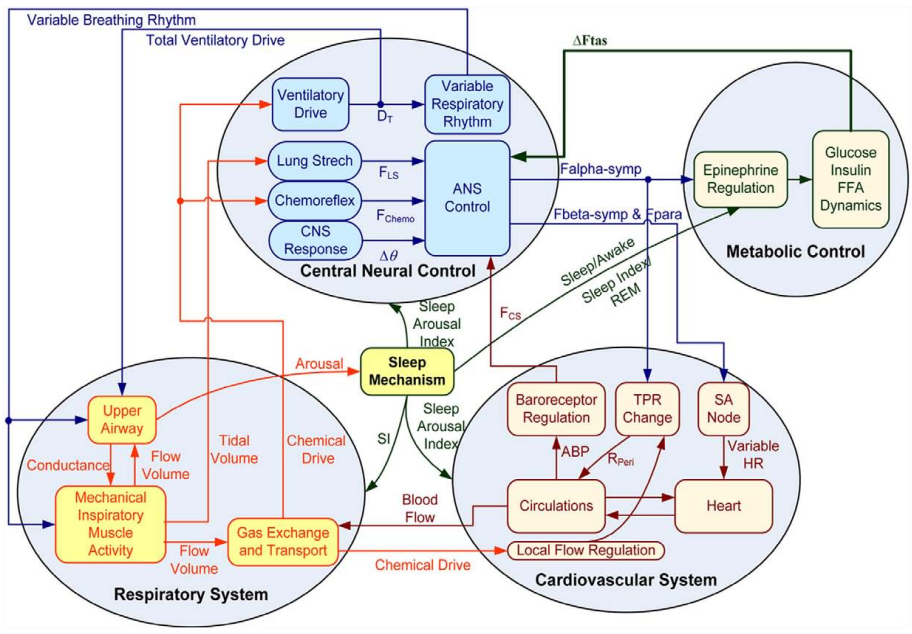

FIGURE 2 | Diagram of integrative model of autonomic and metabolic interactions.

16 h of quiet wakefulness. During sleep, $\omega(\alpha_{symp})$ assumes the form of the negative half of a sine wave, representing decreased sympathetic activity in sleep. This decreased baseline in sympathetic activity is punctuated by relatively short pulses, representing increases in sympathetic activity during REM sleep over the subsequent 8 h of sleep (**Figure 3A**). The corresponding fluctuations in epinephrine concentration $[E(t)]$, glucose concentration $[G(t)]$, insulin concentration $[I(t)]$, and FFA concentration $[F(t)]$ are shown in **Figure 3B**. G_{in} represents the time-course of the external glucose inputs that arise from meal ingestion three times a day.

When the model extension is linked with the rest of PNEUMA (see **Figure 2**), $\omega(\alpha_{symp})$ is replaced by $\omega(f_{tas,meta})$ which contains the sum of all efferent alpha-sympathetic firing rates and a modulatory factor that reflects sleep–wake state changes, as shown in Eq. 11 below. $E(0)$ is now no longer a constant (E_b) as in the stand-alone version of the model extension, but this variable is assumed to vary dynamically around its basal level E_b and is controlled by the efferent alpha-sympathetic firing rate and sleep state index as given in Eq. 14.

$$\omega\left(f_{tas,meta}\right) = \left[f_{tas,meta} - f_{tas,meta0} + 1\right]^{-SI \cdot G_{as\_sleep}} \times (1 + b_{REM} \cdot REM) \cdot (1 - SI \cdot a_{\omega}) \quad (11)$$

$$f_{tas,meta} = f_{tas} \cdot \left(1 - SI \cdot G_{as\_sleep}\right) \quad (12)$$

$$f_{tas,meta0} = f_{tas,0} \cdot \left(1 - SI \cdot G_{as\_sleep}\right) \quad (13)$$

$$E(0) = E_b + K_{Ce,0} \cdot \left(f_{tas,meta} - f_{tas,meta0}\right) \cdot (1 - SI) \quad (14)$$

When the extended version of PNEUMA is said to operate "*with metabolic feedback*," we are referring to the configuration in which plasma insulin concentration is allowed to influence alpha-sympathetic firing rate dynamically through Eq. 15 through Eq. 17.

$$W(I) = k_{as} + k_{as} \cdot f_{tas,I0} \cdot \frac{\exp\left[(I - I_b)/k_{isc,I}\right] - 1}{\exp\left[(I - I_b)/k_{isc,I}\right] + 1} \quad (15)$$

$$\Delta f_{tas} = W(I) \cdot \left[1 - exp\left(-t/\tau_I\right)\right] \quad (16)$$

$$f_{tas,FB} = f_{tas} + \Delta f_{tas} \quad (17)$$

where $f_{tas} = f_{tas,\,res}$ and $f_{tas,\,vein}$, respectively.

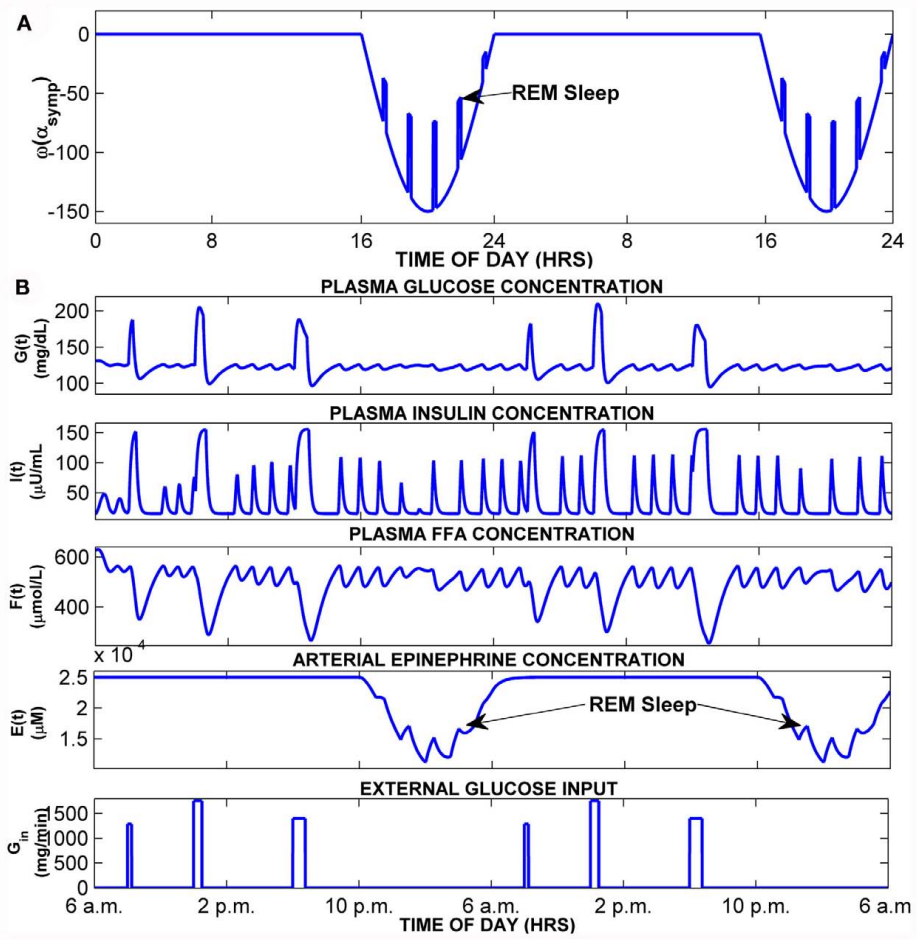

FIGURE 3 | Simulation of normal subject in stand-alone model extension. (A) Time-course of $\omega(\alpha_{symp})$, the function that converts changes in alpha-sympathetic activity into changes in epinephrine amount. **(B)** Model simulation showing 2-day time-courses of blood glucose, insulin, FFA, epinephrine, and external glucose inputs (meals).

The extended version of PNEUMA has been tested for simulation durations as long as 84 days (12 weeks). Each simulation generally begins with sleep onset (10 pm) on the first day. Meals during the day are simulated as step increases in blood glucose, with "breakfast" starting 90 min after the end of sleep cycle. However, since the model of sleep–wake regulation employed by PNEUMA can produce variable sleep durations, depending on whether the factor known as "sleep propensity" is sufficiently reduced to a threshold value during sleep (Cheng et al., 2010), the start times for breakfast can vary from 7 am to 9 am. Simulations with PNEUMA have previously shown that the sleep fragmentation resulting from repetitive arousals during the night in OSA delays the rate at which sleep propensity is reduced in the model during sleep (Cheng et al., 2010). As such, simulated sleep duration is longer in the subject with OSA compared to the subject with normal breathing, if sleep is not artificially interrupted. However, in reality, total sleep duration is constrained due to the occurrence of time cues, such as a clock alarm that goes off at a set time each day. If one factors this in, then the "subject" who has OSA will suffer from a small amount of sleep deprivation each day, since the sleep propensity index is not allowed to decrease to its natural minimum before sleep is terminated and wakefulness occurs. In the results that are presented here, we assume that sleep is terminated 7 h after the start of sleep onset.

The implementation of the model using Simulink® (The Mathworks, Natick, MA, USA) introduces the advantages of modularity, flexibility, and platform-independence, and provides a convenient basis for any future model extensions for modeling, simulating, and analyzing dynamic physiological systems. In its current implementation, PNEUMA is a large model with 557 parameters and 92 states. It takes approximately 12 h of computational time to run a 10-day simulation with variable time step where maximum time step is 10 ms on a PC with an Intel Core 2 Duo E8500 central processing unit. PNEUMA is implemented using a combination of discrete and continuous states, solving ordinary differential and algebraic equations that characterize physiological processes that cover a broad temporal scale, ranging from milliseconds (e.g., heartbeat) to hours (e.g., changes in blood glucose) to days (e.g., circadian rhythm).

An accompanying graphical user interface (GUI) panel allows users to conveniently change the values of a large number of parameters or impose a variety of physiological conditions without having to modify the program directly. Advanced users can vary parameter values or make changes to the underlying models by directly modifying the graphical objects in the Simulink® code. The details of the software are described in the PNEUMA manual. The software and manual can be downloaded free of charge from the following web-link: *http://bmsr.usc.edu/Software/BMSRsoftware.html*

RESULTS

STAND-ALONE MODEL EXTENSION RESULTS

In the stand-alone version of the model extension, epinephrine dynamics are generated through Eq. 10 with its own generated input source of $\omega(\alpha_{symp})$ plotted in **Figure 3A** which presents the effects from autonomic function to the metabolic system. Within this initial closed-loop model without any external inputs and external links, the resulting glucose–insulin and FFA dynamics with epinephrine regulation for a 2-day simulation in the middle of a 60-day simulation is shown in **Figure 3B**. During sleep, sympathetic tone is reduced below the wakefulness baseline, but in REM sleep, the model assumes that there are transient surges in sympathetic activity, which lead to small elevations of epinephrine during the REM episodes. In wakefulness, during each meal, the blood glucose level increases followed by a corresponding increase in plasma insulin and subsequent drop in the plasma FFA, illustrating the antilipolytic effect of insulin. The model predicts the occurrence of oscillations (with periodicities of ∼120 min) that arise from the dynamic interactions among glucose, insulin, and FFA, in particular between the meals. However, these "ultradian" oscillations, most evident in insulin and FFA, persist during sleep when there are no meals. In general, higher baseline levels of plasma epinephrine enhance the frequency and amplitude of these oscillations. These predictions are consistent with observations of ultradian oscillations of insulin and glucose reported in the literature (Polonsky et al., 1988; Sturis et al., 1991; Simon, 1998).

SIMULATION OF NORMAL SUBJECT: EFFECTS OF "METABOLIC FEEDBACK"

Figure 4 shows the results for a *normal* subject on day 10 of simulation time. Breakfast is assumed to start 90 min after the end of sleep. The predicted time-courses of the cardiovascular, respiratory, and metabolic variables following 10 days of simulation *without* metabolic feedback (Δf_{tas}) are displayed in blue, whereas the corresponding model predictions *with* metabolic feedback are shown in red. The mean levels of systolic blood pressure (SBP) and diastolic blood pressure (DBP) are higher in the case with metabolic feedback relative to the case without metabolic feedback, consistent with the increased epinephrine amount in heart and skeleton muscle during wakefulness when metabolic feedback is present (**Figure 4A** – only a segment of 200 s is displayed for purposes of clarity). On average, SBP/DBP values in wakefulness are 117/82 mmHg with metabolic feedback vs. 105/73 mmHg without metabolic feedback. During sleep, the corresponding SBP/DBP values are 108/72 with metabolic feedback vs. 102/67 without metabolic feedback. There is a certain amount of autonomic compensation for the elevation in blood pressure via the baroreflex through a decrease in heart rate (HR). In wakefulness, mean HR is approximately 78 beats/min with metabolic feedback vs. 85 beats/min without metabolic feedback, whereas in sleep, the corresponding mean HR values are 74 vs. 76 beats/min.

The dynamics of glucose, insulin, FFA, and epinephrine over the course of 24 h on "Day 10" are shown in **Figure 4B**. The surges in glucose concentration represent the impact of meals taken during the wakefulness period. As in the stand-alone case presented in the previous section, the model predicts the occurrence of ultradian oscillations in insulin, FFA, and (to a smaller extent) glucose. These oscillations are most evident during sleep, consistent with the ultradian fluctuations observed by others (Sturis et al., 1991; Simon, 1998; Porksen et al., 2002; Kim et al., 2007). These display a periodicity of ∼54 min, which is within the range consistent with experimental observations (Polonsky et al., 1988; Simon and Brandenberger, 2002). During REM sleep, the epinephrine concentration in plasma is slightly higher than NREM sleep due to

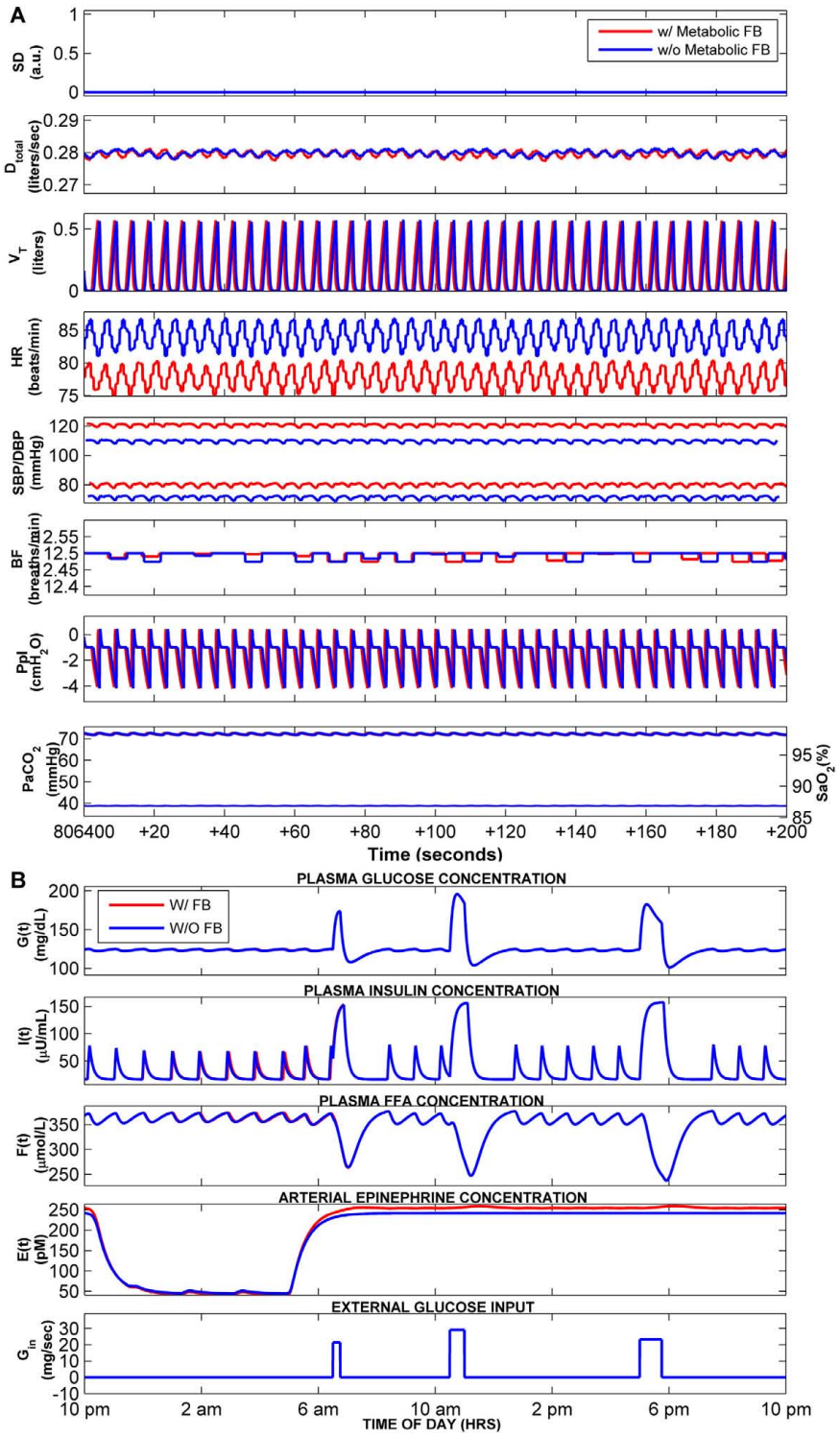

FIGURE 4 | Cardiorespiratory and metabolic responses predicted by the extended model on Day 10 of total simulation duration. The case with metabolic feedback (red) is compared with the case without metabolic feedback (blue). Sleep starts at 10 pm and ends at 5 am every day. **(A)** Time-courses of the key cardiorespiratory variables – a segment of only 200 s duration, starting at 6 am of Day 10, is displayed for clarity. SD, sleep state index (wake/sleep = 0/1); D_{total}, total ventilatory drive (L/s); V_T, tidal volume (L); HR, heart rate (beat/min); SBP/DBP, systolic and diastolic blood pressure (mmHg); BF, breathing frequency (breaths/min); P_{pl}, pleural pressure (cmH_2O); P_aCO_2 (Thin Lines), arterial PCO_2 (mmHg); SO_2 (Thick Lines), saturation of oxygen (%). **(B)** Predicted time-courses of plasma glucose, insulin, FFA, epinephrine, and the external glucose inputs to the model (representing three meals during wakefulness).

increased sympathetic activity – this has also been reported in the experimental literature (Linares et al., 1987). The plasma epinephrine concentration is slightly higher with metabolic feedback vs. no feedback during wakefulness. However, the model predicts that the effect of metabolic feedback on the predicted time-courses of glucose, insulin, and FFA is minimal. This result is somewhat surprising and contrary to initial expectations that the plasma insulin level would be higher in the case with metabolic feedback. We believe that this prediction reflects saturation effects that are derived from the non-linear relationship between epinephrine level and its effects on plasma glucose and FFA.

NORMAL BREATHING VS. OSA WITH METABOLIC FEEDBACK

As in our previous work (Cheng et al., 2010), to allow the model to simulate OSA sleep, the upper airway sensitivity parameter (S_{ua}) was increased from its control value of 0.01 in normal breathing to at least 0.38. **Figure 5A** (second through eighth panels) displays the predicted time-courses of the key cardiovascular and respiratory variables for the OSA "subject" during sleep (displayed as blue tracings) on the 10th day of simulated time, contrasted against the corresponding time-courses in a normal control (displayed as red tracings). In both cases, the model simulations have been run with metabolic feedback, and sleep duration has been limited to 7 h. The first panel of **Figure 5A** shows the sleep state index ("SD"), with SD = 1 representing deep sleep and SD = 0 representing wakefulness. The normal subject remains asleep (SD = 1) throughout the duration displayed, whereas in the OSA subject, arousals are triggered (SD changes from 1 to 0) at the end of the obstructive episodes. Without or with metabolic feedback, simulations of OSA during sleep produce the cardiovascular, respiratory, and neural responses similar in form to what we had shown previously, as well as to observations reported in the literature (Bradley and Floras, 2003). With the metabolic feedback, the model still predicts periodicities on the order of ∼52 s, which is consistent with our previous work and literature (Leung and Bradley, 2001; Cheng et al., 2010). The corresponding dynamics of glucose, insulin, FFA, and epinephrine over the 10th day of simulation are shown in **Figure 5B**. During sleep, reduced sympathetic nervous system activity decreases epinephrine amount in heart and skeleton muscle in both normal breathing and OSA, but there is higher level of epinephrine in OSA sleep than in normal sleep due to the elevated level of sympathetic activity in OSA sleep. Epinephrine levels in OSA are further enhanced in REM sleep relative to non-REM sleep, reflecting the relatively higher sympathetic activity in REM. Because of the elevated epinephrine levels during sleep in OSA, the ultradian oscillations in insulin in the OSA subject are noticeably higher in amplitude compared to the corresponding insulin oscillations in the normal subject.

TIME-COURSE OF DEVELOPMENT OF METABOLIC AND AUTONOMIC EFFECTS IN OSA

Figure 6 displays the results of a simulation (N → OSA) in which the model is first run with the upper airway parameter S_{ua} set at 0.01 for several days until a clear steady state has been achieved, following which S_{ua} is increased to 0.38 and the simulation trial is continued for 10 more days. This simulation is equivalent to conducting a hypothetical experiment in which a normal subject "abruptly" develops OSA, allowing us to track, on a day-to-day basis, the time-course of development of the metabolic and cardiovascular effects of OSA, as predicted by the extended model. In **Figure 6**, "Day 0" marks the point at which the change in S_{ua} occurs. The top two panels of **Figure 6** show the serial values of fasting plasma glucose (FPG) level and the fasting plasma insulin (FPI) level, determined by averaging the predicted plasma glucose and insulin values that appear during wakefulness in the hour before "breakfast" occurs. The third panel displays the day-to-day values of plasma epinephrine obtained by averaging predicted epinephrine concentration over 1-h duration before and after breakfast in each day. The remaining panels in **Figure 6** show averages of the key cardiovascular variables calculated over the corresponding simulation segment between 120 and 60 min before sleep ends for each day. Mean HR, SBP, and DBP attain their new steady-state levels within a day following the "switchover" from normal to OSA status. Also displayed in **Figure 6** are the corresponding amplitudes of the dominant oscillations in HR, SBP, and DBP; these oscillations occur at the tidal breathing frequencies (respiratory sinus arrhythmia for HR and pulsus paradoxus for blood pressure) in normal breathing, but in OSA, they occur with considerably larger amplitudes and cycle durations consistent with the repetitive episodes of apnea and arousals. FPG, FPI, and epinephrine attain their new steady-state levels after 2 days. All three variables are higher in the OSA vs. normal states, consistent to what has been reported in clinical studies (McArdle et al., 2007).

The autonomic and metabolic effects of artificially eliminating OSA by administering CPAP are presented in the simulation results displayed in **Figure 7**. Here, the model is first run with S_{ua} set at a value of 0.4 to represent OSA for several days in simulation time. Subsequently, during the duration of sleep on "Day 1," CPAP at a level of 15 cmH_2O is applied. This eliminates the obstructive apnea episodes, thus drastically reducing the large amplitude cyclic swings in HR, SBP, and DBP. Mean SBP and DBP attain their new lower steady-state levels within a day of this change. FPG, FPI, and epinephrine are lowered to their new steady-state levels after 2 days, consistent with observations reported in the clinical literature (Harsch et al., 2004).

Figure 8 summarizes and compares the magnitudes of the changes in steady-state autonomic and metabolic responses for the two cases ((N → OSA and OSA → OSA + CPAP) discussed above. It is clear that the results produced by OSA → OSA + CPAP are, in general, opposite in direction to those obtained in N → OSA, except that mean HR is elevated in both cases. We believe that this apparent inconsistency can be explained as follows. In N → OSA, the onset of OSA led to an overall increase in sympathetic tone (as manifested in the elevation of epinephrine), which increased both blood pressure and HR. In OSA → OSA + CPAP, CPAP administration led to a decrease in sympathetic tone and epinephrine level, which decreased blood pressure – however, the reduction in blood pressure triggered the baroreflexes, and this increased HR.

Simulations of the OSA case were conducted over a range of S_{ua} values, representing varying degrees of upper airway obstruction. **Figure 9** summarizes the model predictions: FPI

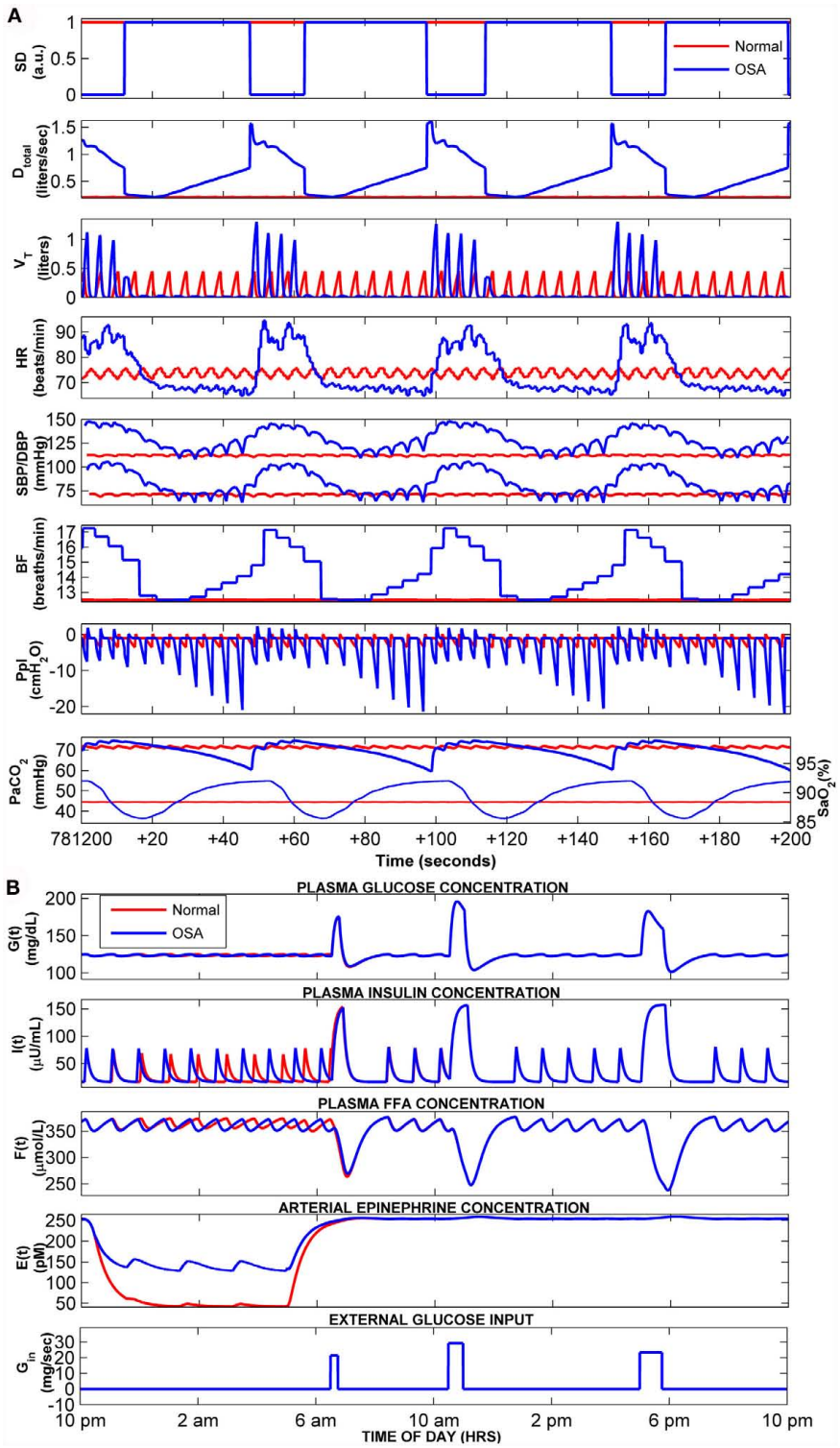

FIGURE 5 | Comparison of cardiorespiratory and metabolic responses in normal breathing (red) vs. OSA (blue). Results displayed are from Day 10 of the total simulation duration. Sleep starts at 10 pm and ends at 5 am each day. **(A)** Time-courses of the key cardiorespiratory variables – a segment of only 200 s duration, starting at 11 pm of Day 10, is displayed for clarity. SD, sleep state index (wake/sleep = 0/1); D_{total}, total ventilator drive (L/s); V_T, tidal volume (L); HR, heart rate (beat/min); SBP/DBP, systolic and diastolic blood pressure (mmHg); BF, breathing frequency (breaths/min); P_{pl}, pleural pressure (cmH_2O); P_aCO_2 (Thin Lines), arterial PCO_2 (mmHg); SO_2 (Thick Lines), saturation of oxygen (%). **(B)** Predicted time-courses of plasma glucose, insulin, FFA, epinephrine, and the external glucose inputs to the model (representing three meals during wakefulness).

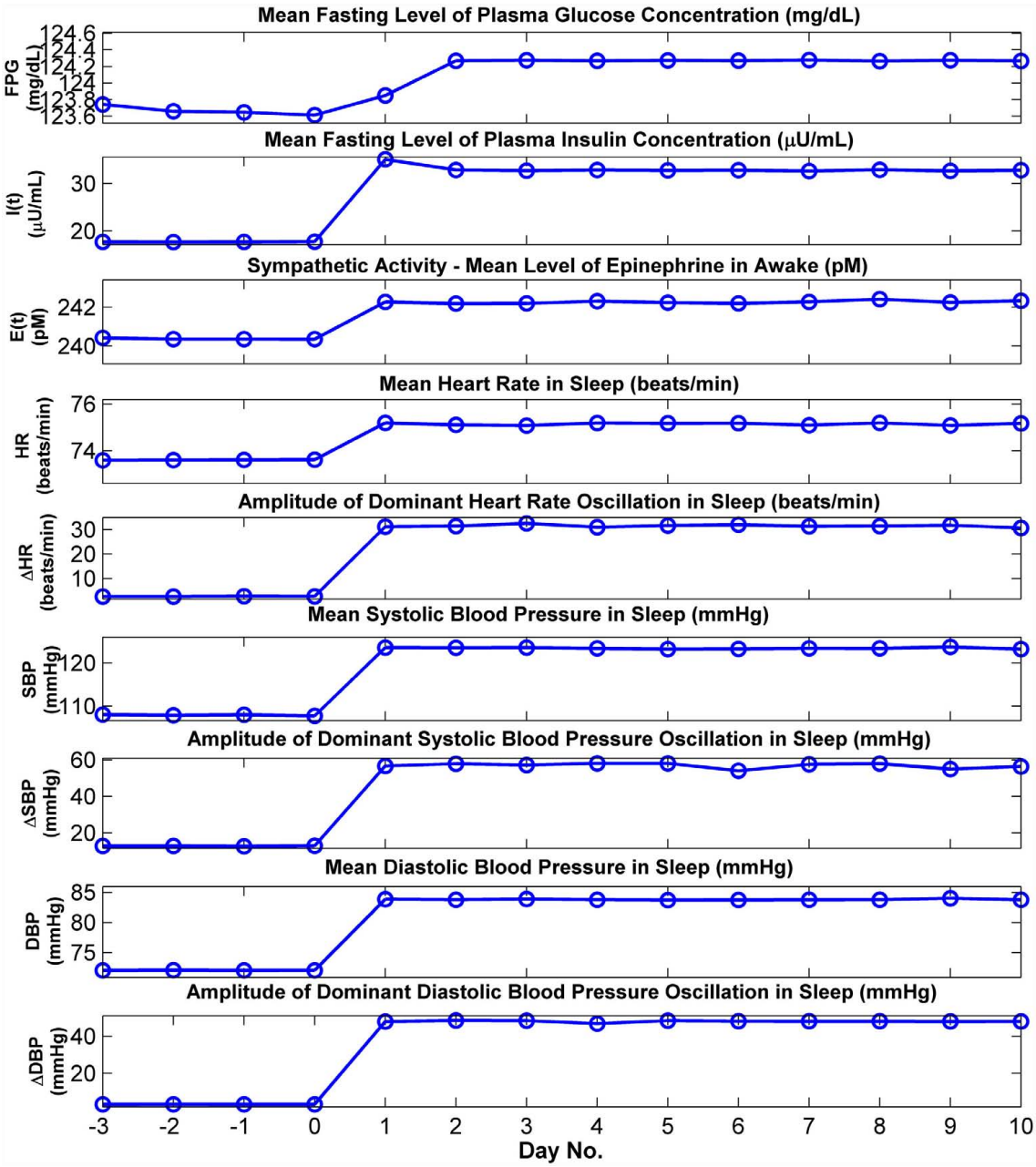

FIGURE 6 | Cardiovascular and metabolic responses predicted by model before, during, and after abrupt transition from normal breathing to OSA. In this simulation, the model is run in normal breathing mode until a steady state has been achieved, and at the end of "Day 0," the upper airway sensitivity parameter (S_{ua}) is abruptly increased to simulate OSA. FPG and FPI: mean levels of plasma glucose and insulin, respectively, calculated from the 30 min segment immediately before the start of breakfast. Other cardiovascular and metabolic values for wakefulness displayed above are the means derived from the corresponding simulation segment between 60 and 120 min. after sleep ends. All cardiovascular values for sleep displayed above are the means derived from the corresponding simulation segment between 120 and 60 min before sleep ends.

concentration increases as severity of OSA, as assessed using the apnea–hypopnea index, increases. We believe that the mechanistic basis for this result, as implemented in the model, is as follows. Greater severity of OSA leads to increased sympathetic tone, which increases epinephrine levels. The latter stimulates glycogenolysis and gluconeogenesis, thus increasing the plasma glucose level. This, in turn, stimulates the production of insulin, which is also enhanced by the elevated epinephrine level. The increased insulin level helps to attenuate the rise in blood glucose. However, the system is left with a consequent hyperinsulinemia. Thus, although the parameters that collectively represent insulin sensitivity remain unchanged in the model, whole-body insulin

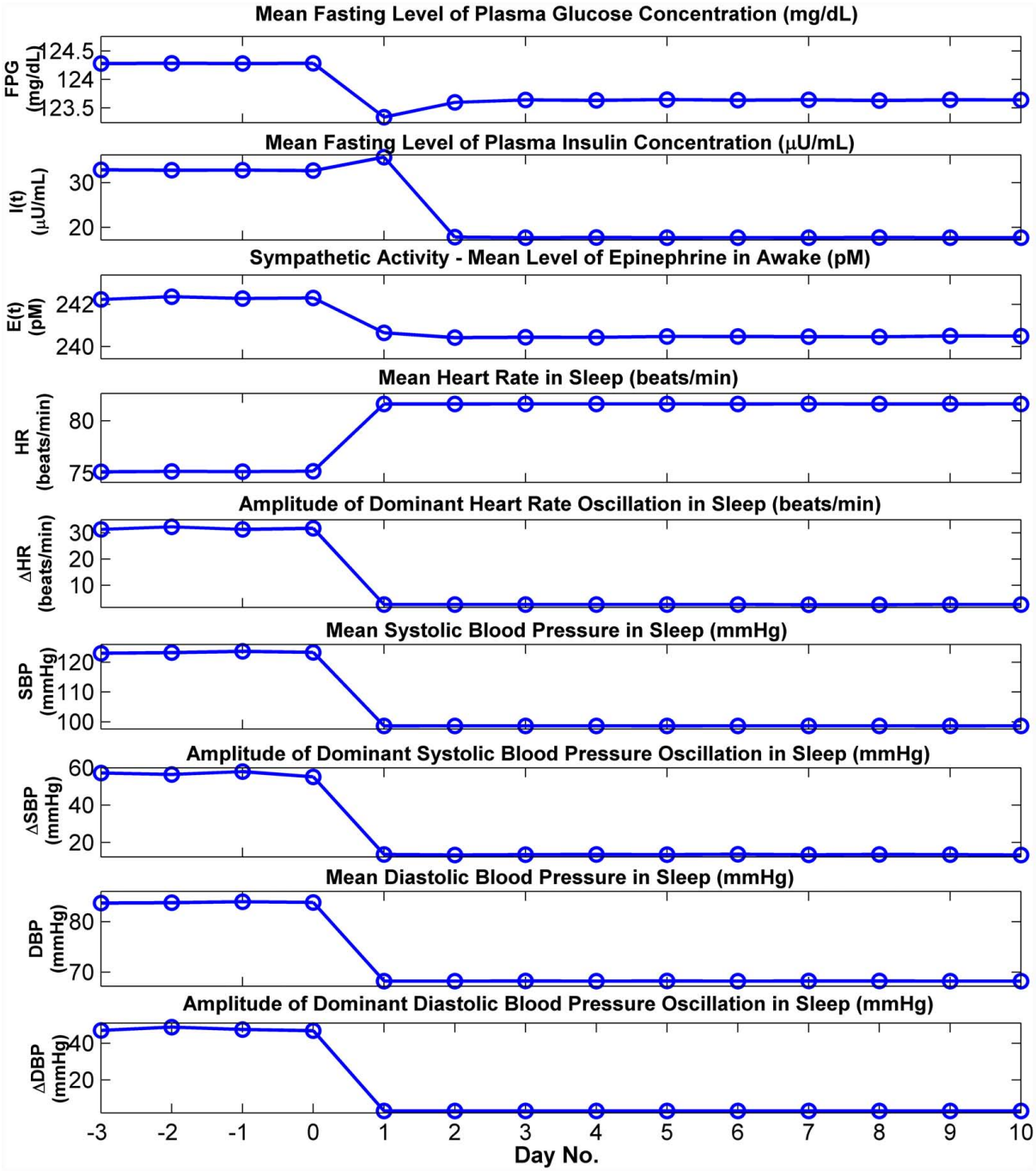

FIGURE 7 | Cardiovascular and metabolic responses predicted by model before and after the start of CPAP administration. In this simulation, the model is run in OSA mode until a steady state has been achieved, and at the end of "Day 0," continuous positive airway pressure (CPAP) at 15 cmH_2O is applied. FPG and FPI: mean levels of plasma glucose and insulin, respectively, calculated from the 30 min segment immediately before the start of breakfast. Other cardiovascular and metabolic values for wakefulness displayed above are the means derived from the corresponding simulation segment between 60 and 120 min. after sleep ends. All cardiovascular values for sleep displayed above are the means derived from the corresponding simulation segment between 120 and 60 min before sleep ends.

resistance is effectively increased. These results are consistent with several recent studies that point to the independent contribution of OSA to insulin resistance (Manzella et al., 2002; Punjabi et al., 2002).

SIMULATION OF EXTERNAL INTERVENTIONS: GLUCOSE CLAMPS

The hyperglycemic glucose clamp technique is used for the quantification of beta-cell sensitivity to glucose and the euglycemic hyperinsulinemic clamp technique is used for measuring tissue

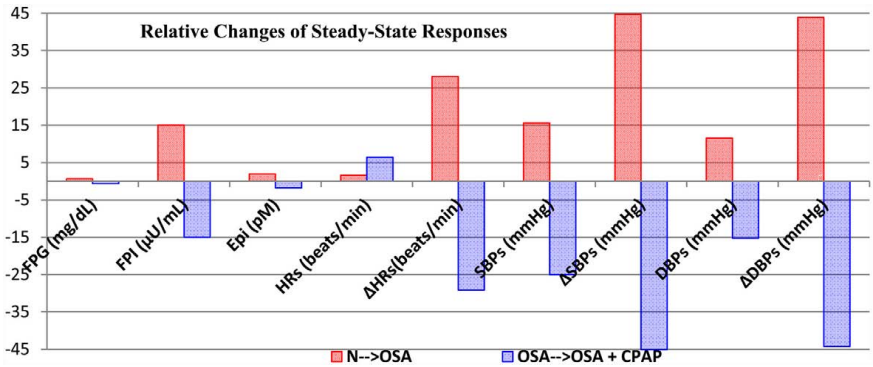

FIGURE 8 | Summary and comparison of the changes in steady-state autonomic and metabolic responses for the two cases, N → OSA (red) and OSA → OSA + CPAP (blue), displayed in Figures 6 and 7, respectively. Each column represents the relative change from previous steady-state value to the post-transition steady-state response. FPG, fasting plasma glucose; FPI, fasting plasma insulin; Epi, arterial epinephrine concentration. ΔHR, ΔSBP, and ΔDBP correspond to maximum amplitude of fluctuation in heart rate (beats/min), maximum amplitude of fluctuation in systolic blood pressure (mmHg), and maximum amplitude of fluctuation in diastolic blood pressure (mmHg), respectively. Subscript "s" represents sleep.

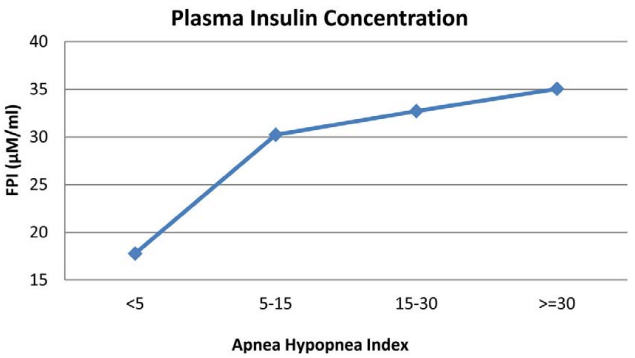

FIGURE 9 | Correlation between plasma insulin and severity of OSA.

sensitivity to insulin. The extended model has been tested using virtual experiments to simulate these intervention techniques. To simulate a hyperglycemic +125 mg glucose clamp, the glucose concentration in plasma is first gradually increased to 125 mg/dl above its basal level (G_b) by a series of stair-like priming blood glucose infusion, and then maintained at the hyperglycemic level by dynamically and continuously adjusting the rate of glucose infusion. The dynamics of glucose, insulin, and FFA and corresponding glucose infusion rate during first 2 h of hyperglycemic clamp are shown in **Figure 10**, where the basal level of plasma glucose concentration (G_b) is given as 98 mg/dL, the basal levels of plasma insulin concentration (I_b) and plasma FFA concentration (F_b) are assumed to be 6 μU/mL and 380 μmol/L, respectively. The glucose and insulin responses predicted by our model are comparable to the corresponding observations reported in the literature (Figure 1 in DeFronzo et al., 1979).

To determine the response of the extended model to various euglycemic clamps, assuming G_b to be 98 mg/dL and I_b to be 6 μU/mL, simulations have been conducted in which insulin is infused at dynamically changing rates to maintain plasma insulin concentration at various hyperinsulinemic levels. **Figure 11** displays the results at the three hyperinsulinemic levels of 20, 30, and 100 μU/ml above its basal level (I_b), respectively, with two stair-like inputs in the priming dose of glucose infusion for each hyperglycemic level. These results also confirm that the predicted dynamics of glucose, insulin, and FFA concentrations in plasma are consistent with the literature (Figure 1 in Howard et al., 1984; Figure 3 in Roy and Parker, 2006).

SENSITIVITY ANALYSES

The extended model contains 557 parameters, each of which is assigned a value (if available) that is consistent with the subject group and condition under study. This represents 85 parameters more than the 472 parameters employed in PNEUMA prior to this study. Thus we focused on identifying the key parameters that mediate the most significant interactions between the autonomic and metabolic subsystems, in order to minimize the number of free parameters that have to be specified prior to running a simulation. Sensitivity analyses were conducted to determine the relative contributions of the key parameters that played the most significant roles in various conditions. These sensitivity analyses were also useful as checks of internal consistency and model stability within the ranges of the parameter values considered physiologically "realistic."

Interaction between key parameters contributing to autonomic and metabolic interactions

Table 2 displays the model predictions obtained from different values of key parameters (gains K_{as} and $K_{isc,I}$) that influence the impact of metabolic feedback on autonomic function, as well as the key parameters (gains $K_{ce,0}$ and G_b) that control how sympathetic activity influences the metabolic subsystem. In the control set of normal subject and OSA subject, these key parameters are set to equal to their initial values described in **Table 1**. For each simulation, there is only one parameter changed by the desired percentage or amount. We found, as might be expected, that the ability to simulate the effect of metabolic feedback on α-sympathetic activity depends most sensitively on its gain K_{as}. This is shown in the percentage change of mean HR, SBP/DBP from their control values in

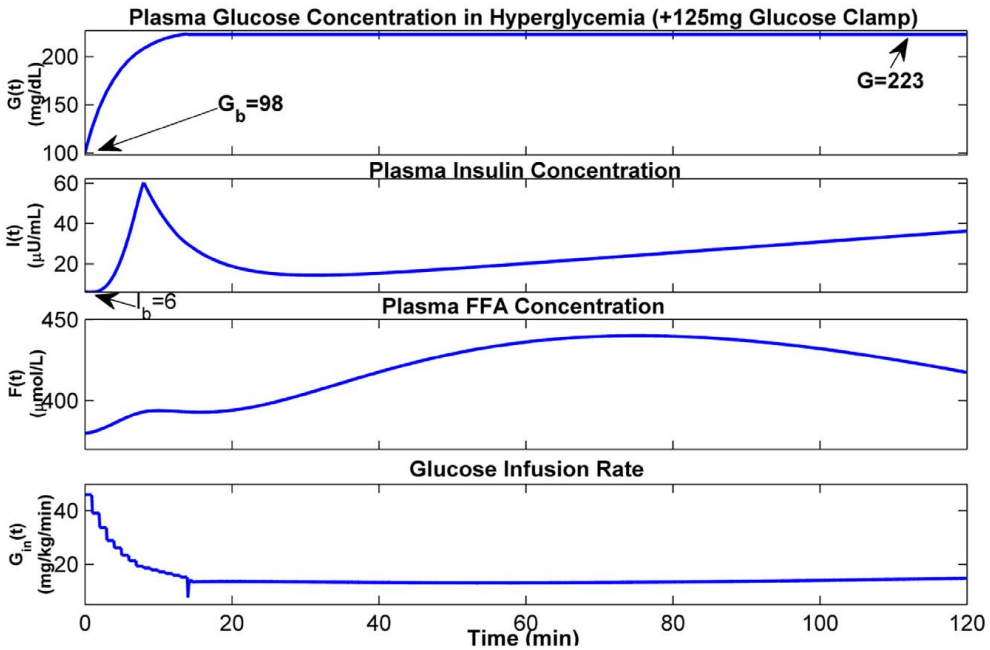

FIGURE 10 | Dynamics of glucose–insulin and FFA during hyperglycemia with +125 mg glucose clamp.

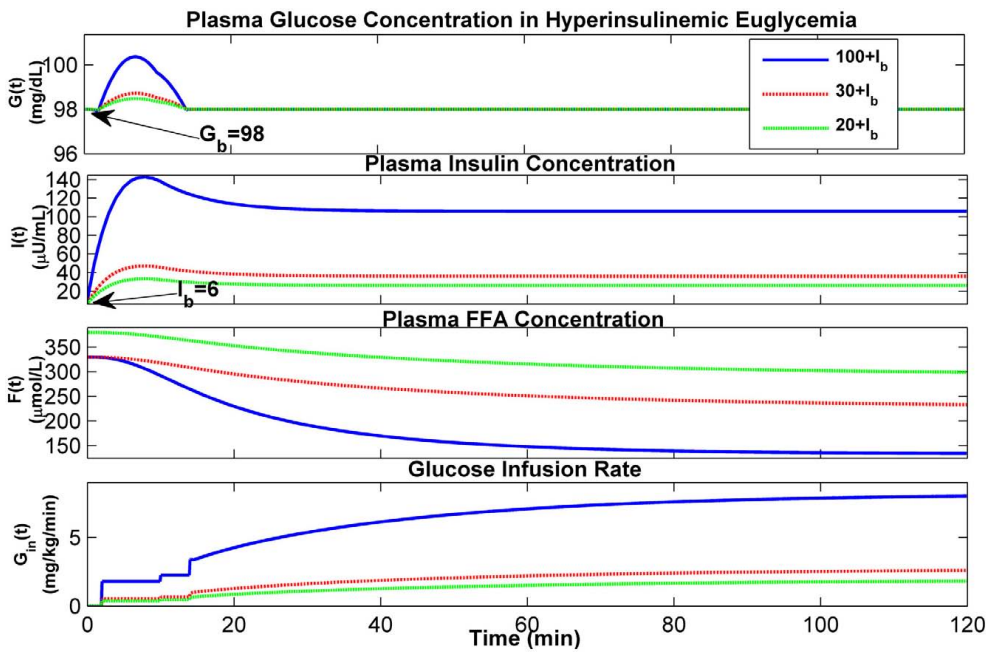

FIGURE 11 | Dynamics of glucose–insulin and FFA during hyperinsulinemic euglycemia with glucose clamps.

both normal and OSA subject and during both wakefulness and sleep, as well as in the epinephrine level from its control corresponding to the change of α-sympathetic activity. Also, as might be expected, the analysis shows that the gain ($K_{ce,0}$) for basal level of epinephrine is the most sensitive parameter for epinephrine regulation in wakefulness.

Interactions between key parameters contributing to epinephrine regulation on glucose and FFA dynamics

Table 3 displays the model results of different levels of internal inputs controlled by the gains from epinephrine to glucose and FFA, Keg and Kef, respectively. To start the simulations, basal levels of glucose and insulin concentrations in plasma are

Table 2 | Sensitivity analysis of key parameters in metabolic model that contribute to autonomic and metabolic interactions.

Percentage change from control	K_{as}		$K_{isc,I}$		$K_{ce,0}$		G_b	
	50%	−50%	50%	−50%	50%	−50%	1	−1
NORMAL DAY 10								
FPG (%)	−0.04	0.07	0.02	0.00	0.05	−0.04	0.75	−0.72
FPI (%)	0.68	−0.61	−0.23	0.00	−0.59	0.60	0.81	−0.30
Epi (%)	2.69	−2.10	−0.22	0.41	10.98	−10.97	0.00	0.01
Mean HR_w (%)	−4.16	5.22	0.38	−0.61	0.00	−0.02	−0.03	−0.02
Mean HR_s (%)	−1.32	3.02	−1.53	−0.35	0.24	−0.01	0.01	−0.03
ΔHR_w (%)	−2.33	2.08	0.46	0.27	3.74	1.60	−1.19	−0.80
ΔHR_s (%)	−4.47	1.06	2.20	−2.89	0.88	0.55	3.75	−3.89
Mean SBP_w (%)	3.92	−5.22	−0.35	0.57	0.00	0.00	0.01	0.03
Mean SBP_s (%)	2.13	−2.80	−0.20	0.35	0.00	−0.01	−0.01	0.02
ΔSBPw (%)	−4.79	3.99	−0.26	−0.17	−1.58	−0.30	−0.28	0.04
ΔSBP_s (%)	−1.95	0.66	−0.18	−0.83	−1.02	−0.61	−0.83	−0.03
Mean DBP_w (%)	4.68	−6.16	−0.39	0.68	0.00	0.01	0.02	0.02
Mean DBP_s (%)	2.60	−3.40	−0.23	0.45	0.00	0.00	0.00	0.01
ΔDBP_w (%)	−2.70	3.83	−0.06	−0.23	−0.07	0.03	−0.29	−0.24
ΔDBP_s (%)	−0.28	0.01	−0.38	−0.30	0.04	−0.08	−0.13	0.03
OSA DAY 10								
FPG (%)	0.00	0.00	−0.01	0.00	−0.04	0.02	0.81	−0.83
FPI (%)	0.07	0.03	0.46	0.11	2.10	−2.53	−1.06	1.69
Epi (%)	2.69	−2.16	−0.23	0.37	11.05	−11.11	−0.01	−0.02
AHI (%)	−0.03	0.00	0.93	−0.98	−0.01	0.93	−0.02	−0.01
Mean HR_w (%)	−4.24	5.38	0.43	−0.63	0.00	0.03	0.03	−0.01
Mean HR_s (%)	−1.64	1.92	0.15	−0.33	−0.01	0.03	−0.02	0.01
ΔHR_w (%)	−1.76	−0.52	2.08	1.52	−0.19	−0.23	2.15	2.35
ΔHR_s (%)	2.75	3.45	−1.28	1.68	−3.31	−1.48	0.74	0.17
Mean SBPw (%)	3.87	−5.34	−0.46	0.57	−0.02	−0.03	0.00	−0.02
Mean SBP_s (%)	1.71	−2.31	−0.05	0.35	0.03	0.03	0.15	0.12
ΔSBPw (%)	−3.86	4.69	−0.46	−0.40	−1.15	−1.27	−0.83	0.86
ΔSBP_s (%)	−4.52	6.89	−0.76	0.44	0.50	−0.46	−0.26	−0.03
Mean DBP_w (%)	4.70	−6.27	−0.50	0.71	0.03	−0.02	0.00	0.02
Mean DBP_s (%)	1.82	−2.61	−0.09	0.38	0.02	−0.01	0.11	0.06
ΔDBP_w (%)	−2.11	3.83	0.15	−0.41	0.17	0.11	−0.01	0.19
ΔDBP_s (%)	−3.97	2.26	−0.10	0.16	1.13	0.16	−0.19	0.57

All results displayed are based on 10th day simulation (steady-state responses). FPG, fasting plasma glucose; FPI, fasting plasma insulin; Epi, arterial epinephrine concentration in wakefulness; AHI, apnea–hypopnea index (per hour); ΔHP, maximum amplitude of fluctuation in heart period (ms); ΔSDP, maximum amplitude of fluctuation in systolic blood pressure (mmHg); ΔDBP, maximum amplitude of fluctuation in diastolic blood pressure (mmHg). Subscript "w" means wakefulness, subscript "s" means sleep.

set to 98 mg/dL and 6 μU/mL, respectively. As the gains gradually increase, both FPG and FPI levels are elevated as the epinephrine concentration in plasma increases. This leads to more oscillations in insulin concentration between meals. Also, as the gains increase, blood pressure is increased slightly and this leads to slightly decreased HR in wakefulness and during sleep.

Interactions between key parameters contributing to the severity of obstructive sleep apnea effects

Table 4 shows the model predictions obtained from various combinations of values for the upper airway sensitivity to collapse, S_{ua}, and the arousal threshold upper limit. In normal subject, S_{ua} is set equal to 0.01 and the critical closing pressure, P_{crit}, for upper airway during sleep is $-29.6\,cmH_2O$. With stable sleep, apnea–hypopnea index (AHI) is zero and maximum fluctuations in HR, SBP, and DBP are consistent with normal respiration. When S_{ua} is increased to 0.38, P_{crit} is less negative and obstructive apnea starts to appear and be terminated by non-frequent arousals (AHI = 9) with large amplitudes of fluctuations in HR, SBP, and DBP during sleep and a large growth in FPI and slightly increase in FPG and epinephrine level in plasma in wakefulness. Raising S_{ua} a little more to 0.4 leads to greater periodicity of obstructive apnea and arousals (AHI = 18) and slightly increases in FPI and epinephrine level in plasma, and increasing S_{ua} further to 0.5 produces more apnea and arousals

Table 3 | Sensitivity analysis of gains from epinephrine to glucose and FFA that have effects on autonomic and metabolic interactions.

NORMAL DAY 10						
Keg	0.04	0.20	0.40	0.60	0.80	1.00
Kef	0.01	0.05	0.10	0.15	0.20	0.25
FPG (mg/dL)	101.02	113.11	124.14	123.96	125.62	126.05
FPI (μU/mL)	6.60	6.60	21.79	56.98	97.17	142.32
Epi (pM)	238.55	238.61	240.66	244.45	246.85	247.83
Insulin oscillations between meals?	No	No	Few	More	Many	Many
AHI (per hour)	0	0	0	0	0	0
Mean HR_w (beats/min)	78.44	78.35	77.18	75.44	74.43	74.07
Mean HR_s (beats/min)	73.93	73.93	73.93	73.38	72.86	72.61
ΔHR_w (beats/min)	3.01	3.14	3.02	3.01	2.96	2.95
ΔHRs (beats/min)	2.73	2.79	2.75	2.55	2.53	2.50
Mean SBPw (mmHg)	119.69	119.82	121.57	124.18	125.55	126.06
Mean SBP_s (mmHg)	111.52	111.52	111.52	112.85	114.19	114.77
ΔSBPw (mmHg)	2.93	2.91	2.86	2.78	2.77	2.76
ΔSBP_s (mmHg)	2.35	2.33	2.35	2.32	2.31	2.33
Mean DBP_w (mmHg)	79.26	79.36	80.73	82.78	83.90	84.27
Mean DBP_s (mmHg)	70.46	70.46	70.46	71.49	72.50	72.98
ΔDBP_w (mmHg)	3.20	3.20	3.19	3.13	3.10	3.10
ΔDBP_s (mmHg)	2.49	2.49	2.49	2.49	2.49	2.47
OSA DAY 10						
FPG (mg/dL)	101.03	113.19	124.15	124.32	125.50	126.39
FPI (μU/mL)	6.60	6.60	25.81	52.82	94.42	137.18
Epi (pM)	240.22	240.18	242.48	246.62	249.16	250.01
Insulin oscillations between meals?	No	No	Few	More	Many	Many
AHI (per hour)	18	18	18	18	18	18
Mean HR_w (beats/min)	78.43	78.35	77.06	75.25	74.34	74.00
Mean HR_s (beats/min)	75.52	75.50	75.50	74.48	74.03	73.72
ΔHR_w (beats/min)	3.03	3.06	2.99	3.05	2.96	2.95
ΔHR_s (beats/min)	32.14	31.79	32.09	30.50	31.21	30.45
Mean SBPw (mmHg)	119.68	119.81	121.78	124.48	125.72	126.15
Mean SBP_s (mmHg)	127.62	127.67	127.63	129.20	130.53	130.44
ΔSBPw (mmHg)	2.92	2.93	2.83	2.77	2.80	2.79
ΔSBP_s (mmHg)	48.45	48.78	48.55	46.22	46.15	45.02
Mean DBP_w (mmHg)	79.27	79.36	80.90	83.05	83.99	84.35
Mean DBP_s (mmHg)	82.25	82.26	82.27	83.48	84.49	84.37
ΔDBP_w (mmHg)	3.20	3.20	3.18	3.12	3.10	3.09
ΔDBP_s (mmHg)	48.06	47.75	46.80	45.11	45.17	44.65

All results displayed are based on 10th day simulations (steady-state responses). FPG, fasting plasma glucose; FPI, fasting plasma insulin; Epi, arterial epinephrine concentration in wakefulness; AHI, apnea–hypopnea index (per hour); ΔHP, maximum amplitude of fluctuation in heart period (ms); ΔSDP, maximum amplitude of fluctuation in systolic blood pressure (mmHg); ΔDBP, maximum amplitude of fluctuation in diastolic blood pressure (mmHg). Subscript "w" means wakefulness, subscript "s" means sleep.

(AHI = 46) and slightly more increases in FPI and epinephrine level in plasma. But the maximum amplitudes of the swings in HR, SBP, and DBP remain relatively constant, and FPG remains slightly increased from its control level. Increasing arousal threshold delays the appearance of obstructive apnea and arousals as S_{ua} is progressively increased. For the same value of S_{ua}, the periodicity of AHI is lower for mild and moderate OSA and approximately the same for severe OSA. However, the amplitudes of the swings in HR, SBP, and DBP are substantially higher, FPG is relatively unchanged and FPI and epinephrine amount in plasma are lower.

DISCUSSION

In this study, we have introduced the first comprehensive, structured physiological model that incorporates dynamic interactions between the autonomic and metabolic control systems. The approach we have taken has been to extend an existing integrative model of cardiorespiratory system with sleep–wake state control ("PNEUMA") to include the regulation of epinephrine, glucose, insulin, and FFAs. Although extended PNEUMA is based largely on previously published models of the various subsystems in question, our contribution has been to adapt the existing sub-models for integration into the overall model structure. In particular,

Table 4 | Sensitivity analysis of OSA effects on autonomic and metabolic interactions by changing key parameters in upper airway model.

S_{ua}	0.01(Control)	0.3	0.38	0.4	0.5
P_{crit} during Sleep (cmH_2O)	−29.6	−3.5	−2.8	−2.7	−2.2
AROUSAL THRESHOLD UPPER LIMIT = 0.75 (CONTROL VALUE)					
FPG (mg/dL)	123.62	123.62	124.31	124.28	123.87
FPI (μU/mL)	17.76	17.77	30.23	32.72	35.05
Epi (pM)	240.41	240.39	241.37	242.35	244.26
AHI (per hour)	0	0	9	18	46
Mean HR_w (beats/min)	77.47	77.46	77.21	77.16	77.12
Mean HR_s (beats/min)	74.12	74.59	74.99	75.18	76.02
ΔHR_w (beats/min)	3.01	3.01	2.99	3.01	3.09
ΔHR_s (beats/min)	2.65	3.04	32.66	31.73	32.69
Mean SBPw (mmHg)	121.13	121.11	121.55	121.63	121.65
Mean SBP_s (mmHg)	113.04	114.36	129.34	127.96	128.04
ΔSBP_w (mmHg)	2.91	2.86	2.85	2.89	2.86
ΔSBP_s (mmHg)	2.79	3.58	44.73	47.22	44.42
Mean DBP_w (mmHg)	80.38	80.39	80.73	80.75	80.79
Mean DBP_s (mmHg)	71.72	72.76	83.22	82.65	83.34
ΔDBP_w (mmHg)	3.18	3.18	3.19	3.18	3.18
ΔDBP_s (mmHg)	3.00	3.93	44.21	46.27	45.21
AROUSAL THRESHOLD UPPER LIMIT = 1.15					
FPG (mg/dL)	123.62	123.62	123.82	124.12	124.06
FPI (μU/mL)	17.76	17.77	18.38	24.41	34.51
Epi (pM)	240.41	240.39	240.78	241.51	243.69
AHI (per hour)	0	0	5	12	45
Mean HR_w (beats/min)	77.47	77.47	77.43	77.31	77.14
Mean HR_s (beats/min)	73.61	74.12	72.39	72.57	74.57
ΔHR_w (beats/min)	3.02	3.01	2.99	3.01	3.04
ΔHR_s (beats/min)	2.62	2.65	30.76	33.52	33.66
Mean SBPw (mmHg)	121.12	121.13	121.22	121.41	121.66
Mean SBP_s (mmHg)	112.32	113.04	143.95	144.82	140.81
ΔSBPw (mmHg)	2.89	2.91	2.86	2.89	2.85
ΔSBP_s (mmHg)	2.35	2.79	51.26	54.86	57.30
Mean DBP_w (mmHg)	80.37	80.38	80.44	80.59	80.79
Mean DBP_s (mmHg)	71.08	71.72	91.37	92.24	91.07
ΔDBP_w (mmHg)	3.19	3.18	3.19	3.19	3.19
ΔDBP_s (mmHg)	2.49	3.00	52.46	55.62	60.55

All results displayed are based on 10th day simulations (steady-state responses). FPG, fasting plasma glucose; FPI, fasting plasma insulin; Epi, arterial epinephrine concentration in wakefulness; AHI, apnea–hypopnea index (per hour), ΔHP, maximum amplitude of fluctuation in heart period (ms); ΔSDP, maximum amplitude of fluctuation in systolic blood pressure (mmHg); ΔDBP, maximum amplitude of fluctuation in diastolic blood pressure (mmHg). Subscript "w" indicates wakefulness, subscript "s" indicates sleep.

we have incorporated the following new features: a direct link between sympathetic activity and epinephrine level, the coupling between the epinephrine sub-model and the metabolic sub-model that characterizes glucose, insulin, and FFA dynamics, the effect of insulin on peripheral vascular sympathetic activity, and the effect of sleep–wake state on epinephrine regulation. The primary focus of extended PNEUMA is the simulation of a range of sleep-related breathing disorders and the physiological consequences of these disorders on cardiorespiratory control, sleep–wake regulation, and metabolic regulation, along with the interactions among these various subsystems. The comprehensive simulation model allows the user to conduct virtual experiments such as isocapnic and hypercapnic and/or hypoxic gas administration, the Valsalva and Mueller maneuvers, and the application of CPAP on OSA subjects, as well as external metabolic interventions such as different glucose clamps, IVGTT, and insulin pumps.

Food intake triggers the release of insulin which acts to regulate glucose metabolism. However, excessive feeding in obese individuals can lead to chronic hyperinsulinemia, which predisposes to insulin resistance. Since OSA is highly prevalent in obese individuals, it is likely that chronic exposure to the IH and sleep fragmentation that accompany upper airway obstruction and transient arousal from sleep would constitute another factor that contributes to metabolic dysfunction. Moreover, OSA is associated

with sympathetic overactivity (Leung and Bradley, 2001) and a number of prospective studies, such as the canine model of Brooks et al. (1997), have demonstrated that OSA can lead to systemic hypertension. Thus, it is reasonable to expect that OSA could play an important role in the development of hyperinsulinemia. Recently, a couple of studies have demonstrated significant correlations among OSA, type 2 diabetes, and metabolic syndrome (Shaw et al., 2008; Tasali and Ip, 2008; Jun and Polotsky, 2009). A comprehensive simulation model, such as extended PNEUMA, provides a systematic framework with which we can investigate *in silico* potential mechanistic pathways that could lead to the observed correlations. For instance, with the extended model, the metabolic feedback can be attenuated or eliminated to simulate pharmaceutical blockade of autonomic nervous system activities. Such interventions may be difficult to implement or sometimes impossible to conduct in real experiments. *In silico* investigations would also allow us to determine the relative importance of the various potential mechanisms, including sympathetic overactivity, that link OSA to metabolic dysfunction.

As mentioned in previous work, this model is largely an integration of smaller sub-models that have already been peer-reviewed and validated; many of the other parameters were assigned values employed in these previously published sub-models (Cheng et al., 2010). For the extended model with the new metabolic system, wherever possible, the parameter values employed in the model are based on population values published in the literature, as indicated in **Table 1** for the new parameters. In some cases where the physiological values are unclear, the parameters have been tuned to ensure that the dynamic behavior of the model under the various conditions explored remains realistic. Model verification and validation are performed by comparing the simulation output under baseline conditions in normal breathing and sleep-disordered breathing and under different interventions to the general population-averaged cardiorespiratory data and glucose–insulin–FFA dynamics reported in the literature. Since the focus of this study is on the dynamic interactions among the various mechanisms between autonomic and metabolic interactions, verification, and validation are guided by employing a qualitative goodness of fit approach. This contrasts with smaller, more focused models in which the key parameters are estimated based on quantitative fits to experimental data obtained from individual subjects. In the present case, there is no single complete experimental dataset that the model can be validated against. Rather, we focus on comparing the model responses with the empirically derived responses that represent the "average subject" in each patient/subject population. The utility of this comprehensive, highly parameterized model is "proven" by testing the internal consistency of the simulated responses of a significant number of state variables over a range of perturbations and conditions.

LIMITATIONS OF THE MODEL

The model that we have proposed here focuses on the question of whether the autonomic changes resulting from sleep apnea characterized with IH and repetitive arousal from sleep can lead to chronic changes of metabolic consequences in glucose, insulin, and fatty acid levels. This is the first quantitative model that has ever addressed this question – and as such, it should be seen as a first step in many further explorations in this area of work. Animal models of IH have shown that chronic IH induces augmented sympathetic activities, insulin resistance, systemic inflammation, oxidative stress, hyperlipidemia, hepatic inflammation, and increase in cholesterol content and glycogen content in the liver. Nevertheless, very little is known about the ways in which IH and OSA can lead directly to changes in the glucose–insulin–fatty acid metabolic system –even in the experimental literature. Our approach is to attack this problem one layer at a time – first start with how the autonomic changes affect the metabolic control system – and then move on to other mechanistic pathways that may link IH and metabolic dysfunction more directly. A key premise in the present model is that OSA leads to sympathetic overactivity (partly due to chronic IH) which increases plasma epinephrine levels which, in turn, alters the regulation of glucose, insulin, and FFA, leading eventually to hyperinsulinemia.

The mechanisms for the long-term effects of IH on autonomic and metabolic control are not well understood, but current studies have shown that the systemic and cellular responses for a given level and duration of hypoxia exposure are more potent with IH than with the sustained hypoxia (Prabhakar and Kumar, 2004). There are several potential alternative pathways by which IH can lead to insulin resistance and impaired insulin secretion. Results from IH animal models show that IH can lead directly to hyperlipidemia. The mechanism of dyslipidemia induced by IH is unclear, but it is believed to be stimulated through (1) up-regulation of key hepatic transcription factors of lipid biosynthesis, (2) increased lipolysis which might induce increased FFA delivery and impaired beta oxidation which in turn can associate with OSA and fat liver, liver injury, oxidative stress, and non-alcoholic steatohepatitis, and (3) inhibited very-low density lipoprotein clearance (Drager et al., 2010). Hepatic dyslipidemia can cause hepatic insulin resistance. In addition, IH involves hypoxia-reoxygenation cycles that could increase oxidative stress by hypoxia-inducible factor 1 (HIF-1; Semenza, 1998) and thus may influence glucose metabolism by modulating glucose transport and utilization through HIF-1. The effect of IH in oxidative stress is similar to the effect of ischemia–reperfusion injury. However, oxidative stress in OSA and IH has not been clearly described (Svatikova et al., 2005) and the mechanism by which it can produce metabolic dysfunction is under investigation. It is likely that the IH associated with OSA could also lead directly to insulin resistance by reducing the rate of oxidative metabolism and decreasing the rate of glycolysis in some tissues, and thus making insulin less effective in disposing glucose (Iiyori et al., 2008). IH can alter both acute and chronic glucose homeostasis through decreased oxidative phosphorylation, leptin signaling, and growth hormone axis suppression (Jun and Polotsky, 2009). IH could also affect many other processes, such as circadian glucose homeostasis, lipid metabolism, and cholesterol synthesis. However, much remains unknown and further studies are needed to answer these questions. As such, these alternative pathways have not been included in the model. Moreover, our goal in this paper is to first introduce a basic model structure that allows interactions between the autonomic and metabolic aspects of the model. Subsequently, we will add other relevant pathways that can more accurately characterize the effect of IH on autonomic and metabolic consequences of OSA.

The current model postulates that α-sympathetic activity influences insulin production indirectly through the effect of epinephrine on plasma glucose and FFA concentrations, and that insulin affects α-sympathetic activity only. Some studies have shown that insulin also has a direct vasodilatory effect (Anderson and Mark, 1993), and this may offset the vasoconstrictive effect of insulin through its action on sympathetic activity. Thus, the "feedback effect" of insulin on sympathetic drive may not be as important as one might generally surmise. Another major factor not included in the present model is the effect of sympathetic drive, and thus epinephrine, on insulin production in the pancreas (Kim et al., 2006).

While recent clinical research shows that high-fat diets contribute to progressive insulin resistance, in the present model, meals are represented simply as step boluses of blood glucose without consideration of the digestion process and the inevitable lags between oral ingestion and appearance of glucose and FFA in the bloodstream.

The time-course of "disease progression," as currently predicted by the model in terms of the development of elevated epinephrine, insulin, and FFA levels, is substantially more rapid than one might expect based on clinical observation. This is likely related to the fact that the model parameters in both the autonomic and metabolic subsystems remain unchanged, even though the model variables (e.g., mean blood pressures, insulin levels, and FFA levels) are altered by the presence or absence of OSA. This limitation stems from the lack of information about how the disease process leads to time-varying changes in the model parameters. Clearly, future efforts to improve the model will require the incorporation of this knowledge from either empirical observations or an advanced understanding of the underlying mechanistic processes that give rise to such time-varying alterations.

CONCLUSION

We have extended an existing integrative model of respiratory, cardiovascular, and sleep–wake state control, to incorporate a sub-model of glucose–insulin–fatty acid regulation. This computational model is capable of simulating the complex dynamics of cardiorespiratory control, chemoreflex and state-related control of breath-to-breath ventilation, state-related and chemoreflex control of upper airway potency, respiratory and circulatory mechanics, as well as the metabolic control of glucose–insulin dynamics and its interactions with the autonomic control. The interactions between autonomic and metabolic control include the circadian regulation of epinephrine secretion, epinephrine regulation on dynamic fluctuations in glucose and FFA in plasma, metabolic coupling among tissues and organs provided by insulin and epinephrine, as well as the effect of insulin on peripheral vascular sympathetic activity. This extended model represents a starting point from which further *in silico* investigations into the interaction between the autonomic nervous system and the metabolic control system can proceed. The predictions generated from this model may provide insight into the relative importance of the various mechanisms that determine the acute and chronic physiological effects of sleep-disordered breathing.

ACKNOWLEDGMENTS

This work was supported by the USC Biomedical Simulations Resource through NIH Grant EB-001978, as well as by NIH Grant HL090451 and the USC Center for Transdisciplinary Research on Energetics and Cancer (TREC U54 CA116848).

REFERENCES

Ackerman, E., Gatewood, L. C., Rosevear, J. W., and Molnar, G. D. (1965). Model studies of blood-glucose regulation. *Bull. Math. Biophys.* 27, 21–38.

Anderson, E. A., and Mark, A. L. (1993). The vasodilator effect of insulin: implications for the insulin hypothesis of hypertension. *Hypertension* 21, 136–141.

Andres, R., Swerdloff, R., Pozesky, T., and Coleman, D. (1966). "Manual feedback technique for control of glucose concentration," in *Automation in Analytical Chemistry*, ed. J. L. Skeggs (New York: Medicaid), 486–501.

Bamshad, M., Aoki, V. T., Adkison, M. G., Warren, W. S., and Bartness, T. J. (1998). Central nervous system origins of the sympathetic nervous system outflow to white adipose tissue. *Am. J. Physiol. Regul. Integr. Comp. Physiol.* 275, R291–R299.

Berger, M., and Rodbard, D. (1989). Computer simulation of plasma insulin and glucose dynamic after subcutaneous insulin injection. *Diabetes Care* 12, 725–736.

Bergman, R. N. (1989). Toward physiological understanding of glucose tolerance: minimal-model approach. *Diabetes* 38, 1512–1527.

Bergman, R. N., Ider, Y. Z., Bowden, C. R., and Cobelli, C. (1979). Quantitative estimation of insulin sensitivity. *Am. J. Physiol.* 236, E667–E677.

Bergman, R. N., Kim, S. P., Catalano, K. J., Hsu, I. R., Chiu, J. D., Kabir, M., Hucking, K., and Ader, M. (2006). Why visceral fat is bad: mechanisms of the metabolic syndrome. *Obesity* 14, S16–S19.

Bergman, R. N., Phillips, L. S., and Cobelli, C. (1981). Physiologic evaluation of factors controlling glucose tolerance in man. *J. Clin. Invest.* 68, 1456–1467.

Berman, N., Chou, H. F., Berman, A., and Ipp, E. (1993). A mathematical model of oscillatory insulin secretion. *Am. J. Physiol. Regul. Integr. Comp. Physiol.* 264, 839–851.

Bolie, V. W. (1961). Coefficients of normal blood glucose regulation. *J. Appl. Physiol.* 16, 783–788.

Bradley, T. D., and Floras, J. S. (2003). Sleep apnea and heart failure part I: obstructive sleep apnea. *Circulation* 107, 1671–1678.

Brooks, D., Horner, R. L., Kozar, L. F., Render-Teixera, C. L. B., and Phillipson, E. A. (1997). Obstructive sleep apnea as a cause of systemic hypertension: evidence from a canine model. *J. Clin. Invest.* 99, 106–119.

Chasens, E. R. (2007). Obstructive sleep apnea, daytime sleepiness, and type 2 diabetes. *Diabetes Educ.* 33, 475–482.

Cheng, L., Ivanova, O., Fan, H., and Khoo, M. C. K. (2010). An integrative model of respiratory and cardiovascular control in sleep-disordered breathing. *Respir. Physiol. Neurobiol.* 174, 4–28.

DeFronzo, R. A., Tobin, J. D., and Andres, R. (1979). Glucose clamp technique: a method of quantifying insulin secretion and resistance. *Am. J. Physiol.* 237, E214–E233.

Drager, L. F., Jun, J. C., and Polotsky, V. Y. (2010). Metabolic consequences of intermittent hypoxia: relevance to obstructive sleep apnea. *Best Pract. Res. Clin. Endocrinol. Metab.* 24, 843–851.

Genter, P., Berman, N., Jacob, M., and Ipp, E. (1998). Counterregulatory hormones oscillate during steady-state hypoglycemia. *Am. J. Physiol. Endocrinol. Metab.* 275, E821–E829.

Harsch, I. A., Schahin, S. P., Radespiel-Troger, M., Weintz, O., Jahreiss, H., Fuchs, F. S., Wiest, G. H., Hahn, E. G., Lohmann, T., Konturek, P. C., and Ficker, J. H. (2004). Continuous positive airway pressure treatment rapidly improves insulin sensitivity in patients with obstructive sleep apnea syndrome. *Am. J. Respir. Crit. Care Med.* 169, 156–162.

Himsworth, H., and Ker, R. (1939). Insulin-sensitive and insulin insensitive types of diabetes mellitus. *Clin. Sci.* 4, 119–122.

Howard, B. V., Klimes, I, Vasquez, B., Brady, D., Nagulesparan, M., and Unger, R. H. (1984). The antilipolytic action of insulin in obese subjects with resistance to its glucoregulatory action. *J. Clin. Endocrinol. Metab.* 58, 544–548.

Hucking, K., Hsu, I. R., Ionut, V., and Bergman, R. N. (2007). Deconvolution as a novel approach to analyze moment-to-moment free fatty acid release. *Obesity* 15, 2416–2423.

Iiyori, N., Alonso, L. C., Li, J., Sanders, M. H., Garcia-Ocana, A., O'Doherty, R. M., Polotsky, V. Y., and O'Donnell, C. P. (2008). Intermittent hypoxia causes insulin resistance in lean mice independent of autonomic activity. *Am. J. Respir. Crit. Care Med.* 175, 851–857.

Insel, P. A., Liljenquist, J. E., Tobin, J. D., Sherwin, R. S., Watkins, P., Andres, R., and Berman, M. (1975). Insulin control of glucose metabolism in man: a new kinetic analysis. *J. Clin. Invest.* 55, 1057–1056.

Jun, J., and Polotsky, V. Y. (2009). Metabolic consequences of sleep-disordered breathing. *ILAR J.* 50, 289–306.

Kim, J., Saidel, G. M., and Cabrera, M. E. (2006). Multi-scale computational model of fuel homeostasis during exercise: effect of hormonal control. *Ann. Biomed. Eng.* 35, 69–90.

Kim, S. P., Catalano, K. J., Hsu, I. R., Chiu, J. D., Richey, J. M., and Bergman, R. N. (2007). Nocturnal free fatty acids are uniquely elevated in the longitudinal development of diet-induced insulin resistance and hyperinsulinemia. *Am. J. Physiol. Endocrinol. Metab.* 292, E1590–E1598.

Leung, R. S., and Bradley, T. D. (2001). Sleep apnea and cardiovascular disease. *Am. J. Respir. Crit. Care Med.* 164, 2147–2165.

Linares, O. A., Jacquez, J. A., Zech, L. A., Smith, M. J., Sanfield, J. A., Morrow, L. A., Rosen, S. G., and Halter, J. B. (1987). Norepinephrine metabolism in humans. *J. Clin. Invest.* 80, 1332–1341.

Manzella, D., Parillo, M., Razzino, T., Gnasso, P., Buonanno, S., Gargiulo, A., Caputi, M., and Paolisso, G. (2002). Soluble leptin receptor and insulin resistance as determinant of sleep apnea. *Int. J. Obes. Relat. Metab. Disord.* 26, 370–375.

McArdle, N., Hillman, D., Beilin, L., and Watts, G. (2007). Metabolic risk factors for vascular disease in obstructive sleep apnea: a matched controlled study. *Am. J. Respir. Crit. Care Med.* 175, 190–195.

Nolan, C. J., Madiraju, M. S. R., Delghingaro-Augusto, V., Peyot, M.-L., and Prentki, M. (2006). Fatty acid signaling in the β-cell and insulin secretion. *Diabetes* 55, S16–S23.

Parker, R. S., Doyle, F. J. III, and Peppas, N. A. (1999). A model-based algorithm for blood glucose control in type I diabetic patients. *IEEE Trans. Biomed. Eng.* 46, 148–156.

Polonsky, K. S., Given, B. D., and Van Cauter, E. (1988). Twenty-four-hour profiles and pulsatile patterns of insulin secretion in normal and obese subject. *J. Clin. Invest.* 81, 442–448.

Porksen, N., Hollingdal, M., Juhl, C., Butler, P., Veldhuis, J. D., and Schmitz, O. (2002). Pulsatile insulin secretion: detection, regulation, and role in diabetes. *Diabetes* 51, S245–S254.

Prabhakar, N. R., and Kumar, G. K. (2004). Oxidative stress in the systemic and cellular responses to intermittent hypoxia. *Biol. Chem.* 385, 217–221.

Punjabi, N. M., Sorkin, J. D., Katzel, L. I., Goldberg, A. P., Schwartz, A. R., and Smith, P. L. (2002). Sleep-disordered breathing and insulin resistance in middle-aged and overweight men. *Am. J. Respir. Crit. Care Med.* 165, 677–682.

Randle, P. J., Kerbey, A. L., and Esinol, J. (1988). Mechanisms decreasing glucose oxidation in diabetes and starvation: role of lipid fuels and hormones. *Diabetes Metab. Rev.* 4, 623–628.

Reaven, G. M. (1980). Insulin-independent diabetes mellitus: metabolic characteristics. *Metab. Clin. Exp.* 29, 445–454.

Rebrin, K., Steil, G. M., Getty, L., and Bergman, R. N. (1995). Free fatty acid as a link in regulation of hepatic glucose production by peripheral insulin. *Diabetes* 44, 1038–1045.

Reilly, M. P., and Rader, D. J. (2003). The metabolic syndrome: more than the sum of its parts? *Circulation* 108, 1546–1551.

Roy, A., and Parker, R. S. (2006). Dynamic modeling of free fatty acid, glucose, and insulin: an extended "Minimal Model". *Diabetes Technol. Ther.* 8, 617–626.

Semenza, G. L. (1998). Hypoxia-inducible factor 1: master regulation of O2 homeostasis. *Curr. Opin. Genet. Dev.* 8, 588–594.

Shaw, J. E., Punjabi, N. M., Wilding, J. P., Alberti, K. G. M. M., and Zimmet, P. Z. (2008). Sleep-disordered breathing and type 2 diabetes: a report from the international diabetes federation taskforce on epidemiology and prevention. *Diabetes Res. Clin. Pract.* 8, 2–12.

Sherwin, R. S., Kramer, K. J., Tobin, J. D., Insel, P. A., Liljenquist, J. E., Berman, M., and Andres, R. (1974). A model of the kinetics of insulin in man. *J. Clin. Invest.* 53, 1481–1492.

Simon, C. (1998). Ultradian pulsatility of plasma glucose and insulin secretion rate: circadian and sleep modulation. *Horm. Res.* 49, 185–190.

Simon, C., and Brandenberger, G. (2002). Ultradian oscillations of insulin secretion in humans. *Diabetes* 51, S258–S261.

Skowronski, R., Hollenbeck, C. B., Varasteh, B. B., Chen, Y.-D. I., and Reaven, G. M. (1991). Regulation of non-esterified fatty acid and glycerol concentration by insulin in normal individuals and patients with type 2 diabetes. *Diabet. Med.* 8, 330–333.

Srinivasan, R., Kadish, A. H., and Sridhar, R. (1970). A mathematical model for the control mechanism of free fatty acid-glucose metabolism in normal human. *Comput. Biomed. Res.* 3, 146–165.

Steele, R. (1959). Influences of glucose loading and of injected insulin on hepatic glucose output. *Ann. N. Y. Acad. Sci.* 82, 420–430.

Sturis, J., Polonsky, K. S., Mosekilde, E., and Cauter, E. V. (1991). Computer model for mechanisms underlying ultradian oscillations of insulin and glucose. *Am. J. Physiol.* 260, E801–E809.

Svatikova, A., Wolk, R., Lerman, L. O., Juncos, L. A., Greene, E. L., McConnell, J. P., and Somers, V. K. (2005). Oxidative stress in obstructive sleep apnoea. *Eur. Heart J.* 26, 2435–2439.

Tasali, E., and Ip, M. S. M. (2008). Obstructive sleep apnea and metabolic syndrome: alterations in glucose metabolism and inflammation. *Proc. Am. Thorac. Soc.* 5, 207–217.

Toffolo, G., Bergman, R. N., Finegood, D. T., Bowden, C. R., and Cobelli, C. (1980). Quantitative estimation of beta cell sensitivity to glucose in the intact organism: a minimal model of insulin kinetics in the dog. *Diabetes* 29, 979–990.

Turner, R. C., Holman, R. R., Matthews, D., Hockaday, T. D. R., and Peto, J. (1979). Insulin deficiency and insulin resistance interaction in diabetes: Estimation of their relative contribution by feedback analysis from basal plasma insulin and glucose concentrations. *Metab. Clin. Exp.* 28, 1086–1096.

Xie, A., Skatrud, J. B., Crabtree, D. C., Puleo, D. S., Goodman, B. M., and Morgan, B. J. (2000). Neurocirculatory consequences of intermittent asphyxia in humans. *J. Appl. Physiol.* 89, 1333–1339.

Conflict of Interest Statement: The authors declare that the research was conducted in the absence of any commercial or financial relationships that could be construed as a potential conflict of interest.

Received: 28 September 2011; accepted: 09 December 2011; published online: 04 January 2012.

*Citation: Cheng L and Khoo MCK (2012) Modeling the autonomic and metabolic effects of obstructive sleep apnea: a simulation study. Front. Physio. **2**:111. doi: 10.3389/fphys.2011.00111*

This article was submitted to Frontiers in Computational Physiology and Medicine, a specialty of Frontiers in Physiology.

frontiers in
PHYSIOLOGY

ORIGINAL RESEARCH ARTICLE
published: 25 July 2012
doi: 10.3389/fphys.2012.00298

Estimation of cardiac output and peripheral resistance using square-wave-approximated aortic flow signal

Nima Fazeli and Jin-Oh Hahn*

Department of Mechanical Engineering, University of Alberta, Edmonton, AB, Canada

Edited by:
Zhe Chen, Massachusetts Institute of Technology, USA

Reviewed by:
Lucy T. Zhang, Rensselaer Polytechnic Institute, USA
Marek Matejak, Charles University, Czech Republic

***Correspondence:**
Jin-Oh Hahn, Department of Mechanical Engineering, University of Alberta, 4-9 Mechanical Engineering Building, Edmonton, AB T6G 2G8, Canada.
e-mail: jinoh.hahn@alum.mit.edu

This paper presents a model-based approach to estimation of cardiac output (CO) and total peripheral resistance (TPR). In the proposed approach, the response of cardiovascular system (CVS), described by the windkessel model, is tuned to the measurements of systolic, diastolic and mean arterial blood pressures (BP) so as to yield optimal individual- and time-specific system time constant that is used to estimate CO and TPR. Unique aspects of the proposed approach are that it approximates the aortic flow as a train of square waves and that it also assumes pressure-dependent arterial compliance, as opposed to the traditional windkessel model in which aortic flow is approximated as a train of impulses and constant arterial compliance is assumed. It was shown that the proposed model encompasses the standard windkessel model as a limiting case, and that it also yields more realistic BP waveform response than the standard windkessel model. The proposed approach has potential to outperform its standard counterpart by treating systolic, diastolic, and mean BP as independent features in estimating CO and TPR, rather than solely resorting to pulse pressure as in the case of the standard windkessel model. Experimental results from *in-vivo* data collected from a number of animal subjects supports the viability of the proposed approach in that it could achieve approximately 29% and 24% reduction in CO and TPR errors when compared with its standard counterpart.

Keywords: cardiovascular system, cardiac output, peripheral resistance, windkessel model, pressure-dependent arterial compliance

INTRODUCTION

Cardiac output (CO) is one of the most important hemodynamic parameters to be monitored and assessed in ambulatory and critically ill patients (Jansen et al., 1990). It is frequently used for disease diagnostics and monitoring (Heldt, 2006). It is also a very important hemodynamic variable for therapeutic titrations (Heldt, 2006). In contrast to the use of arterial blood pressures (BP) [which is a late indicator of hemodynamic instability (Barcroft et al., 1944)], CO allows early detection of hemodynamic collapse. Despite its clinical significance, direct measurement of CO is extremely difficult. Presently, the clinical gold standard accepted for CO measurement is the thermo-dilution (Ganz et al., 1971), but it is known to be a highly invasive procedure that has limited accuracy (Botero et al., 2004) and may incur cardiovascular risk (Manecke et al., 2002). Non-intrusive techniques such as echo-cardiography (Ihlen et al., 1984) and electrical velocimetry (Suttner et al., 2006; Zoremba et al., 2007) are promising alternatives, but often their accuracy is not satisfactory enough yet to be clinically applicable (Siegel and Pearl, 1992).

In order to overcome these drawbacks, efforts have been made to estimate CO from arterial BP waveform(s) (see Liljestrand and Zander, 1928; Welkowitz et al., 1991; Martin et al., 1994; Redling and Akay, 1997; Jansen et al., 2001; Ishihara et al., 2004; Mukkamala et al., 2006; Parlikar et al., 2007; Xu et al., 2009; Arai et al., 2010; Reisner et al., 2011 for examples of recent efforts), which are collectively known as the pulse contour methods. In this framework, CO is estimated using the morphological features in the BP waveform(s). Most of the existing pulse contour methods are built upon the windkessel model of cardiovascular system (CVS) that involves lumped arterial compliance and total peripheral resistance (TPR) [e.g., Modelflow (Jansen et al., 2001; Reisner et al., 2011) and pulse pressure methods (Reisner et al., 2011) and its variants (Ishihara et al., 2004), cycle-averaged windkessel model-based method (Jansen et al., 2001), hybrid windkessel model-based method (Jansen et al., 1990)], although there are methods based on empiric features in the arterial BP waveforms (Liljestrand and Zander, 1928; Parlikar et al., 2007; Arai et al., 2010), more detailed distributed-parameter models (Martin et al., 1994; Redling and Akay, 1997) and black-box models combined with advanced signal processing (Welkowitz et al., 1991; Mukkamala et al., 2006; Xu et al., 2009).

Inspired by its wide acceptance and frequent application in CO and TPR estimation, this study aims at developing a universal approach that has potential to enhance the efficacy of CO and TPR estimation based on the standard windkessel model (Frank, 1930) (collectively referred to as the standard windkessel-model-based method hereafter). In this method, the aortic flow signal is approximated as an impulse train, which essentially yields a CO estimator based on the pulse pressure (see Section "Methods" for details). Noting that a number of existing developments on CO estimation (Jansen et al., 2001; Ishihara et al., 2004; Parlikar et al., 2007; Reisner et al., 2011) are variants and/or extensions of this traditional method, it is anticipated

that successful improvement of CO and TPR estimation methods based on the standard windkessel model with aortic flow approximated as impulse train has potential to enhance its variants and/or extensions as well. In this study, we focus on two main opportunities to enhance the CO and TPR estimation efficacy of the standard windkessel-model-based method: (1) to use a better approximation of aortic flow signal that can result in more realistic BP waveform(s), and (2) to exploit independent morphological features in the arterial BP waveform more rigorously rather than solely relying on the pulse pressure as in the standard CO estimator implemented with traditional windkessel model.

This paper presents a new universal approach to the estimation of CO and TPR that can improve the efficacy of windkessel model-based CO and TPR estimation methods. In this approach, the CVS model is characterized using the measurements of systolic, diastolic, and mean BP. In contrast to the standard windkessel-model-based approach to CO and TPR estimation (which approximates the aortic flow signal as a train of impulses), the proposed approach uses the aortic flow signal that is approximated as a train of square waves, which can yield morphologically more realistic arterial BP waveforms. It is shown that the proposed method encompasses its standard counterpart as a limiting case. It is also suggested that the proposed method can outperform the standard method by treating systolic, diastolic, and mean BP as independent features, rather than solely resorting to a single feature (i.e., the pulse pressure) as in the standard method. Experimental results from *in-vivo* animal study illustrated that the proposed approach could achieve 29% and 24% reduction in CO and TPR errors against the standard windkessel model-based method. We anticipate that the proposed approach can be combined with a variety of existing windkessel model-based CO and TPR estimation methods to enhance the methods, accuracy, and reliability.

This paper is organized as follows. Section "Methods" describes the proposed approach to CO and TPR estimation by comparing it to the standard windkessel-model-based method. Section "Methods" presents the details of experimental protocol and data analysis. Section "Results" presents the results, which are discussed in Section "Discussion". Section "Conclusion" concludes the paper with future directions.

METHODS

Our proposed method is built upon the two-parameter windkessel model of the CVS (see **Figure 1**), which is essentially an electrical circuit consisting of a capacitor (to represent the compliance of the conduit arteries) and a resistor (to represent the resistance of the peripheral arteries). First of all, the governing equation for the two-parameter windkessel model is given by (1):

$$\frac{dP}{dt} = -\frac{1}{RC}P + \frac{1}{C}Q \tag{1}$$

where P is BP and Q is aortic flow. **Figure 1** demonstrates that the proposed windkessel method has strengths over its standard counterpart in that (1) by using the aortic flow signal approximated as a train of square waves, the resulting BP waveform is morphologically more realistic compared with its standard counterpart (see the upper and lower right corners of **Figure 1** for BP waveforms resulting from impulse and square wave trains, respectively), and (2) it exploits the features in BP waveform more rigorously, i.e., it uses systolic, diastolic, and mean BP as independent features to characterize the CVS model and estimate CO and TPR, whereas the standard method depends solely on the pulse pressure.

To clearly demonstrate the distinction between the standard and the proposed estimation methods for CO and TPR, the standard windkessel method is first introduced,

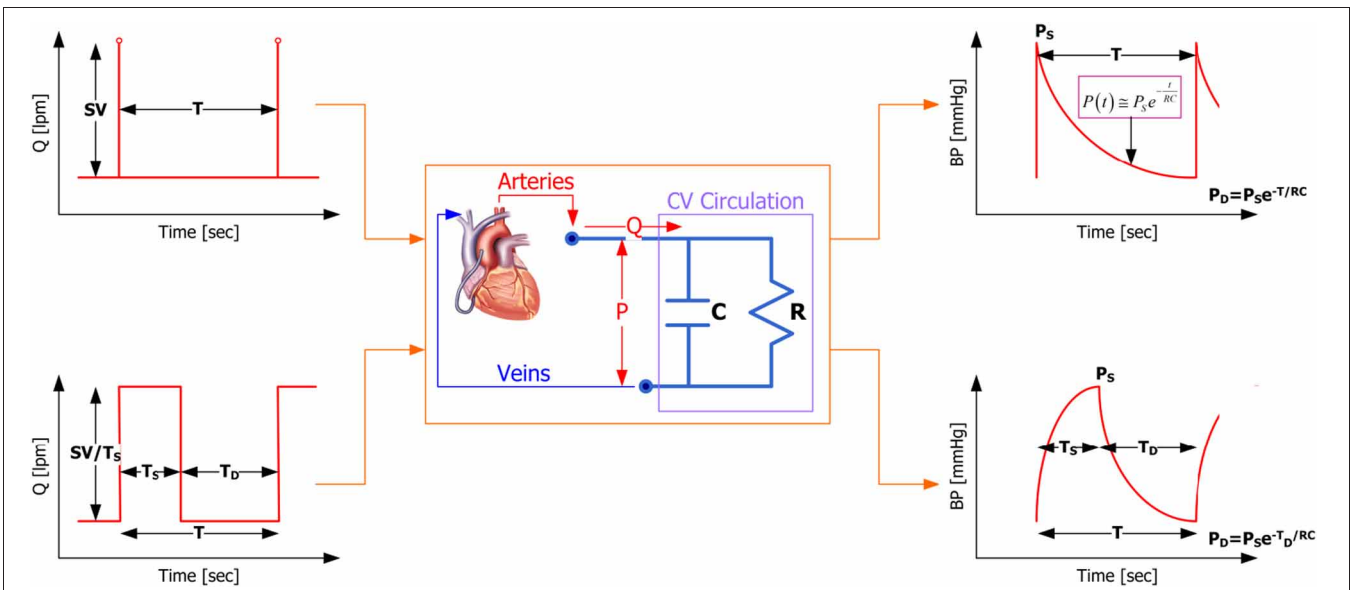

FIGURE 1 | Standard versus proposed windkessel-model-based CVS model characterization methods.

and then the proposed windkessel method is described in detail.

STANDARD WINDKESSEL METHOD

Given the aortic flow signal approximated as a train of impulses shown in the upper left corner of **Figure 1**, which has amplitude equal to the stroke volume (SV) and the period equal to a cardiac cycle (i.e., heart period) T, the resulting BP response of the windkessel model (1) is given by:

$$P(t) = P_D e^{-\frac{t}{RC}} + \frac{\overline{Q}}{C} T e^{-\frac{t}{RC}}, \tag{2}$$

where P_D is diastolic BP and $\overline{Q}$ is CO. Equation (2) is valid for a single cardiac cycle, i.e., $0 \le t \le T$. The systolic as well as diastolic BP corresponds to the value of BP at $t = 0$ and $t = T$:

$$P_S = P_D + \frac{\overline{Q}}{C} T \tag{3a}$$

$$P_D = P_S e^{-\frac{t}{RC}} \tag{3b}$$

where P_S is systolic BP. Equation (3a) is of particular interest in estimating CO and TPR; rearranging it yields (4):

$$\widehat{\overline{Q}} = C\frac{P_S - P_D}{T} \propto \frac{P_P}{T}, \tag{4a}$$

$$\hat{R} = \frac{1}{C}\overline{P}\frac{T}{P_p} \propto \overline{P}\frac{T}{P_p}, \tag{4b}$$

where $\widehat{\overline{Q}}$ and $\hat{R}$ are the estimated CO and TPR, and P_P denotes the pulse pressure. Under the assumption that arterial compliance C remains constant over a time window under consideration, Equation (4) can be utilized to estimate the trend of CO and TPR as the ratio of pulse pressure and heart period as well as mean BP. Equation (4) can also be used to estimate the absolute CO and TPR if initial measurements to calibrate C are available. It is obvious that the only information the standard windkessel method exploits in the BP waveform for estimating CO and TPR is pulse pressure.

PROPOSED WINDKESSEL METHOD

In contrast to its standard counterpart, the proposed windkessel method for estimating CO and TPR intends to rigorously exploit multiple independent features in the BP waveform in characterizing the CVS model. For this purpose, the aortic flow signal is approximated as a train of square waves shown in the lower left corner of **Figure 1**, as opposed to a train of impulses used in the standard windkessel method (shown in the upper left corner of **Figure 1**). In this approximation, the amplitude of each square wave is given by $\overline{Q}\frac{T}{T_S}$ where T_S is the left ventricular ejection period, since the area under each square wave must be equal to SV. It then follows that solving Equation (1) for BP during $0 \le t \le T_S$ yields

$$\begin{aligned} P(t) &= P_D e^{-\frac{t}{RC}} + \int_0^t e^{-\frac{t-\tau}{RC}} \frac{\overline{Q}}{C}\frac{T}{T_S} d\tau \\ &= P_D e^{-\frac{t}{RC}} + R\overline{Q}\frac{T}{T_S}\left[1 - e^{-\frac{t}{RC}}\right] \\ &= P_D e^{-\frac{t}{RC}} + \overline{P}\frac{T}{T_S}\left[1 - e^{-\frac{t}{RC}}\right]. \end{aligned} \tag{5}$$

During $T_S \le t + T_S \le T$, on the other hand, BP is given by

$$\begin{aligned} P(t) &= P_S e^{-\frac{t}{RC}} \\ &= P_D e^{-\frac{t+T_S}{RC}} + \overline{P}\frac{T}{T_S} e^{-\frac{t}{RC}}\left[1 - e^{-\frac{T_S}{RC}}\right]. \end{aligned} \tag{6}$$

Based on (5) and (6), the following expressions for systolic and diastolic BP are obtained:

$$P_S = P_D e^{-\frac{T_S}{RC}} + \overline{P}\frac{T}{T_S}\left[1 - e^{-\frac{T_S}{RC}}\right], \tag{7a}$$

$$P_D = P_S e^{-\frac{T_D}{RC}} = P_D e^{-\frac{T}{RC}} + \overline{P}\frac{T}{T_S} e^{-\frac{T_D}{RC}}\left[1 - e^{-\frac{T_S}{RC}}\right]. \tag{7b}$$

In addition, mean BP can be obtained as follows based on (5) and (6):

$$\begin{aligned} \overline{P} = \frac{1}{T}\Bigg\{ &\int_0^{T_S} P_D e^{-\frac{\tau}{RC}} + \overline{P}\frac{T}{T_S}\left[1 - e^{-\frac{\tau}{RC}}\right] d\tau \\ &+ \int_0^{T_D} P_S e^{-\frac{\tau}{RC}} d\tau \Bigg\}. \end{aligned} \tag{8}$$

In the proposed windkessel method, the model-based expressions in Equations (7) and (8) for systolic, diastolic, and mean BP are compared with the actual BP measurements, and the set of parameters in the windkessel model characterizing Equations (7) and (8), i.e., RC, T_S and T_D, is optimized so that the discrepancy between the model-predicted versus actual systolic, diastolic, and mean BP are minimized. Specifically, the model-predicted systolic, diastolic and mean BP values are evaluated as follows:

$$\hat{P}_S = P_D e^{-\frac{T_S}{RC}} + \overline{P}\frac{T}{T_S}\left[1 - e^{-\frac{T_S}{RC}}\right], \tag{9a}$$

$$\hat{P}_D = P_D e^{-\frac{T}{RC}} + \overline{P}\frac{T}{T_S} e^{-\frac{T_D}{RC}}\left[1 - e^{-\frac{T_S}{RC}}\right], \tag{9b}$$

$$\begin{aligned} \widehat{\overline{P}} = \frac{1}{T}\Bigg\{ &\int_0^{T_S} P_D e^{-\frac{\tau}{RC}} + \overline{P}\frac{T}{T_S}\left[1 - e^{-\frac{\tau}{RC}}\right] d\tau \\ &+ \int_0^{T_D} \hat{P}_S e^{-\frac{\tau}{RC}} d\tau \Bigg\}, \end{aligned} \tag{9c}$$

Noting that $T_S + T_D = T$, the optimal set of the windkessel model parameters $\{RC^*,\ T_S^*\}$ is determined by solving the following constrained optimization problem:

$$\begin{aligned} \{RC^*,\ T_S^*\} = \arg\min \Big[&\left\| P_S - \hat{P}_S \right\| \\ &+ \left\| P_D - \hat{P}_D \right\| + \left\| \overline{P} - \widehat{\overline{P}} \right\| \Big], \end{aligned} \tag{10a}$$

where, with T inferred directly from measured BP, T_D^* given by

$$T_D^* = T - T_S^*. \tag{10b}$$

Using the CVS model parameters in (10a) thus identified, the trend of CO and TPR can be estimated in two alternative ways, depending on the assumption made in regards to the behavior of arterial compliance C: (1) constant or (2) pressure-dependent. First, assuming C is constant, the trend of CO can be estimated by dividing the measured mean BP by RC^*, and the trend of TPR can be estimated directly by RC^*:

$$\widehat{\overline{Q}} \propto \frac{\overline{P}}{RC^*}, \tag{11a}$$

$$\hat{R} \propto RC^*, \tag{11b}$$

where $\hat{R}$ is the estimated TPR. On the other hand, if C is assumed to be pressure-dependent, its effect must be cancelled out in estimating the trend of CO and TPR. This can be accomplished by first dividing the measured mean BP by RC^*, then multiplying C as a function of BP:

$$\overline{Q} = \frac{\overline{P}}{RC^*} \times C(P_S, P_D, \overline{P}), \tag{12a}$$

$$\hat{R} = \frac{RC^*}{C(P_S, P_D, \overline{P})}. \tag{12b}$$

Note that the relationships in Equation (12) are strict equalities. In this preliminary study, C is assumed as a simple monotonic linear function of mean BP, i.e.,

$$C(P_S, P_D, \overline{P}) = \eta_1 \overline{P} + \eta_2. \tag{13}$$

Using Equation (13), Equation (12) can be re-formulated into the following:

$$\widehat{\overline{Q}} = \frac{\overline{P}}{RC^*} \times (\eta_1 \overline{P} + \eta_2) = \eta_1 \frac{\overline{P}^2}{RC^*} + \eta_2 \frac{\overline{P}}{RC^*}, \tag{14a}$$

$$\hat{R} = \frac{RC^*}{C(P_S, P_D, \overline{P})} = \frac{RC^*}{\eta_1 \overline{P} + \eta_2}. \tag{14b}$$

One advantage of Equation (14) compared with Equation (11) is that it can accommodate into CO and TPR estimation the physiological nature of the arterial compliance that indeed changes with BP. However, a pre-calibration procedure is usually required to determine η_1 and η_2, since arterial compliance is rarely known a priori.

In essence, the proposed method is distinct from its standard counterpart in the sense that it regards systolic, diastolic and mean BP as independent features in characterizing the windkessel CVS model and estimating CO and TPR, whereas the standard method only concerns the pulse pressure.

METHODS

EXPERIMENTAL PROTOCOL

Under the experimental protocol #01–055 approved by the MIT Committee of Animal Care, aortic flow and radial BP data were collected from eight anaesthetized swine subjects.

The chest was opened with a midline sternotomy. An ultrasonic flow probe was placed around the aortic root for the central aortic flow (T206 with A-series probes, Transonic Systems, Ithaca, NY). Besides, a 25-gauge angiocatheter was placed in the foreleg, distal to the brachial artery, and attached to an external pressure transducer via short, rigid tubing for the radial arterial BP. Each transducer output was interfaced to a microcomputer via an A/D conversion system (MP150WSW, Biopac Systems).

The physiological conditions of the swine subjects were widely altered in order to investigate how the CO estimation method behaves over a broad range of physiological conditions. The following interventions were performed to vary the physiological conditions of the swine subjects: the infusions of crystalloid volume, phenylephrine, dobutamine, isoproterenol, esmolol, nitroglycerine, and a progressive hemorrhage. The administration of each medicine was followed by a brief recovery period.

DATA COLLECTION, SIGNAL PROCESSING, AND STATISTICAL ANALYSIS

The aortic flow and radial BP waveforms were first measured at 250 Hz without filtering from each swine subject, which were then pre-filtered using an FIR low-pass digital filter with 30 Hz cut-off frequency and down-sampled to 125 Hz. Following filtering and down-sampling, the aortic flow-radial BP data pair was segmented into 8 s-long time series sequences having 1000 data samples. Totally 4638 data segments were used in this study.

For each of the 8 s-long data segments obtained, CO and mean BP representative of a data segment were calculated by averaging the aortic flow and radial BP waveforms in the segment, respectively. The systolic and diastolic BP were calculated by averaging systolic and diastolic BP in all the cardiac cycles in the segment. In each data segment, the estimate of the trend of CO associated with the standard windkessel method was calculated based on the pulse pressure associated with the data segment using Equation (4). Also, the trend of TPR was obtained directly from dividing mean BP by the estimated trend of CO; $\hat{R} = \overline{P}\frac{T}{P_P}$. For the proposed method, the optimal windkessel model parameters $\left\{RC^*,\ T_S^*,\ T_D^*\right\}$ were determined by solving the constrained optimization problem in Equation (10) using the measurements of systolic, diastolic and mean BP associated with the data segment. Then the estimates of the trends of CO and TPR were calculated with Equations (11) and (14) for constant and pressure-dependent arterial compliance, respectively.

Once the measured versus estimated CO $\left\{\overline{Q}_i,\ \widehat{\overline{Q}}_i\right\}$ and TPR $\left\{R_i,\ \hat{R}_i\right\}$ pairs for all the data segments were obtained for each swine subject ($i = 1, \cdots 8$), the estimated CO and TPR were calibrated to the measurements via linear regression analysis in order to compare the estimates with the gold standard measurements. Specifically, the following calibration was applied to the standard windkessel method:

$$\overline{Q} = a_{1,Q}\widehat{\overline{Q}} + a_{2,Q} = a_{1,Q}\frac{P_P}{T} + a_{2,Q}, \tag{15a}$$

$$R = a_{1,R}\hat{R} + a_{2,R}. \tag{15b}$$

For the proposed windkessel method, different calibration procedure was applied to Equations (11) and (14). For CO and TPR estimation with constant arterial compliance, i.e., Equation (11), the calibration similar to Equation (15) was applied:

$$\overline{Q} = b_{1,Q}\widehat{\overline{Q}} + b_{2,Q} = b_{1,Q}\frac{\overline{P}}{RC^*} + b_{2,Q}, \tag{16a}$$

$$R = b_{1,R}\hat{R} + b_{2,R} = b_{1,R}RC^* + b_{2,R}. \tag{16b}$$

For CO and TPR estimation with pressure-dependent arterial compliance i.e., Equation (14), on the other hand, the slope of the linear regression must be unity because the relationship in Equation (14) are strict equalities. Therefore, a simple intercept calibration was applied to CO:

$$\overline{Q} = \widehat{\overline{Q}} + \eta_3 = \eta_1\frac{\overline{P}^2}{RC^*} + \eta_2\frac{\overline{P}}{RC^*} + \eta_3, \tag{17a}$$

where η_1 and η_2 represent pressure-dependent arterial compliance [see Equation (14)], whereas the intercept η_3 is intended to compensate for the inaccuracy in approximating arterial compliance to a monotonic linear function of mean BP. Using η_1 and η_2 obtained above, TPR is calibrated as follows:

$$R = c_{1,R}\hat{R} + c_{2,R} = \frac{RC^*}{\eta_1\overline{P} + \eta_2} + c_{2,R}, \tag{17b}$$

where $c_{1,R} = 1$ was assumed because Equation (14b) is strict equality.

Once calibrated, the fidelity of the standard and proposed CO and TPR estimation methods were assessed quantitatively by calculating (1) the coefficient of determination (CoD; r^2 value), (2) the limits of agreement (i.e., the Bland-Altman statistics) between measured versus estimated CO and TPR, and (3) the root-mean-squared normalized errors (RMNSE) between measured versus estimated CO and TPR, respectively. RMNSE was calculated first for each swine subject as follows:

$$e_{i,Q} = 100 \times \sqrt{\frac{1}{N_i}\sum_{k=1}^{N_i}\left[\frac{\overline{Q}_i(k) - \widehat{\overline{Q}}_i(k)}{\overline{Q}_i(k)}\right]^2}, \tag{18a}$$

$$e_{i,R} = 100 \times \sqrt{\frac{1}{N_i}\sum_{k=1}^{N_i}\left[\frac{R_i(k) - \hat{R}_i(k)}{R_i(k)}\right]^2}, \tag{18b}$$

where N_i is the total number of data segments associated with the i^{th} swine subject, $\overline{Q}_i(k)$ and $\widehat{\overline{Q}}_i(k)$ are measured versus estimated (and calibrated) CO for the k^{th} data segment of the i^{th} swine subject, and $R_i(k)$ and $\hat{R}_i(k)$ are measured versus estimated (and calibrated) TPR for the k^{th} data segment of the i^{th} swine subject. The comparison of standard versus proposed methods was conducted based on the CoD, limits of agreement and RMNSE aggregated over all the swine subjects. Statistical significance was assessed using the repeated-measures ANOVA applied to CoD and RMSNE associated with standard versus proposed CO and TPR estimation methods. Difference was regarded as significant if $p < 0.05$.

RESULTS

The ranges of the physiological conditions associated with the experimental swine subjects are summarized in **Table 1**. It is obvious that all the subjects experienced large physiological changes due to medical interventions.

Table 2 lists CoD and RMSNE values associated with standard versus proposed CO and TPR estimation methods, where values associated with constant Equation (11) and pressure-dependent Equation (14) arterial compliance are presented for the proposed method. **Table 3** presents the limits of agreement between measured versus estimated (using standard method and proposed method with pressure-dependent arterial compliance) CO and TPR. **Figure 2** shows a representative (a) correlation between measured versus estimated CO and TPR and (b) Bland Altman plot between measured versus estimated CO and TPR, in which the proposed method is shown to outperform its standard counterpart. Aggregated over all animal subjects, the proposed method (both with constant and pressure-dependent arterial compliance) resulted in CoD and RMSNE values significantly different from those associated with the standard method ($p < 0.05$). The coefficients of the pressure-dependent arterial compliance model in Equation (13), determined by the calibration shown in Equation (17a), are shown in **Table 4**. On the average, arterial compliance was inversely proportional to mean BP ($\eta_1 < 0$) but assumed positive values ($\eta_2 > 0$), as physiologically anticipated.

Table 1 | Physiological conditions of experimental swine subjects.

Subject ID	Mean HR [bpm]	Mean BP [mmHg]	Mean CO [lpm]	Mean TPR [mmHg/lpm]
1	68/120 (89)	41.0/119.0 (59.7)	1.6/4.8 (2.8)	13.0/26.4 (21.3)
2	150/195 (177)	36.5/93.9 (66.0)	1.9/7.3 (4.1)	12.7/20.2 (16.1)
3	97/165 (120)	40.6/104.0 (71.6)	1.9/5.5 (3.8)	12.0/35.0 (18.8)
4	97/180 (120)	50.5/157.2 (78.6)	2.3/4.9 (3.1)	15.0/53.3 (25.4)
5	90/187 (125)	58.9/123.7 (88.4)	1.5/5.9 (3.8)	12.4/43.4 (23.3)
6	97/195 (120)	44.0/112.1 (79.7)	1.8/4.6 (3.0)	14.4/37.4 (26.6)
7	90/203 (136)	53.0/121.2 (87.7)	2.4/5.7 (3.7)	12.8/37.8 (23.7)
8	68/165 (129)	27.1/123.3 (80.4)	0.6/6.2 (3.9)	12.6/48.2 (20.6)
All	68/203 (123)	27.1/157.2 (79.3)	0.6/7.3 (3.4)	12.0/53.3 (22.9)

Table 2 | CoD and RMSNE associated with standard versus proposed CO and TPR estimation methods.

	1	2	3	4	5	6	7	8	All
(A) CoD: CO ESTIMATION. VALUES IN () INDICATES IMPROVEMENT AGAINST STANDARD METHOD									
Standard	0.895	0.985	0.823	0.663	0.712	0.600	0.720	0.876	0.737
Proposed (Constant C)	0.908	0.984	0.785	0.747	0.796	0.788	0.828	0.918	0.819 (11.1%)
Proposed ($C = \eta_1 \overline{P} + \eta_2$)	0.948	0.985	0.855	0.746	0.868	0.804	0.881	0.931	0.855 (16.0%)
(B) RMSNE: CO ESTIMATION. VALUES IN () INDICATES IMPROVEMENT AGAINST STANDARD METHOD									
Standard	9.9	5.4	11.8	9.1	17.5	16.0	12.7	22.4	13.7
Proposed (Constant C)	9.2	5.7	13.3	8.0	14.6	11.5	9.6	18.3	11.4 (16.8%)
Proposed ($C = \eta_1 \overline{P} + \eta_2$)	7.1	5.6	10.0	8.0	12.0	10.5	7.8	16.1	9.7 (29.2%)
(C) CoD: TPR ESTIMATION. VALUES IN () INDICATES IMPROVEMENT AGAINST STANDARD METHOD									
Standard	0.160	0.665	0.848	0.836	0.834	0.639	0.815	0.765	0.717
Proposed (Constant C)	0.647	0.716	0.888	0.905	0.668	0.765	0.872	0.692	0.781 (8.9%)
Proposed ($C = \eta_1 \overline{P} + \eta_2$)	0.782	0.711	0.872	0.907	0.758	0.789	0.899	0.748	0.808 (12.7%)
(D) RMSNE: TPR ESTIMATION. VALUES IN () INDICATES IMPROVEMENT AGAINST STANDARD METHOD									
Standard	14.2	6.0	12.5	10.3	10.6	14.1	11.0	12.6	11.8
Proposed (Constant C)	9.6	4.9	10.4	7.9	13.2	10.8	9.0	14.0	10.3 (12.7%)
Proposed ($C = \eta_1 \overline{P} + \eta_2$)	6.8	4.9	9.9	7.8	11.3	10.3	7.4	13.0	8.9 (24.3%)

Table 3 | Limits of agreement between measured versus estimated CO and TPR.

	1	2	3	4	5	6	7	8	All
(A) BLAND-ALTMAN STATISTICS: CO ESTIMATION (MEAN ± 1.96SD [mmHg])									
Standard	0 ± 0.31	0 ± 0.15	0 ± 0.39	0 ± 0.29	0 ± 0.54	0 ± 0.43	0 ± 0.41	0 ± 0.47	0 ± 0.40
Proposed ($C = \eta_1 \overline{P} + \eta_2$)	0 ± 0.22	0 ± 0.15	0 ± 0.35	0 ± 0.25	0 ± 0.36	0 ± 0.30	0 ± 0.27	0 ± 0.35	0 ± 0.29
(B) BLAND-ALTMAN STATISTICS: TPR ESTIMATION (MEAN ± 1.96SD [mmHg])									
Standard	0 ± 2.84	0 ± 0.98	0 ± 2.43	0 ± 2.63	0 ± 2.71	0 ± 3.52	0 ± 2.83	0 ± 3.61	0 ± 2.85
Proposed ($C = \eta_1 \overline{P} + \eta_2$)	0 ± 1.45	0 ± 0.91	0 ± 2.23	0 ± 1.99	0 ± 3.28	0 ± 2.69	0 ± 2.09	0 ± 3.73	0 ± 2.30

DISCUSSION

VALIDITY AND EFFICACY OF PROPOSED METHOD

On the average, the proposed method resulted in 16% and 13% reduction in CoD for CO and TPR, respectively (see **Tables 2A,C**). It also resulted in 29% and 24% reduction of CO and TPR errors, respectively, if the pressure-dependent arterial compliance was used, and 17% and 12% reduction, respectively, if constant arterial compliance was used (see **Tables 2B,D**). In addition, the results with pressure-dependent arterial compliance were consistently superior to those with constant arterial compliance (see **Table 2**) with statistical significance. **Table 3** indicates that the proposed method exhibits improved limits of agreement to the measured gold standard CO and TPR than its standard counterpart. Altogether, the above results suggest that (1) the fidelity of CO and TPR estimation may be improved by rigorous exploitation of multiple independent features in the BP waveform rather than resorting to a single feature (i.e., the pulse pressure) as in the case of the standard windkessel method, and (2) the explicit incorporation of pressure-dependent nature of arterial compliance may further benefit high-fidelity estimation of CO and TPR.

Table 4 indicates that the identified models of arterial compliance exhibit physiologically meaningful behavior in most animal subjects (i.e., 6 out of 8), i.e., it is inversely proportional to the underlying BP ($\eta_1 < 0$) and assumes positive values over the underlying BP values ($\eta_2 > 0$). **Figure 3** supports the validity of the pressure-dependent arterial compliance model used in this study: indeed, (14a) suggests that $RC^*\overline{Q}$ must depend on mean BP in a concave parabolic fashion (see the left panel of **Figure 3**):

$$RC^*\overline{Q} = \overline{P} \times (\eta_1 \overline{P} + \eta_2) = \eta_1 \overline{P}^2 + \eta_2 \overline{P}, \tag{19a}$$

while (14b) suggests that $\frac{RC^*}{R}$ must be linearly decreasing with respect to mean BP (see the right panel of **Figure 3**):

$$\frac{RC^*}{R} = C(P_S, P_D, \overline{P}) = \eta_1 \overline{P} + \eta_2. \tag{19b}$$

Figure 3 is consistent with what is anticipated, although some degree of deviation can be found quantitatively. In particular, the quantitative trend of arterial compliance shown in the right panel of **Figure 3** is consistent with its typical pressure-dependent behavior reported in existing literature (e.g., Richter and Mittermayer, 1984). However, this was not the case for some animal subjects. In fact, although qualitatively similar observations to **Figure 3** could be made for subjects #2 and #7, the trends were not as vivid and clear as those seen in **Figure 3**, which led to misleading outcomes for these subjects (see **Table 4**). This can be attributable to (1) the limited validity of the simple linear model of pressure-dependent arterial compliance (see Section

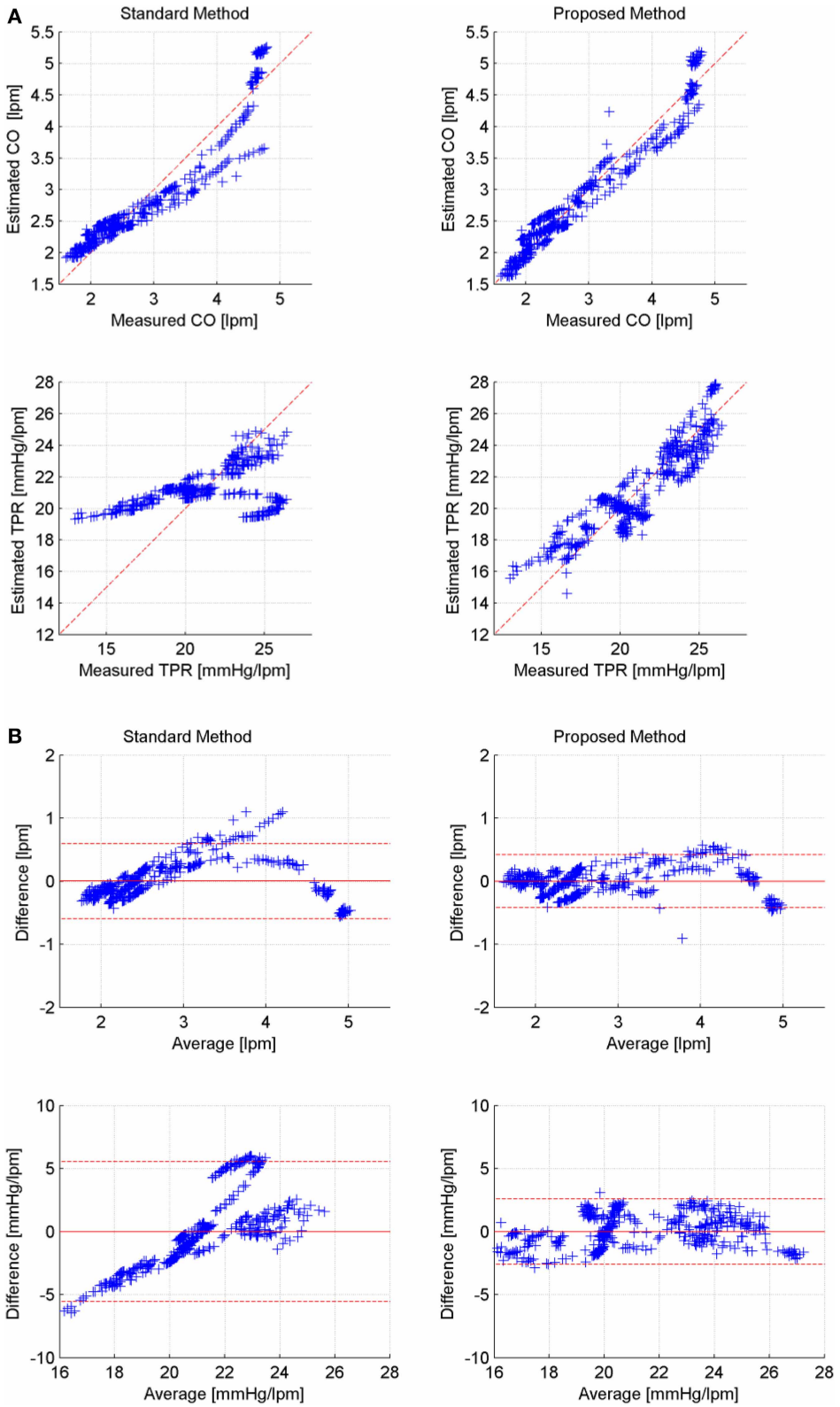

FIGURE 2 | Representative correlation and limits of agreement: measured versus estimated CO and TPR (Subject #1). **(A)** Correlation between measured versus estimated CO and TPR (left: standard, right: proposed). **(B)** Bland-Altman plot between measured versus estimated CO and TPR (left: standard, right: proposed).

Table 4 | Model of pressure-dependent arterial compliance.

	1	2	3	4	5	6	7	8	All
$\eta_1 \times 10^5$	−10.6	6.7	−25.4	−0.74	−13.3	−2.6	8.2	−1.5	−4.9
$\eta_2 \times 10^2$	4.2	2.4	6.1	2.2	4.2	3.6	2.1	3.2	3.5

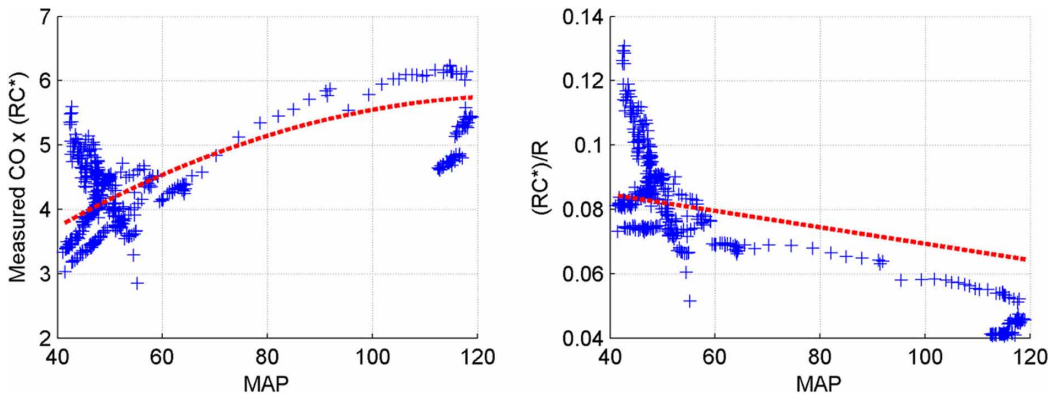

FIGURE 3 | Validity of linear pressure-dependent arterial compliance model (Subject #1).

"Limitations of the study" for more discussion) as well as to (2) the time-varying physiological conditions within the 8 s time window (in which case determining the optimal windkessel time constant RC^* associated with the time window can be challenging, since it is subject to change within the time window when the subject is affected by dynamic physiological states).

The validity of pressure-dependent arterial compliance (13) can further be assessed by scrutinizing the intercept coefficients η_3 and $c_{2,R}$. If the arterial compliance is truly dependent on mean BP in a linear fashion, (13) is fully valid and η_3 and $c_{2,R}$ must be zero. In the absence of any restrictions imposed on the intercepts, our regression analysis revealed that η_3 and $c_{2,R}$ assumed 0.93l pm and -10.6 mmHg/lpm on the average, respectively, suggesting that the proposed approach consistently underestimated CO and overestimated TPR. Considering the underlying CO and TPR values (see **Table 1**), the intercepts for both CO and TPR amounted to approximately 30% of the underlying values. However, noting that the slope coefficients in (17) were constrained at unity, it can be concluded that the proposed approach is able to estimate the absolute change of CO and TPR despite the non-negligible intercept coefficients. It is also important to point out that restricting $c_{2,R}$ to zero in the calibration procedure (17) did not yield any noticeable degradation in performance of the proposed approach. Indeed, even when $c_{2,R} = 0$ was imposed (in which case η_3 was also very close to zero), the proposed approach improved CoD of CO and TPR by 16.0% and 13.5%, respectively, and it also improved RMSNE of CO and TPR by 27.3% and 27.2%, respectively, when compared with its standard counterpart. In essence, the performance of the proposed approach was insensitive against whether or not $c_{2,R}$ was restricted to zero. Therefore, it can be concluded that, though not perfect, (13) may be viewed as a valid approximation of arterial compliance that can be used with the proposed approach in order to reliably estimate CO and TPR.

MATHEMATICAL ANALYSIS OF PROPOSED METHOD

The advantage of the proposed windkessel method over the standard windkessel method in better estimating CO and TPR can be demonstrated by analyzing the systolic BP it represents as a function of T_S. First, assuming $T_S = 0$, the systolic BP predicted in the proposed method in Equation (7a) becomes

$$\lim_{T_S \to 0} P_S = \lim_{T_S \to 0} \left\{ P_D e^{-\frac{T_S}{RC}} + \overline{P} \frac{T}{T_S} \left[1 - e^{-\frac{T_S}{RC}} \right] \right\} = P_D + \overline{P} \frac{T}{RC} = P_D + \frac{\overline{Q}}{C} T, \tag{20}$$

which is equivalent to Equation (3a). Thus, the proposed windkessel method reduces to its standard counterpart as expected, because the square wave approaches to impulse by shrinking T_S to zero. By virtue of its generalization capability, therefore, the proposed method can outperform its standard windkessel counterpart. On the other hand, if $T_S = T$, the systolic BP becomes

$$\lim_{T_S \to T} P_S = P_D e^{-\frac{T}{RC}} + \overline{P} \left[1 - e^{-\frac{T}{RC}} \right]. \tag{21}$$

In the proposed method, an increase in T_S results in decrease in T_D since T is fixed from the measurement of heart period. Further, the relationship in Equation (7) on the ratio of systolic and diastolic BP given by $e^{-\frac{T_D}{RC}}$ together with their given measurements dictates that the ratio of RC and T_D must be kept at a constant regardless of the value of T_D. Therefore, RC has to decrease as T_S increases in the proposed method. Since $T_S \approx T$ is equivalent to $T_D \approx 0$, RC must be very small as well. If RC is sufficiently small such that $e^{-\frac{T}{RC}} \approx 0$ is valid, the systolic BP in

Equation (21) can be approximated to:

$$\lim_{T_S \to T} P_S = P_D e^{-\frac{T}{RC}} + \overline{P}\left[1 - e^{-\frac{T}{RC}}\right] \approx \overline{P}, \qquad (22)$$

which is simply the behavior of the CVS in the steady state. Given the BP waveforms shown in **Figure 4** associated with $T_S = 0$ and $T_S = T$ as well as the constraint that the mean BP derived from the model should be equal to its measured counterpart regardless of the value of T_S, it is obvious that the systolic BP in Equation (20) is greater than the one in Equation (22). Representative BP waveforms for $0 \leq T_S \leq T$ are also shown in **Figure 4**, where systolic BP is shown to decrease as T_S increases, which is anticipated from Equation (20) to Equation (22). Moreover, scrutinizing the mean BP constraint in Equation (9c) reveals that it essentially reduces to a constraint on diastolic BP weighted by RC. Indeed, it can be shown that evaluating the integration terms in Equation (9c) yields

$$\widetilde{\overline{P}} = \widehat{\overline{P}} - \overline{P} = -\frac{RC}{T}(\hat{P}_D - P_D) = -\frac{RC}{T}\tilde{P}_D. \qquad (23)$$

which essentially reduces Equation (10a) to the following:

$$\{RC^*,\ T_S^*\} = \arg\min\left[\left\|P_S - \hat{P}_S\right\| + \left(1 + \frac{RC}{T}\right)\left\|P_D - \hat{P}_D\right\|\right]. \qquad (24)$$

Though yet to be fully validated, we expect that, compared with Equation (9b) which leads to the diastolic BP error term $\left\|P_D - \hat{P}_D\right\|$ in Equation (10a), (9c) which yields the mean BP error term $\left\|\overline{P} - \widehat{\overline{P}}\right\|$ in Equation (10a) is useful in regularizing RC (i.e., keeping it from growing too large) as well as minimizing the diastolic BP error. Indeed, noting that systolic and diastolic BP can be tuned independently of each other with T_S and $\frac{T_D}{RC}$ in the proposed method, incorporating the mean BP error term into Equation (10a) via Equation (9c) allows the proposed method to exploit the range of $\{RC,\ T_S, T_D\}$ beyond the standard windkessel method, i.e., the range corresponding to $T_s > 0$. In this context, a unique strength of the proposed method is its capability to characterize the CVS model by tuning the parameters $\{RC,\ T_S, T_D\}$ in order to fit the model-predicted systolic, diastolic and mean BP to their measured counterparts, yielding a CVS model whose parameters can be utilized to improve the fidelity of CO and TPR estimation in comparison with the standard windkessel method that is solely built upon the pulse pressure.

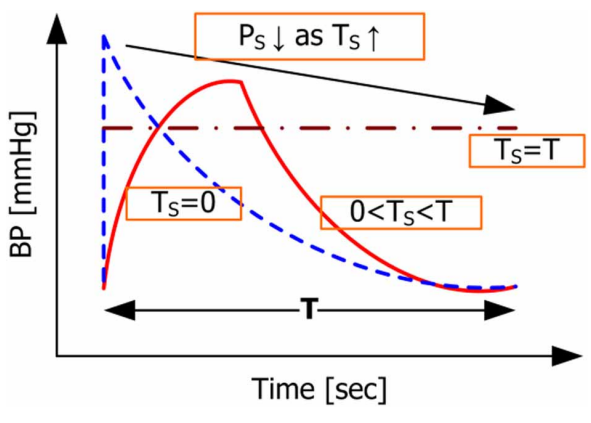

FIGURE 4 | Model-predicted BP waveforms associated with different values of T_S.

LIMITATIONS OF THE STUDY

This study has a number of limitations. First, it was assumed that physiological condition of the animal subjects was time-invariant over each time window of 8 s. Although this should be a reasonable assumption for majority of the experimental data segments, it may not be well justified in part of the data, such as those corresponding to transient responses to the onset of drug administrations. Second, simple linear model was used to represent the pressure dependence of arterial compliance, although in reality it is known to be dependent on BP in highly nonlinear fashion. The linearity assumption may be valid for local approximation of arterial compliance within small pulse pressure range, but its validity will be deteriorated as the range of pulse pressure encompassed in the 8 s time window increases. In this regard, future work on the use of globally valid arterial compliance model in the proposed method is required. Third, despite the significantly large improvement in CO and TPR estimation provided by the proposed method, its utility may be limited to an extent by its requirement for calibration. In this regard, the hybrid use of proposed method with both constant and pressure-dependent arterial compliance can be a viable resolution. For example, CO and TPR can be estimated using Equation (11) until a number of CO measurements become available for calibration, after which Equation (14) can be used to estimate CO and TPR more accurately.

CONCLUSION

In this paper, a novel universal approach was proposed to improve the performance of standard windkessel-model-based method in estimating the trend of CO and TPR. The validity and initial proof-of-principle of the proposed method was established via experimental evaluation and its comparison with the standard method. It has been suggested that the fidelity of CO and TPR estimation can be improved by rigorous exploitation of multiple features in the BP waveform to better characterize the CVS model. Future work is required in regards to further understanding on the capability and limitation of the proposed method as well as its application to extensions and variants of the standard windkessel-model-based CO and TPR estimation methods.

ACKNOWLEDGMENTS

This research was supported in part by the Natural Science and Engineering Research Council of Canada (NSERC) and the University of Alberta. The *in-vivo* animal data used in this paper was collected by Dr. Andrew Reisner (Massachusetts General Hospital), Dr. Horacio Hojman (Yale University), and Dr. Ramakrishna Mukkamala (Michigan State University).

REFERENCES

Arai, T., Lee, K., and Cohen, R. J. (2010). "Cardiac output and stroke volume estimation using a hybrid of three windkessel models," in *Proceedings of the IEEE Engineering in Medicine and Biology Conference,* (Buenos Aires), 4971–4974.

Barcroft, H., Edholm, O. G., McMichael, J., and Sharpy-Schafer, E. P. (1944). Posthaemorrhagic fainting: study by cardiac output and forearm flow. *Lancet* 15, 489–491.

Botero, M., Kirby, D., Lobato, E. B., Staples, E. D., and Gravenstein, N. (2004). Measurement of cardiac output before and after cardiopulmonary bypass: comparison among aortic transit-time ultrasound, thermodilution, and noninvasive partial CO_2 rebreathing. *J. Cardiothorac. Vasc. Anesth.* 18, 563–572.

Frank, O. (1930). Schätzung des Schlagvolumens des mensch-lichen Herzens auf Grund der Wellen und Windkesselthe-orie. *Zeitschrift fur Biologie* 90, 405–409.

Ganz, W., Donoso, R., Marcus, H. S., Forrester, J. S., and Swan, H. J. (1971). A new technique for measurement of cardiac output by thermodilution in man. *Am. J. Cardiol.* 27, 392–396.

Heldt, T. (2006). Continuous blood pressure-derived cardiac output monitoring-should we be thinking long term? *J. Appl. Physiol.* 101, 373–374.

Ihlen, H., Amlie, J. P., Dale, J., Forfang, K., Nitter-Hauge, S., Otterstad, J. E., Simonsen, S., and Myhre, E. (1984). Determination of cardiac output by Doppler echocardiography. *Br. Heart J.* 51, 54–60.

Ishihara, H., Okawa, H., Tanabe, K., Tsubo, T., Sugo, Y., Akiyama, T., and Takeda, S. (2004). A new noninvasive continuous cardiac output trend solely utilizing routine cardiovascular monitors. *J. Clin. Monit. Comput.* 18, 313–320.

Jansen, J. R. C., Wesseling, K. H., Settels, J. J., and Schreuder, J. J. (1990). Continuous cardiac output monitoring by pulse contour during cardiac surgery. *Eur. Heart J.* 11, 26–32.

Jansen, J. R. C., Schreuder, J. J., Mulier, J. P., Smith, N. T., Settels, J. J., and Wesseling, K. H. (2001). A comparison of cardiac output derived from the arterial pressure wave against thermodilution in cardiac surgery patients. *Br. J. Anesth.* 87, 212–222.

Liljestrand, G., and Zander, E. (1928). Vergleichende bestimmung des minutenvolumens des herzens beim menschen mittels der stickoxydulmethode und durch blutdruckmessung. *Res. Exp. Med.* 59, 105–122.

Manecke, G. R. Jr., Brown, J. C., Landau, A. A., Kapelanski, D. P., St. Laurent, C. M., and Auger, W. R. (2002). An unusual case of pulmonary artery catheter malfunction. *Anesth. Analg.* 95, 302–304.

Martin, J. F., Volfson, L. B., Kirzon-Zolin, V. V., and Schukin, V. G. (1994). Application of pattern recognition and image classification techniques to determine continuous cardiac output from the arterial pressure waveform. *IEEE Trans. Biomed. Eng.* 41, 913–920.

Mukkamala, R., Reisner, A. T., Hojman, H. M., Mark, R. G., and Cohen, R. J. (2006). Continuous cardiac output monitoring by peripheral blood pressure waveform analysis. *IEEE Trans. Biomed. Eng.* 53, 459–467.

Parlikar, T. A., Heldt, T., Ranade, G. V., and Verghese, G. C. (2007). Model-based estimation of cardiac output and total peripheral resistance. *Comput. Cardiol.* 34, 379–382.

Redling, J. D., and Akay, M. (1997). Noninvasive cardiac output estimation: a preliminary study. *Biol. Cybern.* 77, 111–122.

Reisner, A. T., Xu, D., Ryan, K. L., Convertino, V. A., Rickards, C. A., and Mukkamala, R. (2011). Comparison of cardiac output by blood pressure waveform analysis methods during experimental hypovolemia and resuscitation. *Br. J. Anesth.* 106, 23–30.

Richter, H. A., and Mittermayer, C. H. (1984). Volume elasticity, modulus of elasticity and compliance of normal and arteriosclerotic human aorta. *Biorheology* 21, 723–734.

Siegel, L. C., and Pearl, R. G. (1992). Noninvasive cardiac output measurement: troubled technologies and troubled studies. *Anesth. Analg.* 74, 790–792.

Suttner, S., Schöllhorn, T., Boldt, J., Mayer, J., Röhm, K. D., Lang, K., and Piper, S. N. (2006). Noninvasive assessment of cardiac output using thoracic electrical bioimpedance in hemodynamically stable and unstable patients after cardiac surgery: a comparison with pulmonary artery thermodilution. *Intensive Care Med.* 32, 2053–2058.

Welkowitz, W., Cui, Q., Qi, Y., and Kostis, J. B. (1991). Noninvasive estimation of cardiac output. *IEEE Trans. Biomed. Eng.* 38, 1100–1105.

Xu, D., Oliver, N. B., and Mukkamala, R. (2009). Cardiac output and left atrial pressure monitoring by right ventricular pressure waveform analysis for potential implantable device application. *IEEE Trans. Biomed. Eng.* 56, 2335–2339.

Zoremba, N., Bickenbach, J., Krauss, B., Rossaint, R., Kuhlen, R., and Schälte, G. (2007). Comparison of electrical velocimetry and thermodilution techinques for the measurement of cardiac output. *Acta Anaesthesiol. Scand.* 51, 1314–1319.

Conflict of Interest Statement: The authors declare that the research was conducted in the absence of any commercial or financial relationships that could be construed as a potential conflict of interest.

Received: 16 May 2012; accepted: 10 July 2012; published online: 25 July 2012.
*Citation: Fazeli N and Hahn J-O (2012) Estimation of cardiac output and peripheral resistance using square-wave-approximated aortic flow signal. Front. Physio. **3**:298. doi: 10.3389/fphys.2012.00298*
This article was submitted to Frontiers in Computational Physiology and Medicine, a specialty of Frontiers in Physiology.

frontiers in
PHYSIOLOGY

ORIGINAL RESEARCH ARTICLE
published: 09 March 2012
doi: 10.3389/fphys.2012.00045

Modulation of the sympatho-vagal balance during sleep: frequency domain study of heart rate variability and respiration

Ramona Cabiddu[1], Sergio Cerutti[1]*, Geoffrey Viardot[2], Sandra Werner[2] and Anna M. Bianchi[1]

[1] *Department of Biomedical Engineering, Politecnico di Milano, Milano, Italy*
[2] *Forenap R&D, Rouffach, France*

Edited by:
Riccardo Barbieri, Harvard Medical School, USA

Reviewed by:
Ramakrishna Mukkamala, Michigan State University, USA
Thomas Penzel, Charite Universitätsmedizin Berlin, Germany

***Correspondence:**
Sergio Cerutti, Department of Biomedical Engineering, Politecnico di Milano, Piazza L. da Vinci 32, Milano 20133, Italy.
e-mail: sergio.cerutti@polimi.it

Sleep is a complex state characterized by important changes in the autonomic modulation of the cardiovascular activity. Heart rate variability (HRV) greatly changes during different sleep stages, showing a predominant parasympathetic drive to the heart during non-rapid eye movement (NREM) sleep and an increased sympathetic activity during rapid eye movement (REM) sleep. Respiration undergoes important modifications as well, becoming deeper and more regular with deep sleep and shallower and more frequent during REM sleep. The aim of the present study is to assess both autonomic cardiac regulation and cardiopulmonary coupling variations during different sleep stages in healthy subjects, using spectral and cross-spectral analysis of the HRV and respiration signals. Polysomnographic sleep recordings were performed in 11 healthy women and the HRV signal and the respiration signal were obtained. The spectral and cross-spectral parameters of the HRV signal and of the respiration signal were computed at low frequency and at breathing frequency (high frequency, HF) during different sleep stages. Results attested a sympatho-vagal balance shift toward parasympathetic modulation during NREM sleep and toward sympathetic modulation during REM sleep. Spectral analysis of the HRV signal and of the respiration signal indicated a higher respiration regularity during deep sleep, and a higher parasympathetic drive was also confirmed by an increase in the coherence between the HRV and the respiration signal in the HF band during NREM sleep. Our findings about sleep stage-dependent variations in the HRV signal and in the respiratory activity are in line with previous evidences and confirm spectral analysis of the HRV and the respiration signal to be a suitable tool for investigating cardiac autonomic modulation and cardio-respiratory coupling during sleep.

Keywords: heart rate variability signal, respiration, autonomic modulation, sympatho-vagal balance, sleep

INTRODUCTION

Although cardiac automaticity is intrinsic to various pacemaker tissues, it is well established that the heart rate variability (HRV), i.e., the oscillation in the interval between consecutive heart beats (RR intervals), is under the control of the autonomic nervous system (ANS), the main regulation circuit of internal body functions (Pagani et al., 1986; Vanderlei et al., 2009). Thus, the study of the HRV represents one of the most reliable and widely used tools to investigate the cardiac autonomic modulation (Task Force of the European Society of Cardiology and the North American Society of Pacing and Electrophysiology, 1996). HRV measurements, thanks to their relatively easy derivation and non-invasivity, are useful to provide additional valuable insight into physiological and pathological conditions (Pumprla et al., 2002). By analyzing the HRV in the time and in the frequency domains, information about autonomous activity can be obtained; three main spectral components can be identified on the HRV signal spectrum: very low frequency (VLF: 0.01–0.04 Hz), low frequency (LF: 0.04–0.15 Hz), and high frequency (HF: 0.15–0.4 Hz) components. The HF is considered as a quantitative marker of parasympathetic activity, while in the LF frequency band, both sympathetic and parasympathetic contributions have been recognized. However, as the power in the LF band always increases with sympathetic stimulation, a rise in the LF band is considered as a marker of a sympathetic drive to the heart. The LF/HF ratio is therefore thought to reflect the sympatho-vagal balance controlling the heart rate (HR; Rajendra et al., 2006). Physiological interpretation of the VLF component has not been completely elucidated yet (Task Force of the European Society of Cardiology and the North American Society of Pacing and Electrophysiology, 1996), but it seems to be related to slow regulation mechanisms that cannot be studied in the time intervals typically considered for the spectral analysis of the HRV signal.

The distribution of the power and the central frequency of the HRV spectral components are not fixed, but vary in relation to changes in autonomic modulation of the HR and depending on the central nervous system state.

In recent years, a growing interest has been manifested on the cardiovascular control during sleep, also given the fact that many sleep disorders, including insomnia and sleep apnea, have been

proved to be associated with cardiovascular disorders (Caples et al., 2007). Sleep is a complex state characterized, in physiological conditions, by important changes in the autonomic regulation of the cardiovascular activity (Viola et al., 2011). HRV is largely affected during sleep by sleep stage organization: specifically, evidence suggests a predominant parasympathetic drive to the heart and a reduced sympathetic efferent vasomotor tone during non-rapid eye movement (NREM) sleep and an increased sympathetic modulation, with remarkable fluctuations between parasympathetic and sympathetic influences, during rapid eye movement (REM) sleep (Scholz et al., 1997; Lanfranchi et al., 2007).

Respiration undergoes important modifications during sleep as well, becoming deeper and more regular with synchronization of sleep (deep sleep) and shallower and more frequent during REM sleep (Lanfranchi et al., 2007). The association between cardiac and respiratory rhythms has been widely recognized (Kabir et al., 2010). Respiratory sinus arrhythmia (RSA), which consists in rhythmic HR modifications that oscillate around the respiratory frequency, has been reported in healthy humans (Lotric and Stefanovska, 2000), both during wakefulness and sleep (Cysarz et al., 2004). It is one of the main contributors to HRV, whose spectral analysis typically reveals a HF component centered around the respiratory frequency (Penttilä et al., 2001). Although the mechanisms underlying the cardio-respiratory interaction and its physiological significance have not been elucidated yet, there is clinical evidence that reduced RSA is a prognostic indicator for cardiac mortality (Casolo et al., 1992). The aim of the present study was to assess autonomic cardiac regulation, respiratory variations, and cardio-respiratory coupling during different sleep stages and along the whole night in healthy subjects, using spectral analysis of HRV and respiration variability signals.

MATERIALS AND METHODS

SUBJECTS

Eleven healthy women, with age ranging between 18 and 45 years, participated in the study. None of them suffered from any psychiatric disorders, neither did any of them have a history of, or family history of psychiatric disorders. None of them was undergoing chronic medication. All participants provided their informed and written consent to participate in the study.

POLYSOMNOGRAPHIC ACQUISITION

The acquisition protocol was implemented within the PSYCHE European project and performed at Forenap R&D sleep laboratory. For each subject several signals were recorded simultaneously through standard polysomnography during a night of sleep. The electrocardiogram (ECG) and the respiratory activity were recorded with a sampling rate of 256 Hz. The electroencephalogram (EEG), the electrooculogram (EOG), and the electromyogram (EMG) were also recorded. The study was approved by the local independent Ethical Committee.

SIGNAL PROCESSING

For each subject the hypnogram was obtained by visual scoring performed on the EEG, EOG, and EMG signals by an expert physician according to the standardized procedure presented in the American Academy of Sleep Medicine (AASM) Manual for the Scoring of Sleep and Associated Events (Iber et al., 2007). Concerning sleep stages visual scoring, these new rules are intended to replace those introduced in 1968 by Rechtschaffen and Kales and worldwide accepted. According to the AASM classification, sleep stages S1 to S4 are referred to as N1, N2, and N3, with N3 comprising slow-wave sleep stages S3 and S4. REM and wakefulness states are referred to as stage R and stage W, respectively. Following the AASM indications, wakefulness and sleep stages were scored by 30-s epochs.

The RR-interval signal was extracted from the ECG signal. Peaks were detected from the ECG through the Pan–Tompkins algorithm (Pan and Tompkins, 1985), which reliably recognizes QRS complexes based upon the analyses of the signal slope, amplitude, and width. As the original ECG signal might contain outliers due to movement, noise, ectopic beats, or arrhythmias, in order to identify and eliminate them, the following procedure was performed: the ECG derived RR sequence was analyzed and samples were considered as outliers when the following condition was met:

$$\left|\mathrm{RR}i - \mathrm{Average}_{100}\right| > 5 * \mathrm{Std}_{100}$$

where RR_i is the ith sample in the tachogram and $\mathrm{Average}_{100}$ and Std_{100} are the mean and the SD values, respectively, of the previous 100 samples without outliers. A filtered signal was obtained by applying a moving average filter with a 1000 sample window to the original RR sequence and identified outliers were replaced with the value of the corresponding sample in the filtered RR sequence (Kemper et al., 2007).

The respirogram was extracted from the respiration signal by sampling it in correspondence of each R peak identified in the ECG (Baselli et al., 1988).

ANALYSIS

Stationary and free of artifacts signal portions were manually selected within different sleep stages on both the tachogram and the respirogram; autoregressive (AR) analysis was performed on each portion of the signals in order to obtain an AR model, whose general expression is as follows:

$$y(t) = \sum_{k=1}^{p} a_k y(t-k) + \varepsilon(t)$$

where $y(t)$ is the series under investigation, a_k are the autoregressive coefficients and $\varepsilon(t)$ is the residual term, whose whiteness was always verified.

The model order was chosen using the AKAIKE information criterion (AIC) and the model coefficients were obtained using the least squares method based upon the Yule–Walker equations (Kay and Marple, 1981).

The AR model was used to calculate the power spectral density (PSD) of each signal portion, which can be expressed as follows:

$$PSD(\omega) = |H(\omega)|^2\sigma^2 = \frac{\sigma^2\Delta t}{\left|1 + \sum_{k=1}^{N} a_k e^{-j\omega k}\right|^2} = \frac{C(z)^2\sigma^2\Delta t}{\left|\prod (z - p_k)\right|^2}$$

where $H(\omega)$ is the model transfer function, z is defined as $exp(2\pi ifT)$, $C(z)$ is the function bearing the zeros of the system, Δt is the sampling period and p_k are the poles of the process. The poles were identified in order to decompose the PSD into single spectral components, according to the method described in Baselli et al. (1997). The frequency and power values associated to each rhythmic component were calculated. The values of the normalized power of the LF and the HF components [LF n. u. and HF n. u., obtained as LF power/(total power–VLF power) and as HF power/(total power–VLF power)], along with the LF/HF ratio, were calculated for each analyzed signal portion of the tachogram, while for the respirogram only the main peak, corresponding to the HF component (respirogram HF%, obtained as HF power/respirogram total power), was taken into account.

For each stationary portion of the tachogram and of the respirogram a bivariate analysis was also performed, in order to obtain the cross-spectrum between the two variability signals.

According to the method described in Bianchi et al. (1990) a bivariate AR model was estimated, whose general expression is as follows:

$$\mathbf{Y}(t) = \sum_{k=1}^{p} \mathbf{A}(k)\mathbf{Y}(t-k) + \mathbf{W}(k)$$

where $\mathbf{Y}(t)$ is the vector of the series under investigation $y(t)$ and $x(t)$, $\mathbf{A}$ is the autoregression coefficient matrix and $\mathbf{W}(t)$ is the vector of the residual terms $\varepsilon(t)$ and $\eta(t)$.

The AR bivariate model was used to calculate the cross-spectrum of each signal portion, which can be expressed as follows:

$$\mathrm{PSD}_{xy}(\omega) = \mathrm{PSD}_{yx}(\omega) = X(\omega)Y*(\omega)$$

where $X(\omega)$ and $Y(\omega)$ are the autospectra of the signals.

The quadratic coherence between the signals in the LF and in the HF bands was calculated as:

$$K^2_{xy}(f) = \frac{\left|\mathrm{PSD}_{xy}(f)\right|^2}{\left|\mathrm{PSD}_x(f)\right| \left|\mathrm{PSD}_y(f)\right|}$$

where the cross-spectrum between the signals is normalized with regard to the signals' PSDs. The percentages of coherent and not-coherent power between the signals were calculated for each analyzed signal portion. An example of signals, spectra, and cross-spectrum is illustrated in **Figure 1**. The parameters of interest (LF n. u., HF n. u., LF/HF ratio, HF band coherence, % of tachogram power coherent, and not-coherent with respiration) were studied within each sleep cycle and their average value was calculated on all subjects, for the whole night. For each subject the variation of the LF/HF ratio for the tachogram and the tachogram–respirogram coherence in the HF band were studied during the whole night in relation with the subject's hypnogram; average values over the whole night were also calculated on all subjects. Analysis of Variance (ANOVA) was performed on the data in order to identify statistically significant differences in the tachogram LF n. u., HF

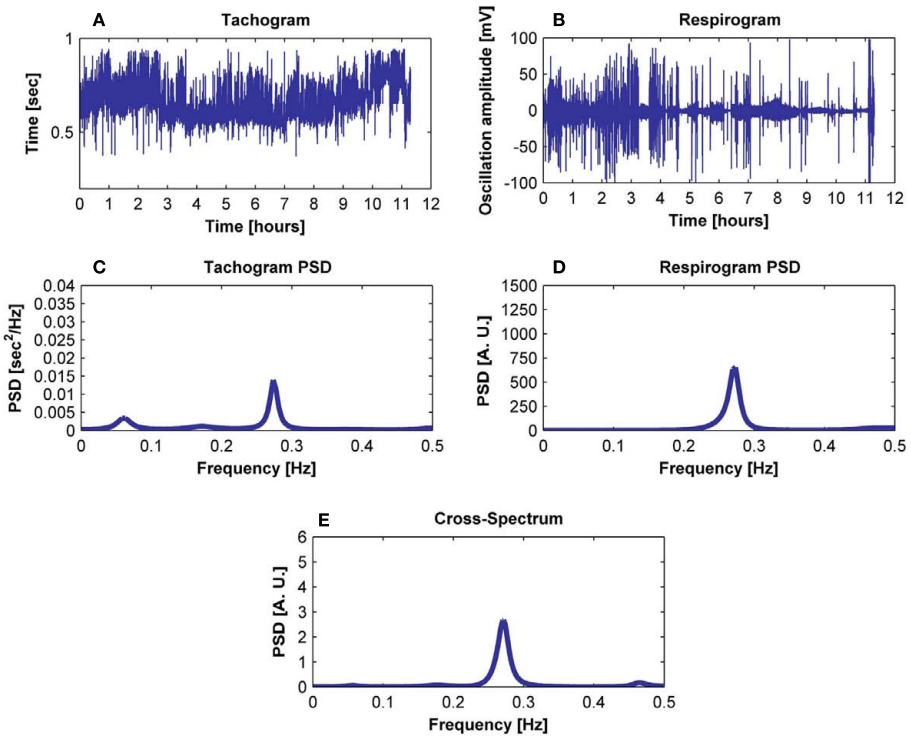

FIGURE 1 | Exemplification of the procedure followed to obtain (E) the cross-spectrum of (A) the tachogram and (B) the respirogram of a subject using (C) the tachogram spectrum and (D) the respirogram spectrum.

n. u. and LF/HF ratio values, in the respirogram HF% power and in the tachogram–respirogram coherence in the HF band values during deep NREM sleep (stage N3) and REM sleep stages, during the whole night.

RESULTS

The tachogram and respirogram were studied for each subject. A typical example of the signals for one subject, along with the hypnogram, is shown in **Figure 2**. PSDs for both the tachogram and the respirogram were calculated and the cross-spectrum between the two signals was computed for different sleep stages, according to the clinical classification summarized in the hypnogram. **Figure 3** shows the results obtained for a single subject, during wakefulness and different sleep stages, during the first NREM–REM cycle. The tachogram PSD shows that the LF component, larger during wakefulness, decreases during NREM sleep periods, and increases during the REM period; the HF component, after an initial decrease during sleep stage 1, increases during deep sleep stages, with the characteristic peak becoming narrower and more pronounced, and decreases during REM sleep, when the peak is only slightly visible. The VLF component, very large during wakefulness, decreases during NREM sleep, and greatly increases during REM sleep. A similar trend is followed by the respirogram PSDs, which show an increase in the HF component during NREM sleep, with the characteristic peak progressively becoming more pronounced as sleep deepness increases, and decreases during REM sleep, when a less pronounced and more widely distributed peak can be observed. The cross-spectra between the tachogram and the respirogram show an increase in the synchronization between the two signals during NREM periods, which reaches its highest value during sleep stage N3, and a decrease during the REM period, when synchronization is hardly visible. For the tachogram, the average values of the VLF power, LF n. u. and HF n. u., and of the LF/HF ratio were calculated for wakefulness and for each sleep stage, over the whole night, for each subject. The average values of the respirogram HF% power, of the maximum of the coherence between the tachogram and the respirogram in the HF band and of the coherent and not-coherent power percentages between the two signals were also calculated. The results for a typical subject, along with corresponding SD values, are plotted in **Figure 4**. The average values of the same parameters calculated for all subjects during wakefulness and different sleep stages, during the whole night, along with corresponding SD values, are plotted in **Figure 5**. The results obtained from the tachogram indicate that the LF n. u. and the HF n. u. show an opposite behavior, with the LF n. u. power increasing during sleep stage N1, progressively decreasing with synchronization of sleep and increasing during REM sleep and with the HF n. u. component decreasing during sleep stage N1, progressively increasing during deeper sleep stages and finally decreasing during REM sleep.

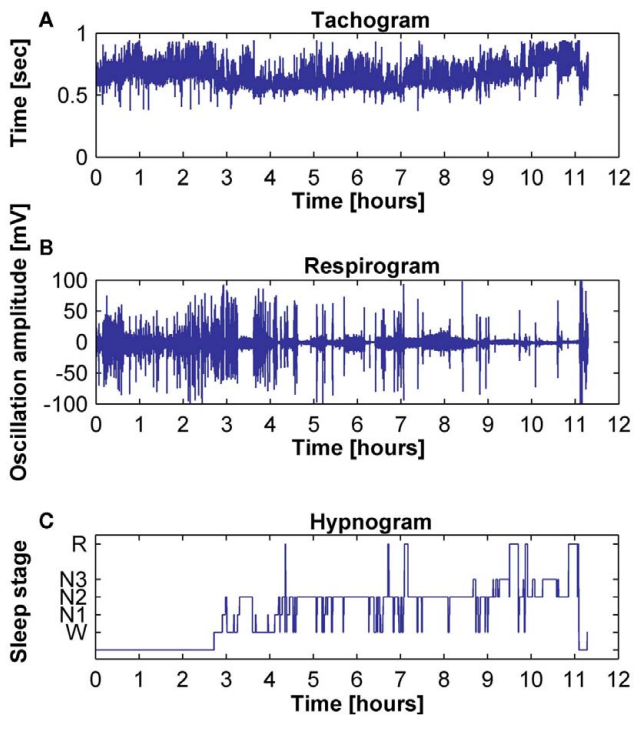

FIGURE 2 | Typical examples of (A) tachogram, (B) respirogram, and (C) hypnogram for a subject.

The LF/HF ratio, an index of sympathetic activation, after an initial increase during sleep stage N1, decreases with synchronization of sleep (deep sleep), and increases during REM sleep. The results obtained from the elaboration of the respirogram show that the HF% power increases during deep sleep and decreases during REM sleep.

The bivariate analysis results show that the coherence between the tachogram and the respirogram in the HF band progressively increases with synchronization of sleep and decreases during REM sleep.

The behavior of the LF/HF ratio and that of the coherence between the tachogram and the respirogram in the HF band were studied during the whole night to investigate the changes among the different sleep cycles. Results obtained on two different subjects are presented in **Figures 6** and **7**. For the first subject the tachogram LF/HF ratio increases during the REM phase of every sleep cycle and the increase becomes slightly more pronounced during the last part of the night, with the LF/HF ratio reaching its highest value during the last sleep cycle REM phase. An opposite behavior was observed for the second subject, with the LF/HF ratio increase during the REM stage becoming less pronounced as the night progresses. **Table 1** summarizes the average values of the tachogram normalized power in the LF and HF bands, of the LF/HF ratio, of the respirogram power in the HF band and of the tachogram–respirogram coherence in the HF band observed on all subjects during each stage of each sleep cycle. The results obtained from the ANOVA analysis between the values observed during deep NREM sleep periods (stage N3) and during REM sleep periods are also reported in **Table 1**.

DISCUSSION

During the past decades a number of studies demonstrated that fluctuations in the autonomic modulation on the HR are reflected

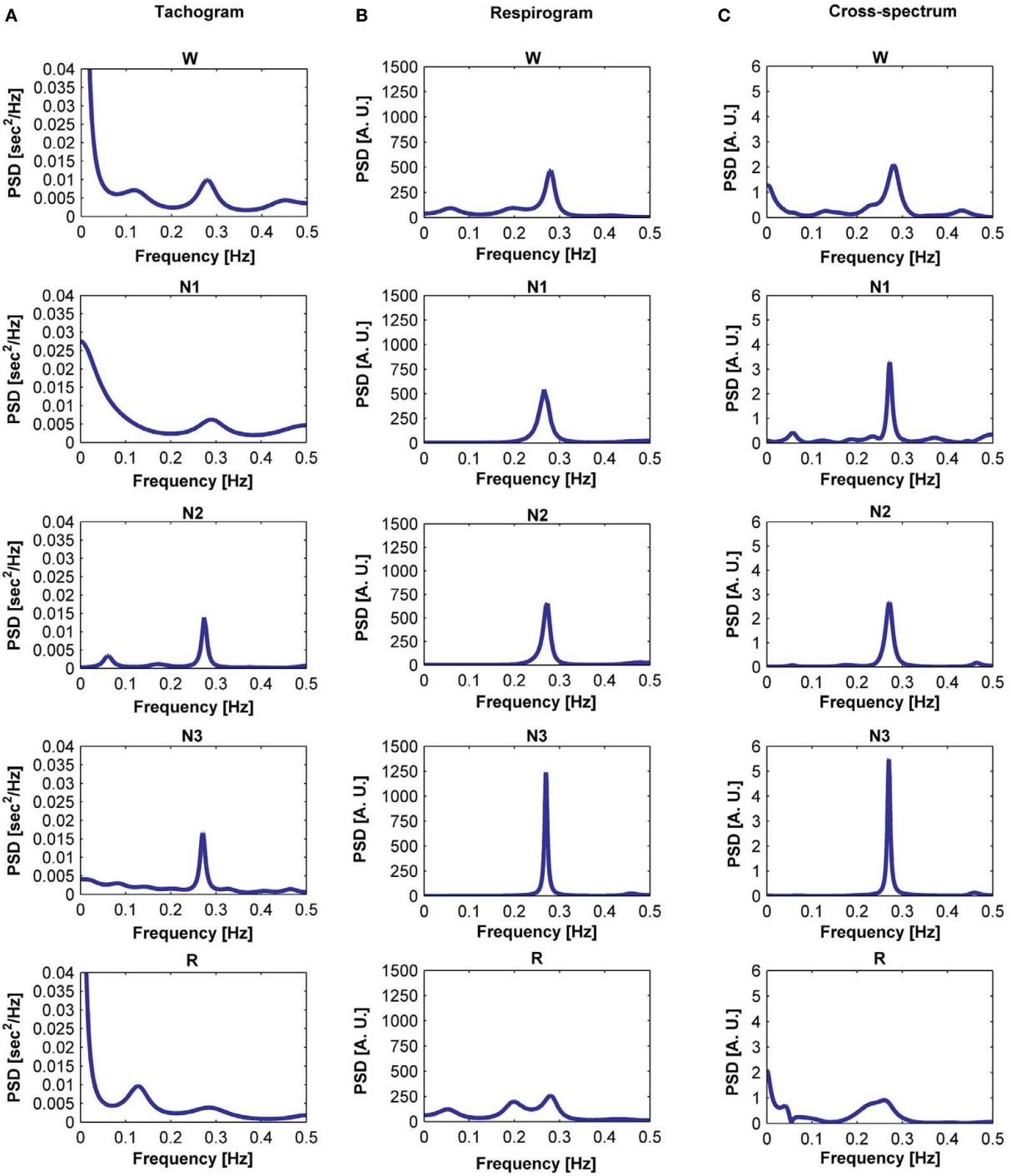

FIGURE 3 | Power spectral density (PSD) computed from the tachogram of a subject during wakefulness, sleep stages N1, N2, and N3 and REM sleep, during the first sleep cycle (A); PSD computed from the respirogram of the same subject during wakefulness, sleep stages N1, N2, and N3 and REM sleep, during the first sleep cycle (B); cross-spectrum between the tachogram and the respirogram of the same subject during wakefulness, sleep stages N1, N2, and N3 and REM sleep, during the first sleep cycle (C).

in changes in the spectral distribution of the HRV signal (Pagani et al., 1986; Task Force of the European Society of Cardiology and the North American Society of Pacing and Electrophysiology, 1996; Pumprla et al., 2002). This was confirmed to be an accurate indicator of the ANS activity, with the LF and the HF components being considered as representative of the sympathetic and parasympathetic activity, respectively, and the LF/HF ratio providing information about the sympatho-vagal balance (Task

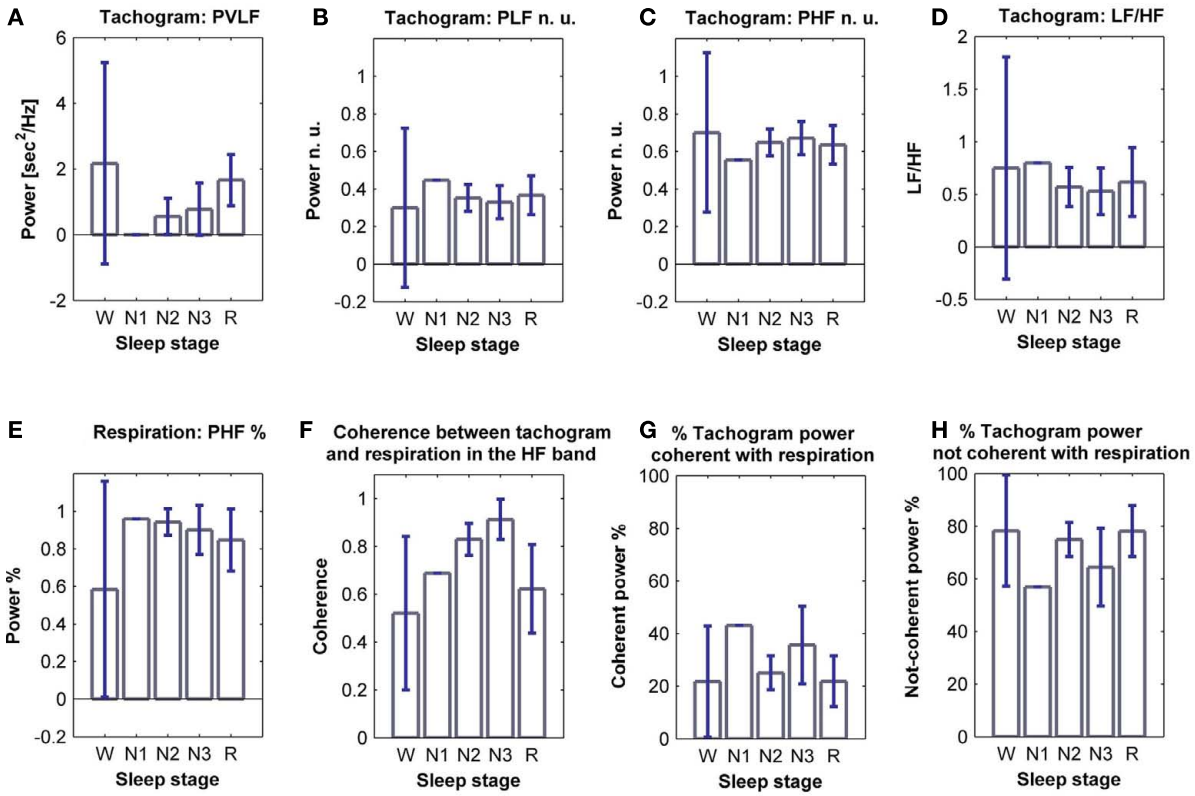

FIGURE 4 | Power of (A) VLF, (B) LF n. u. and (C) HF n. u. power, and (D) LF/HF ratio calculated from the tachogram of one subject, for wakefulness and the different sleep stages, for the whole night; (E) HF % power calculated from the respirogram of the same subject, for wakefulness and the different sleep stages, for the whole night; (F) coherence between the tachogram and the respirogram in the HF band, tachogram power % (G) coherent and (H) not-coherent with the respirogram, calculated on the same subject for wakefulness and the different sleep stages, for the whole night. SD values are indicated in blue.

Force of the European Society of Cardiology and the North American Society of Pacing and Electrophysiology, 1996; Rajendra et al., 2006).

In the present study the HRV signal and the respiration signal recorded from 11 healthy subjects during sleep were studied to investigate the effects of the autonomic nervous modulation during different sleep stages. Stage-dependent changes in the autonomic modulation of cardiac activity were observed.

The LF n. u. power decrease during deep sleep and increase during REM sleep suggested a diminished sympathetic modulation during deep sleep as compared to the wakefulness state and an augmented sympathetic tone toward the end of each sleep cycle. The HF n. u. behavior was indicative of an increased vagal drive to the heart during sleep, which decreased during REM sleep.

The sympatho-vagal balance drift toward the sympathetic component during deep sleep and toward the parasympathetic component during REM sleep was confirmed by the LF/HF ratio behavior. The LF/HF ratio decreased during sleep, reaching its minimum in correspondence of sleep stage N3 and increasing in correspondence of the REM phase. Altogether, the observed behavior is in accordance with previous studies (Scholz et al., 1997; Viola et al., 2011). The changes in the sympatho-vagal balance could be driven by oscillations in the metabolic demand during sleep, which markedly decreases during deep sleep (Wilde-Frenz and Schulz, 1983), and increases during REM sleep.

A bivariate analysis was conducted in order to take into account also the cardio-respiratory coupling during the different sleep stages. The correlation between cardiac and respiratory rhythms has been widely acknowledged (Kabir et al., 2010). The HF range of the HRV signal coincides with the respiratory rhythm; thus, the HF component is able to provide information about respiration frequency and its modulation (Kobayashi, 2009). The cross-spectrum between the tachogram and the respirogram presents a more pronounced peak centered in the HF band during sleep stages N1, N2, and N3 as compared to that of the wake state, whereas the peak practically disappears during REM sleep. The peak becoming more pronounced and more narrowly distributed during deep sleep stages is indicative of a more regular respiratory rhythm, synchronized with heart activity; the presence of a less pronounced peak during REM sleep indicates that a less regular respiratory rhythm and a less marked synchronization between respiration and heart rhythm characterize this sleep stage, in line with the results obtained from previous studies (Kabir et al., 2010). The coherence value between the tachogram and the respirogram in the HF band increases during deep sleep and decreases during REM sleep. This confirms that a more pronounced synchronization

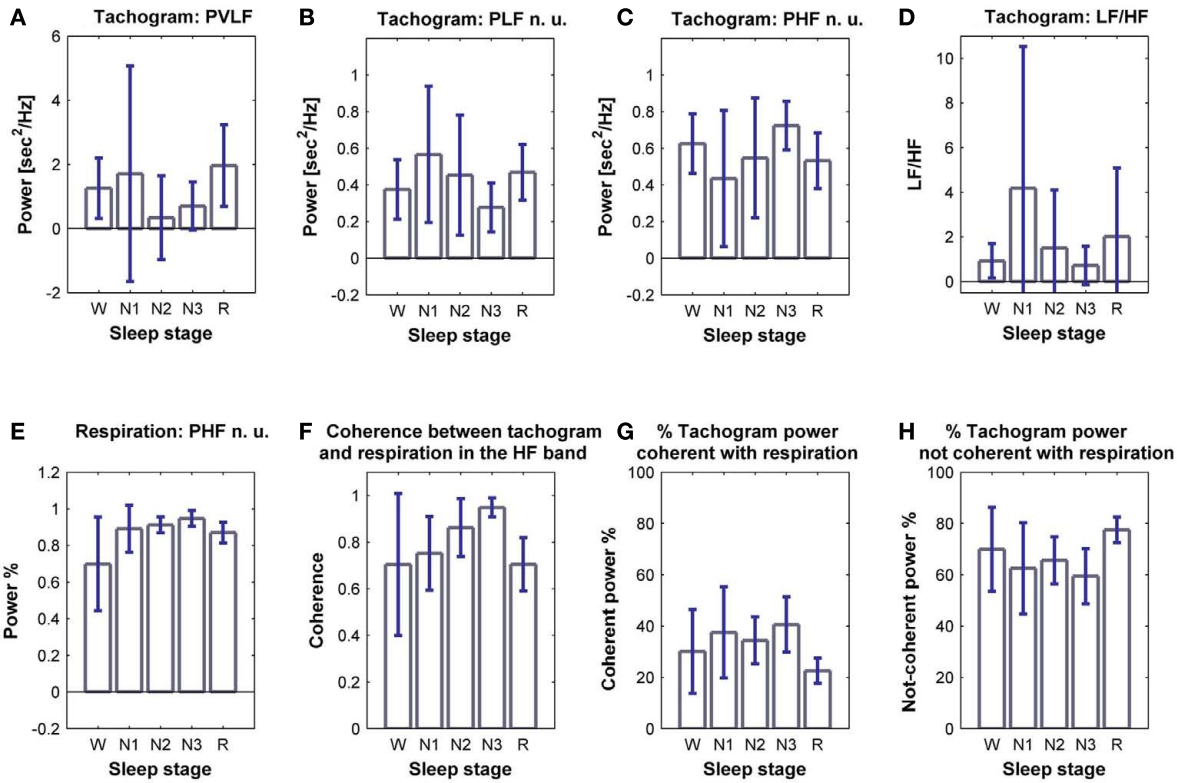

FIGURE 5 | Average power of (A) VLF, (B) LF n. u. and (C) HF n. u. power, and (D) LF/HF ratio calculated from the tachogram, on all subjects, for wakefulness and the different sleep stages, for the whole night; (E) average HF % power calculated from the respirogram, on all subjects, for wakefulness and the different sleep stages, for the whole night; (F) coherence between the tachogram and the respirogram in the HF band, tachogram power % (G) coherent and (H) not-coherent with the respirogram, calculated on all subjects for wakefulness and the different sleep stages, for the whole night. SD values are indicated in blue.

between respiration and heart beat is acquired with progression of sleep, with them becoming less synchronized during the REM phase, in accordance with a previous study (Unbehaun et al., 1996). Cardiac and respiratory rhythms have been long known to interact with each other and the investigation of their synchronization can provide useful indications about the way they interact. Synchronization was demonstrated to change during specific states, such as during mechanical ventilation (Mangin et al., 2009), anesthesia (Galletly and Larsen, 2001), physical exercise (Kenwright et al., 2008), and sleep (Kabir et al., 2010). Cardio-respiratory coordination during sleep changes in pathological conditions, as demonstrated in patients affected by Obstructive Sleep Apnea (Kabir et al., 2010) or Sleep Disordered Breathing (Guo et al., 2011). Furthermore, it changes depending on the general health status of a subject, resulting, e.g., more pronounced in athletes than in non-athletes (Kenwright et al., 2008). Thus, although the functional role and physiological origin of such interaction remain uncertain, synchronization analysis could be used as a tool to obtain information about the health status of an individual. To summarize, strong evidence was found of a drift of the sympatho-vagal balance toward the parasympathetic activity during deep sleep and toward the sympathetic activity during REM sleep, in line with previous experimental evidence (Scholz et al., 1997; Lanfranchi et al., 2007). Regularization of respiration was found to go along with synchronization of sleep, with respiration becoming more irregular during REM sleep.

A statistically significant difference (p-value ≤ 0.05) was found between the values of the tachogram normalized power in the LF and HF bands, of the tachogram LF/HF ratio values, of the respirogram % power in the HF band and of the tachogram–respirogram coherence in the HF band values recorded during deep sleep NREM periods and REM sleep periods, during the whole night, as the ANOVA results show. The global results presented in **Table 1** show that, with progression of sleep, sleep stage N1 tends to disappear, suggesting a better quality of sleep is progressively reached along the night. Anyway, a clear trend in the sympatho-vagal balance during the night could not be identified for the whole group: a shift toward the sympathetic component during REM sleep was more evident during the final sleep cycles for some subjects and during the initial ones for others. Disagreement exists about whether the sympathetic drive to the heart during REM sleep becomes more or less intense along the night (Cajochen et al., 1994; Marciani et al., 2003; Lanfranchi et al., 2007). Discordant results might be due to differences in experimental protocols and analysis methodologies and the sympatho-vagal behavior with progression of the night needs to be further investigated.

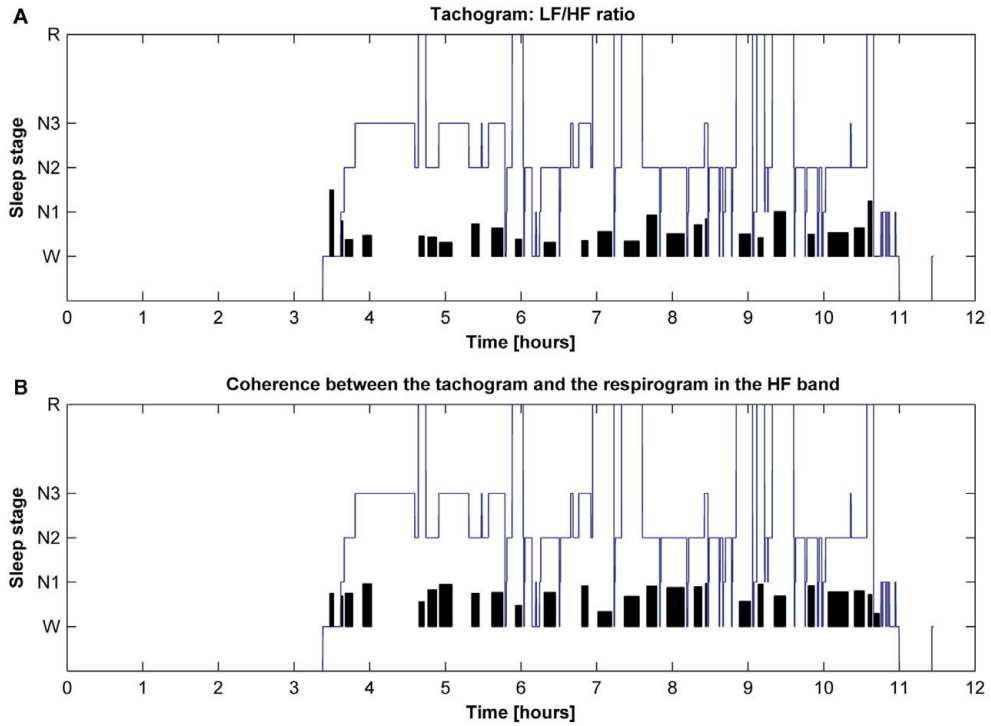

FIGURE 6 | Hypnogram of one subject with indication in black of (A) the trend of the tachogram LF/HF ratio for the whole night and of (B) the trend of the coherence between the tachogram and the respirogram in the HF band.

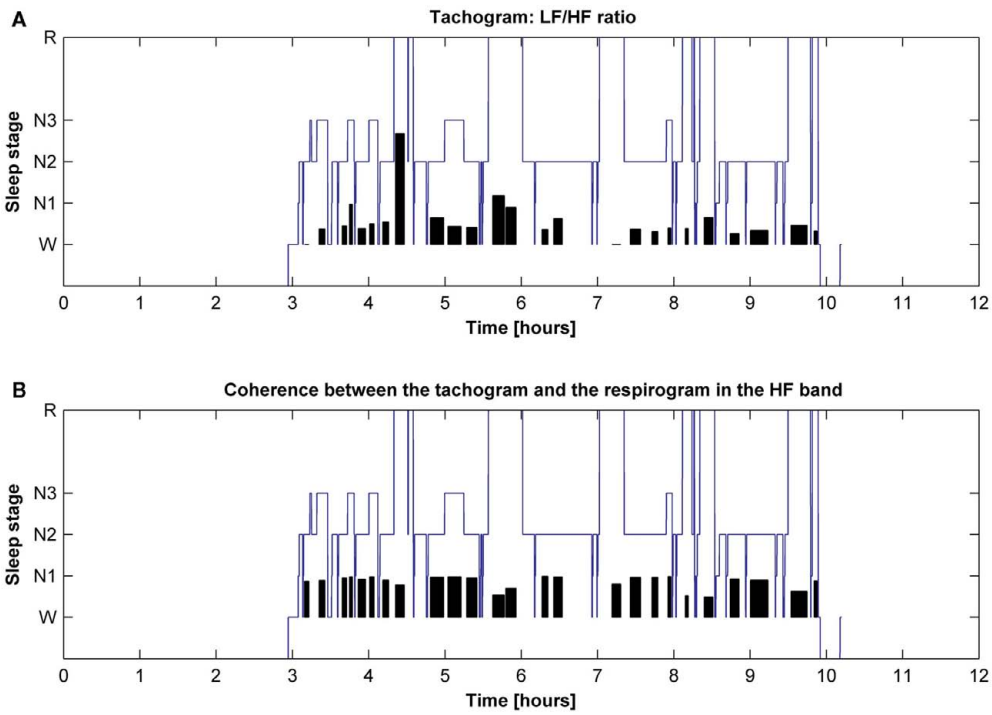

FIGURE 7 | Hypnogram of one subject with indication in black of (A) the trend of the tachogram LF/HF ratio for the whole night and of (B) the trend of the coherence between the tachogram and the respirogram in the HF band.

Table 1 | Average values of the tachogram normalized power in the LF and HF bands, of the LF/HF ratio values, of the respirogram % power in the HF band and of the tachogram–respirogram coherence in the HF band values observed on all subjects during each stage of each sleep cycle.

Sleep cycle	Sleep Stage	Tachogram LF n. u. (mean ± SD)	Tachogram HF n. u. (mean ± SD)	Tachogram LF/HF ratio (mean ± SD)	Respirogram HF% power (mean ± SD)	Coherence in HF band (mean ± SD)
1	W	0.371 ± 0.04	0.645 ± 0.04	0.905 ± 0.84	0.784 ± 0.07	0.767 ± 0.30
	N1	0.565 ± 0.14	0.579 ± 0.08	4.183 ± 6.35	0.890 ± 0.02	0.751 ± 0.16
	N2	0.936 ± 4.09	0.076 ± 4.11	0.882 ± 1.99	0.904 ± 0.02	0.814 ± 0.14
	N3	0.270 ± 0.02	0.741 ± 0.02	0.439 ± 0.40	0.963 ± 0.00	0.949 ± 0.06
	R	0.592 ± 0.03	0.408 ± 0.03	2.156 ± 1.53	0.904 ± 0.02	0.816 ± 0.12
2	W	0.586 ± 0.08	0.414 ± 0.03	1.538 ± 0.77	0.306 ± 0.05	0.381 ± 0.34
	N1	0	0	0	0	0
	N2	0.480 ± 0.15	0.528 ± 0.15	2.013 ± 3.04	0.895 ± 0.01	0.867 ± 0.15
	N3	0.392 ± 0.02	0.706 ± 0.05	0.620 ± 0.62	0.938 ± 0.01	0.962 ± 0.04
	R	0.484 ± 0.03	0.587 ± 0.06	1.361 ± 1.35	0.899 ± 0.00	0.686 ± 0.14
3	W	0	0	0	0	0
	N1	0	0	0	0	0
	N2	0.367 ± 0.05	0.656 ± 0.05	1.546 ± 3.36	0.915 ± 0.01	0.875 ± 0.12
	N3	0.400 ± 0.10	0.766 ± 0.02	1.290 ± 1.92	0.932 ± 0.02	0.914 ± 0.07
	R	0.550 ± 0.05	0.450 ± 0.07	2.903 ± 5.82	0.904 ± 0.00	0.689 ± 0.16
4	W	0	0	0	0	0
	N1	0	0	0	0	0
	N2	0.379 ± 0.02	0.621 ± 0.02	0.855 ± 0.81	0.921 ± 0.01	0.885 ± 0.21
	N3	0.329 ± 0.10	0.671 ± 0.10	0.666 ± 0.57	0.938 ± 0.01	0.965 ± 0.03
	R	0.474 ± 0.02	0.549 ± 0.02	1.084 ± 0.68	0.787 ± 0.03	0.747 ± 0.16
5 (Present in only 10 subjects)	W	0	0	0	0	0
	N1	0	0	0	0	0
	N2	0.316 ± 0.01	0.719 ± 0.02	0.527 ± 0.27	0.917 ± 0.00	0.867 ± 0.11
	N3	0.217 ± 0.00	0.783 ± 0.00	0.273 ± 0.02	0.996 ± 0.00	0.966 ± 0.07
	R	0.414 ± 0.02	0.603 ± 0.02	0.799 ± 0.45	0.777 ± 0.09	0.689 ± 0.14
Stage N3-REM ANOVA		*p*-Value = 0.0048	*p*-Value = 0.0012	*p*-Value = 0.0445	*p*-Value = 0.0143	*p*-Value = 3.339e-005

Parameters were assigned value "0" when the corresponding sleep stage was not identified within a sleep cycle (values equal to "0" were not considered in the subsequent ANOVA analysis). The p-values obtained from the ANOVA analysis between the values observed during deep NREM sleep periods (stage N3) and during REM sleep periods are reported.

In the present work sophisticated biosignal processing methods were applied to assess autonomic cardiac and respiratory regulation during different sleep stages. Spectral analysis has long been applied to the HRV signal; the authors presented the results of the application of spectral analysis methods to the respiration signal, aimed to investigate the cardiopulmonary coupling during sleep.

Our findings affirm spectral analysis of HRV and respiration signals to be a useful tool to non-invasively and accurately investigate the autonomous modulation of not only the cardiac activity, but also of the respiratory activity and to assess the cardio-respiratory coupling variations during sleep.

ACKNOWLEDGMENTS

The research presented in this paper was supported by the EU project PSYCHE, Grant Agreement: 247777.

REFERENCES

Baselli, G., Cerutti, S., Civardi, S., Malliani, A., and Pagani, M. (1988). Cardiovascular variability signals: towards the identification of a closed-loop model of the neural control mechanisms. *IEEE Trans. Biomed. Eng.* 35, 1033–1046.

Baselli, G., Porta, A., Rimoldi, O., Pagani, M., and Cerutti, S. (1997). Spectral decomposition in multichannel recordings based on multivariate parametric identification. *IEEE Trans. Biomed. Eng.* 44, 1092–1101.

Bianchi, A., Bontempi, B., Cerutti, S., Gianogli, P., Comi, G., and Natali Sora, M. G. (1990). Spectral analysis of heart rate variability signal and respiration in diabetic subjects. *Med. Biol. Eng. Comput.* 28, 205–211.

Cajochen, C., Pischke, J., Aeschbach, D., and Borbely, A. A. (1994). Heart rate dynamics during human sleep. *Physiol. Behav.* 55, 769–774.

Caples, S. M., Garcia-Touchard, A., and Somers, V. K. (2007), Sleep-disordered breathing and cardiovascular risk. *Sleep* 30, 291–303.

Casolo, G. C., Stroder, P., Signorini, C., Calzolari, F., Zucchini, M., Balli, E., Sulla, A., and Lazzerini, S. (1992). Heart rate variability during the acute phase of myocardial infarction. *Circulation* 85, 2073–2079.

Cysarz, D., Bettermann, H., Lange, S., Geue, D., and van Leeuwen, P. (2004). A quantitative comparison of different methods to detect cardiorespiratory coordination during night-time sleep. *Biomed. Eng. Online* 3, 44.

Galletly, D. C., and Larsen, P. D. (2001). Inspiratory timing during anaesthesia: a model of cardioventilatory coupling. *Br. J. Anaesth.* 86, 777–788.

Guo, D., Peng, C. K., Wu, H. L., Mietus, J. E., Liu, Y., Sun, R. S., and Thomas, R. J. (2011). ECG-derived cardiopulmonary analysis of pediatric sleep-disordered breathing. *Sleep Med.* 12, 384–389.

Iber, C., Ancoli-Israel, S., Chesson, A. L., and Quan, S. F. (2007). *The AASM Manual for the Scoring of Sleep and Associated Events: Rules, Terminology, and Technical Specifications.* Westchester, IL: American Academy of Sleep Medicine.

Kabir, M. M., Dimitri, H., Sanders, P., Antic, R., Nalivaiko, E., Abbott, D., and Baumert, M. (2010). Cardiorespiratory phase-coupling is reduced in patients with obstructive sleep apnea. *PLoS ONE* 5, 10602. doi:10.1371/journal.pone.0010602

Kay, S. M., and Marple, S. L. (1981). Spectrum analysis: a modern perspective. *Proc. IEEE* 69, 1380–1429.

Kemper, K. J., Hamilton, C., and Atkinson, M. (2007). Heart rate variability: impact of differences in outlier identification and management strategies on common measures in three clinical populations. *Pediatr. Res.* 62, 337–342.

Kenwright, D. A., Bahraminasab, A., Stefanovska, A., and McClintock, P. V. (2008). The effect of low-frequency oscillations on cardiorespiratory synchronization: observations during rest and exercise. *Eur. Phys. J. B* 65, 425–433.

Kobayashi, H. (2009). Does paced breathing improve the reproducibility of heart rate variability measurements? *J. Physiol. Anthropol.* 28, 225–230.

Lanfranchi, P. A., Fradette, L., Gagnon, J. F., Colombo, R., and Montplaisir, J. (2007). Cardiac autonomic regulation during sleep in idiopathic REM sleep behavior disorder. *Sleep* 30, 1019–1025.

Lotric, M. B., and Stefanovska, A. (2000). Synchronization and modulation in the human cardiorespiratory system. *Physica A* 283, 451–461.

Mangin, L., Clerici, C., Similowski, T., and Poon, C. S. (2009). Chaotic dynamics of cardioventilatory coupling in humans: effects of ventilatory modes. *Am. J. Physiol. Regul. Integr. Comp. Physiol.* 296, R1088–R1097.

Marciani, M. G., Placidi, F., Aquilani, S., Romigi, A., Tombini, M., Massaro, M., Galante, A., and Iellamo, F. (2003). Sleep-related changes in baro reflex sensitivity and cardiovascular autonomic modulation. *J. Hypertens.* 21, 1555–1561.

Pagani, M., Lombardi, F., Guzzetti, S., Rimoldi, O., Furlan, R., Pizzinelli, P., Sandrone, G., Malfatto, G., Dell'Orto, S., Piccaluga, E., Turiel, M., Baselli, G., Cerutti, S., and Malliani, A. (1986). Power spectral analysis of heart rate and arterial pressure variabilities as a marker of sympatho-vagal interaction in man and conscious dog. *Circ. Res.* 59, 178–193.

Pan, J., and Tompkins, W. J. (1985). A real-time QRS detection algorithm. *IEEE Trans. Biomed. Eng.* 32, 230–236.

Penttilä, J., Helminen, A., Jartti, T., Kuusela, T., Huikuri, H. V., Tulppo, M. P., Coffeng, R., and Scheinin, H. (2001). Time domain, geometrical and frequency domain analysis of cardiac vagal outflow: effects of various respiratory patterns. *Clin. Physiol.* 21, 365–376.

Pumprla, J., Howorka, K., Groves, D., Chester, M., and Nolan, J. (2002). Functional assessment of heart rate variability: physiological basis and practical applications. *Int. J. Cardiol.* 84, 1–14.

Rajendra, A. U., Paul, J. K., Kannathal, N., Lim, C. M., and Suri, J. S. (2006). Heart rate variability: a review. *Med. Biol. Eng. Comput.* 44, 1031–1051.

Scholz, U. J., Bianchi, A. M., Cerutti, S., and Kubicki, S. (1997). Vegetative background of sleep: spectral analysis of the heart rate variability. *Physiol. Behav.* 62, 1037–1043.

Task Force of the European Society of Cardiology and the North American Society of Pacing and Electrophysiology. (1996). Heart rate variability. Standards of measurement, physiological interpretation and clinical use. *Eur. Heart J.* 17, 354–381.

Unbehaun, A., Mrowka, R., Schubert, E., Patzak, A., and Schwarz, V. (1996). Interaction of heart-rate fluctuations and respiration in 12 to 14-year-old children during sleeping and waking. *J. Auton. Nerv. Syst.* 57, 141–143.

Vanderlei, L. C., Pastre, C. M., Hoshi, R. A., Carvalho, T. D., and Godoy, M. F. (2009). Basic notions of heart rate variability and its clinical applicability. *Rev. Bras. Cir. Cardiovasc.* 24, 205–217.

Viola, A. U., Tobaldini, E., Chellappa, S. L., Casali, K. R., Porta, A., and Montano, N. (2011). Short-term complexity of cardiac autonomic control during sleep: REM as a potential risk factor for cardiovascular system in aging. *PLoS ONE* 6, e19002.doi:10.1371/journal.pone.0019002

Wilde-Frenz, J., and Schulz, H. (1983). Rate and distribution of body movements during sleep in humans. *Percept. Mot. Skills* 56, 275–283.

Conflict of Interest Statement: The authors declare that the research was conducted in the absence of any commercial or financial relationships that could be construed as a potential conflict of interest.

Received: 14 December 2011; accepted: 20 February 2012; published online: 09 March 2012.

Citation: Cabiddu R, Cerutti S, Viardot G, Werner S and Bianchi AM (2012) Modulation of the sympatho-vagal balance during sleep: frequency domain study of heart rate variability and respiration. Front. Physio. ***3****:45. doi: 10.3389/fphys.2012.00045*

This article was submitted to Frontiers in Computational Physiology and Medicine, a specialty of Frontiers in Physiology.

frontiers in
PHYSIOLOGY

ORIGINAL RESEARCH ARTICLE
published: 30 September 2011
doi: 10.3389/fphys.2011.00065

Increased non-Gaussianity of heart rate variability predicts cardiac mortality after an acute myocardial infarction

Junichiro Hayano[1]*†, Ken Kiyono[2]†, Zbigniew R. Struzik[3], Yoshiharu Yamamoto[3], Eiichi Watanabe[4], Phyllis K. Stein[5], Lana L. Watkins[6], James A. Blumenthal[6] and Robert M. Carney[7]

[1] *Department of Medical Education, Nagoya City University Graduate School of Medical Sciences, Nagoya, Japan*
[2] *College of Engineering, Nihon University, Koriyama, Japan*
[3] *Educational Physiology Laboratory, Graduate School of Education, University of Tokyo, Tokyo, Japan*
[4] *Division of Cardiology, Department of Internal Medicine, Fujita Health University School of Medicine, Toyoake, Japan*
[5] *Department of Medicine, Washington University School of Medicine, St. Louis, MO, USA*
[6] *Department of Psychiatry, Duke University Medical Center, Durham, NC, USA*
[7] *Department of Psychiatry, Washington University School of Medicine, St. Louis, MO, USA*

Edited by:
Riccardo Barbieri, Harvard Medical School, USA

Reviewed by:
Omer Berenfeld, University of Michigan, USA
Sarah S. Knox, West Virginia University School of Medicine, USA

****Correspondence:***
Junichiro Hayano, Department of Medical Education, Nagoya City University Graduate School of Medical Sciences, 1 Kawasumi, Mizuho-cho, Mizuho-ku, Nagoya 467-8601, Japan. e-mail: hayano@med.nagoya-cu.ac.jp

†Junichiro Hayano and Ken Kiyono have contributed equally to this work.

Non-Gaussianity index (λ) is a new index of heart rate variability (HRV) that characterizes increased probability of the large heart rate deviations from its trend. A previous study has reported that increased λ is an independent mortality predictor among patients with chronic heart failure. The present study examined predictive value of λ in patients after acute myocardial infarction (AMI). Among 670 post-AMI patients, we performed 24-h Holter monitoring to assess λ and other HRV predictors, including SD of normal-to-normal interval, very-low frequency power, scaling exponent α_1 of detrended fluctuation analysis, deceleration capacity, and heart rate turbulence (HRT). At baseline, λ was not correlated substantially with other HRV indices ($|r| < 0.4$ with either indices) and was decreased in patients taking β-blockers ($P = 0.04$). During a median follow-up period of 25 months, 45 (6.7%) patients died (32 cardiac and 13 non-cardiac) and 39 recurrent non-fatal AMI occurred among survivors. While all of these HRV indices but λ were significant predictors of both cardiac and non-cardiac deaths, increased λ predicted exclusively cardiac death (RR [95% CI], 1.6 [1.3–2.0] per 1 SD increment, $P < 0.0001$). The predictive power of increased λ was significant even after adjustments for clinical risk factors, such as age, diabetes, left ventricular function, renal function, prior AMI, heart failure, and stroke, Killip class, and treatment ([95% CI], 1.4 [1.1–2.0] per 1 SD increment, $P = 0.01$). The prognostic power of increased λfor cardiac death was also independent of all other HRV indices and the combination of increased λ and abnormal HRT provided the best predictive model for cardiac death. Neither λ nor other HRV indices was an independent predictor of AMI recurrence. Among post-AMI patients, increased λ is associated exclusively with increased cardiac mortality risk and its predictive power is independent of clinical risk factors and of other HRV predictors.

Keywords: heart rate variability, myocardial infarction, ambulatory ECG, sudden cardiac death, mortality, non-Gaussianity, prospective study, ENRICHD study

INTRODUCTION

Experimental models for sudden cardiac death after myocardial infarction (AMI) indicate that sympathetic stimulation under impaired reflex vagal antagonism provokes ventricular vulnerability to fibrillation during transient myocardial ischemia (Schwartz et al., 1984; Vanoli et al., 1991). Usefulness of the detection of autonomic dysfunction by heart rate variability (HRV) has been proposed for post-AMI risk stratification (Kleiger et al., 1987; La Rovere et al., 1998; Schmidt et al., 1999; Bauer et al., 2006). Most of HRV indices proposed, however, primarily reflect reduced or impaired vagal function (Camm et al., 1996; Marine et al., 2002; Bauer et al., 2006). In contrast, few HRV indices have been related to sympathetic function and their prognostic significance is still uncertain. For example, a decrease in low-frequency-to-high-frequency ratio, but not its increase, is associated with increased risk of mortality (Tsuji et al., 1994; Huikuri et al., 2000).

As a marker potentially related to sympathetic cardiac overdrive, we have recently proposed increased non-Gaussianity of HRV (Kiyono et al., 2008). Non-Gaussianity has been used in fluid dynamics for characterizing intermittency of turbulence (Castaing

Abbreviations: AC, acceleration capacity; AMI, acute myocardial infarction; CI, confidence interval; DC, deceleration capacity; DFA, detrended fluctuation analysis; ENRICHD, enhancing recovery in coronary heart disease; HF, high frequency; HRT, heart rate turbulence; HRV, heart rate variability; IRQ, inter quartile range; LF, low frequency; LF/HF, LF-to-HF ratio; PDF, probability density function; RR, relative risk; SD, standard deviation; SDNN, SD of all normal-to-normal intervals; TO, turbulence onset; TS, turbulence slope; ULF, ultra-low frequency; VLF, very-low frequency.

et al., 1990). When applied to analysis of HRV, it captures the occurrence of intermittent heart rate increments (Kiyono et al., 2004, 2007). In a cohort of chronic heart failure (Kiyono et al., 2008),we previously observed that the increased non-Gaussianity of HRV predicts increased risk of mortality, while none of the conventional HRV indices were predictive of death among these patients. In the present study, we sought to determine if increased non-Gaussianity of HRV in post-AMI patients is also associated with their increased mortality risk independent of clinical risk factors and of the established HRV predictors.

MATERIALS AND METHODS

STUDY PATIENTS

Patients admitted to the coronary care units of four of the eight clinical trial sites (Washington University, St. Louis, MO, USA; Duke University, Durham, NC, USA; Harvard University, Boston, MA, USA; Yale University, New Haven, CT, USA) of the enhancing recovery in coronary heart disease (ENRICHD) study (Berkman et al., 2003) for an attack of AMI between October 1997 and January 2000 were enrolled in this substudy. AMI was diagnosed if a patient had at least 2 of the following findings: chest pain for $\geq$20 min, creatine kinase $>$200 U/L, and ST-segment elevation of $\geq$0.1 mV in two or more limb leads or $\geq$0.2 mV in two or more contiguous precordial leads at the time of admission. The sample included 358 participants of the ENRICHD clinical trial who scored 10 or higher on the Beck Depression Inventory (BDI; Steeds et al., 2004) and 408 AMI control participants who were not randomized in the ENRICHD trial because they were not depressed (BDI $<$ 10), but were otherwise medically eligible for the trial. Patients were excluded if they: (1) had other life-threatening illnesses; (2) were too ill or logistically unable to participate; (3) had analyzable electrocardiographic data $<$22 h or sinus rhythm $<$80% of total recorded beats in Holter monitoring; (4) had atrial fibrillation, atrial flutter, or animplanted pacemaker or defibrillator; or (5) declined to provide informed written consent.

MEASUREMENTS

Holter electrocardiograms were recorded for 24 h within 28 (median [inter quartile range, IQR], 13 [6–19]) days after the index AMI. To assure standardization of the Holter recordings, we used Marquette Model 8500 monitors at each site. Holter recordings were scanned at the Heart Rate Variability Core laboratory at Washington University on a Marquette SXP Laser scanner with software version 5.8 (Marquette Electronics) using standard procedures. The labeled beat file was exported to a personal computer and a workstation for analysis of non-Gaussianity and other HRV indices.

ANALYSIS OF NON-GAUSSIANITY INDEX

This analysis is designed to detect intermittency of heart rate increment. The intermittent behavior of HRV is related to non-Gaussian probability distribution with marked fat tails and a peak around the mean value, indicative of a higher probability of the interspersed appearance of large and small increments than the Gaussian fluctuations. To quantify such non-Gaussian behavior, we calculated a non-Gaussianity index. The background and a mathematical description of the non-Gaussianity index have been reported previously (Kiyono et al., 2004, 2007). Briefly, this index has been derived from a method for analyzing multi-scale statistics of complex fluctuations, originally used for characterizing intermittency of hydrodynamic turbulence (alternating transition of a fluid regime between laminar flow and its breakdown into bursty disorganized eddies, occurring in a seemingly random manner at a variety of scales; Castaing et al., 1990).

The analysis of non-Gaussianity of HRV is divided into four steps. In step 1, time series of normal-to-normal R–R intervals are interpolated with a cubic spline function and resampled at an interval (Δt) of 250 ms (4 Hz), yielding interpolated time series $b(t)$ (**Figure 1**). After subtracting average interval b_{ave}, integrated time series $B(t)$ are obtained by integrating $b(t)$ over the entire length,

$$B(t) = \sum_{i=1}^{t/\Delta t} \{b(i\Delta t) - b_{\mathrm{ave}}\}.$$

In step 2, the local trend of $\{B(t)\}$ is eliminated by third-order polynomial that is fit to $\{B(t)\}$ within moving windows of length $2s$, where s is the scale of analysis. In step 3, intermittent deviation $\Delta_s B(t)$ is measured as the increment with a time lag s of the detrended time series $\{B^*(t)\}$. For instance, in a window from $T-s$ to $T+s$, the increments are calculated as

$$\Delta_s B(t) = \{B(t+s/2) - f_{\mathrm{fit}}(t+s/2)\} - \{B(t-s/2) - f_{\mathrm{fit}}(t-s/2)\}$$

where $T-s/2 \leq t < T+s/2$ and $f_{\mathrm{fit}}(t)$ is the polynomial representing the local trend of $B(t)$, of which the elimination assures the zero-mean probability density function in the next step. In step 4, $\Delta_s B$ is normalized by the SD to quantify the probability density function (PDF). Then, the non-Gaussianity index λ_s is estimated as

$$\lambda_s = \sqrt{\frac{2}{q(q-2)}\left[\ln\left(\frac{\sqrt{\pi}\langle|\Delta_s B|^q\rangle}{2^{q/2}}\right) - \ln\Gamma\left(\frac{q+1}{2}\right)\right]},$$

where $\langle|\Delta_s B|^q\rangle$ denotes an estimated value of the q-th order absolute moment of $\{\Delta_s B\}$. If the λ_s is close to zero, the observed PDF is close to a Gaussian distribution. On the other hand, a larger value of λ_s means that the observed PDF has fatter tails and a sharper peak in comparison with the Gaussian distribution. This λ_s was originally introduced as a parameter of a phenomenological model to describe non-Gaussian distributions in the study of intermittency of hydrodynamic turbulence (Castaing et al., 1990). Kiyono et al. (2007) further showed that the λ_s can be estimated by the above equation based on the q-th order absolute moment of a time series independently of q.

In the present study, we calculated the λ_s based on the 0.25th order moment ($q = 0.25$) to emphasize the center part of PDF and to reduce the effects of large outliers such as those by ectopic beats, if any, even after the correction. This implies that our non-Gaussianity index with $q = 0.25$ more strongly characterize speaked PDF around the center of the observed non-Gaussian distribution, differently from that with higher order moments, such

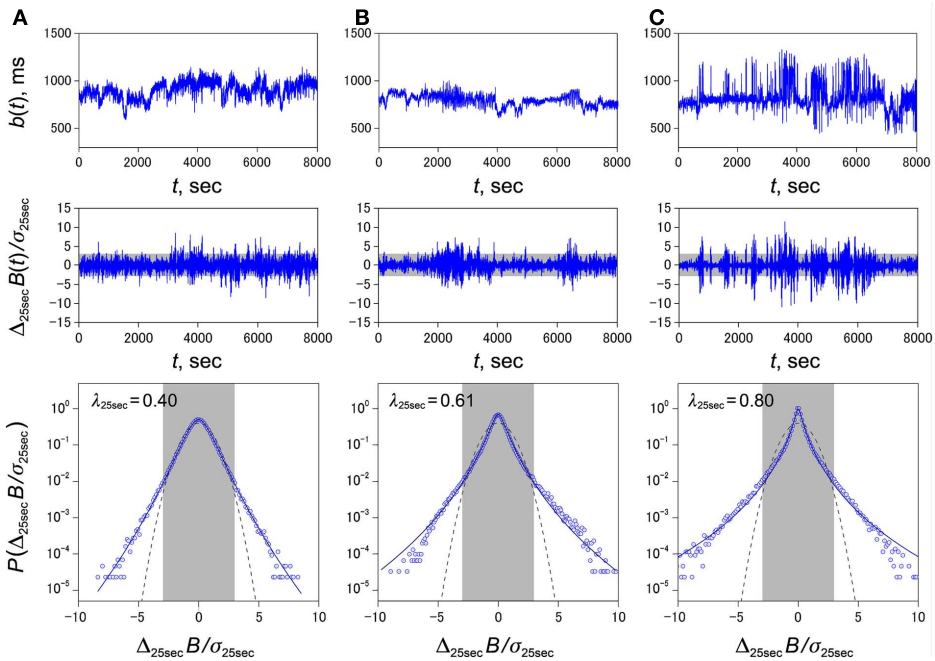

FIGURE 1 | Representative examples of non-Gaussian heart rate fluctuations with different values of λ_{25s} in post-AMI patients, survivor (A) and cardiac death (B, C). Trend graphs of normal-to-normal sinus rhythm interval (Top row), standardized time series of heart rate increments $\{\Delta_{25s}B(t)\}$ (middle row), and standardized PDFs of heart rate increments $\{\Delta_{25s}B(t)\}$ (bottom row). Estimated values of the non-Gaussianity index of λ_{25s} are shown in each panel in the bottom row. In the solidline, we superimposed the PDF approximated by a non-Gaussian model (Kiyono et al., 2007) with the parameter λ_{25s}. The non-Gaussian model provides an excellent approximation of the peaked PDF around center (particularly in the gray shaded area covering ±3 SD) of the observed distribution, caused mainly by intermittent alterations of quiet (laminar) phase and busty phase (middle row), because our non-Gaussianity index with $q = 0.25$ characterizes peaked shape of the observed non-Gaussian distribution and reduces the effects of extreme outliers, if any. The dashed lines represent the Gaussian distribution ($\lambda_{25s} \to 0$).

as kurtosis based on the fourth moment, emphasizing heavy tails, and extreme deviations. Also, we previously showed that the accuracy of estimation of λ_s for typical Holter records (data points, $n \approx 10^5$) is much higher when using $q < 2$, as compared to $q > 2$ (see Figure 3 of Kiyono et al., 2007). The C source codes and executables for computing the non-Gaussianity index are available online at *www.ge.ce.nihon-u.ac.jp/~kiyono/app/*.

In the present study, we set the scale s at 25 s. In a previous cohort study of chronic heart failure, we noted that $\lambda_{40\,beat} > 0.6$ had the best predictive power for mortality (Kiyono et al., 2008). Because the $\lambda_{40\,beat}$ is based on beat scale, could be affected by both inter- and intra-individual differences in heart rate, we reanalyzed the previous data using time (s) as the unit of scale (see Appendix). Then, we found that $\lambda_{25\,s}$ was comparable to $\lambda_{40\,beat}$ in predictive power for mortality. We therefore used $\lambda_{25\,s}$ as the non-Gaussianity index and $\lambda_{25\,s} > 0.6$ as the cutoff threshold in survival curve analyses.

ANALYSIS OF CONVENTIONAL HRV INDICES

We calculated the conventional indices of HRV that are recognized as post-AMI risk predictors by the Task Force of the European Society of Cardiology and the North American Society of Pacing and Electrophysiology (Camm et al., 1996): mean N–N interval, SD of all N–N intervals (SDNN), the variances corresponding to ultra-low frequency (ULF; 0–0.0033 Hz), very-low frequency (VLF; 0.0033–0.04 Hz), low frequency (LF; 0.04–0.15 Hz) and high frequency (HF; 0.15–0.40 Hz) bands, and LF/HF. The variances of these frequency components were transformed in the natural logarithmic values (Ln). We examined the fractal correlation properties of heart rate dynamics using detrended fluctuation analysis (DFA) and calculated the short-term (4–11 beat) and long-term (≥11 beats) scaling exponents as α_1 and α_2, respectively (Peng et al., 1995). We also computed the deceleration and acceleration capacity (DC and AC) by the phase rectified signal averaging of the 24-h N–N interval time series (Bauer et al., 2006). Finally, we assessed indices of heart rate turbulence (HRT; Schmidt et al., 1999). In accordance with previous reports (Barthel et al., 2003; Bauer et al., 2009), we defined abnormal turbulence onset (TO) as ≥0%, abnormal turbulence slope (TS) as ≤2.5 ms/beat and abnormal HRT as an instance when both TO and TS were abnormal. If ventricular premature contractions suitable for calculating HRT were five or less in the 24-h recording, the patients were classified as having normal HRT.

ENDPOINT ANALYSIS

The end points of the present study were all-cause mortality and recurrent non-fatal AMI. Patients underwent follow-up assessments 6 months after study enrollment and annually thereafter for up to 30 months. The end points were identified from follow-up visits, telephone calls, routine hospital surveillance, and contacts with patients' physicians. The records of every identified hospitalization were obtained for review and confirmation.

The ENRICHD ECG core laboratory classified electrocardiograms obtained during hospitalizations by the Minnesota code using serial change rules. Death certificates were obtained for all reported deaths. The mortality endpoints used for the present study were either cardiac deaths (AMI, cardiac failure, and sudden cardiac death) or non-cardiac deaths. Sudden cardiac death was defined as unexpected death within 1 h after the onset of a new symptom, or unexpected unwatched death.

STATISTICAL ANALYSIS

Cox proportional hazards regression analyses were used for determining the significant predictors of mortality and recurrent non-fatal AMI. The independent associations of predictors were evaluated with the multivariable hazards regression analysis adjusted for the ENRICHD risk score, which is a weighted sum of all independent risk factors for mortality in the ENRICHD trial (Jaffe et al., 2006). Potential risk factors that were considered included factors such as smoking, and medications, including beta blockers. The final risk score included age, diabetes, left ventricular ejection fraction, creatinine level, prior AMI, history of pulmonary disease, prior transient ischemic attack or stroke, history of congestive heart failure, Killip class at time of index AMI, and treatment with vasodilators. The predictors of mortality were determined in the entire subjects, while those of recurrent non-fatal AMI were determined within survivors. The survival curves were estimated by the Kaplan–Meier method and compared using the Mantel–Haenszel log-rank test.

The data are reported as the median and IQR for continuous variables and counts and percentage for categorical variables unless otherwise noted. Comparisons between groups were performed by Chi-square test for categorical variables and one-way analysis of variance for continuous variables with Tukey's Studentized range test for multiple comparisons. Pearson's correlation coefficient (r) was used to evaluate correlations between different variables and an $|r| \geq 0.4$ was interpreted to show a substantial correlation. We judged a P value of less than 0.05 to be significant.

RESULTS

Holter electrocardiograms were analyzable in 670 out of 766 eligible patients (88%). The 96 excluded patients were medically and demographically similar to those included, except that they were more likely to have diabetes and less likely to be currently smoking. **Table 1** shows the clinical characteristics of the 670 patients. β-Blockers were prescribed at the Holter monitoring in 556 patients (83%).

Table 1 | Characteristics of patients.

Number of patients, *n*	**670**
OUTCOME	
Follow-up (days), median (IQR)	748 (556–947)
Cardiac death	32 (4.8%)
Non-cardiac death	13 (1.9%)
Non-fatal AMI	57 (8.5%)
CLINICAL AND DEMOGRAPHIC CHARACTERISTICS	
Age (years), median (IQR)	59 (51–68)
Women	270 (40%)
Body mass index (kg/m^2), median (IQR)	28.1 (25.2–31.9)
Hypertension	140 (21%)
Diabetes mellitus	189 (28%)
Current smoker	220 (33%)
History of myocardial infarction	141 (21%)
History of coronary bypass surgery	72 (11%)
LVEF (%), median (IQR)	48 (25–55)
LVEF > 35%	388 (58%)
Creatinine (mg/dL), median (IQR)	1.0 (0.8–1.2)
Beck Depression Inventory score, median (IQR)	8 (3–15)
CHARACTERISTICS OF INDEX MI	
Killip class III–IV	34 (5.1%)
Anterior wall AMI	219 (33%)
Inferior wall AMI	302 (45%)
TREATMENT	
β-Blockers	556 (83%)
Angiotensin converting enzyme inhibitors	320 (48%)
Aspirin	602 (90%)
Calcium channel blockers	96 (14%)
Thrombolytic therapy after AMI	210 (31%)
Coronary bypass after AMI	89 (13%)
Coronary angioplasty <24 h after AMI	419 (63%)
Acute reperfusion ≤12 h after AMI	307 (47%)

AMI, acute myocardial infarction; IQR, inter quartile range.

HRV AND NON-GAUSSIANITY INDICES

The HRV indices that are considered as relating to cardiac vagal function were highly correlated with each other, while the non-Gaussianity index of $\lambda_{25\,s}$ showed no substantial correlations with these indices (**Table 2**). Also, $\lambda_{25\,s}$ correlated with neither the number of ventricular ectopies per 24 h ($r = -0.01$) nor its products with TO or TS ($r = 0.01, -0.07$), indicating that $\lambda_{25\,s}$ is unrelated to heart rate fluctuations accompanying ventricular arrhythmias ("HRT"). On the other hand, $\lambda_{25\,s}$ was lower in patients taking β blockers than in those not taking (mean [SD], 0.53 [0.12], and 0.56 [0.13], respectively, $P = 0.04$). No such effect on $\lambda_{25\,s}$ was observed for angiotensin converting enzyme inhibitors, aspirin, or calcium channel blockers.

INCREASED NON-GAUSSIANITY AND PROGNOSIS

During follow-up for a median of 25 months, 45 (6.7%) patients died, with 32 deaths classified as cardiac and 13 as non-cardiac deaths, and 39(6.2%) patients among survivors had recurrent non-fatal AMI. On average, all HRV indices including $\lambda_{25\,s}$ and HRT category showed no significant difference between survivors with and without recurrent non-fatal AMI (**Figure 2**). SDNN, lnVLF, DFA α_1 and DC were lower and abnormal HRT was more prevalent in patients suffering both cardiac death and non-cardiac death compared to survivors, whereas $\lambda_{25\,s}$ was greater only in the cardiac death patients. The typical relationships between $\lambda_{25\,s}$ and other HRV indices are shown in **Figure 3**. The surviving patient (**Figure 3A**) showed large N–N interval variability, while both cardiac (**Figure 3B**) and non-cardiac (**Figure 3C**) death patients showed decreased variability. **Figure 3D** shows standardized PDFs of heart rate increment constructed from the same data. The

Table 2 | Correlations among HRV indices, HRT, and $\lambda_{25\,s}$.

Variable	SDNN	LnVLF	DFA α1	DC	TO	TS	$\lambda_{25\,s}$
Mean N–N	0.58	0.57	0.18	0.50	−0.17	0.37	−0.05
SDNN	–	0.85	0.23	0.61	−0.33	0.41	−0.02
LnULF	0.93	0.80	0.30	0.58	−0.30	0.36	−0.08
LnVLF	0.85	–	0.45	0.71	−0.35	0.44	−0.15
LnLF	0.83	0.91	0.38	0.70	−0.36	0.47	−0.06
LnHF	0.77	0.73	−0.09	0.56	−0.26	0.38	0.06
LF/HF	0.00	0.16	0.72	0.12	−0.10	0.12	−0.13
DFA α1	0.23	0.45	–	0.43	−0.20	0.23	−0.17
DFA α2	−0.26	−0.41	−0.21	−0.34	0.15	−0.30	−0.19
AC	0.66	0.72	0.35	0.92	−0.37	0.53	−0.34
DC	0.61	0.71	0.43	–	−0.38	0.52	−0.33
TO	−0.33	−0.35	−0.20	−0.38	–	−0.28	0.16
TS	0.41	0.44	0.23	0.52	−0.28	–	−0.15

Values are correlation coefficients (|r| > 0.4 are shaded). Abbreviations for HRV indices are defined in the text.

surviving and non-cardiac death patients showed similar PDF curves and comparable $\lambda_{25\,s}$ (0.40 and 0.44, respectively) despite the large difference in absolute variability. In contrast, the cardiac death patient showed a PDF curve with a more tapered center and fatter tails with a $\lambda_{25\,s}$ of 0.80.

The unadjusted Cox hazards regression analysis revealed that decreases in SDNN and DC were increased risk of recurrent non-fatal AMI, while DFA α1, HRT, and $\lambda_{25\,s}$ had no predictive power for the recurrence (**Table 3**). All HRV indices but $\lambda_{25\,s}$ and abnormal HRT predicted increased risk of both cardiac and non-cardiac death, while increased $\lambda_{25\,s}$ predicted increased risk of only cardiac death but not of non-cardiac death. The associations of $\lambda_{25\,s}$ and other HRV indices with mortality risk remained significant even after adjustment for the ENRICHD risk score, while the associations of HRV indices with AMI recurrence were no longer significant (**Table 3**).

The predictive power of $\lambda_{25\,s}$ for cardiac death was independent of the other HRV indices. Increased $\lambda_{25\,s}$ was a significant predictor in the models including either HRV predictors (**Table 4**). Among these models, the risk of cardiac death was best predicted by the combination of increased $\lambda_{25\,s}$ and abnormal HRT (**Table 4**). We therefore generated Kaplan–Meier curves for this combination along with those for $\lambda_{25\,s}$ dichotomized at 0.6 (**Figure 4**). As expected, mortality was highest in the patients who had both increased $\lambda_{25\,s}$ and abnormal HRT. More importantly, however, mortality was low not only in patients who had neither of the two factors but also was low in those who had either one factor alone, suggesting that these factors acted synergistically.

DISCUSSION

We assessed non-Gaussianity of HRV in post-AMI patients and found that increased non-Gaussianity index of $\lambda_{25\,s}$ predicts risk of cardiac death in these patients. The $\lambda_{25\,s}$ showed no substantial correlation with HRV indices reflecting cardiac vagal functions and was decreased in patients taking β-blockers. While the other HRV indices were associated with both cardiac and non-cardiac deaths, the increased $\lambda_{25\,s}$ was associated exclusively with cardiac death but not with non-cardiac death. The predictive power of increased $\lambda_{25\,s}$ was independent of clinical risk factors and of the other HRV predictors. The survival curve analyses revealed that increased $\lambda_{25\,s}$ and abnormal HRT have a synergistic effect on the risk of cardiac mortality. Additionally, $\lambda_{25\,s}$ showed no predictive power for the recurrence of non-fatal AMI, suggesting that $\lambda_{25\,s}$ may not be associated with the mechanisms developing AMI itself.

The non-Gaussianity of heart rate has several unique features that had been undetected by conventional indices of HRV. First, $\lambda_{25\,s}$ is unrelated to the cardiac autonomic responsiveness reflected in the magnitude of HRV. As shown in **Figure 3**, surviving and non-cardiac death patients exhibited comparable $\lambda_{25\,s}$ despite a large difference in other HRV indices. Second, $\lambda_{25\,s}$ captures intermittent heart rate increments within a scale of 25 s. Although the heart rate fluctuations in this scale are mediated almost exclusively by neural autonomic activities (Camm et al., 1996), $\lambda_{25\,s}$ showed no substantial correlation with the HRV indices reflecting vagal heart rate regulation and was decreased in patients taking β blockers. Thus, $\lambda_{25\,s}$ is likely to capture heart rate fluctuation mediated by intermittent activations of cardiac sympathetic activity at least partly. Third, $\lambda_{25\,s}$ is independent of heart rate fluctuations caused by ectopic beats, i.e., HRT (Schmidt et al., 1999). Indeed, $\lambda_{25\,s}$ showed no significant correlation with the number of ventricular ectopies per 24 h or its products with TO or TS. Additionally, $\lambda_{25\,s}$ is also independent of erratic rhythms detected by Poincare plot (Woo et al., 1992; Stein et al., 2005), because beat-to-beat changes in N–N intervals are averaged out when calculating $\lambda_{25\,s}$ (Kiyono et al., 2008).

The present study indicates that the risk of mortality is particularly high in the presence of increased $\lambda_{25\,s}$ and abnormal HRT compared with the presence of only one alone. This synergistic effect between $\lambda_{25\,s}$ and HRT is compatible with a pathophysiologic paradigm for post-AMI sudden cardiac death; i.e., sympathetic stimulation under impaired reflex vagal antagonism precipitates ventricular fibrillation during transient myocardial ischemia in the heart with healed AMI (Schwartz et al., 1984; Vanoli et al., 1991). The increased $\lambda_{25\,s}$ appears to detect frequent

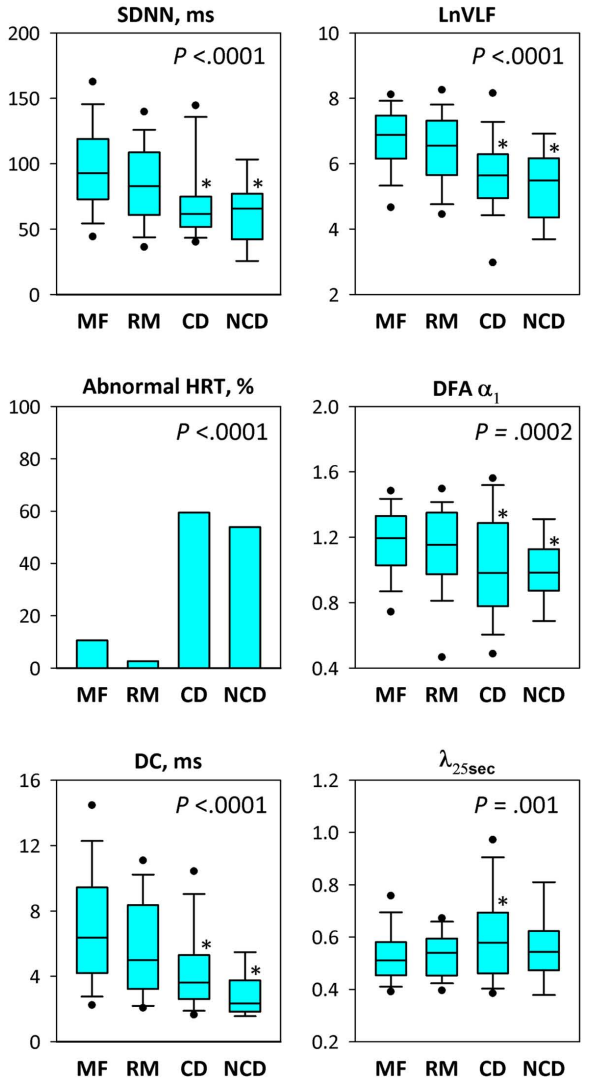

FIGURE 2 | Heart rate variability indices, HRT, and non-Gaussianity index (λ_{25s}) in post-AMI patients grouped by the endpoint of follow-up: MF, recurrent AMI-free survival; RM, recurrent non-fatal AMI; CD, cardiac death; and NCD, non-cardiac death. For box plots, upper and lower boundaries of the box indicate the 75th and 25th percentiles and a line within the box marks the median. Whiskers above and below the box indicate the 90th and 10th percentiles and dots above and below the whiskers indicate 95th and 5th percentiles. *P* values show significance of ANOVA except for abnormal HRT, for which bar graphs show percentage of patients who showed abnormal HRT and *P* value indicates the significance of chi-square test. *Significantly different from the value for recurrent AMI-free survivors (Tukey's Studentized range test).

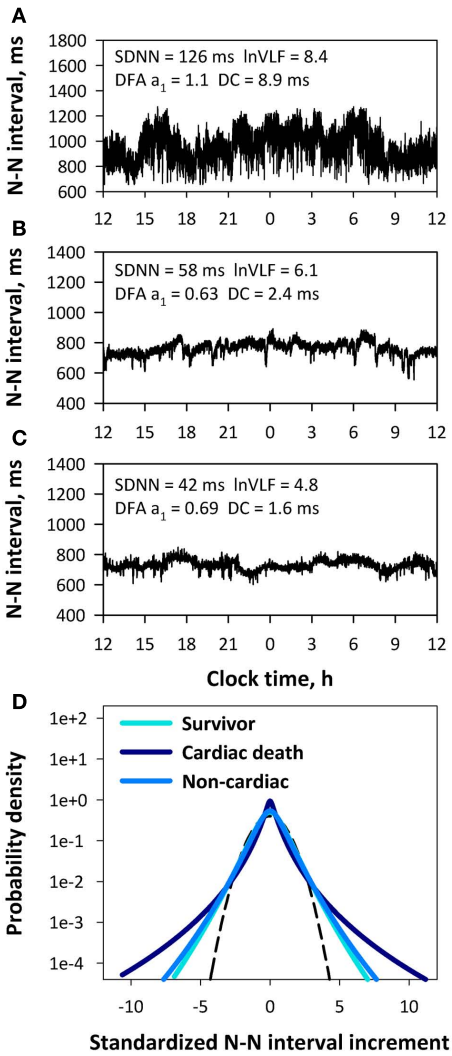

FIGURE 3 | Trend graphs of 24-h N–N interval in three representative patients, recurrent AMI-free survivor (A), cardiac death (B) and non-cardiac death (C), and their standardized PDF of intermittent heart rate increments (D). Insets of panels **(A–C)** show values of HRV indices obtained from each N–N interval time series. In panel **(D)**, the Gaussian distribution ($\lambda_{25s} = 0$), an inverted parabola in this semi-log plot without "tapered" centers and "fat" tails, is shown as a dashed line. Abbreviations for HRV indices are defined in the text.

sympathetic activations and the abnormal HRT to reflect impaired reflex vagal antagonism. The absence of the association of λ_{25s} with the AMI recurrence also supports the hypothesis, suggesting that the increased λ_{25s} maybe associated with the mechanisms precipitating cardiac death after AMI rather than those developing AMI.

The present findings also indicate that λ_{25s} is unrelated to the risk of non-cardiac death. This finding was not observed for the other HRV indices. Decreased HRV is associated with various health conditions (Priori et al., 2001), including diabetes, uremia, alcoholism, obesity, smoking, depression, and aging (Malik and Camm, 2004) and with mortality among general elderly populations (Tsuji et al., 1994), which may explain the non-specific associations of decreased HRV with increased risk for all – cause mortality (Kleiger et al., 1987; La Rovere et al., 1998; Schmidt et al., 1999; Bauer et al., 2006). The selective associations of increased λ_{25s} with cardiac death seems useful for predicting patients who would benefit from preventive approaches, such as those with implantable cardioverter defibrillators (Moss et al., 2002).

Table 3 | Unadjusted and adjusted mortality risk in post-AMI patients.

Predictor	SD	Non-fatal AMI				Cardiac death				Non-cardiac death			
		Unadjusted		Adjusted*		Unadjusted		Adjusted*		Unadjusted		Adjusted*	
		RR (95% CI)	*P*	RR (95% CI)	*P*	RR (95% CI)	*P*	RR (95% CI)	*P*	RR (95% CI)	*P*	RR (95% CI)	*P*
SDNN, ms	36	1.4 (1.0–2.1)	0.04	1.4 (0.97–2.0)	0.07	2.3 (1.5–3.7)	0.0003	1.9 (1.2–3.1)	0.01	3.9 (1.7–8.9)	0.001	3.5 (1.5–8.3)	0.004
LnVLF	1.2	1.3 (0.97–1.8)	0.07	1.3 (0.93–1.7)	0.1	1.9 (1.5–2.5)	<0.0001	1.7 (1.3–2.3)	0.0005	2.3 (1.6–3.3)	<0.0001	2.1 (1.5–3.2)	0.0001
DFA α_1	0.23	1.2 (0.87–1.6)	0.2	1.1 (0.83–1.6)	0.4	1.7 (1.3–2.3)	0.0005	1.5 (1.1–2.1)	0.01	1.8 (1.1–2.9)	0.01	1.6 (0.99–2.7)	0.05
DC, ms	3.9	1.6 (1.0–2.3)	0.02	1.5 (0.99–2.3)	0.05	3.0 (1.6–5.4)	0.0003	2.0 (1.0–3.8)	0.03	14 (3.9–53)	<0.0001	15 (3.6–61)	0.0002
Abnormal HRT		0.61 (0.32–1.2)	0.1	0.53 (0.27–1.0)	0.06	11 (5.3–22)	<0.0001	5.7 (2.7–12)	<0.0001	8.6 (2.9–26)	<0.0001	6.0 (1.9–19)	0.002
λ_{25s}	0.13	0.99 (0.71–1.4)	0.9	0.95 (0.68–1.3)	0.7	1.6 (1.3–2.0)	<0.0001	1.4 (1.1–1.8)	0.01	1.2 (0.74–1.9)	0.4	1.0 (0.61–1.7)	0.9

CI, confidence interval; RR, relative risk.

RRs represent those for 1 SD decrement in SDNN, LnVLF, DFA α_1, and DC, for 1 SD increment in λ_{25s}, and for the presence of abnormal HRT.

**Adjusted for ENRICHD risk score that is the weighted sum of independent predictors of post-AMI mortality included age, diabetes, left ventricular ejection fraction, creatinine level, prior AMI, history of pulmonary disease, prior transient ischemic attack or stroke, history of congestive heart failure, Killip class at time of index AMI, and treatment with vasodilators (Jaffe et al., 2006).*

Table 4 | Independent relative risk of $\lambda_{25\,s}$ for post-AMI cardiac mortality.

Prediction model	$\lambda_{25\,s}$		Model fit (likelihood ratio test)	
	Adjusted RR (95% CI)	*P*	χ^2	*P*
SDNN + $\lambda_{25\,s}$	1.4 (1.1–1.7)	0.007	21.6	<0.0001
LnVLF + $\lambda_{25\,s}$	1.3 (1.0–1.6)	0.04	22.6	<0.0001
DFA α_1 + $\lambda_{25\,s}$	1.4 (1.1–1.8)	0.007	17.3	<0.0001
DC + $\lambda_{25\,s}$	1.3 (1.0–1.7)	0.01	22.5	<0.0001
Abnormal HRT + $\lambda_{25\,s}$	1.3 (1.0–1.6)	0.02	45.0	<0.0001

CI, confidence interval; RR, relative risk.
Adjusted RRs represent those for 1 SD (0.13) increment in $\lambda_{25\,s}$.

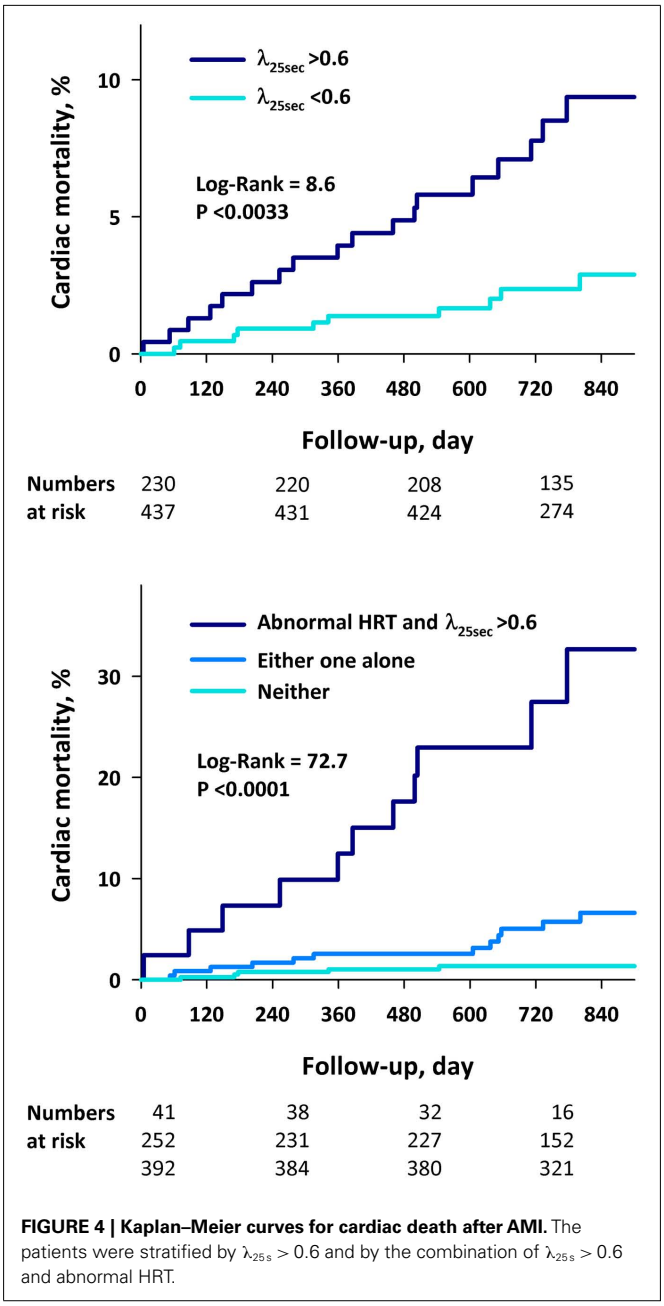

FIGURE 4 | Kaplan–Meier curves for cardiac death after AMI. The patients were stratified by $\lambda_{25\,s} > 0.6$ and by the combination of $\lambda_{25\,s} > 0.6$ and abnormal HRT.

STUDY LIMITATIONS

Our study has several limitations. First, the sample included a subset of patients enrolled in the ENRICHD trial who had elevated symptoms of depression, which could affect the generalizability of our results. However, the proportion of the depressed patients with BDI scores ≥ 10 was 47%, which is comparable to the reported prevalence of depression (45–47%) in general post-AMI populations (Schleifer et al., 1989; Steeds et al., 2004). Second, we did not consider sudden cardiac death as a separate endpoint because the causes of cardiac death were not subcategorized in the record of ENRICHD study. Furthermore, the number of deaths, particularly that of non-cardiac death was small (13) and the power to detect a possible association between $\lambda_{25\,s}$ and non-cardiac death was inadequate. Finally, to establish the $\lambda_{25\,s}$ as a clinical risk factor of post-AMI cardiac death, it will be necessary to demonstrate that a reduction of this index improves clinical outcomes; however, our observations suggest a potential effect of β-blockers in reducing $\lambda_{25\,s}$.

CONCLUSION

Among post-AMI patients, an increase in non-Gaussianity index of $\lambda_{25\,s}$ is independently associated with increased risk of cardiac death. Our observations suggest that the increased $\lambda_{25\,s}$ may reflect the deleterious effects of heightened sympathetic cardiac activation, which may contribute to the increased risk of cardiac death in post-AMI patients.

ACKNOWLEDGMENTS

We thank Dr Lisa Berkman of the Department of Epidemiology at the Harvard School of Public Health for providing data from the Yale University clinical site for our analysis. This research was supported by a Grant-in-Aid for Scientific Research(C) from the Japan Society for the Promotion of Science (JSPS), Japan, by a Research Grant (20B-7) for Nervous and Mental Disorders from the Ministry of Health, Labor and Welfare, Japan and by Grant HL 093374, HL080664, and HL58946 from the National Heart, Lung and Blood Institute, National Institutes of Health, Bethesda, MD, USA.

REFERENCES

Barthel, P., Schneider, R., Bauer, A., Ulm, K., Schmitt, C., Schomig, A., and Schmidt, G. (2003). Risk stratification after acute myocardial infarction by heart rate turbulence. *Circulation* 108, 1221–1226.

Bauer, A., Barthel, P., Schneider, R., Ulm, K., Muller, A., Joeinig, A., Stich, R., Kiviniemi, A., Hnatkova, K., Huikuri, H., Schomig, A., Malik, M., and Schmidt, G. (2009). Improved stratification of autonomic regulation for risk prediction in post-infarction patients with preserved left ventricular function (ISAR-Risk). *Eur. Heart J.* 30, 576–583.

Bauer, A., Kantelhardt, J. W., Barthel, P., Schneider, R., Makikallio, T., Ulm, K., Hnatkova, K., Schomig, A., Huikuri, H., Bunde, A., Malik, M., and Schmidt, G. (2006). Deceleration capacity of heart rate as a predictor of mortality after myocardial infarction: cohort study. *Lancet* 367, 1674–1681.

Berkman, L. F., Blumenthal, J., Burg, M., Carney, R. M., Catellier, D., Cowan, M. J., Czajkowski, S. M., DeBusk, R., Hosking, J., Jaffe, A., Kaufmann, P. G., Mitchell, P., Norman, J., Powell, L. H., Raczynski, J. M., and Schneiderman, N. (2003). Effects of treating depression and low perceived social support on clinical events after myocardial infarction: the Enhancing recovery in coronary heart disease patients (ENRICHD) randomized trial. *JAMA* 289, 3106–3116.

Camm, A. J., Malik, M., Bigger, J. T. Jr., Breithardt, G., Cerutti, S., Cohen, R. J., Coumel, P., Fallen, E. L., Kleiger, R. E., Lombardi, F., Malliani, A., Moss, A. J., Rottman, J. N., Schmidt, G., Schwartz, P. J., and Singer, D. H. (1996). Task force of the European Society of Cardiology and the North American Society of Pacing and Electrophysiology. Heart rate variability: standards of measurement, physiological interpretation and clinical use. *Circulation* 93, 1043–1065.

Castaing, B., Gagne, Y., and Hopfinger, F. J. (1990). Velocity probability density-functions of high Raynolds-number turbulence. *Physica D* 46, 177–200.

Huikuri, H. V., Mäkikallio, T. H., Peng, C. K., Goldberger, A. L., Hintze, U., Moller, M., and Grp, D. S. (2000). Fractal correlation properties of R-R interval dynamics and mortality in patients with depressed left ventricular function after an acute myocardial infarction. *Circulation* 101, 47–53.

Jaffe, A. S., Krumholz, H. M., Catellier, D. J., Freedland, K. E., Bittner, V., Blumenthal, J. A., Calvin, J. E., Norman, J., Sequeira, R., O'Connor, C., Rich, M. W., Sheps, D., and Wu, C. (2006). Prediction of medical morbidity and mortality after acute myocardial infarction in patients at increased psychosocial risk in the enhancing recovery in coronary heart disease patients (ENRICHD) study. *Am. Heart J.* 152, 126–135.

Kiyono, K., Hayano, J., Watanabe, E., Struzik, Z. R., and Yamamoto, Y. (2008). Non-Gaussian heart rate as an independent predictor of mortality in patients with chronic heart failure. *Heart Rhythm* 5, 261–268.

Kiyono, K., Struzik, Z. R., Aoyagi, N., Sakata, S., Hayano, J., and Yamamoto, Y. (2004). Critical scale invariance in a healthy human heart rate. *Phys. Rev. Lett.* 93, 178103.

Kiyono, K., Struzik, Z. R., and Yamamoto, Y. (2007). Estimator of a non-Gaussian parameter in multiplicative log-normal models. *Phys. Rev. E Stat. Nonlin. Soft Matter Phys.* 76, 041113.

Kleiger, R. E., Miller, J. P., Bigger, J. T. Jr., and Moss, A. J. (1987). Decreased heart rate variability and its association with increased mortality after acute myocardial infarction. *Am. J. Cardiol.* 59, 256–262.

La Rovere, M. T., Bigger, J. T. Jr., Marcus, F. I., Mortara, A., and Schwartz, P. J. (1998). Baroreflex sensitivity and heart-rate variability in prediction of total cardiac mortality after myocardial infarction. *Lancet* 351, 478–484.

Malik, M., and Camm, A. J. (2004). "Heart rate variability," in *Dynamic Electrocardiography*, eds M. Malik and A. J. Camm (New York: Blackwell), 3–213.

Marine, J. E., Watanabe, M. A., Smith, T. W., and Monahan, K. M. (2002). Effect of atropine on heart rate turbulence. *Am. J. Cardiol.* 89, 767–769.

Moss, A. J., Zareba, W., Hall, W. J., Klein, H., Wilber, D. J., Cannom, D. S., Daubert, J. P., Higgins, S. L., Brown, M. W., and Andrews, M. L. (2002). Prophylactic implantation of a defibrillator in patients with myocardial infarction and reduced ejection fraction. *N. Engl. J. Med.* 346, 877–883.

Peng, C. K., Havlin, S., Stanley, H. E., and Goldberger, A. L. (1995). Quantification of scaling exponents and crossover phenomena in nonstationary heartbeat time series. *Chaos* 5, 82–87.

Priori, S. G., Aliot, E., Blomstrom-Lundqvist, C., Bossaert, L., Breithardt, G., Brugada, P., Camm, A. J., Cappato, R., Cobbe, S. M., Di Mario, C., Maron, B. J., McKenna, W. J., Pedersen, A. K., Ravens, U., Schwartz, P. J., Trusz-Gluza, M., Vardas, P., Wellens, H. J., and Zipes, D. P. (2001). Task force on sudden cardiac death of the European Society of Cardiology. *Eur. Heart J.* 22, 1374–1450.

Schleifer, S. J., Macari-Hinson, M. M., Coyle, D. A., Slater, W. R., Kahn, M., Gorlin, R., and Zucker, H. D. (1989). The nature and course of depression following myocardial infarction. *Arch. Intern. Med.* 149, 1785–1789.

Schmidt, G., Malik, M., Barthel, P., Schneider, R., Ulm, K., Rolnitzky, L., Camm, A. J., Bigger, J. T. Jr., and Schomig, A. (1999). Heart-rate turbulence after ventricular premature beats as a predictor of mortality after acute myocardial infarction. *Lancet* 353, 1390–1396.

Schwartz, P. J., Billman, G. E., and Stone, H. L. (1984). Autonomic mechanisms in ventricular fibrillation induced by myocardial ischemia during exercise in dogs with healed myocardial infarction: an experimental preparation for sudden cardiac death. *Circulation* 69, 790–800.

Steeds, R. P., Bickerton, D., Smith, M. J., and Muthusamy, R. (2004). Assessment of depression following acute myocardial infarction using the Beck depression inventory. *Heart* 90, 217–218.

Stein, P. K., Domitrovich, P. P., Hui, N., Rautaharju, P., and Gottdiener, J. (2005). Sometimes higher heart rate variability is not better heart rate variability: results of graphical and nonlinear analyses. *J. Cardiovasc. Electrophysiol.* 16, 954–959.

Tsuji, H., Venditti, F. J. Jr., Manders, E. S., Evans, J. C., Larson, M. G., Feldman, C. L., and Levy, D. (1994). Reduced heart rate variability and mortality risk in an elderly cohort: the Framingham Heart Study. *Circulation* 90, 878–883.

Vanoli, E., G. M. De Ferrari, Stramba-Badiale, M., Hull, S. S. Jr., Foreman, R. D., and Schwartz, P. J. (1991). Vagal stimulation and prevention of sudden death in conscious dogs with a healed myocardial infarction. *Circ. Res.* 68, 1471–1481.

Woo, M. A., Stevenson, W. G., Moser, D. K., Trelease, R. B., and Harper, R. M. (1992). Patterns of beat-to-beat heart rate variability in advanced heart failure. *Am. Heart J.* 123, 704–710.

Conflict of Interest Statement: The authors declare that the research was conducted in the absence of any commercial or financial relationships that could be construed as a potential conflict of interest.

Received: 10 June 2011; accepted: 12 September 2011; published online: 30 September 2011.

Citation: Hayano J, Kiyono K, Struzik ZR, Yamamoto Y, Watanabe E, Stein PK, Watkins LL, Blumenthal JA and Carney RM (2011) Increased non-Gaussianity of heart rate variability predicts cardiac mortality after an acute myocardial infarction. Front. Physio. ***2****:65. doi: 10.3389/fphys.2011.00065*

This article was submitted to Frontiers in Computational Physiology and Medicine, a specialty of Frontiers in Physiology.

APPENDIX

REANALYSIS OF PREVIOUS OBSERVATIONS IN A COHORT STUDY OF CONGESTIVE HEART FAILURE PATIENTS

In a previously study (Kiyono et al., 2008), we reported that non-Gaussian index $\lambda_{40\,\mathrm{beat}}$ is an independent predictor of increased risk for mortality in patients with congestive heart failure (CHF). We studied 108 patients who were consecutively referred for evaluation or treatment of CHF. They underwent 24-h Holter ECG monitoring prior to hospital discharge and were subsequently followed up for 33 ± 17 months. The Holter ECG was analyzed to determine non-Gaussian index together with time and frequency domain indices of heart rate variability (HRV), fractal HRV measures, and heart rate turbulence.

In this previous study (Kiyono et al., 2008), we computed the non-Gaussian index λ based on beat scale and we found that the λ at a scale of 40 beats ($\lambda_{40\,\mathrm{beat}}$) showed the best predictive power for mortality. However, analyses based on beat scale could be affected by both inter- and intra-individual differences in heart rate. We therefore reanalyzed the same data based on time (s) scale. Time series of R–R intervals were interpolated with cubic spline function, resampled at 4 Hz, and submitted to the algorithm for estimating λ. Cox proportional hazards regression analysis was performed to determine the relative mortality risk of the indices. Then, we found that the λ at a scale of 25 s ($\lambda_{25\,\mathrm{s}}$) was the best independent predictor of both all-cause and cardiac mortality. The predictive power of $\lambda_{25\,\mathrm{s}}$ was comparable to that of $\lambda_{40\,\mathrm{beat}}$ for both all-cause and cardiac mortality and even after adjustment for other predictors (**Table A1**).

Table A1 | Associations of HRV indices with mortality risk in CHF patients.

Predictor	SD	All-cause death				Cardiac death			
		Unadjusted		Adjusted*		Unadjusted		Adjusted*	
		RR (95% CI)†	*P*	RR (95% CI)†	*P*	RR (95% CI)†	*P*	RR (95% CI)†	*P*
SDNN, ms	35	0.9 (0.7–1.3)	0.69	1.2 (0.8–1.6)	0.39	0.9 (0.7–1.3)	0.55	1.1 (0.8–1.6)	0.52
LnVLF	1.2	1.2 (0.9–1.6)	0.31	1.2 (0.9–1.6)	0.30	1.1 (0.8–1.6)	0.41	1.1 (0.8–1.6)	0.42
DFAα_1	0.25	1.2 (0.9–1.6)	0.30	1.3 (0.9–1.8)	0.11	1.2 (0.8–1.6)	0.36	1.3 (0.9–1.9)	0.14
DC, ms	1.7	1.2 (0.8–1.6)	0.34	1.2 (0.8–1.6)	0.39	1.2 (0.9–1.8)	0.23	1.2 (0.9–1.8)	0.27
Abnormal HRT		1.6 (0.8–3.0)	0.15	1.4 (0.7–2.6)	0.31	1.6 (0.8–3.)	0.17	1.4 (0.7–2.7)	0.35
$\lambda_{\text{-40 beat}}$	0.16	1.6 (1.2–2.2)	0.001	1.5 (1.1–2.0)	0.005	1.6 (1.2–2.1)	0.003	1.4 (1.1–1.9)	0.01
$\lambda_{\text{-25 s}}$	0.16	1.6 (1.2–2.1)	0.001	1.5 (1.1–2.0)	0.003	1.6 (1.2–2.1)	0.002	1.5 (1.1–2.0)	0.01

CI, confidence interval; DC, deceleration capacity; DFA, detrended fluctuation analysis; HRT, heart rate turbulence; lnVLF, logarithm of the power of very-low frequency component; RR, relative risk; SD, standard deviation; SDNN, SD of normal-to-normal R–R intervals during 24 h.

**Adjusted for risk score that is the weighted sum of independent predictors of age, presence of ischemia, and natural logarithm of brain natriuretic protein level (Kiyono et al., 2008).*

† RR for 1 SD decrement in SDNN, LnVLF, and DC, and for 1 SD increment in DFA α_1, λ_{25s}, and for the presence of abnormal HRT.

frontiers in
PHYSIOLOGY

ORIGINAL RESEARCH ARTICLE
published: 22 February 2012
doi: 10.3389/fphys.2012.00034

Non-Gaussianity of low frequency heart rate variability and sympathetic activation: lack of increases in multiple system atrophy and Parkinson disease

Ken Kiyono[1], Junichiro Hayano[2], Shin Kwak[3], Eiichi Watanabe[4] and Yoshiharu Yamamoto[5]*

[1] College of Engineering, Nihon University, Koriyama, Japan
[2] Department of Medical Education, Nagoya City University Graduate School of Medical Sciences, Nagoya, Japan
[3] Department of Neurology, Graduate School of Medicine, University of Tokyo, Tokyo, Japan
[4] Department of Cardiology, Fujita Health University School of Medicine, Toyoake, Japan
[5] Educational Physiology Laboratory, Graduate School of Education, University of Tokyo, Tokyo, Japan

Edited by:
Riccardo Barbieri, Massachusetts General Hospital, USA

Reviewed by:
Der Chyan Bill Lin, Ryerson University, Canada
Roberto Sassi, Università degli Studi di Milano, Italy

***Correspondence:**
Yoshiharu Yamamoto, Graduate School of Education, The University of Tokyo, 7-3-1 Hongo, Bunkyo-ku, Tokyo 113-0033, Japan.
e-mail: yamamoto@p.u-tokyo.ac.jp

The correlates of indices of long-term ambulatory heart rate variability (HRV) of the autonomic nervous system have not been completely understood. In this study, we evaluated conventional HRV indices, obtained from the daytime (12:00–18:00) Holter recording, and a recently proposed non-Gaussianity index (λ; Kiyono et al., 2008) in 12 patients with multiple system atrophy (MSA) and 10 patients with Parkinson disease (PD), known to have varying degrees of cardiac vagal and sympathetic dysfunction. Compared with the age-matched healthy control group, the MSA patients showed significantly decreased HRV, most probably reflecting impaired vagal heart rate control, but the PD patients did not show such reduced variability. In both MSA and PD patients, the low-to-high frequency (LF/HF) ratio and the short-term fractal exponent α_1, suggested to reflect the sympathovagal balance, were significantly decreased, as observed in congestive heart failure (CHF) patients with sympathetic overdrive. In contrast, the analysis of the non-Gaussianity index λ showed that a marked increase in intermittent and non-Gaussian HRV observed in the CHF patients was not observed in the MSA and PD patients with sympathetic dysfunction. These findings provide additional evidence for the relation between the non-Gaussian intermittency of HRV and increased sympathetic activity.

Keywords: heart rate variability, ambulatory ECG, multiple system atrophy, Parkinson disease, autonomic failure

INTRODUCTION

The correlates of indices of long-term ambulatory heart rate variability (HRV) of the autonomic nervous system have not been completely understood. In particular, there is yet no established index for sympathetic activation, and most HRV indices proposed primarily reflect reduced or impaired vagal function (Camm et al., 1996; Marine et al., 2002; Bauer et al., 2006). Considering a key role played by the sympathetic overdrive as one of the universal precipitating factors for various chronic illnesses (McEwen, 1998, 2007) and as a factor responsible for cardiac electrical instability (Schwartz et al., 1984), the quest for HRV indices probing sympathetic activation would be of great importance.

As a marker potentially related to the sympathetic cardiac overdrive, we have recently proposed increased non-Gaussianity of HRV (Kiyono et al., 2008). This form of non-Gaussianity has been used in fluid dynamics for characterizing intermittency of turbulence (Castaing et al., 1990). When applied to HRV analysis, it captures the occurrence of intermittent heart rate increments (Kiyono et al., 2004, 2007). In a cohort of congestive heart failure (CHF), Kiyono et al. (2008) initially observed that the increased non-Gaussianity of HRV predicts increased mortality risk, while none of the conventional HRV indices, including those reflecting vagal heart rate control, were predictive of death among these patients. More recently, Hayano et al. (2011) also reported that the increased non-Gaussianity index, λ_{25s}, which captures intermittent heart rate increments within a scale of 25 s similar to that used in the study by Kiyono et al. (2008), is associated with increased cardiac mortality risk in a cohort of acute myocardial infarction (AMI), with the predictive power independent of other HRV indices. As heart rate fluctuations in the scale within a minute are mediated almost exclusively by neural autonomic activities (Camm et al., 1996), but λ_{25s} showed no substantial correlation with vagally mediated HRV indices and the patients taking β-blockers had lower λ_{25s}, Hayano et al. (2011) conjectured that the non-Gaussianity index in this scale probably captures heart rate fluctuations mediated by intermittent activations of cardiac sympathetic activity, affecting independently the mortality of cardiac patients.

Abbreviations: AC, acceleration capacity; AMI, acute myocardial infarction; CHF, congestive heart failure; DC, deceleration capacity; DFA, detrended fluctuation analysis; ECG, electrocardiogram; HF, high frequency; HRV, heart rate variability; LF, low frequency; LF/HF, LF-to-HF ratio; MRI, magnetic resonance imaging; MSA, multiple system atrophy; NN, normal-to-normal; PD, Parkinson disease; PDF, probability density function; RMSSD, root mean square of successive difference of NN intervals; SD, standard deviation; SDANN, standard deviation of 5 min averaged NN intervals; SDNN, standard deviation of all NN intervals; ULF, ultra-low frequency; VLF, very low frequency.

In the present study, this conjecture is more directly tested by studying long-term ambulatory HRV in patients with multiple system atrophy (MSA). MSA is a sporadic and rapidly progressive neurodegenerative disorder that presents with autonomic failure in combination with Parkinsonism or cerebellar ataxia (Wenning et al., 2008; Stefanova et al., 2009). The autonomic symptoms are believed to be due to neuropathological abnormalities in both preganglionic sympathetic (Sone et al., 2005) and vagal (Benarroch et al., 2006) neurons. In previous HRV studies, decreased high frequency, vagally mediated HRV was observed in MSA patients than in age-matched healthy controls (Gurevich et al., 2004; Kuriyama et al., 2005), resembling the reduced or impaired vagal function in cardiac patients (Camm et al., 1996; Bauer et al., 2006). In contrast, because of degeneration of the preganglionic sympathetic neurons, it is hypothesized that the non-Gaussianity of HRV fails to markedly increase, such as that observed in cardiac patients (Kiyono et al., 2008; Hayano et al., 2011), in MSA patients. We test this hypothesis by comparing the results for MSA with those for CHF (Kiyono et al., 2008); the results were reanalyzed in the same methodological framework.

In the present study, we also studied ambulatory HRV in patients with Parkinson disease (PD) in which autonomic failure is commonly observed (Lipp et al., 2009). As the autonomic pathology of PD is different from that of MSA, being primarily postganglionic as evidenced by decreased uptake of adrenergic markers such as iodine-123 metaiodobenzylguanidine (Braune et al., 1998, 1999), the degree, and balance of sympathetic and vagal impairments could be different. Thus, it would be intriguing to examine if the lack of increased non-Gaussianity is still observed in PD.

MATERIALS AND METHODS

STUDY PATIENTS

Twelve MSA patients (six male and six female subjects; 61.9 ± 7.1, 54–76 years) and 10 patients with PD (two male and eight female subjects; 71.1 ± 6.0, 63–81 years) at the Department of Neurology of the University of Tokyo Hospital participated in this study (**Tables 1** and **2**, respectively). Diagnosis was made according to the UK Parkinson's Disease Society Brain Bank Clinical Diagnostic Criteria (Hughes et al., 1992) and the second consensus statement on MSA diagnosis (Gilman et al., 2008). All patients were

Table 1 | Clinical characteristics of multiple system atrophy (MSA) patients.

No	Age (years)	Sex	Clinical diagnosis	Symptoms at onset	Illness duration (years)	Ataxia	Parkinsonism	Autonomic failure
1	60	F	MSA-C	Instability of gait	4	++	−	+
2	64	M	MSA-P	Gait disturbance	1	−	++	+
3	61	M	MSA-C	Dysautonomia	3	++	−	+
4	57	M	MSA-C	Orthostatic symptoms	9	+	−	+
5	64	F	MSA-C	Instability of gait	3	++	+	+
6	54	M	MSA-P	Dysuria	4	−	++	+
7	75	F	MSA-C	Urinary urgency	4	++	−	+
8	56	F	MSA-C	Instability of gait	2	++	−	+
9	60	M	MSA-C	Dysarthria, gait disturbance	2	++	++	+
10	61	F	MSA-C	Gait disturbance	4	++	++	+
11	55	M	MSA-P	Instability of gait	2	++	++	+
12	76	F	MSA-C	Orthostatic symptoms	2	+		+

MSA-C, MSA with predominant cerebellar ataxia; MSA-P, MSA with predominant Parkinsonism.

Table 2 | Clinical characteristics of patients with Parkinson disease.

No	Age (years)	Sex	Clinical diagnosis	Symptoms at onset	Illness duration (years)	Drug	Hoehn–Yahr score
1	68	M	PD	Tremor	3	D, AC, DA	III
2	63	M	PD	Hand tremor	21	D, M, DA	IV
3	75	F	PD	Hand tremor, gait disturbance	11	D, DA, AM	IV
4	66	F	PD	Gait disturbance, dysarthria	13	D, DA	III
5	75	F	PD	Tremor, gait disturbance	31	D. DA. AM, AC	IV
6	81	F	PD	Gait disturbance	5	D	V
7	68	F	PD	Tremor	8	D, AC, AM, DA, M	III
8	65	F	PD	Hand Tremor	8	D, DA	III
9	72	F	PD	Gait disturbance	5	D, DA, AC, AM	IV
10	78	F	PD-D	Gait disturbance, dysarthria	2	D	III

PD, Parkinson disease; PD-D, PD with dementia; D, L-DOPA/carbidopa or benserazide; DA, dopamine agonists; A, anticholinergic; AM, amantadine; M, selegiline.

examined by neurologists, and all PD patients exhibited a response to L-DOPA without remarkable MRI findings. All MSA patients fulfilled the criteria for probable MSA (Gilman et al., 2008), and most of them took adrenergic stimulants for controlling severe orthostatic hypotension and anti-adrenergic or anti-muscarinic medications for their neurogenic bladder.

In addition, we studied 108 patients who were consecutively referred for evaluation or treatment of CHF (61 male and 47 female subjects; 66.1 ± 14.8, 21–92 years). Of these patients, 39 (36.1%) died within the follow-up period of 33 ± 17 months (range, 1–59 months). The medication status before discharge from the hospital was not significantly different between survivors and non-survivors. The clinical details of the CHF patients were reported previously (Kiyono et al., 2008).

The results were compared with data from age-matched healthy subjects; the details of which were reported elsewhere (Kiyono et al., 2004). All individuals within ±2 years of each patient's age were selected from a pool of 122 healthy subjects.

MEASUREMENTS AND PROTOCOL

The original electrocardiogram (ECG) data were derived from 24-h Holter recordings. The ECG signals were digitized at 125 Hz and 12 bits and processed offline using a personal computer equipped with a dedicated software. All QRS complexes in each recording were detected and labeled automatically. The results of automatic analysis were reviewed, and any errors in R wave classification were corrected manually. Computer files were generated containing the duration of individual R–R intervals and morphology classifications of individual QRS complexes (normal, supraventricular, and ventricular premature complexes). The series of intervals between two successive R waves of sinus rhythm [normal-to-normal (NN) intervals] was analyzed. To avoid the adverse effects of any remaining errors in the detection of the R wave, large (>20%) consecutive R–R interval differences were thoroughly reviewed until all errors were corrected. In addition, when atrial or ventricular premature complexes were encountered, the corresponding R–R intervals were interpolated by the median of the two successive beat-to-beat intervals. We also confirmed that no sustained tachyarrhythmias were present in our HRV recordings. In this study, all HRV indices were obtained from the daytime (12:00–18:00) data.

ANALYSIS OF CONVENTIONAL HRV INDICES

The following HRV indices were calculated: mean NN intervals, standard deviation (SD) of all NN intervals (SDNN), SD of 5 min averaged NN intervals (SDANN), root mean square of successive difference of NN intervals (RMSSD), the variances corresponding to ultra-low frequency (ULF; 0–0.0033 Hz), very low frequency (VLF; 0.0033–0.04 Hz), low frequency (LF; 0.04–0.15 Hz), and high frequency (HF; 0.15–0.40 Hz) bands, and LF/HF ratio, all of which were proposed by the Task Force of the European Society of Cardiology and the North American Society of Pacing and Electrophysiology (Camm et al., 1996). The variances of these frequency components were transformed to natural logarithmic values (ln ms^2).

In addition, we also computed the deceleration and acceleration capacity (DC and AC) based on the phase rectified signal averaging of NN intervals (Bauer et al., 2006), and the fractal scaling exponents, the short-term exponent α_1 and the long-term α_2, using detrended fluctuation analysis (DFA; Peng et al., 1995).

MULTISCALE PROBABILITY DENSITY FUNCTION ANALYSIS

Recent studies from our group have shown that human HRV exhibits the intermittent dynamics or temporal heterogeneity of variance leading to non-Gaussian probability density function (PDF) of heart rate increments (Kiyono et al., 2004), especially in cardiac patients within timescales corresponding to LF and VLF ranges (Kiyono et al., 2008; Hayano et al., 2011). As such a feature, called *heteroscedasticity*, cannot be captured by conventional HRV indices, we conducted multiscale PDF analysis to characterize intermittent large deviations and the resultant non-Gaussianity of HRV.

The procedure starts from interpolating observed series of NN intervals with a cubic spline function and resampling at an interval (Δt) of 250 ms (4 Hz), yielding interpolated time series $b(t)$. Next after subtracting average interval b_{ave}, integrated time series $B(t)$ are obtained by integrating $b(t)$ over the entire length,

$$B(t) = \sum_{i=1}^{t/\Delta t} \{b(i\Delta t) - b_{ave}\}.$$

As in previous studies (Kiyono et al., 2004, 2008; Hayano et al., 2011), the local trend of $B(t)$ is eliminated by a third-order polynomial fit to $B(t)$ within moving windows of length 2*s*, where *s* is the scale of analysis. Thereafter, intermittent deviation $\Delta_s B(t)$ is measured as the increment with a time lag *s* of the detrended time series. For instance, in a window from time $T-s$ to $T+s$, the increments are calculated as follows:

$$\Delta_s B(t) = \left\{B(t + s/2) - f_{fit}(t + s/2)\right\} - \left\{B(t - s/2) - f_{fit}(t - s/2)\right\}$$

where $T - s/2 \le t < T + s/2$ and $f_{\mathrm{fit}}(t)$ is the polynomial representing the local trend of $B(t)$. $\Delta_s B(t)$ reflects an average degree of tachycardia if negative [$b(t) < b_{\mathrm{ave}}$] or bradycardia if positive [$b(t) > b_{\mathrm{ave}}$] over a moving window with length *s* (in seconds) after detrending. To quantitatively characterize the non-Gaussian property of $\Delta_s B(t)$ at scale *s*, the standardized PDF (variance set to one) constructed from all $\Delta_s B(t)$ values is approximated by the Castaing's model (Castaing et al., 1990) with a single parameter λ_s, which we refer to as the non-Gaussianity index. A greater λ_s indicates a fatter non-Gaussian tail and a sharper peak of PDF compared to the Gaussian distribution. On the other hand, if λ_s is close to zero, PDF is close to a Gaussian distribution. The parameter λ_s is estimated as follows:

$${\lambda_s}^2 = \frac{2}{q(q-2)}\left[\ln\left(\sqrt{\pi}\left\langle|\Delta_s B|^q\right\rangle\right) - \ln\Gamma\left(\frac{q+1}{2}\right) - \frac{q}{2}\ln 2\right],$$

where $q \neq 0$ or 2, $q > -1$, and $\langle|\Delta_s B|^q\rangle$ denotes the estimated value of the q-th order absolute moment of $\Delta_s B$ (Kiyono et al., 2007).

In the present study, we calculated λ_s using the 0.25-th order moment ($q = 0.25$) to emphasize the center part of PDF and

reduce the effects of large outliers such as those resulting from ectopic beats. This implies that our non-Gaussianity index with $q = 0.25$ more strongly characterizes peak PDF around the center of the observed non-Gaussian distribution, as opposed to higher-order moments, such as kurtosis based on the fourth moment, emphasizing heavy tails and extreme deviations. Based on our recent findings that increased λ_s at scale $s = 25$ s is associated with increased cardiac mortality risk and that this predictive power is independent of clinical risk factors in CHF and AMI patients (Kiyono et al., 2008; Hayano et al., 2011), we evaluated the non-Gaussianity index λ_{25s} at $s = 25$ s, which is at the edge of LF and VLF ranges.

An important feature of this multiscale PDF analysis is that if a time series has temporally homogeneous and finite variance, the increment PDF of the integrated series rapidly converges to a Gaussian distribution as the time-scale s increases because of the well-known statistical law called the central limit theorem. On the other hand, if neither condition is fulfilled, slow convergence to a Gaussian distribution or a scale-dependent λ_s and non-Gaussian fat tail can arise, suggestive of increased intermittency as observed in hydrodynamic turbulence (Castaing et al., 1990; Ghashghaie et al., 1996). Indeed, in the so-called multiplicative cascade model (Monin and Yaglom, 1975), one of the representative models describing intermittency of hydrodynamic turbulence and also used as a model of heart rate intermittency (Lin and Hughson, 2001), λ_s is known to have scale dependence in the form of $\lambda_s^2 \sim \ln s$ (Kiyono et al., 2007; **Figure 1**). In the cascade model, multiscaling properties of the increments called structure functions also exist in the corresponding scales (Kiyono et al., 2007). To evaluate such a dynamic (cascade-like) aspect of intermittent fluctuations, we calculated the slope of λ_s^2 vs. ln s (λ^2-slope) in the range $20 < s < 200$ s (mainly covering LF and VLF ranges).

STATISTICAL ANALYSIS

The data are reported as the mean ± SD. One-way ANOVA was used to test for statistical differences across groups, and Tukey's honestly significant difference test was used for pair-wise comparisons. For variables with skewed distributions, values were transformed to natural logarithms. The Kolmogorov–Smirnov test was used to assess differences in age distribution between groups. In addition, the bootstrap method (Efron and Tibshirani, 1993) was used to assess possible selection biases of age-matched control groups. Bootstrap samples having the same size as each of MSA and PD groups were generated by randomly drawing age-matched subjects with replacement from a pool of healthy subjects. $P < 0.05$ was considered significant.

RESULTS

Indices of autonomic function were derived from HRV recordings from MSA, PD, and CHF patients as well as from the three separate age-matched control groups (MSA controls, 63.6 ± 8.6 years vs.

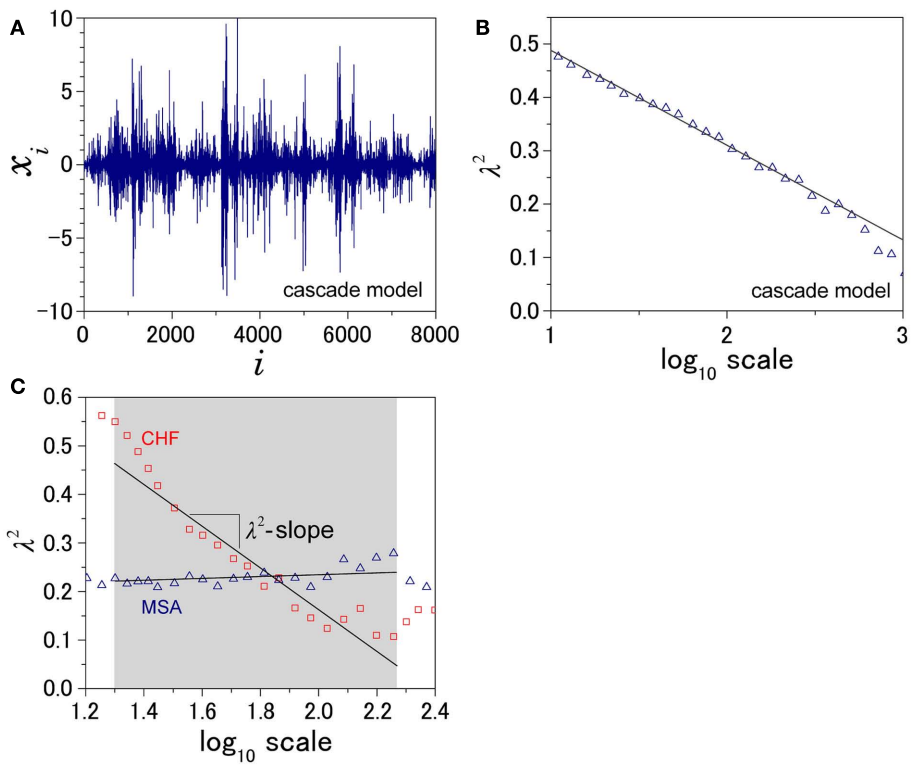

FIGURE 1 | Illustration of the definition of λ^2-slope. (A) An example of intermittent fluctuation generated by a cascade model (Kiyono et al., 2007) and **(B)** the scale dependence of λ^2, which is proportional to the logarithmic scale. To quantify this kind of intermittent behavior of HRV, λ^2-slope is defined as the slope of a regression line between λ^2 and the logarithmic scale in the range between 20 and 200 s. **(C)** Scale dependence of λ^2 for a patient with multiple system atrophy (MSA) and a patient with congestive heart failure (CHF).

MSA patients, 62.3 ± 7.4 years; PD controls, 68.5 ± 8.3 years vs. PD patients, 68.6 ± 7.9 years; CHF controls, 59.1 ± 16.0 years vs. CHF patients, 66.1 ± 14.8 years). The age distributions for the control groups were not significantly different from those for the patients' groups. Mean duration since MSA diagnosis was 3.3 ± 2.1 years (range, 1–9 years; **Table 1**). Mean duration since PD diagnosis was 10.7 ± 9.1 years (range, 2–31 years), and the mean Hoehn and Yahr score was 3.6 ± 0.7 (range, 3–5; **Table 2**).

CONVENTIONAL HRV INDICES

Table 3 presents HRV indices derived from HRV recordings from MSA patients and age-matched healthy control subjects, together with the bootstrap estimators for the healthy controls. Compared with the control group, the MSA patients showed significantly decreased HRV as indicated by lower SDNN, SDANN, and RMSSD values, reduced power in all spectral bands (HF, LF, VLF, ULF), and lower DC and AC. Indices such as LF/HF and DFA α_1 were also significantly decreased. Compared with the control group, the PD patients showed significant decreases only in LF and VLF power and significantly lower DC and AC (**Table 4**). LF/HF and DFA α_1 were significantly decreased. As shown in **Tables 3** and **4**, these findings were largely supported also by comparing mean values for the patient groups with 95%-confidence intervals of the bootstrap estimators. **Table 5** presents the HRV indices in CHF patients and age-matched healthy control subjects. Compared with the control group, both surviving and non-surviving CHF patients exhibited significantly decreased HRV as indicated by lower SDNN and SDANN, reduced power in LF, VLF, and ULF ranges, and lower

Table 3 | Heart rate variability measures in patients with multiple system atrophy (MSA) and age-matched controls.

	MSA ($n = 12$)	Age-matched control ($n = 69$)	*P* value	Bootstrap samples of age-matched control ($n = 12$)
Mean NN, ms	766 ± 89	775 ± 110	0.745	776 (723–832)
SDNN, ms	59.7 ± 23.0	90.4 ± 28.6	<0.001	89.0 (75.4–104.2)
SDANN, ms	19.9 ± 6.5	47.5 ± 28.7	<0.001	48.8 (35.5–64.5)
RMSSD, ms	13.6 ± 4.4	22.5 ± 11.4	<0.001	21.6 (16.3–27.6)
ln HF, ln ms^2	3.75 ± 0.90	4.97 ± 1.08	<0.001	4.93 (4.34–5.50)
ln LF, ln ms^2	4.02 ± 0.90	5.90 ± 0.97	<0.001	5.90 (5.39–6.36)
ln VLF, ln ms^2	5.92 ± 0.84	7.26 ± 0.81	<0.001	7.30 (6.89–7.72)
ln ULF, ln ms^2	7.78 ± 0.93	8.47 ± 0.64	0.029	8.45 (8.14–8.79)
LF/HF ratio	1.69 ± 1.24	3.28 ± 2.49	0.002	3.47 (2.25–4.87)
DC, ms	3.38 ± 0.98	6.23 ± 1.59	<0.001	5.82 (5.11–6.53)
AC, ms	−3.38 ± 0.93	−6.51 ± 1.77	<0.001	−6.13 (−6.94 to −5.28)
α_1	0.86 ± 0.24	1.17 ± 0.15	<0.001	1.21 (1.08–1.33)
α_2	1.23 ± 0.09	1.18 ± 0.04	0.118	1.19 (1.15–1.23)
λ_{25s}	0.46 ± 0.07	0.39 ± 0.07	0.005	0.38 (0.35–0.43)
λ^2-slope	−0.05 ± 0.12	−0.01 ± 0.08	0.309	0.00 (−0.04 to 0.04)

Fifth column shows mean value and 95%-confidence interval based on 2000 bootstrap samples. P< 0.05.

Table 4 | Heart rate variability measures in patients with Parkinson disease and age-matched controls.

	Parkinson disease ($n = 10$)	Age-matched control ($n = 60$)	*P* value	Bootstrap samples of age-matched control ($n = 10$)
Mean NN, ms	779 ± 118	780 ± 112	0.975	801 (717–885)
SDNN, ms	70.4 ± 33.5	91.6 ± 29.6	0.086	95.8 (76.1–118.7)
SDANN, ms	34.0 ± 26.7	46.6 ± 27.4	0.191	44.4 (30.3–62.2)
RMSSD, ms	18.2 ± 11.6	23.1 ± 12.8	0.240	26.3 (17.9–35.5)
ln HF, ln ms^2	4.21 ± 1.19	4.96 ± 1.13	0.089	5.00 (4.30–5.71)
ln LF, ln ms^2	4.22 ± 1.31	5.70 ± 0.97	0.006	5.69 (5.21–6.17)
ln VLF, ln ms^2	5.82 ± 1.20	7.17 ± 0.82	0.006	7.13 (6.68–7.56)
ln ULF, ln ms^2	8.15 ± 0.77	8.55 ± 0.64	0.148	8.66 (8.25–9.08)
LF/HF ratio	1.30 ± 1.03	2.62 ± 1.69	0.003	2.48 (1.60–3.54)
DC, ms	3.93 ± 1.41	5.46 ± 1.60	0.008	5.27 (4.45–6.11)
AC, ms	−4.03 ± 1.57	−5.80 ± 1.81	0.007	−5.74 (−6.80 to −4.73)
α_1	0.83 ± 0.28	1.12 ± 0.24	0.011	1.07 (0.96–1.19)
α_2	1.17 ± 0.08	1.19 ± 0.07	0.456	1.18 (1.14–1.23)
λ_{25s}	0.42 ± 0.09	0.40 ± 0.08	0.574	0.41 (0.37–0.46)
λ^2-slope	−0.01 ± 0.11	−0.02 ± 0.09	0.81	−0.02 (−0.06 to 0.03)

Fifth column shows mean value and 95%-confidence interval based on 2000 bootstrap samples. P< 0.05.

Table 5 | Heart rate variability indices in patients with congestive heart failure and age-matched controls.

	CHF (NS; $n=39$)	CHF (SV; $n=69$)	Control ($n=90$)	P value NS–SV	P value NS–C	P value SV-C
Mean NN, ms	758 ± 114	755 ± 140	782 ± 110	0.99	0.56	0.37
SDNN, ms	59.1 ± 31.1	59.7 ± 39.6	93.4 ± 29.0	0.99	<0.001	<0.001
SDANN, ms	33.0 ± 27.2	37.7 ± 33.6	51.6 ± 30.0	0.73	0.006	0.016
RMSSD, ms	37.6 ± 40.0	40.0 ± 48.3	24.5 ± 12.8	0.94	0.13	0.017
ln HF, ln ms^2	5.43 ± 1.57	5.30 ± 1.67	5.13 ± 1.12	0.89	0.82	0.75
ln LF, ln ms^2	4.97 ± 1.80	4.85 ± 1.63	5.97 ± 1.01	0.90	0.001	<0.001
ln VLF, ln ms^2	5.73 ± 1.36	6.04 ± 1.45	7.33 ± 0.83	0.40	<0.001	<0.001
ln ULF, ln ms^2	5.73 ± 1.23	6.04 ± 1.45	8.81 ± 0.64	0.66	<0.001	<0.001
LF/HF ratio	0.83 ± 0.79	0.93 ± 0.78	3.01 ± 2.31	0.95	<0.001	<0.001
DC, ms	3.39 ± 1.60	3.84 ± 2.01	5.87 ± 1.70	0.43	<0.001	<0.001
AC, ms	−4.34 ± 2.29	−4.69 ± 2.13	−6.27 ± 1.96	0.68	<0.001	<0.001
α_1	0.79 ± 0.26	0.72 ± 0.24	1.17 ± 0.25	0.44	<0.001	<0.001
α_2	0.93 ± 0.16	1.00 ± 0.21	1.18 ± 0.08	0.048	<0.001	<0.001
λ_{25s}	0.57 ± 0.18	0.48 ± 0.15	0.40 ± 0.08	<0.001	<0.001	<0.001
λ^2-slope	−0.21 ± 0.23	−0.13 ± 0.18	−0.02 ± 0.08	0.03	<0.001	<0.001

$P< 0.05$.

DC and AC. Indices such as LF/HF, and DFA α_1 and α_2 were also significantly decreased.

In the MSA patients, the pattern of changes in conventional HRV indices was similar to that observed in the CHF patients. While the decreased HRV in both MSA and CHF patients might reflect reduced vagal heart rate control, decreases in LF/HF and DFA α_1 were observed for both MSA, a disease with reported preganglionic sympathetic failure (Sone et al., 2005), and for CHF, a pathology associated with sympathetic overdrive (Packer, 1988; Ciarka et al., 2008). In contrast, no decreases in SDNN and HF power, indices of reduced HRV, were observed in the PD patients, which might reflect relatively intact vagal heart rate control. However, decreases in LF/HF and DFA α_1 were also observed in PD, a disease with reported postganglionic sympathetic failure (Braune et al., 1998, 1999).

NON-GAUSSIAN AND INTERMITTENT PROPERTIES OF HRV

Figure 2 shows representative results of the multiscale PDF analysis for MSA, CHF, and PD patients (one patient from each group) and a healthy subject. As shown in **Figures 2M–P**, HRV data from the MSA and PD patients and the healthy subject yielded similar PDF curves at each scale. In contrast, recordings from the CHF patient yielded a PDF curve with a more tapered center and fatter tails at relatively smaller scales. This reflects intermittent large deviations or *bursts* observed at $s = 20$ s in CHF patients (**Figure 2G**), while this increased intermittency was not observed in the MSA and PD patients. In addition, as the scale s increases, deformation of PDFs toward a Gaussian distribution was clearly observed only in the CHF patient. The deformation process of the non-Gaussian PDF can be described by the relation between the non-Gaussianity index λ_s and scale s. As shown in **Figure 3**, the MSA and PD patient groups and the healthy subject groups showed nearly constant λ_s^2 values across a wide range of scales s, resulting in an almost zero value λ^2-slope. In contrast, the CHF patient group, particularly non-survivors, was characterized by almost linear increases in λ_s^2 as the log scale decreased from 200 to 20 s, similar to that observed for a cascade model of intermittent turbulence (**Figure 1B**). Consequently, the λ^2-slope for the CHF patients was significantly more negative than that for the healthy controls.

λ_{25s} for the MSA patients was slightly but significantly higher than that for healthy controls (**Table 3**), although the level was much lower than that for CHF non-survivors (**Table 5**). λ_{25s} for the PD patients failed to increase compared with that for healthy controls (**Table 4**). Both MSA and PD patients with sympathetic failure had λ^2-slopes of almost zero, which were not significantly different from those of healthy controls (**Tables 3** and **4**). Only CHF patients with known sympathetic overdrive had significantly negative λ^2-slopes (**Table 5**).

DISCUSSION

Long-term ambulatory HRV continues to attract clinical interest as a useful tool for risk stratification in AMI (Kleiger et al., 1987; Bigger et al., 1996; La Rovere et al., 1998; Schmidt et al., 1999; Huikuri et al., 2000; Bauer et al., 2006) and chronic heart failure (Ho et al., 1997; Nolan et al., 1998; Mäkikallio et al., 2001). Patients at higher mortality risk frequently have higher heart rates with reduced and less complex (or monotonic) HRV, and most indices used to characterize such HRV dynamics primarily reflect reduced or impaired vagal function (Camm et al., 1996; Marine et al., 2002; Bauer et al., 2006). In contrast, few HRV indices are related to sympathetic function and their autonomic correlates and prognostic significance are still uncertain. For example, a decrease, but not the increase, in LF/HF, believed to reflect the sympathovagal balance (Pagani et al., 1986), is associated with increased mortality risk (Tsuji et al., 1994; Huikuri et al., 2000) in patients exhibiting sympathetic activation (Ciarka et al., 2008). Similarly, a decrease in DFA α_1, known to be correlated with LF/HF and sensitive to changes in the sympathovagal balance (Huikuri et al., 2009), is associated with increased mortality risk (Huikuri et al., 2000; Mäkikallio et al., 2001). The present study further demonstrated that both of these indices are also decreased in MSA, a neurodegenerative disorder associated with preganglionic sympathetic failure

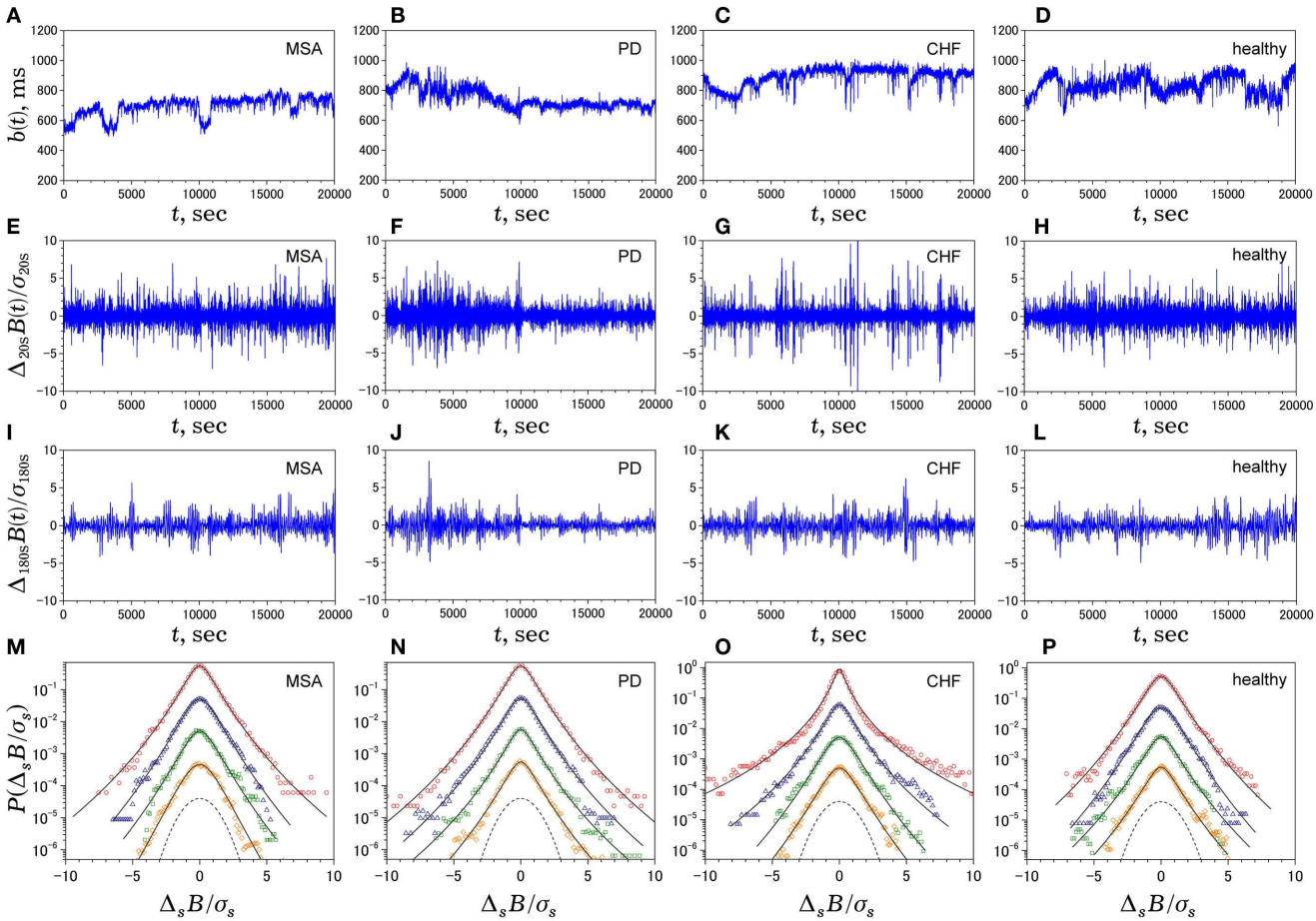

FIGURE 2 | Multiscale PDF characterization of heart rate variability. Illustrative examples of time series of NN intervals $b(t)$ **(A–D)**, time series of $\Delta_{20sB}(i)$ **(E–H)**, time series of $\Delta_{180sB}(i)$ **(I–L)**, and standardized PDFs (in logarithmic scale) of $\Delta_s B(i)$ for (from the top to bottom) $s = 20$, 60, 180, 300 s **(M–P)**, where σ_s denotes the SD of $\Delta_s B(i)$. In solid lines, we superimpose the PDF approximated by Castaing's model (Castaing et al., 1990). The panels on the leftmost side **(A,E,I,M)** are data for a 60-year-old male patient with multiple system atrophy (MSA). The panels on the left-of-center side **(B,F,J,N)** are data for a 68-year-old male patient with Parkinson disease (PD). The panels on the right-of-center side **(C,G,K,O)** are data for a 83-year-old female patient with congestive heart failure (CHF) who died 54 days after the measurement. The panels on the rightmost side **(D,H,L,P)** are data for a control subject (84-year-old male). For comparison, the dashed line denotes a Gaussian distribution. Note that, while the raw $b(t)$ for the patients looks much different from that for the control subject, the degrees of non-Gaussianity (i.e., the shapes of PDF) remain unaltered across scales for MSA and PD patients and the healthy control, except for those for the CHF patient at shorter scales **(G,O)**.

(Sone et al., 2005), and in PD, which is often accompanied by postganglionic sympathetic failure (Braune et al., 1998, 1999).

As a marker potentially related to sympathetic cardiac overdrive, we have recently introduced increased non-Gaussianity of HRV within LF and VLF ranges in patients with CHF and AMI (Kiyono et al., 2008; Hayano et al., 2011), cardiopathologies known to be associated with sympathetic overdrive (Packer, 1988; Ciarka et al., 2008). In the present study, we further demonstrated that a marked increase in intermittent and non-Gaussian HRV was not observed in MSA and PD patients with sympathetic failure. We still have not determined why λ_{25s} for the MSA patients was slightly but significantly higher than that for healthy controls; this enhanced non-Gaussianity may be due to adrenergic stimulants administered to ameliorate severe orthostatic symptoms in the MSA patients. However, the scale-dependent increase in λ_s^2 with decreasing log scales mainly within the VLF range, leading to a markedly higher λ_{25s} in the CHF patients (**Table 5**), was not observed in MSA. Therefore, we suggest that the systematically increased non-Gaussianity of HRV within LF and VLF ranges could be a hallmark of sympathetic cardiac overdrive and that indices such as λ_{25s} and λ^2-slope could be used to measure the degree of sympathetic activation. Indeed, we recently observed decreased λ_{25s} in the AMI patients taking (anti-sympathetic) β-blockers (Hayano et al., 2011).

Using concepts developed in statistical and non-linear physics, it has been demonstrated that the healthy human heart rate fluctuates in a complex manner even under resting conditions, exhibiting fractal long-range correlations (Peng et al., 1993; Yamamoto and Hughson, 1994) and multifractal properties (Ivanov et al., 1999; Amaral et al., 2001; Ching and Tsang, 2007). Based on these findings, Lin and Hughson (2001) proposed an analogy between heart rate dynamics and hydrodynamic turbulence because a

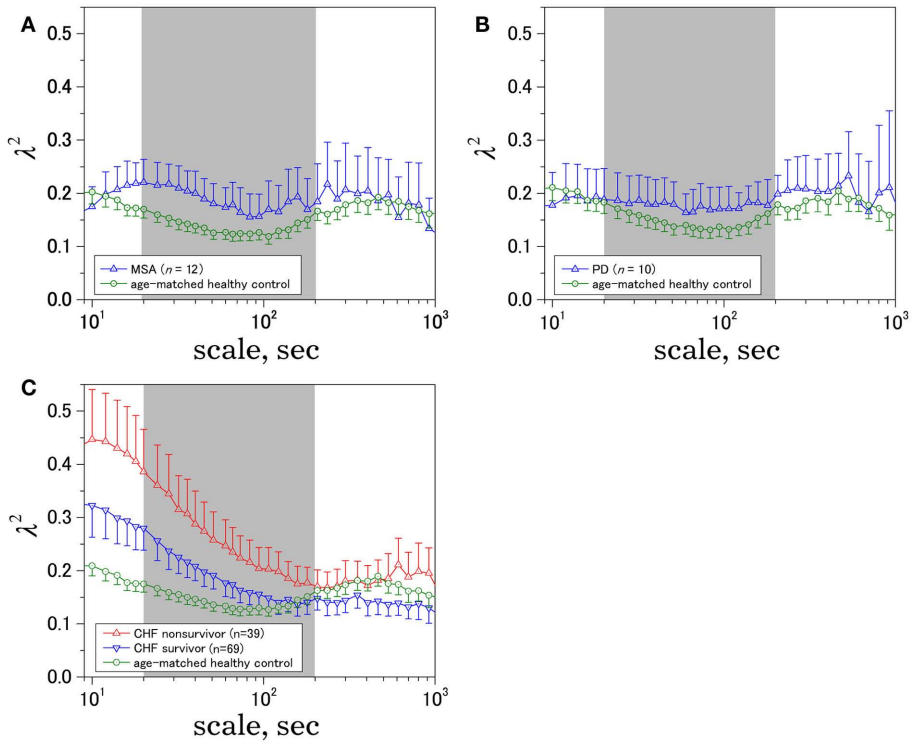

FIGURE 3 | Time-scale dependence of the non-Gaussianity index, λ^2. The results for **(A)** multiple system atrophy (MSA), **(B)** Parkinson disease (PD), and **(C)** congestive heart failure (CHF) patients, both for survivor (SV; $n = 69$) and non-survivor (NS; $n = 39$). Age-matched controls were selected from a database of healthy subjects. Error bars indicate 95%-confidence intervals of the group averages.

phenomenological model of hydrodynamic turbulence, called the multiplicative cascade model (Monin and Yaglom, 1975), can also have multifractal properties. Using multiscale PDF analysis, we later demonstrated that the healthy human HRV does not show slow and gradual convergence to a Gaussian distribution (Kiyono et al., 2004; **Figure 3**), an important requirement of the multiplicative cascade model (**Figure 1B**). In contrast, the present study and previous work (Kiyono et al., 2008) suggest that HRV within LF and VLF ranges of CHF patients, especially non-survivors, is more compatible with the multiplicative cascade model.

The multiplicative (log-normal) cascade model used to generate fluctuations with intermittent bursts such as those shown in **Figure 1A** is given by

$$x_i = \xi_i \exp\left[\sum_{j=1}^{m} \omega^{(j)}\left(\left\lfloor \frac{j-1}{2^{m-j}} \right\rfloor\right)\right],$$

where ξ_i is Gaussian white noise with zero mean, $\omega^{(j)}(k)$ are independent Gaussian random variables with zero mean and constant variance, and $(\cdot($ is the floor function (Kiyono et al., 2007). The m is the total number of cascade steps, yielding the total number of data points 2^m ($i = 1, \ldots, 2^m$). An essential part of the model is that ξ_i is modulated by multiplication of random (log-normal) weights $\exp[\omega^{(j)}(k)]$ ($k = 0, 1, \ldots, 2^j - 1$) at the j-th step every 2^{m-j} subintervals; therefore, large fluctuations are observed only when the momentary weights for (many) different steps with varying timescales are simultaneously large (refer to Figure 5 of Kiyono et al., 2007). Using multiscale PDF analysis, Kiyono et al. (2007) further showed that this model exhibits the scale dependence of a non-Gaussianity index in the form of $\lambda_s^2 \sim \ln s$ (**Figure 1B**).

The fact that heart rate dynamics of CHF patients with sympathetic activation exhibit a non-Gaussianity index which decays with scales within LF and VLF ranges suggests a sympathetic origin for HRV intermittency. In these scales (20–200 s), heart rate dynamics reflect cardiovascular regulation by neural, humoral, and thermal influences (Kitney and Rompelman, 1980). These subsystems are considered to be compensatory; therefore, it is likely that only simultaneous failure of all these subsystems operating at multiple timescales, compatible with the reciprocal of cascade steps "j" in the above example, could result in sympathetic overdrive, leading to large and intermittent heart rate deviations. We propose that such a *multiplicative picture* would provide a deeper physiological understanding of the nature of sympathetic function. In addition, it would provide a reason why methods requiring stationary, not intermittent, dynamics have not been successful in finding the sympathetic correlates of ambulatory HRV.

In the present study, we focused on daytime HRV for the following reasons. First, as reported in our previous study (Kiyono et al., 2005), there are large differences in non-Gaussianity and its scale dependence between day and night in healthy humans, presumably because of the difference in the sympathovagal balance. Second,

disorders of sleep and sleep breathing are common in MSA (Colosimo, 2011); therefore, incorporating nighttime data would inevitably introduce additional complexity. Third, one of our goals is to assess sympathetic activity, which is predominant during the day. Note that this shift from 24-h HRV to daytime HRV does not change our previous finding of the increased non-Gaussianity of low frequency HRV in CHF patients than in healthy controls (Kiyono et al., 2008).

In agreement with previous studies (Gurevich et al., 2004; Kuriyama et al., 2005), our MSA patients showed significantly decreased HRV, as evidenced by lower SDNN and HF power. This decrease is probably related to the known abnormalities in central vagal (Benarroch et al., 2006) and sympathetic function in these patients (Sone et al., 2005). On the other hand, changes in SDNN and HF power were not significant in PD patients, implying relatively intact vagal heart rate control despite the impaired peripheral, cardiac sympathetic function (Braune et al., 1998, 1999). Thus, analyses of ambulatory HRV may facilitate discriminative diagnosis between MSA and PD, particularly the difficult distinction between early stage PD and MSA with predominant Parkinsonian symptoms (Lipp et al., 2009).

ACKNOWLEDGMENTS

This research was supported in part by a Grant-in-Aid for Scientific Research (A) (23240094; to Yoshiharu Yamamoto) from the Japan Society for the Promotion of Science (JSPS) and by Core Research for Evolutional Science and Technology from Japan Science and Technology Agency (JST; to Yoshiharu Yamamoto).

REFERENCES

Amaral, L. A. N., Ivanov, P., Aoyagi, N., Hidaka, I., Tomono, S., Goldberger, A. L., Stanley, H. E., and Yamamoto, Y. (2001). Behavioral-independent features of complex heartbeat dynamics. *Phys. Rev. Lett.* 86, 6026–6029.

Bauer, A., Kantelhardt, J. W., Barthel, P., Schneider, R., Mäkikallio, T., Ulm, K., Hnatkova, K., Schömig, A., Huikuri, H. V., Bunde, A., Malik, M., and Schmidt, G. (2006). Deceleration capacity of heart rate as a predictor of mortality after myocardial infarction: cohort study. *Lancet* 367, 1674–1681.

Benarroch, E. E., Schmeichel, A. M., Sandroni, P., Low, P. A., and Parisi, J. E. (2006). Involvement of vagal autonomic nuclei in multiple system atrophy and Lewy body disease. *Neurology* 66, 378–383.

Bigger, J. T., Steinman, R. C., Rolnitzky, L. M., Fleiss, J. L., Albrecht, P., and Cohen, R. J. (1996). Power law behavior of RR-interval variability in healthy middle-aged persons, patients with recent acute myocardial infarction, and patients with heart transplants. *Circulation* 93, 2142–2151.

Braune, S., Reinhardt, M., Bathmann, J., Krause, T., Lehmann, M., and Lücking, C. H. (1998). Impaired cardiac uptake of meta-[123I]iodobenzylguanidine in Parkinson's disease with autonomic failure. *Acta Neurol. Scand.* 97, 307–314.

Braune, S., Reinhardt, M., Schnitzer, R., Riedel, A., and Lücking, C. H. (1999). Cardiac uptake of [123I]MIBG separates Parkinson's disease from multiple system atrophy. *Neurology* 53, 1020–1025.

Camm, A. J., Malik, M., Bigger, J. T. Jr., Breithardt, G., Cerutti, S., Cohen, R. J., Coumel, P., Fallen, E. L., Kleiger, R. E., Lombardi, F., Malliani, A., Moss, A. J., Rottman, J. N., Schmidt, G., Schwartz, P. J., and Singer, D. H. (1996). Heart rate variability: standards of measurement, physiological interpretation and clinical use. Task Force of the European Society of Cardiology and the North American Society of Pacing and Electrophysiology. *Circulation* 93, 1043–1065.

Castaing, B., Gagne, Y., and Hopfinger, E. (1990). Velocity probability density functions of high Reynolds number turbulence. *Physica D* 46, 177–200.

Ching, E. S. C., and Tsang, Y.-K. (2007). Multifractality and scale invariance in human heartbeat dynamics. *Phys. Rev. E Stat. Nonlin. Soft Matter Phys.* 76, 041910.

Ciarka, A., van de Borne, P., and Pathak, A. (2008). Myocardial infarction, heart failure and sympathetic nervous system activity: new pharmacological approaches that affect neurohumoral activation. *Expert Opin. Investig. Drugs* 17, 1315–1330.

Colosimo, C. (2011). Nonmotor presentations of multiple system atrophy. *Nat. Rev. Neurol.* 7, 295–298.

Efron, B., and Tibshirani, R. J. (1993). *An Introduction to the Bootstrap*. New York: Chapman & Hall.

Ghashghaie, S., Breymann, W., Peinke, J., Talkner, P., and Dodge, Y. (1996). Turbulent cascades in foreign exchange markets. *Nature* 381, 767–770.

Gilman, S., Wenning, G. K., Low, P. A., Brooks, D. J., Mathias, C. J., Trojanowski, J. Q., Wood, N. W., Colosimo, C., Dürr, A., Fowler, C. J., Kaufmann, H., Klockgether, T., Lees, A., Poewe, W., Quinn, N., Revesz, T., Robertson, D., Sandroni, P., Seppi, K., and Vidailhet, M. (2008). Second consensus statement on the diagnosis of multiple system atrophy. *Neurology* 71, 670–676.

Gurevich, T. Y., Groozman, G. B., Giladi, N., Drory, V. E., Hausdorff, J. M., and Korczyn, A. D. (2004). R-R interval variation in Parkinson's disease and multiple system atrophy. *Acta Neurol. Scand.* 109, 276–279.

Hayano, J., Kiyono, K., Struzik, Z. R., Yamamoto, Y., Watanabe, E., Stein, P. K., Watkins, L. L., Blumenthal, J. A., and Carney, R. M. (2011). Increased non-Gaussianity of heart rate variability predicts cardiac mortality after an acute myocardial infarction. *Front. Physiol.* 2:65. doi:10.3389/fphys.2011.00065

Ho, K. K. L., Moody, G. B., Peng, C.-K., Mietus, J. E., Larson, M. G., Levy, D., and Goldberger, A. L. (1997). Predicting survival in heart failure case and control subjects by use of fully automated methods for deriving nonlinear and conventional indices of heart rate dynamics. *Circulation* 96, 842–848.

Hughes, A. J., Daniel, S. E., Kilford, L., and Lees, A. J. (1992). Accuracy of clinical diagnosis of idiopathic Parkinson's disease: a clinico-pathological study of 100 cases. *J. Neurol. Neurosurg. Psychiatr.* 55, 181–184.

Huikuri, H. V., Mäkikallio, T. H., Peng, C.-K., Goldberger, A. L., Hintze, U., and Møller, M. (2000). Fractal correlation properties of R-R interval dynamics and mortality in patients with depressed left ventricular function after an acute myocardial infarction. *Circulation* 101, 47–53.

Huikuri, H. V., Perkiömäki, J. S., Maestri, R., and Pinna, G. D. (2009). Clinical impact of evaluation of cardiovascular control by novel methods of heart rate dynamics. *Philos. Transact. A Math. Phys. Eng. Sci.* 367, 1223–1238.

Ivanov, P. C., Amaral, L. A. N., Goldberger, A. L., Havlin, S., Rosenblum, M. G., Struzik, Z. R., and Stanley, H. E. (1999). Multifractality in human heart rate dynamics. *Nature* 399, 461–465.

Kitney, R. I., and Rompelman, O. (eds). (1980). *The Study of Heart-Rate Variability*. Oxford: Clarendon Press.

Kiyono, K., Hayano, J., Watanabe, E., Struzik, Z. R., and Yamamoto, Y. (2008). Non-Gaussian heart rate as an independent predictor of mortality in patients with chronic heart failure. *Heart Rhythm* 5, 261–268.

Kiyono, K., Struzik, Z. R., Aoyagi, N., Sakata, S., Hayano, J., and Yamamoto, Y. (2004). Critical scale invariance in a healthy human heart rate. *Phys. Rev. Lett.* 93, 178103.

Kiyono, K., Struzik, Z. R., Aoyagi, N., Togo, F., and Yamamoto, Y. (2005). Phase transition in a healthy human heart rate. *Phys. Rev. Lett.* 95, 058101.

Kiyono, K., Struzik, Z. R., and Yamamoto, Y. (2007). Estimator of a non-Gaussian parameter in multiplicative log-normal models. *Phys. Rev. E Stat. Nonlin. Soft Matter Phys.* 76, 041113.

Kleiger, R. E., Miller, J. P., Bigger, J. T., Moss, A. J., and The Multicenter Post-Infarction Research Group. (1987). Decreased heart rate variability and its association with increased mortality after acute myocardial infarction. *Am. J. Cardiol.* 59, 256–262.

Kuriyama, N., Mizuno, T., Iida, A., Watanabe, Y., and Nakagawa, M. (2005). Autonomic nervous evaluation in the early stages of olivopontocerebellar atrophy. *Auton. Neurosci.* 123, 87–93.

La Rovere, M. T., Bigger, J. T., Marcus, F. I., Mortara, A., and Schwartz, P. J. (1998). Baroreflex sensitivity and heart-rate variability in prediction of total cardiac mortality after myocardial infarction. *Lancet* 351, 478–484.

Lin, D., and Hughson, R. L. (2001). Modeling heart rate variability in healthy humans: a turbulence analogy. *Phys. Rev. Lett.* 86, 1650–1653.

Lipp, A., Sandroni, P., Ahlskog, J. E., Fealey, R. D., Kimpinski, K., Iodice, V., Gehrking, T. L., Weigand, S. D., Sletten, D. M., Gehrking, J. A., Nickander, K. K., Singer, W., Maraganore, D. M., Gilman, S., Wenning, G. K., Shults, C. W., and Low, P. A. (2009). Prospective differentiation of multiple system atrophy from Parkinson disease, with and without autonomic failure. *Arch. Neurol.* 66, 742–750.

Mäkikallio, T. H., Huikuri, H. V., Hintze, U., Videbaek, J., Mitrani, R. D., Castellanos, A., Myeburg, R. J., Møller, M., and Myerburg, R. J. (2001). Fractal analysis and time- and frequency-domain measures of heart rate variability as predictors of mortality in patients with heart failure. *Am. J. Cardiol.* 87, 178–182.

Marine, J. E., Watanabe, M. A., Smith, T. W., and Monahan, K. M. (2002). Effect of atropine on heart rate turbulence. *Am. J. Cardiol.* 89, 767–769.

McEwen, B. S. (1998). Protective and damaging effects of stress mediators. *N. Engl. J. Med.* 338, 171–179.

McEwen, B. S. (2007). Physiology and neurobiology of stress and adaptation: central role of the brain. *Physiol. Rev.* 87, 873–904.

Monin, A. S., and Yaglom, A. M. (1975). *Statistical Fluid Mechanics.* Cambridge, MA: MIT Press.

Nolan, J., Batin, P. D., Andrews, R., Lindsay, S. J., Brooksby, P., Mullen, M., Baig, W., Flapan, A. D., Cowley, A., Prescott, R. J., Neilson, J. M., and Fox, K. A. (1998). Prospective study of heart rate variability and mortality in chronic heart failure. Results of the United Kingdom heart failure evaluation and assessment of risk trial (UK-Heart). *Circulation* 98, 1510–1516.

Packer, M. (1988). Neurohormonal interactions and adaptations in congestive heart failure. *Circulation* 77, 721.

Pagani, M., Lombardi, F., Guzzetti, S., Rimoldi, O., Furlan, R., Pizzinelli, P., Sandrone, G., Malfatto, G., Dell'Orto, S., Piccaluga, E., Turiel, M., Baselli, G., Cerutti, S., and Malliani, A. (1986). Power spectral analysis of heart rate and arterial pressure variabilities as a marker of sympatho-vagal interaction in man and conscious dog. *Circ. Res.* 59, 178–193.

Peng, C. K., Havlin, S., Stanley, H. E., and Goldberger, A. L. (1995). Quantification of scaling exponents and crossover phenomena in nonstationary heartbeat time series. *Chaos* 5, 82–87.

Peng, C.-K., Mietus, J., Hausdorff, J. M., Havlin, S., Stanley, H. E., and Goldberger, A. L. (1993). Long-range anticorrelations and non-Gaussian behavior of the heartbeat. *Phys. Rev. Lett.* 70, 1343–1346.

Schmidt, G., Malik, M., Barthel, P., Schneider, R., Ulm, K., Rolnitzky, L., and Camm, A. J. (1999). Heart-rate turbulence after ventricular premature beats as a predictor of mortality after acute myocardial infarction. *Lancet* 353, 1390–1396.

Schwartz, P. J., Billman, G. E., and Stone, H. L. (1984). Autonomic mechanisms in ventricular fibrillation induced by myocardial ischemia during exercise in dogs with healed myocardial infarction. An experimental preparation for sudden cardiac death. *Circulation* 69, 790–800.

Sone, M., Yoshida, M., Hashizume, Y., Hishikawa, N., and Sobue, G. (2005). alpha-Synuclein-immunoreactive structure formation is enhanced in sympathetic ganglia of patients with multiple system atrophy. *Acta Neuropathol.* 110, 19–26.

Stefanova, N., Bücke, P., Duerr, S., and Wenning, G. K. (2009). Multiple system atrophy: an update. *Lancet Neurol.* 8, 1172–1178.

Tsuji, H., Venditti, F. J., Manders, E. S., Evans, J. C., Larson, M. G., Feldman, C. L., and Levy, D. (1994). Reduced heart rate variability and mortality risk in an elderly cohort. The Framingham Heart Study. *Circulation* 90, 878–883.

Wenning, G. K., Stefanova, N., Jellinger, K. A., Poewe, W., and Schlossmacher, M. G. (2008). Multiple system atrophy: a primary oligodendrogliopathy. *Ann. Neurol.* 64, 239–246.

Yamamoto, Y., and Hughson, R. L. (1994). On the fractal nature of heart rate variability in humans: effects of data length and beta-adrenergic blockade. *Am. J. Physiol.* 266, R40–R49.

Conflict of Interest Statement: The authors declare that the research was conducted in the absence of any commercial or financial relationships that could be construed as a potential conflict of interest.

Received: 09 December 2011; accepted: 07 February 2012; published online: 22 February 2012.

Citation: Kiyono K, Hayano J, Kwak S, Watanabe E and Yamamoto Y (2012) Non-Gaussianity of low frequency heart rate variability and sympathetic activation: lack of increases in multiple system atrophy and Parkinson disease. Front. Physio. ***3****:34. doi: 10.3389/fphys.2012.00034*

This article was submitted to Frontiers in Computational Physiology and Medicine, a specialty of Frontiers in Physiology.

frontiers in
PHYSIOLOGY

ORIGINAL RESEARCH ARTICLE
published: 07 November 2011
doi: 10.3389/fphys.2011.00080

Information domain approach to the investigation of cardio-vascular, cardio-pulmonary, and vasculo-pulmonary causal couplings

Luca Faes[1]*, Giandomenico Nollo[1] and Alberto Porta[2]

[1] *Department of Physics and BIOtech, University of Trento, Trento, Italy*
[2] *Department of Technologies for Health, Galeazzi Orthopaedic Institute, University of Milan, Milan, Italy*

Edited by:
Riccardo Barbieri, Massachusetts Institute of Technology, USA

Reviewed by:
Silvina Ponce Dawson, Universidad de Buenos Aires, Argentina
Lilianne Rivka Mujica-Parodi, State University of New York at Stony Brook, USA
Andreas Voss, University of Applied Sciences Jena, Germany

***Correspondence:**
Luca Faes, Department of Physics and BIOtech, University of Trento, via delle Regole 101, 38060 Mattarello, Trento, Italy.
e-mail: luca.faes@unitn.it

The physiological mechanisms related to cardio-vascular (CV), cardio-pulmonary (CP), and vasculo-pulmonary (VP) regulation may be probed through multivariate time series analysis tools. This study applied an information domain approach for the evaluation of non-linear causality to the beat-to-beat variability series of heart period (t), systolic arterial pressure (s), and respiration (r) measured during tilt testing and paced breathing (PB) protocols. The approach quantifies the causal coupling from the series i to the series j (C_{ij}) as the amount of information flowing from i to j. A measure of directionality is also obtained as the difference between two reciprocal causal couplings ($D_{i,j} = C_{ij} - C_{ji}$). Significant causal coupling and directionality were detected respectively when the median of C_{ij} over subjects was positive ($C_{ij} > 0$), and when $D_{i,j}$ was statistically different from zero ($D_{i,j} > 0$ or $D_{i,j} < 0$). The method was applied on t, s, and r series measured in 15 healthy subjects (22–32 years, 8 males) in the supine (su) and upright (up) positions, and in further 15 subjects (21–29 years, 7 males) during spontaneous (sp) and paced (pa) breathing. In the control condition (su, sp), a significant causal coupling was observed for C_{rs}, C_{rt}, C_{st}, and C_{ts}, and significant directionality was present only from r to t ($D_{r,t} > 0$). During head-up tilt (up, sp), C_{rs} was preserved, C_{rt} decreased to zero median, and C_{st} and C_{ts} increased significantly; directionality vanished between r and t ($D_{r,t} = 0$) and raised from s to t ($D_{s,t} > 0$). During PB (su, pa), C_{rs} increased significantly, C_{rt} and C_{ts} were preserved, and C_{st} decreased to zero median; directionality was preserved from r to t ($D_{r,t} > 0$), and raised from r to s ($D_{r,s} > 0$). These results suggest that the approach may reflect modifications of CV, CP, and VP mechanisms consequent to altered physiological conditions, such as the baroreflex engagement and the dampening of respiratory sinus arrhythmia induced by tilt, or the respiratory driving on arterial pressure induced by PB. Thus, it could be suggested as a tool for the non-invasive monitoring of CV and cardiorespiratory control systems in normal and impaired conditions.

Keywords: arterial pressure variability, baroreflex, causality, conditional entropy, head-up tilt, heart rate variability, paced breathing, respiratory sinus arrhythmia

INTRODUCTION

The heart period (HP), measured from the ECG as the duration of the temporal interval occurring between two consecutive R waves in the ECG (RR interval), and the systolic arterial pressure (SAP), measured from the arterial pressure signal as the maximum pressure value following each R wave (**Figure 1A**), exhibit spontaneous beat-to-beat fluctuations around their mean value, which are clearly visible in time series recordings of few hundred beats (**Figures 1B–D**). These fluctuations, generally known as cardio-vascular (CV) variability, are the result of the complex interplay of several physiological mechanisms (Malpas, 2002). It is indeed well known that HP and SAP interact in a closed-loop: HP changes affect SAP variations according to Starling law and arterial Windkessel, while, in turn, SAP changes are sensed by baroreceptors and induce corresponding HP variations through the baroreflex (Baselli et al., 1988; Saul et al., 1991; Taylor and Eckberg, 1996; Mullen et al., 1997; Nollo et al., 2005; Porta et al., 2011b). Besides the reciprocal regulation of HP and SAP, CV variability is continually perturbed by the respiratory activity, in accordance with a number of mechanisms including mechanical effects on intrathoracic pressure and stroke volume (Toska and Eriksen, 1993), Bainbridge reflex (Jones, 1962), and inhibition of central vagal outflow by respiratory neuron firing (Gilbey et al., 1984). As the interaction and/or competition among all these mechanisms is solicited by experimental maneuvers and is altered in the presence of CV diseases, the joint analysis of HP, SAP, and respiratory

Abbreviations: CE, conditional entropy; CP, cardio-pulmonary; CV, cardio-vascular; ECG, electrocardiogram; HP, heart period; pa, paced breathing condition; PB, paced breathing protocol; R wave, deflection in the ECG representing early depolarization of the ventricles; RF, respiratory flow; RR interval, temporal interval between two consecutive R waves in the ECG; SAP, systolic arterial pressure; sp, spontaneous breathing condition; su, supine body position; TT, tilt test protocol; up, upright body position; VP, vasculo-pulmonary.

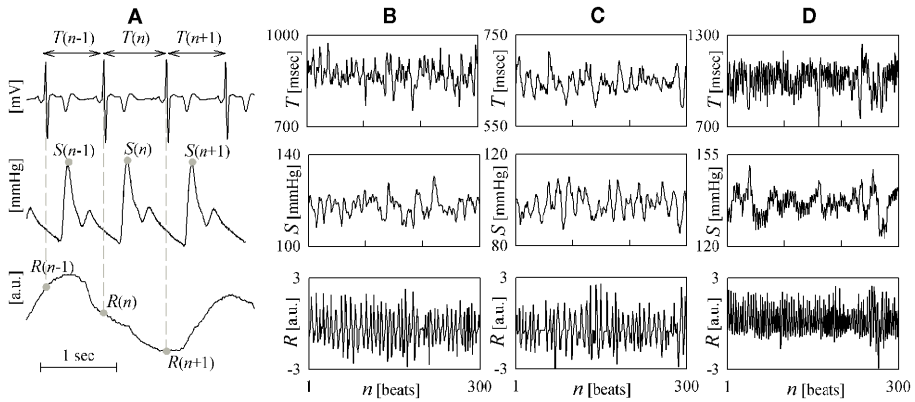

FIGURE 1 | Illustrative example of time series measurement and visualization. (A) Measurement of heart period (*T*), systolic arterial pressure (*S*) and respiration (*R*) variability series from the ECG, arterial blood pressure, and respiratory flow signals; consecutive R waves, representing early depolarization of the ventricles, correspond to the sharp positive deflections of the ECG. Representative examples of the three measured time series are reported for a subject breathing spontaneously in the supine position **(B)** and in the upright position **(C)**, and undergoing paced breathing in the supine position **(D)**.

flow (RF) variability series is widely exploited to non-invasively assess CV, cardio-pulmonary (CP), and vasculo-pulmonary (VP) regulations.

Indeed, a variety of time series analysis methods have been proposed in the last decades to quantify CV and cardiorespiratory interactions through the study of simultaneously measured HP, SAP, and RF spontaneous variability. While classical approaches were used to detect the presence of an interaction and quantify its strength, e.g., by means of linear coherence or non-linear coupling measures (De Boer et al., 1985; Taylor and Eckberg, 1996; Hoyer et al., 1998; Pompe et al., 1998; Cooke et al., 1999; Baumert et al., 2005; Bai et al., 2008; Suhrbier et al., 2010; Kabir et al., 2011), recent developments aimed to infer the causal direction along which a given interaction occurs. The assessment of causality in CV, CP, and VP interactions is relevant because it suggests which is the mechanism governing the interaction under analysis. A common approach to quantify the causal coupling between two variability series is the causal coherence (Porta et al., 2002), which quantifies causality from the frequency domain representation of a linear parametric bivariate model fitted to the two considered series. This method has been exploited to study causality between HP and SAP in physiological and impaired conditions (Nollo et al., 2005; Faes et al., 2006). It has been also extended to multivariate models including respiration for the contemporaneous assessment of CV and CP causal couplings both in the time domain (Porta et al., 2011a) and – following the introduction of partial directed coherence (Baccalà and Sameshima, 2001) – even in the frequency domain (Faes and Nollo, 2010). Linear time series analysis methods are well suited for the study of CV, CP, and VP interactions because they lend themselves to spectral representation, so that coupling and causality can be assessed for specific rhythms such as Mayer waves and respiratory frequency oscillations. Notwithstanding this, non-linear approaches are often desired as they may account better than linear methods for the high number and complexity of the mechanisms underlying CV and cardiorespiratory variability. The evaluation of non-linear causal coupling between cardiac, vascular, and respiratory time series has been performed in the past according to approaches based on phase synchronization (Rosenblum et al., 2002), non-linear prediction (Faes and Nollo, 2006; Faes et al., 2008b), non-linear model identification (Faes et al., 2008a; Riedl et al., 2010), symbolic coupling traces (Wessel et al., 2009; Suhrbier et al., 2010), and information theory (Porta et al., 1999; Palus et al., 2004). Among others, methods based on information theory constitute a valid, model-free approach to quantify non-linear causality based on the information amount transferred from one series to the other. In particular, information theoretic tools based on conditional entropy (CE) estimation have been framed in the so-called information domain (Porta et al., 2000b), and have been exploited to detect causal information transfers in the CV loop in a variety of physiological conditions (Nollo et al., 2002; Faes et al., 2011b; Porta et al., 2011b).

A major issue with the approaches to non-linear causality listed above stands in the fact that their application to CV and cardiorespiratory interactions has been limited so far to bivariate analysis involving only two of the available variability series. When more than two variables are expected to contribute to the dynamics under investigation, time series may be linked to each other in a direct or indirect manner. In this case, the use of bivariate analysis to assess causality between two of the series may be misleading. For example, one series may falsely appear to cause another if they are both influenced by a third series but with different delays. This situation is likely occurring in CP and VP analysis, where respiration acts as an exogenous input on both HP and SAP variability. Therefore, there is the need to extend traditional bivariate approaches to multivariate time series analysis able to settle issues of false causalities. In the frame of information theory, such an extension of is not a trivial task because it is hindered by practical aspects like the bias in CE estimation, or the issues of arbitrariness and redundancy related to the choice of the analysis parameters (Vakorin et al., 2009; Angelini et al., 2010; Faes et al., 2011a). To circumvent these problems, we have recently proposed an approach for estimating in the information domain the non-linear causal

coupling between two series taken from a multivariate data set (Faes et al., 2011a). The approach, which combines an objective and non-redundant procedure for the selection of the analysis parameters with an efficient estimation of the CE (Porta et al., 1998, 1999), has been validated on several simulation schemes and tested on representative multivariate physiological time series. In the present study, it is exploited to assess the causal coupling between cardiac, vascular, and respiratory variability series in physiological conditions. To this end, HP, SAP, and RF series were measured in a group of healthy subjects during two protocols able to solicit CV, CP, and VP regulatory systems, i.e., tilt testing and paced breathing (PB). The subsequent analysis allowed us to describe the physiological mechanisms involved in the regulation of cardiac, vascular, and respiratory systems, and to track their alterations consequent to modification of the experimental conditions.

MATERIALS AND METHODS

EXPERIMENTAL PROTOCOLS AND DATA ANALYSIS

We considered 30 young subjects (25.7 ± 2.7 years old), all normotensive and free from any known disease based on anamnesis and physical examination at the time of the study. Experiments were performed at the Cardiology Unit of the S. Chiara Hospital of Trento, Italy. Informed consent was provided by all subjects, and the experimental protocol was approved by the Ethical Committee of the hospital. Fifteen subjects were assigned to the tilt test (TT) protocol, while the remaining 15 subjects participated to the PB protocol. In both protocols, CV and cardiorespiratory signals were acquired in the morning, in comparably comfortable and quiet ambiance conditions with subjects in sinus rhythm. After a period of 10 min allowed for stabilization of the subjects, signals were acquired for 15 min in the resting supine position with spontaneous breathing. In the TT protocol, head-up tilting of the subjects was then achieved passively using a motorized table, and signals were acquired for further 15 min in the 60° upright position. In the PB protocol, the second part of the experiment consisted in signal acquisition for further 15 min with subjects inhaling and exhaling in time with a metronome acting at 15 cycles per minute (forced respiration at 0.25 Hz).

The acquired signals were the surface ECG (lead II), the finger photoplethysmographic arterial blood pressure (Finapres, Ohmeda), and the respiratory nasal flow (by differential pressure transducer). Signals were collected simultaneously and digitized at 1 kHz sampling rate and 12 bit precision. The beat-to-beat variability series of HP, SAP, and RF were then offline measured respectively as outlined in **Figure 1A**. Specifically, the n-th cardiac interval was identified from the ECG as the temporal interval occurring between the n-th and the $(n+1)$-th R waves, and its duration was taken as the n-th HP and denoted as $T(n)$; the corresponding SAP and RF values, denoted as $S(n)$ and $R(n)$, were measured respectively as the local maximum of the pressure signal inside the n-th cardiac interval, and as the sample of the respiratory tracing taken at the onset of the n-th cardiac interval. This measurement convention allows instantaneous (i.e., non-delayed) effects from $S(n)$ to $T(n)$, as well as from $R(n)$ to $S(n)$ and to $T(n)$. The subsequent data analysis was performed on windows of 300 beats, judged as stationary by visual inspection, taken in the two conditions of each protocol, i.e., supine (su) and upright (up) body positions for the TT protocol, and spontaneous (sp) and paced (pa) respiration for the PB protocol (an example is in **Figures 1B–D**). For each selected window, the measured series T, S, and R were normalized to zero mean and unit variance prior to the execution of non-linear analyses; for each series, normalization was performed by mean subtraction followed by division to the SD, thus obtaining the dimensionless normalized series $t(n)$, $s(n)$, and $r(n)$, $n = 1,\ldots,300$.

ANALYSIS OF NON-LINEAR CAUSAL COUPLING

The assessment of non-linear causal coupling is performed according to the approach proposed in (Faes et al., 2011a). This approach is grounded on the notion of Granger causality (Granger, 1969), that leads to compute the strength of the directional coupling from one series to another, say from x to y, as the improvement in the ability to describe y yielded by incorporating information from x into the considered descriptive scheme. In this study, time series description is framed in the information domain, and causality is quantified exploiting the concept of CE. The CE quantifies the amount of information carried by a time series, conditioned to the knowledge of a so-called *conditioning vector* formed by properly chosen samples of the available time series. As such, the CE is a measure inversely related to the ability to describe a series, because it drops to zero when the series is fully described by the assigned conditioning vector. Then, the assessment of causality from x to y is based on computing two times the CE of y, using different conditioning vectors: in the first repetition the conditioning vector includes past samples of y only, in the second repetition it includes past samples of both x and y. The difference between the CE computed at the two repetitions is a measure of causality from x to y, because it quantifies the amount of information carried by y that can be explained exclusively by the past of x. This idea is at the basis of the concept of transfer entropy proposed by Schreiber (2000), and is exploited also in the present study. The novelty of the approach used here, which is presented in detail in the next subsections, stands in the procedures followed to define the conditioning vector and to estimate the CE from time series data (Faes et al., 2011a).

Scheme for conditional entropy computation

Entropy computation presupposes to work in a probabilistic framework where, for instance, $p(y(n))$ is the probability for the process underlying the measured series y to take the value $y(n)$ at the time instant n. Within this framework, the entropy of the series y, $H(y)$, measures the amount of information carried by its most recent sample, $y(n)$, and is defined as $H(y) = -\Sigma\, p(y(n))\cdot\log p(y(n))$ (Porta et al., 1998). Then, to compute the CE we need to determine a conditioning vector formed by properly chosen terms of y and of the other available time series. Here a "term" is a time series point identified with respect to the present time sample n: for instance, $y(n)$ is the current term of y, $x(n-1)$ is the first past term of x, and so on. Formally, the CE of the series y conditioned to the vector V, $H(y|V)$, is defined as the residual amount of information carried by $y(n)$ when the conditioning vector V is assigned, and is commonly computed as an entropy rate: $H(y|V) = H(y(n), V) - H(V)$.

Since the CE is a measure of the degree of unpredictability of a series when the conditioning vector is known, its interpretation depends on how the conditioning vector is formed. For instance, $H(y|V)$ is a measure of irregularity of y when V is composed exclusively by past terms of y (Porta et al., 1998), while – as shown in the next subsection – $H(y|V)$ can be exploited to assess causality from x to y when V incorporates also past terms of x. In either case, conditioning vectors are traditionally formed according to an uniform scheme whereby all past terms up to a maximum lag are selected simultaneously. However, uniform conditioning introduces issues of arbitrariness and redundancy that are likely to hinder CE estimation in many situations (Faes et al., 2011a). To overcome this limitation, we follow here a conditioning scheme based on a non-uniform, sequential procedure that builds progressively the conditioning vector by selecting, from a properly defined set of *initial candidate terms*, the terms that optimize the description of the observed series; optimization of the description is intended here as minimization of CE. For the generic series y and set of initial candidate terms Y, the procedure starts with an empty conditioning vector V_0 and, at the k-th step, tests all the candidate terms $z \in Y$ computing the entropy of y conditioned to the vector $[z, V_{k-1}]$, i.e., $H(y|[z, V_{k-1}])$; among all candidates, the selected term is the one which minimizes the CE, i.e., the updated conditioning vector at step k is $V_k = [\acute{z}, V_{k-1}]$ such that $\acute{z} = arg\ min(H(y|[z, V_{k-1}]))$. As stopping criterion for the conditioning scheme, we chose to terminate the procedure when a minimum of the CE is found, i.e., at the step K such that $H(y|V_K) > H(y|V_{K-1})$; in non-uniform conditioning, the minimum obtained CE is taken as a measure of the information carried by y when the set of initial candidates is assigned, i.e., $H(y|Y) = H(y|V_{K-1})$. We note that the criterion for candidate selection is based on information reduction (i.e., CE minimization after testing all candidates at each step) rather than on temporal ordering. Hence, it may happen that a past term is selected before a more recent term; however, this does not affect the resulting measure, as the joint probabilities used in entropy computation are insensitive to the ordering of components within vector variables.

An example illustrating the difference between uniform and non-uniform conditioning is depicted in **Figure 2**. If we want to compute the entropy for a generic time series y conditioned to its own past, and we choose to include three terms into the conditioning vector, the uniform scheme simply picks up the terms $y(n-1)$, $y(n-2)$, and $y(n-3)$ to form the conditioning vector $V_u = [y(n-1), y(n-2), y(n-3)]$ (**Figure 2A**); this vector is then used to compute the CE value $H(y|V_u)$ depicted in **Figure 2C** (red dashed line). On the contrary, the non-uniform procedure first defines a set of candidate terms [$Y = \{y(n-1),\ldots,y(n-10)\}$ in this example, white circles in **Figure 2B**], then proceeds iteratively, testing at each step all the terms and selecting the one which minimizes the CE: in the example, the first selected term is $y(n-2)$, the second is $y(n-6)$, and the third is $y(n-4)$; the three CE minimum values obtained progressively using the vectors $V_1 = [y(n-2)]$, $V_2 = [y(n-2), y(n-6)]$, and $V_3 = [y(n-2), y(n-6), y(n-4)]$ are depicted as blue squares in **Figure 2C**, where the final CE value $H(y|Y) = H(y|V_3)$ is also indicated (blue dashed line). Note that the non-uniform procedure reaches a lower

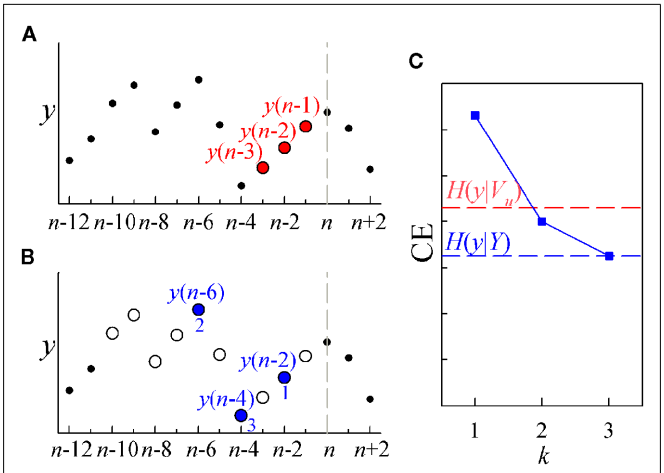

FIGURE 2 | Illustrative example of CE computation for a representative short sequence of a time series *y* (dots), with overlapped the terms exploited for uniform conditioning [(A), red] and for non-uniform conditioning [(B), blue]; in (B), empty circles denote the set of initial candidate terms, while filled circles denote selected terms, with the number indicating the step *k* at which selection occurred; the vertical dashed lines mark the current time sample *n*. (C) CE computed after uniform conditioning [$H(y|V_u)$, red dashed line] and after non-uniform conditioning [$H(y|Y)$, blue dashed line]; the CE computed at each step k of the sequential procedure for non-uniform conditioning is indicated by blue squares.

CE than the uniform one, indicating a higher capability of describing the time series which comes from the purposeful selection of the candidate terms allowed by the repeated exploration of the whole set of candidates.

Conditional entropy-based computation of causal coupling

The assessment of causality between two series taken from a multivariate data set in the information domain is based on performing two times the procedure explained in Section "Scheme for Conditional Entropy Computation," modifying the conditioning vector used to estimate the CE. Specifically, to assess causality from x to y the procedure is repeated starting from different sets of initial candidates: first, using the set Y_1 in which the past samples of the series x are excluded; then, using the set Y_2 in which the terms of x are included. The causal coupling from x to y is defined as the normalized difference between the CE minima estimated for the two repetitions of the procedure, i.e., $C_{x\to y} = 1 - H(y|Y_2)/H(y|Y_1)$. The enlargement of the set of candidates at the second repetition allows the possibility for some terms from x to be included in the conditioning vector describing y. When this happens, the inclusion is interpreted as the existence of causality from x to y; in such a case, the CE decreases compared to the first repetition [$H(y|Y_2) < H(y|Y_1)$], and a positive causal coupling $C_{x\to y}$ is measured; in the limit case when the CE decreases to zero, the maximum causal coupling $C_{x\to y} = 1$ is measured. On the contrary, when no terms from x are selected at the second repetition, the CE is unchanged and $C_{x\to y} = 0$, indicating the absence of causality. Note that the whole analysis may be performed reversing the roles of the two series, so that the causal coupling from y to x,

$C_{y\to x}$, is estimated. Finally, an index of directionality is defined as the difference of the two causal couplings: $D_{x,y} = C_{x\to y} - C_{y\to x}$. With this definition, the directionality index is positive (respectively, negative) when the prevailing causal direction is that from x to y (from y to x).

In this study, the role of the generic series x and y is assumed by two of the available normalized variability series t, s, and r. The sets of initial candidates may include, depending on the specific direction of interaction under analysis, the past values of the normalized HP series, $Yt = \{t(n-\tau),\ldots,t(n-L\tau)\}$, SAP series, $Ys = \{s(n-\tau),\ldots,s(n-L\tau)\}$, and RF series, $Yr = \{r(n-\tau),\ldots, r(n-L\tau)\}$, where L is the number of candidate terms to be included in the initial set for each series ($L = 10$ in this study). Note that in this application the candidate terms are not immediately subsequent terms of the time series, but are separated in time using a so-called time delay τ; the time delay is introduced to optimize the description of the dynamics of each variable accounting for its peculiar time scale (Small, 2005). In this study, the time delay τ was optimized separately for each series by testing it on the range (1, 20) and taking the lag such that the autocorrelation of the series has first dropped below $1/e$ (the so-called decorrelation time Small, 2005). Moreover, when appropriate the extended sets $\tilde{Y}r = \{r(n), Yr\}$ and $\tilde{Y}s = \{s(n), Ys\}$ may be used in place of Yr and Ys as they account for instantaneous causality. Specifically, since the adopted measurement conventions allow for the existence of instantaneous causality from $r(n)$ to $s(n)$ and to $t(n)$, as well as from $s(n)$ to $t(n)$ (see **Figure 1A**), the extended set $\tilde{Y}r$ was used in place of Yr to compute the CE of s and t, while the extended set $\tilde{Y}s$ was used in place of Ys to compute the CE of t. With this notation, we define the following indexes of causal coupling and directionality for the VP regulatory loop:

$$C_{r\to s} = 1 - \frac{H\left(s|\left\{Y_s, \tilde{Y}_r, Y_t\right\}\right)}{H\left(s|\left\{Y_s, Y_t\right\}\right)},\quad C_{s\to r} = 1 - \frac{H\left(r|\left\{Y_s, Y_r, Y_t\right\}\right)}{H\left(r|\left\{Y_r, Y_t\right\}\right)}, \tag{1a}$$

$$D_{r,s} = C_{r\to s} - C_{s\to r}, \tag{1b}$$

the CP regulatory loop:

$$C_{r\to t} = 1 - \frac{H\left(t|\left\{\tilde{Y}_s, \tilde{Y}_r, Y_t\right\}\right)}{H\left(t|\left\{\tilde{Y}_s, Y_t\right\}\right)},\quad C_{t\to r} = 1 - \frac{H\left(r|\left\{Y_s, Y_r, Y_t\right\}\right)}{H\left(r|\left\{Y_s, Y_r\right\}\right)}, \tag{2a}$$

$$D_{r,t} = C_{r\to t} - C_{t\to r}, \tag{2b}$$

and the CV regulatory loop:

$$C_{s\to t} = 1 - \frac{H\left(t|\left\{\tilde{Y}_s, \tilde{Y}_r, Y_t\right\}\right)}{H\left(t|\left\{\tilde{Y}_r, Y\right\}\right)},\quad C_{t\to s} = 1 - \frac{H\left(s|\left\{Y_s, \tilde{Y}_r, Y_t\right\}\right)}{H\left(s|\left\{Y_s, \tilde{Y}_r\right\}\right)}, \tag{3a}$$

$$D_{s,t} = C_{s\to t} - C_{t\to s}. \tag{3b}$$

Figure 3 reports an illustrative example of estimation of the causal coupling from RF to HP (i.e., from the series r to the series t). In the first repetition of the conditioning procedure (**Figure 3A**), the series r is excluded from the analysis so that the conditioning vector is formed drawing terms from the set of initial candidates $Y_1 = \{\tilde{Y}s, Yt\} = \{s(n), s(n-\tau_s),\ldots, s(n-L\tau_s), t(n-\tau_t),\ldots, t(n-L\tau_t)\}$. In the second repetition (**Figure 3B**), all the three series are used so that the set of initial candidates becomes $Y_2 = \{\tilde{Y}s, Yt, \tilde{Y}r\} = \{s(n), s(n-\tau_s),\ldots, s(n-L\tau_s), t(n-\tau_t),\ldots, t(n-L\tau_t), r(n), r(n-\tau_r),\ldots, r(n-L\tau_r)\}$. In the representation of **Figure 3** we set $L = 10$, while the optimal time delays for the HP, SAP, and RF series are $\tau_t = 2$, $\tau_s = 3$, and $\tau_r = 1$, respectively. At the first repetition, the terms selected sequentially from Y_1 are $t(n-2)$, $s(n-3)$, and $t(n-4)$, then the procedure terminates at the step $K = 4$ because the CE minimum, $H(t|\{\tilde{Y}s, Yt\}) = H(t|V_3)$, is reached at $k = 3$ (**Figure 3C**, black). At the second repetition the first selected term is the same as before [i.e., $t(n-2)$], but with $k = 2$ a term from r, $r(n)$, is selected such that a lower CE is estimated; the final conditioning vector is $V_3 = [t(n-2), r(n), s(n-3)]$ and the corresponding CE minimum, $H(t|\{\tilde{Y}s, \tilde{Y}r, Yt\})$, is lower than that at the first repetition, so that the resulting causal coupling, $C_{r\to t}$, is larger than zero.

Estimation of conditional entropy

The implementation of the procedure described above for quantifying non-linear causal coupling requires estimation of the CE from time series of finite length, which in turn relies on estimation of entropy for any vector V composed of terms of the analyzed time series (see Scheme for Conditional Entropy Computation). In this study we adopted the estimation strategy proposed in (Porta et al., 1998, 1999), which is based on performing uniform quantization of the available time series to estimate CE in terms of entropy rate, and then on introducing a corrective term

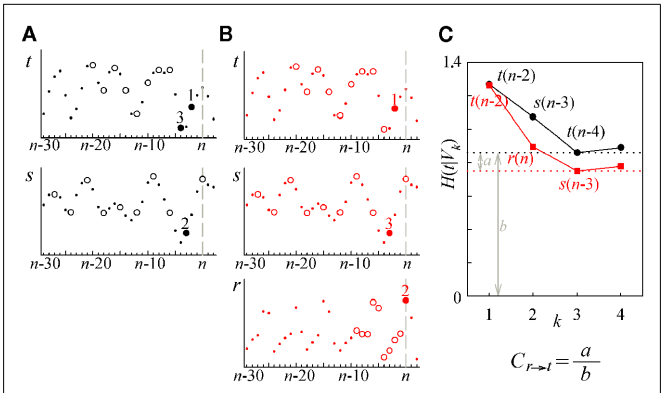

FIGURE 3 | Illustrative example of estimation of causal coupling from respiratory flow to heart period time series. (A,B) Representative short sequences of the three series t, s, and r (dots), plotted together with the sets of initial candidate terms (circles, separated to each other by the lag τ peculiar of each series) for the first repetition **(A)** and the second repetition **(B)** of the conditioning scheme followed to estimate the causal coupling from r to t; filled circles denote the selected terms, with the number indicating the step k at which selection occurred; the vertical dashed lines mark the current time sample n. **(C)** Conditional Entropy computed for the first (black) and second (red) repetitions of the conditioning procedure; the candidate components selected at each step of the procedure are indicated in the plot; horizontal dashed lines mark the resulting entropies $H(t|\{\tilde{Y}s, Yt\})$ and $H(t|\{\tilde{Y}s, \tilde{Y}r, Yt\})$, which, combined as in Eq. 2a, yield the causal coupling $C_{r\to t}$.

to compensate the estimation bias due to shortness of the analyzed time series.

Specifically, each normalized series was coarse grained spreading its dynamics over Q quantization levels, so that a symbol in the range 1,. . .,Q is associated with each sample. For an assigned vector of k terms, uniform quantization corresponds to partitioning the k-dimensional space, into which the terms may take values, in Q^k disjoint hypercubes, such that all vectors falling within the same hypercube are considered as undistinguishable to each other. Once the partition is assigned, entropies may be computed approximating the probabilities with their frequency of occurrence within the hypercubes. In order for this approximation to hold reasonably, a relation should exist between the number of quantization levels Q and the number of time series point N such that $N \approx Q^k$ (Porta et al., 1998). Therefore, we chose $Q = 6$ in this study where $N = 300$ and the length of the conditioning vectors, k, is typically equal to 3 or 4. The strategy for CE estimation is illustrated in the example of **Figure 4**, which makes reference to the estimation of the CE of the series t conditioned to the vector $V_2 = [t(n-2), s(n-3)]$ [**Figure 3A** and $H(t|V_2)$ in **Figure 3C**]. **Figure 4A** refers to the estimation of the entropy $H(V_2)$, where the range of all possible values for the past terms $t(n-2)$ and $s(n-3)$ is quantized in $Q = 6$ levels and then entropy is estimated extending the summation to all hypercubes (which have square form in this case with $k = 2$). In **Figure 4B** the dimensionality of the space is increased as a consequence of considering the present term $t(n)$, and entropy is computed again. Finally, the CE results as the information increase.

A problem with CE estimation consists in the bias due to bad estimation of probabilities in high dimensional spaces and short time series (Porta et al., 1999; Faes et al., 2011a). This bias affects causality estimates, and prevents from reaching a CE minimum to be used as stopping criterion for the sequential procedure of candidate selection. The effect is due to the fact that, letting k increase, an increasing number of vectors V will be found alone within an hypercube of the k-dimensional space (gray squares in the example of **Figure 4A**). As a consequence, the corresponding vectors $[y(n), V]$ will be also alone inside an hypercube of the $(k+1)$-dimensional space (gray squares in **Figure 4B**), and therefore their contribution to the CE will be null. To counteract this bias, we use the corrected CE defined as (Porta et al., 1999; Faes et al., 2011a): $H^c(y|V) = H(y|V) + n(V) \cdot H(y(n))$, where $n(V)$ is the fraction of values for V that fall alone inside a hypercube. With the correction, in the presence of a single point inside a hypercube, its null contribution is substituted with the maximal information amount carried by a white noise with the same amplitude distribution of the observed series y [i.e., $H(y(n))$].

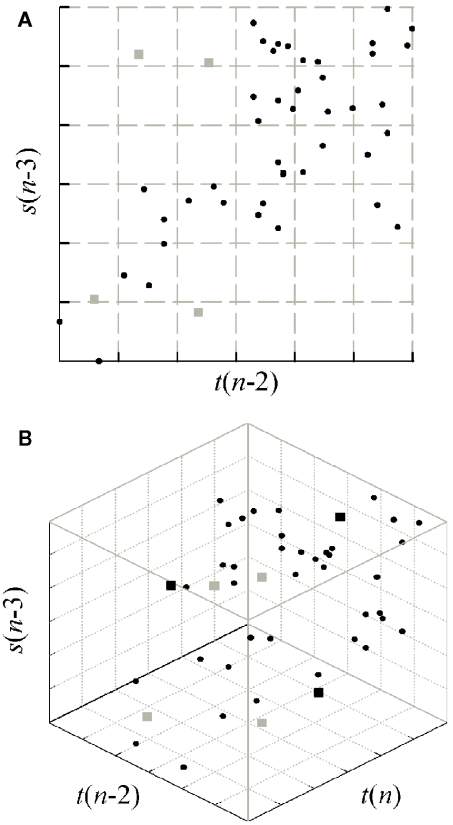

FIGURE 4 | Example of space partitioning for CE computation at the step $k = 2$ of Figure 3A (first repetition of the procedure). (A) To compute $H(V_2)$, all values assumed by the vector $V_2 = [t(n-2), s(n-3)]$ are assigned to hypercubes resulting from uniform quantization of the two coordinates (gray grid); then, the entropy is computed as $H(V_2) = -\Sigma p(V_2) \cdot \log p(V_2)$. **(B)** The analysis is repeated for all values assumed by the vector $[t(n), V_2] = [t(n), t(n-2), s(n-3)]$ to compute $H(t(n), V_2) = -\Sigma p(t(n), V_2) \cdot \log p(t(n), V_2)$. In both cases, the probability p is estimated for an hypercube as the frequency of occurrence of the points inside each hypercube. Then, the CE is measured as $H(t|V_2) = H(t(n), V_2) - H(V_2)$. The corrected CE is finally computed as $H^c(t|V_2) = H(t|V_2) + n(V_2)H(t(n))$, where $n(V_2)$ is the fraction of V_2 values found alone into a hypercube in panel **(A)** (gray squares, $n(V_2) = 4/47$ in this example). Note that single points in **(A)** remain always single also in the higher dimensional space in **(B)**, while other single points may arise in **(B)** (black squares).

STATISTICAL ANALYSIS

We performed the Kolmogorov–Smirnov normality test for each distribution of causal coupling index C and directionality index D obtained for the various pairs of series in the various experimental conditions. If normality was verified, a paired Student's t-test was used to check the significance of differences of C and D between experimental conditions (su vs. up for the TT protocol, or sp vs. pa for the PB protocol). The Student's t-test was used also to assess the significance of the directionality index D, i.e., to test the hypothesis that the data in D come from a distribution with zero mean. If the normality test was not fulfilled, the Wilcoxon signed rank test for paired data was used in place of the Student's t-test.

We used the McNemar test for paired proportions to check the significance of changes in the number of subjects for which the causal coupling C was larger than zero (i.e., at least one candidate term from x is selected at the second repetition of the conditioning procedure for computation of $C_{x \to y}$) between experimental conditions. In all tests, a $p < 0.05$ was considered statistically significant.

RESULTS

TIME DOMAIN ANALYSIS

A representative example of HP, SAP, and RF variability series recorded in the different experimental conditions during the TT and PB protocols is reported in **Figure 1** (**Figure 1B**: su, sp; **Figure 1C**: up, sp; **Figure 1D**: su, pa). The trends of the time domain CV parameters for the whole population are summarized in **Table 1**. While in the control condition of spontaneous breathing in the supine position results were averaged over all 30 subjects, the statistical analysis was performed by paired tests involving only the 15 subjects who underwent tilt testing or PB; in the control condition, no differences were observed for the time domain parameters computed between the groups participating to the two protocols. The mean HP decreased significantly moving from the supine to the upright position, and increased significantly moving from spontaneous to PB. The HP variability, measured as the SD of the RR intervals, was unchanged after tilt and increased significantly with PB. While the mean SAP was not modified, its SD increased significantly during tilt testing.

The optimal time delay for candidate selection estimated in the supine position during spontaneous breathing, reported in **Table 2**, was lower for the RF than for the SAP and HP series ($N = 30$ subjects). When subjects moved to the upright position (TT protocol, $N = 15$) the time delay increased significantly for RF and HP series, and was stable for the SAP series. During paced breathing (PB protocol, $N = 15$), the delay values decreased significantly for RF and HP series, while the decrease was not statistically significant for the SAP series.

CAUSAL COUPLING AND DIRECTIONALITY ANALYSES

The results of causal coupling and directionality analyses performed during the two considered experimental protocols are summarized in **Table 3**. A graphical representation of the results and statistical trends for coupling and directionality indexes is reported in **Figure 5** for the TT protocol, and in **Figure 6** for the PB protocol.

The control condition with subjects in the supine position with spontaneous breathing is described by the distributions of white symbols in **Figures 5** and **6**, which show agreeing results. Specifically, for VP interactions (**Figures 5** and **6**, white triangles) the causal coupling distributions have non-zero median from RF to SAP ($C_{r\to s}$), and zero median from SAP to RF ($C_{s\to r}$); however, the prevalence of causality from RF to SAP is not marked enough to set statistically significant directionality $D_{r,s}$. The causal coupling for CP interactions (**Figures 5** and **6**, white squares) is clearly unidirectional, as $C_{r\to t}$ is remarkable while $C_{t\to r}$ has zero median; moreover, a statistically significant directionality is set from RF to HP variability. As to the CV loop (**Figures 5** and **6**, white circles), both $C_{s\to t}$ and $C_{t\to s}$ have non-zero median, but there is no prevalence of one of the two couplings as $D_{s,t}$ is not significantly different from zero.

Table 1 | Time domain characterization of heart period (HP) and systolic arterial pressure (SAP) variability during tilt test and paced breathing protocols.

	Supine, spontaneous breathing ($N = 30$)	Upright, spontaneous breathing ($N = 15$)	Supine, paced breathing ($N = 15$)
Mean HP, ms	910 ± 116	696 ± 75**	1019 ± 126*
SD HP, ms	46 ± 19	41 ± 18	74 ± 38*
Mean SAP, mmHg	124.0 ± 24.9	117.0 ± 15.1	129.5 ± 24.4
SD SAP, mmHg	3.4 ± 1.4	5.9 ± 1.7**	3.6 ± 1.0

*Values are mean ± SD. *$p < 0.05$, **$p < 0.005$ vs. supine spontaneous breathing (Paired test over $N = 15$ subjects).*

Table 2 | Optimal time delay for the selection of candidate terms to be tested in the estimation of conditional entropy.

	Supine, spontaneous breathing ($N = 30$)	Upright, spontaneous breathing ($N = 15$)	Supine, paced breathing ($N = 15$)
Respiratory flow	1.2 ± 0.4	1.5 ± 0.5*	1.0 ± 0.1*
Systolic arterial pressure	3.7 ± 1.5	3.6 ± 0.8	2.9 ± 1.4
Heart period	1.9 ± 0.6	3.8 ± 0.7**	1.5 ± 0.5*

*Values are measured in beats and are expressed as mean ± SD. *$p < 0.05$, **$p < 0.005$ vs. supine spontaneous breathing (Paired test over $N = 15$ subjects).*

Table 3 | Causal coupling index *C* and directionality index *D* computed between respiratory flow (*r*), systolic arterial pressure (*s*), and heart period (*t*) time series measured during the tilt test protocol (TT; su: supine position, up: upright position) and during the paced breathing protocol (PB; sp: spontaneous breathing, pa: paced breathing) in the study of vasculo-pulmonary (VP), cardio-pulmonary (CP), and cardio-vascular (CV) coupling.

		TT protocol ($N = 15$)		PB protocol ($N = 15$)	
		su	up	sp	pa
VP	$C_{r\to s}$	0.010 (8)	0.031 (9)	0.008 (8)	0.046** (12)
	$C_{s\to r}$	0 (5)	0 (6)	0 (6)	0 (3)
	$D_{r,s}$	0.010	0.022	0	0.046#**
CP	$C_{r\to t}$	0.040 (13)	0** (4§)	0.113 (15)	0.079 (15)
	$C_{t\to r}$	0 (1)	0 (2)	0 (2)	0 (4)
	$D_{r,t}$	0.040#	0**	0.104#	0.067#
CV	$C_{s\to t}$	0.022 (9)	0.118** (15§)	0.017 (9)	0 (6)
	$C_{t\to s}$	0.035 (9)	0.046* (9)	0.017 (9)	0.011 (8)
	$D_{s,t}$	0	0.072#**	0	0

*Values are the median over 15 subjects; values in brackets are the number of subjects (out of 15) for which non-zero causal coupling was found. *$p < 0.05$, **$p < 0.005$ up vs. su and sp vs. pa (paired test); #$p < 0.005$, directionality index D is different from zero (paired test); §$p < 0.05$, su vs. up or sp vs. pa (proportion test).*

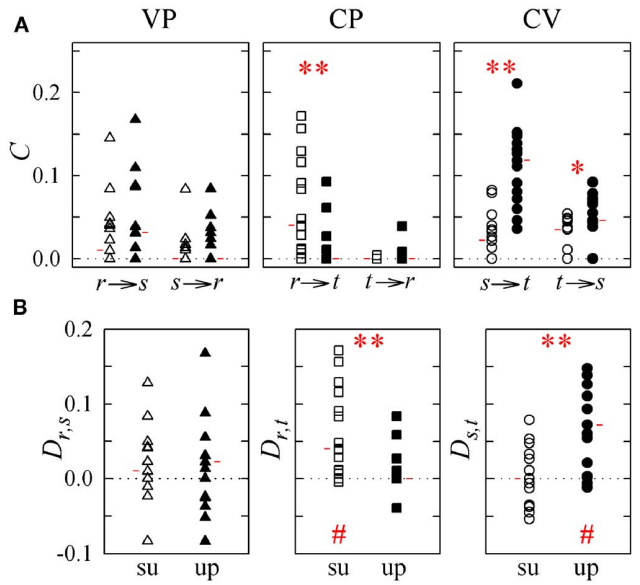

FIGURE 5 | Causal coupling index *C* (A) and directionality index *D* (B) computed for subjects in the supine position (su, white symbols) and in the upright position (up, black symbols) in the study of vasculo-pulmonary (VP, triangles), cardio-pulmonary (CP, squares), and cardio-vascular (CV, circles) coupling (*r*: respiration, *s*: systolic pressure; *t*: heart period). Horizontal red marks denote the median of each distribution. $^{*}p < 0.05$, $^{**}p < 0.005$ supine vs. upright; $^{\#}p < 0.005$, directionality index *D* is different from zero.

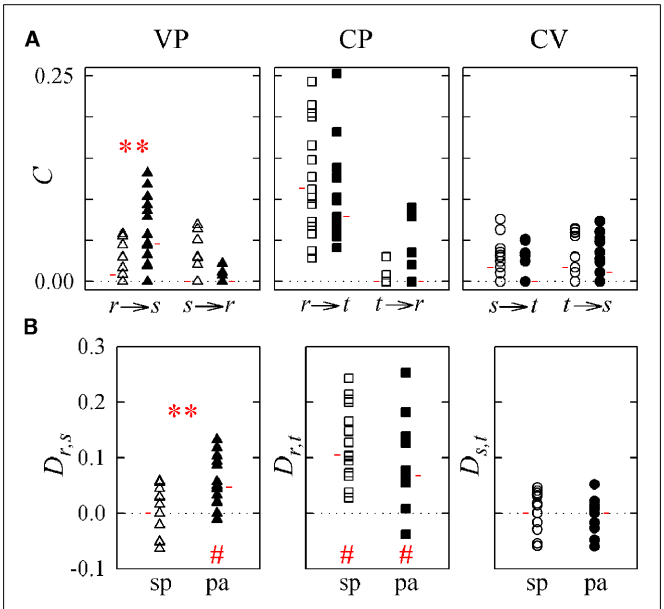

FIGURE 6 | Causal coupling index *C* (A) and directionality index *D* (B) computed for subjects during spontaneous breathing (sp, white symbols) and during paced breathing (pa, black symbols) in the study of vasculo-pulmonary (VP, triangles), cardio-pulmonary (CP, squares), and cardio-vascular (CV, circles) coupling (*r*: respiration, *s*: systolic pressure; *t*: heart period). Horizontal red marks denote the median of each distribution. $^{**}p < 0.005$ spontaneous vs. paced breathing; $^{\#}p < 0.005$, directionality index *D* is different from zero.

When subjects are tilted in the 60° position (**Figure 5**), causal coupling values do not change substantially between *s* and *r*, decrease significantly from *r* to *t*, and increase significantly both from *s* to *t* and from *t* to *s*. As a result, in the upright position directionality is still non-significant for VP interactions, disappears for CP interactions, and is set from *s* to *t* in the CV regulatory loop (**Figure 5B**; **Table 3**). When subjects undergo PB (**Figure 6**), the causal coupling increases significantly from *r* to *s* and does not change significantly along any other direction compared to spontaneous breathing. As a result, directionality is set from *r* to *s* in the VP loop, remains significant from *r* to *t* in the CP loop, and remains non-significant in the CV loop (**Figure 6B**; **Table 3**).

The results of causal coupling and directionality analysis are reflected by looking at the trends of the proportion of subjects for which the adopted conditioning procedure reveals significant causality. As summarized in **Table 3** and depicted in **Figure 7A**, moving from the supine to the upright position the number of subjects for which at least one term from *r* is selected to describe *t* decreases significantly, while the number of subjects for which at least one term from *s* is selected to describe *t* increases significantly. During forced respiration, noticeable variations in the number of subjects for which candidate terms from the input series are selected to describe the output series, though not reaching statistical significance, can be observed from *r* to *s*, from *s* to *r*, and from *s* to *t* (**Figure 7B**). These results suggest that HP variability is driven to a larger extent by SAP and to a lesser

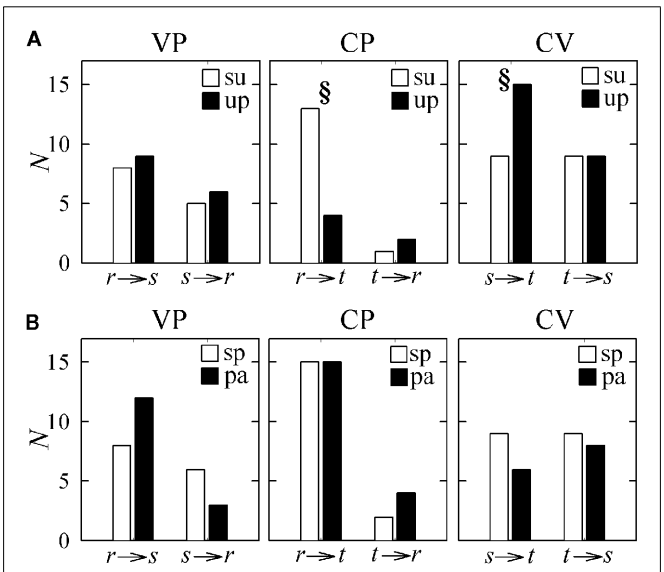

FIGURE 7 | Number of subjects (*N*) for which at least one candidate term of the input series is selected in the causality analysis (i.e., the causal coupling index is non-zero) during the tilt test protocol [(A); su: supine position; up: upright position] and during the paced breathing protocol [(B); sp: spontaneous breathing; pa: paced breathing] in the study of vasculo-pulmonary (VP), cardio-pulmonary (CP), and cardio-vascular (CV) coupling (*r*: respiration, *s*: systolic pressure; *t*: heart period). $^{\S}p < 0.05$, su vs. up or sp vs. pa.

extent by RF during TT, and that SAP is more driven by RF during PB.

DISCUSSION

In this study we exploited an information domain approach to characterize directionality in CV and cardiorespiratory interactions. The method is based on quantifying the information transfer from one variability series to another as the (normalized) amount of information carried by the second series that can be explained exclusively by the first series, in agreement with the notion of Granger causality. We remark that our method performs a "black box" analysis in which physiological mechanisms are not directly probed but are tested from time series data, and that it is based on the assessment of the coupling strength along predetermined causal directions. Therefore, it cannot provide deep information about some basic structures of physiological closed-loop systems such as distinguishing between excitatory or inhibitory or, according to the control system theory, between negative or positive closed-loop systems. Nevertheless, the method is quite helpful in the evaluation of closed-loop interactions between time series. This skill was demonstrated for simulated time series in Faes et al. (2011a), and has been exploited in this study to detect the presence of open-loop or closed-loop interactions between two physiological variability series. Indeed, comparing the information transferred along the two causal pathways of the closed-loop interaction between two series we may infer the dominant causal direction: for instance, if the information transfer from SAP to HP is higher than that from HP to SAP, we conclude that causality of CV interactions is set from SAP to HP. The same analysis performed between RF and SAP, and between RF and HP, allowed us to investigate causal couplings and dominant directions of interaction for the VP regulation and the CP regulation, respectively. Moreover, the utilization of paired tests applied between directions of interaction, or between conditions, brought statistical significance respectively to the observed presence of dominant causal directions, or to the observed modifications of coupling mechanisms occurring in the two considered experimental protocols. To favor physiological interpretation of the main findings, a graphical representation of the statistical results is reported in **Figure 8**.

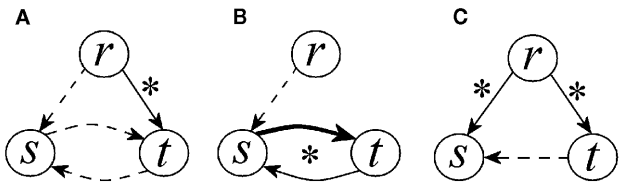

FIGURE 8 | Graphical representation of the results of causality analysis in the three considered conditions: supine position, spontaneous breathing (A), upright position, spontaneous breathing (B), and supine position, paced breathing (C). Arrows between two variability series (*r*: respiration, *s*: systolic pressure; *t*: heart period) are present when the corresponding causal coupling index is non-zero in at least half of the subjects (i.e., the index *C* has a non-zero median). The style of the arrow is arranged so that to reflect the statistical significance of changes in the index *C* observed between conditions (i.e., the coupling is significantly stronger for solid arrows than for dashed arrows, and for bold arrows than for solid arrows). Further, the statistical significance between the two causal directions for a given condition (i.e., the significance of the directionality index *D*) is marked with an asterisk.

METHODOLOGICAL ASPECTS

The information theoretic approach utilized in this study to assess directional interactions was specifically devised to deal with experimental time series measured from complex physiological systems (Faes et al., 2011a). The proposed method is grounded on the concept of transfer entropy (Schreiber, 2000), and follows a recent generalization of this concept – denoted as partial transfer entropy – dealing with estimation of causal information flow within a network of multiple interacting time series (Vakorin et al., 2009). Despite the appeal of these information-based tools in causality assessment, their utilization in experimental time series analysis is usually a daunting task, because entropy estimation is problematic in the presence of short and noisy time series. With the aim of dealing with this issue, the two main peculiarities of the approach proposed in (Faes et al., 2011a) help to improve the estimation of CE and, consequently, the identification of causality: the sequential procedure for candidate selection overcomes the issues of redundancy and arbitrariness which often lead to detection of spurious directionality, while the utilization of a corrected estimator for the CE (Porta et al., 1998, 1999) compensates the bias otherwise affecting traditional estimates. These methodological improvements allow one to obtain accurate causal coupling estimates, and then to exploit the potential advantages of information domain approaches to the study of time series interactions. For instance, these approaches do not make strong assumptions about the nature of the investigated dynamics (e.g., linear stochastic or non-linear deterministic), so that they can be used for CV and cardiorespiratory analysis where the type of interaction cannot be stated *a priori*. On the contrary, other very popular indices able to detect causal coupling in bivariate or multivariate time series, i.e., the causal coherence (Porta et al., 2002) and the partial directed coherence (Baccalà and Sameshima, 2001), are devised to deal with linear stochastic autoregressive processes and thus may fail when non-linear causality occurs and, more generally, when the underlying model does not fit the observed data. While limitations related to the linearity assumption are overcame by recently proposed methods such as non-linear autoregressive exogenous models (Faes et al., 2008a; Riedl et al., 2010) or kernel Granger causality (Marinazzo et al., 2008), these methods may suffer from the shortcomings of model misspecification. Model misspecification is a key issue in modeling connectivity, which can be critical when complex parametric models are identified on short and noisy multivariate time series. Working under the information theoretic framework, the method used in this study offers the advantage of not requiring the prior specification of a model for the investigated interactions. We note that similar model-free statistics for causality detection might be developed extending to the multivariate case other suitable frameworks for time series analysis, such as cross-sample entropy (Richman and Moorman, 2000), local non-linear prediction (Faes et al., 2008b) and causal symbolic coupling traces (Wessel et al., 2009).

Information domain approaches have been already proposed for the assessment of causality in CV interactions (Nollo et al., 2002; Palus et al., 2004; Porta et al., 2011b). In particular, Porta et al. (2011b) have recently shown that cross-CE indexes perform better than more traditional approaches relying on the transformation of frequency domain phase shifts into time delays (Taylor and Eckberg, 1996; Pitzalis et al., 1998; Cooke et al., 1999). Though widely used, approaches inferring causality from a phase diagram require prior knowledge to solve the ambiguities related to multiple admissible phase values (e.g., comparison of time lags from SAP to HP with expected baroreflex latency) and, even with that knowledge, may be misleading (Porta et al., 2011b). On the contrary, information domain methods as well as other methods based on the concept of Granger causality (Granger, 1969) are directly linked to the concept of directionality as they incorporate the flow of time in the procedure developed to estimate the causality index. As this property is shared by many methods for causality assessment, ranging from linear and non-linear parametric models (Baccalà and Sameshima, 2001; Faes et al., 2008a) to symbolic coupling traces (Wessel et al., 2009), we expect that also the causality indexes derived through these methods are able solve the ambiguities related to estimation of causality from phase diagrams.

A key property of the information domain approach proposed in this study stands in its multivariate nature, which lets it to outperform the bivariate approaches followed so far for estimation of causality in CV and cardiorespiratory interactions (Nollo et al., 2002, 2009; Faes et al., 2008a; Suhrbier et al., 2010; Kabir et al., 2011; Porta et al., 2011b). Indeed, the consideration of variables other than the two specifying the causal direction under analysis makes it possible to quantify complex interactions between two variables avoiding the confounding effects of the others (Vakorin et al., 2009). This property allows one to elicit the direct causal effects between the two considered variables, i.e., the effects not mediated by the other considered variables. In the context of our application, this is extremely useful to clarify the nature of joint exogenous influences of respiration on cardiac and vascular variability series. In particular, the joint multivariate analysis of RF, SAP, and HP interactions can be used to rule out possible confounding effects of CP and VP couplings on the estimation of CV interactions.

This study exploits a method based on amplitude quantization to assess causality between two variability series. As such, the method works in practice on sequences of symbols obtained after uniform partitioning of the vector coordinates for each time series. Similar coarse graining procedures are followed by cross-approximate entropy and cross-sample entropy methods (Richman and Moorman, 2000), as well as by methods based on symbolization (Baumert et al., 2005; Wessel et al., 2009), which perform a non-uniform partition of the series amplitudes. Therefore, the coupling indexes derived from these approaches capture relationships related to the dominant oscillations in the time series. With reference to our application, these dominant oscillations are likely the Mayer waves in the upright tilting position, the respiration-related waves during PB, and a combination of both waves during spontaneous breathing in the supine position (Malliani, 1999). Thus, although the estimated causal couplings cannot be assessed for specific oscillations as done by linear frequency domain measures (Porta et al., 2002; Faes and Nollo, 2010), they provide an overall information related to the dominant physiological mechanisms in each specific condition, intended as the mechanisms inducing the larger amplitude variations in the time series. The emergence of dominant oscillations during TT and PB protocols (which is also visible in the example of **Figure 1**) is confirmed indirectly by the analysis of the time delays peculiar of each variability series in the different conditions. Indeed, besides serving in the optimization of the temporal range to be used for candidate selection in non-linear analysis, these delays indicate also the decorrelation time of each series. The reported values suggest that cardiac, vascular, and respiratory dynamics tend to be slower during tilt testing and faster during PB. This presumably reflects the presence of a dominant low frequency oscillation in the upright position, which is enhanced by the sympathetic activation consequent to tilt on one side, and the presence of a dominant, respiration-driven oscillation during PB on the other side.

ANALYSIS OF CARDIO-VASCULAR INTERACTIONS

The study of the causal coupling along the two directions of the CV loop confirmed that HP and SAP are likely to interact in a closed-loop, according to the possible existence of neural baroreflex feedback mechanisms acting from SAP to HP on one side, and of mechanical feedforward mechanisms acting from HP to SAP on the other side (Saul et al., 1991; Taylor and Eckberg, 1996; Mullen et al., 1997; Nollo et al., 2005; Porta et al., 2011b). With the subjects lying in the supine position and breathing spontaneously, we observed a detectable information transfer through both feedback and feedforward pathways of interaction (**Figures 6A**, **7A**, and **8A**). Since the directionality index was not significantly different from zero, we conclude that feedback and feedforward mechanisms are balanced in this resting condition. At variance with this result are the findings of previous studies performing pure bivariate analyses of SAP and HP series, which indicated in supine healthy subjects the prevalence of feedforward mechanisms from HP to SAP over the baroreflex-mediated effects of SAP on HP (Nollo et al., 2005, 2009; Faes et al., 2008a; Porta et al., 2011b). We ascribe the difference to the fact that our analysis of causality between SAP and HP explicitly includes RF, separating its direct contributions to CV variability. Therefore it is likely that, while direct effects between SAP and HP are balanced, bivariate analyses implicitly accounting for indirect effects mediated by respiration detect a stronger coupling over the feedforward branch of the loop. This supposition is also supported by the stronger driving which RF seems to apply on HP than on SAP (**Figure 8A**).

The causal interactions between SAP and HP variability were substantially modified during the two considered experimental protocols. When subjects were tilted from the supine to the upright position, the reciprocal interaction between the two CV variables was substantially enhanced (**Figures 5A** and **8B**). Specifically, the causal coupling was increased over both pathways of the CV loop, with a particular enhancement over the feedback direction documented by the significant directionality set from SAP to HP. These results agree with bivariate analyses performed

in similar protocols (Nollo et al., 2005, 2009; Faes et al., 2008a; Porta et al., 2011b), and document the increased involvement of the baroreflex in controlling heart rate consequent to the tilt-induced activation of the sympathetic nervous system. In this case, the agreement with bivariate measures is likely related to the lower importance of direct effects of respiration on cardiac and vascular variability in the upright position. During PB, direct influences between HP and SAP were not modified substantially (no statistically significant changes are denoted in **Figure 6** for CV causal couplings and directionality measures), although a tendency to decreasing of the feedback causal coupling was noticed (**Figures 5A** and **8C**). Since in this condition CP and VP mechanisms seem predominant (**Figure 8C**), we advocate the necessity of a multivariate approach like ours to properly characterize CV regulation; simple bivariate approaches involving only SAP and HP series in PB protocols (Pitzalis et al., 1998) may indeed be misleading because they tend to reflect more the different strength and latency with which RF affects directly HP and SAP, rather than the true direct coupling between HP and SAP.

ANALYSIS OF CARDIO-PULMONARY AND VASCULO-PULMONARY INTERACTIONS

The utilization of a multivariate approach able to elicit direct effects from one series to another allowed us to disambiguate the effects of respiration on the two CV variables, through the separation of CP and VP interactions from CV interactions. Our analysis of CP and VP interactions indicates that, when present, significant causal coupling occurred always from respiration to HP or arterial pressure, and never over the opposite direction (the distributions of $C_{r\to t}$ and $C_{r\to s}$ always have zero median). This result confirms the expected role of respiration acting as an exogenous variable on the CV loop (Cohen and Taylor, 2002). Moreover, since the result is derived without imposing causality from RF to SAP and/or HP as done in open-loop modeling studies (Baselli et al., 1994; Porta et al., 2000a), the result confirms on physiological data the ability of the approach to capture unidirectional causal interactions between variables.

As regards the strength of the unidirectional coupling in CP and VP interactions, we found that, in the supine position with spontaneous breathing, the information transfer originating from respiration variability is detectable toward both CV variables (**Figures 6A**, **7A**, and **8A**). The causal coupling from RF to HP quantifies the strength of respiratory influences affecting the heart rate independently of arterial pressure changes. Therefore, this coupling can be taken as a measure of the central effects of the respiratory drive on the cardiac vagal motor neurons, reflecting a central mechanism underlying respiratory related fluctuations in the heart rate (Gilbey et al., 1984). On the other hand, the coupling from RF to SAP is thought as the result of the perturbing action of breathing on intrathoracic pressure, causing fluctuations in stroke volume, cardiac output, and thus blood pressure (Toska and Eriksen, 1993; Triedman and Saul, 1994).

The modifications of these two causal couplings observed during PB (**Figures 6** and **8A,C**) may be explained considering that voluntary control of respiration is likely to change respiratory parameters, thus affecting SAP and HP variability through both peripheral and central respiratory effects on the basic CV reflexes (Eckberg, 2000; Pinna et al., 2006). In particular, Pinna et al. (2006) found that PB at 0.25 Hz is accompanied by an increased respiratory drive (increased tidal volume and minute respiration), which in turn increases the amplitude of respiratory related oscillations in SAP but not in HP variability. Accordingly, we may interpret the increase of coupling from RF to SAP with the increased mechanical effect of the respiratory drive on intrathoracic pressure, and the absence of significant modifications in the coupling from RF to HP with the negligible effect of tidal volume on respiratory sinus arrhythmia (Cooke et al., 1998; Pinna et al., 2006).

During head-up tilt, the observed absence of causal coupling from RF to HP (**Figures 5** and **8A,B**) may be explained with regard both to physiological mechanisms and to the adopted methodology. Physiologically, the shift of the sympathovagal balance toward sympathetic activation and vagal withdrawal occurring with the assumption of the upright position decreases the amplitude of respiration-related HP oscillations (Montano et al., 1994; Cooke et al., 1999), and this phenomenon is likely reflected in our study by the decreased causal influence of RF on HP variability. Methodologically, the decrease of respiration-related oscillations and the contemporaneous increase of low frequency, respiration-unrelated HP oscillations consequent to tilt is likely to mask causal effects at the respiratory frequency, which are not detected because the predominant part of the information transfer is that regarding low frequency oscillations. On the contrary, the substantially unaltered causal coupling measured from RF to SAP after the tilting maneuver is in agreement with findings indicating that respiratory fluctuations in arterial pressure are preserved, in their proportion to low frequency fluctuations, in the upright position (Taylor and Eckberg, 1996; Cooke et al., 1999).

RESPIRATORY FLUCTUATIONS IN CARDIAC AND VASCULAR VARIABILITY

In the previous section we have discussed the direct mechanisms that may determine respiration-related fluctuations in heart rate and arterial pressure. Here we integrate the discussion exploiting the combined analysis of the causal couplings measured for CP and VP interactions on one side, and for CV interactions on the other side, to compare direct and indirect mechanisms underlying the effects of RF on HP and on SAP.

The effects of RF on HP, commonly denoted as respiratory sinus arrhythmia, are exerted according to two possible – and still debated – driving mechanisms, i.e., the central vagal effects of RF on HP, and the mechanical effects of RF on SAP which are transferred to HP through the baroreflex (Gilbey et al., 1984; Toska and Eriksen, 1993; Eckberg, 2009). According to our results, both these mechanisms seem to be present at rest, with a prevalence of the central mechanism suggested by the strong direct causal coupling from RF to HP (**Figure 8A**). During head-up tilt the baroreflex-mediated mechanism seems to be predominant, as the coupling is preserved from RF to SAP, is increased from SAP to HP, and is blunted from RF to HP (**Figure 8B**). On the contrary, respiratory sinus arrhythmia seems to be driven by the direct mechanism from RF to HP during PB, in a way even

stronger than during spontaneous breathing (**Figure 8C**). As to respiratory fluctuations in SAP variability, we found that the direct component representing respiration-induced effects on stroke volume (Innes et al., 1993; Toska and Eriksen, 1993) is detectable in all conditions (**Figure 8**). Moreover, indirect effects mirroring the transmission of HP fluctuations through mechanical feedforward mechanisms (Taylor and Eckberg, 1996; Mullen et al., 1997) cannot be excluded, especially in the supine position with either spontaneous or PB.

The discussion above reported completes the characterization of the possible mechanisms underlying the generation of cardiac and vascular variability, as can be done by our multivariate approach considering the information transfer between HP, SAP, and RF time series. It is worth noting that our interpretations cannot describe sources of variability due to regulatory mechanisms which do not involve the three observed variables; these mechanisms may possibly include central autonomic effects determining directly HP variability (Cooley et al., 1998), or mechanisms regulating SAP variability via control variables different from HP and RF (Baselli et al., 1988).

CONCLUSION

The main advantages of the approach applied in this study to assess directional interactions in CV and cardiorespiratory variability can be summarized as: the general applicability (the method captures both linear and non-linear interactions); the possibility to quantify the coupling strength reflecting directional mechanisms, such as baroreflex and CP couplings, which work in physiological, closed-loop conditions; and the multivariate nature that allows one to account for the disturbing action of several variables on the causal interactions between the pair of signals under focus, as done in the characterization of respiration-driven mechanisms. The analysis performed in resting physiological conditions and in response to widely used experimental maneuvers indicated that the approach is able to reflect well known regulatory mechanisms of CV and cardiorespiratory physiology, as well as to support the interpretation of other more debated mechanisms. Hence, the approach may be favorably suggested for the description of mechanism impairment in a wide spectrum of CV and cardiorespiratory pathologies, ranging from heart failure to neurally mediated and breathing disorders.

REFERENCES

Angelini, L., de Tommaso, M., Marinazzo, D., Nitti, L., Pellicoro, M., and Stramaglia, S. (2010). Redundant variables and Granger causality. *Physiol. Rev. E Stat. Nonlin. Soft Matter Phys.* 81, 037201.

Baccalà, L. A., and Sameshima, K. (2001). Partial directed coherence: a new concept in neural structure determination. *Biol. Cybern.* 84, 463–474.

Bai, Y., Siu, K. L., Ashraf, S., Faes, L., Nollo, G., and Chon, K. H. (2008). Nonlinear coupling is absent in acute myocardial patients but not healthy subjects. *Am. J. Physiol. Heart Circ. Physiol.* 295, H578–H586.

Baselli, G., Cerutti, S., Badilini, F., Biancardi, L., Porta, A., Pagani, M., Lombardi, F., Rimoldi, O., Furlan, R., and Malliani, A. (1994). Model for the assessment of heart period and arterial pressure variability interactions and of respiration influences. *Med. Biol. Eng. Comput.* 32, 143–152.

Baselli, G., Cerutti, S., Civardi, S., Malliani, A., and Pagani, M. (1988). Cardiovascular variability signals: towards the identification of a closed-loop model of the neural control mechanisms. *IEEE Trans. Biomed. Eng.* 35, 1033–1046.

Baumert, M., Baier, V., Truebner, S., Schirdewan, A., and Voss, A. (2005). Short- and long-term joint symbolic dynamics of heart rate and blood pressure in dilated cardiomyopathy. *IEEE Trans. Biomed. Eng.* 52, 2112–2115.

Cohen, M. A., and Taylor, J. A. (2002). Short-term cardiovascular oscillations in man: measuring and modelling the physiologies. *J. Physiol.* 542, 669–683.

Cooke, W. H., Cox, J. F., Diedrich, A. M., Taylor, J. A., Beightol, L. A., Ames, J. E., Hoag, J. B., Seidel, H., and Eckberg, D. L. (1998). Controlled breathing protocols probe human autonomic cardiovascular rhythms. *Am. J. Physiol.* 274, H709–H718.

Cooke, W. H., Hoag, J. B., Crossman, A. A., Kuusela, T. A., Tahvanainen, K. U. O., and Eckberg, D. L. (1999). Human response to upright tilt: a window on central autonomic integration. *J. Physiol.* 517, 617–628.

Cooley, R. L., Montano, N., Cogliati, C., van de, B. P., Richenbacher, W., Oren, R., and Somers, V. K. (1998). Evidence for a central origin of the low-frequency oscillation in RR-interval variability. *Circulation* 98, 556–561.

De Boer, R. W., Karemaker, J. M., and Strackee, J. (1985). Relationships between short-term blood-pressure fluctuations and heart-rate variability in resting subjects: a spectral analysis approach. *Med. Biol. Eng. Comput.* 23, 352–358.

Eckberg, D. L. (2000). Physiological basis for human autonomic rhythms. *Ann. Med.* 32, 341–349.

Eckberg, D. L. (2009). Point: counterpoint: respiratory sinus arrhythmia is due to a central mechanism vs. respiratory sinus arrhythmia is due to the baroreflex mechanism. *J. Appl. Physiol.* 106, 1740–1742.

Faes, L., and Nollo, G. (2006). Bivariate nonlinear prediction to quantify the strength of complex dynamical interactions in short-term cardiovascular variability. *Med. Biol. Eng. Comput.* 44, 383–392.

Faes, L., and Nollo, G. (2010). Assessing frequency domain causality in cardiovascular time series with instantaneous interactions. *Methods Inf. Med.* 49, 453–457.

Faes, L., Nollo, G., and Chon, K. H. (2008a). Assessment of Granger causality by nonlinear model identification: application to short-term cardiovascular variability. *Ann. Biomed. Eng.* 36, 381–395.

Faes, L., Porta, A., and Nollo, G. (2008b). Mutual nonlinear prediction as a tool to evaluate coupling strength and directionality in bivariate time series: comparison among different strategies based on k nearest neighbors. *Physiol. Rev. E Stat. Nonlin. Soft Matter Phys.* 78, 026201.

Faes, L., Nollo, G., and Porta, A. (2011a). Information-based detection of nonlinear Granger causality in multivariate processes via a nonuniform embedding technique. *Phys. Rev. E Stat. Nonlin. Soft Matter Phys.* 83, 051112.

Faes, L., Nollo, G., and Porta, A. (2011b). Non-uniform multivariate embedding to assess the information transfer in cardiovascular and cardiorespiratory variability series. *Comput. Biol. Med.* doi: 10.1016/j.compbiomed.2011.02.007

Faes, L., Widesott, L., Del Greco, M., Antolini, R., and Nollo, G. (2006). Causal cross-spectral analysis of heart rate and blood pressure variability for describing the impairment of the cardiovascular control in neurally mediated syncope. *IEEE Trans. Biomed. Eng.* 53, 65–73.

Gilbey, M. P., Jordan, D., Richter, D. W., and Spyer, K. M. (1984). Synaptic mechanisms involved in the inspiratory modulation of vagal cardioinhibitory neurones in the cat. *J. Physiol.* 356, 65–78.

Granger, C. W. J. (1969). Investigating causal relations by econometric models and cross-spectral methods. *Econometrica* 37, 424–438.

Hoyer, D., Bauer, R., Walter, B., and Zwiener, U. (1998). Estimation of nonlinear couplings on the basis of complexity and predictability – a new method applied to cardiorespiratory coordination. *IEEE Trans. Biomed. Eng.* 45, 545–552.

Innes, J. A., De Cort, S. C., Kox, W., and Guz, A. (1993). Within-breath modulation of left ventricular function during normal breathing and positive-pressure ventilation in man. *J. Physiol.* 460, 487–502.

Jones, J. J. (1962). The Bainbridge reflex. *J. Physiol.* 160, 298–305.

Kabir, M. M., Saint, D. A., Nalivaiko, E., Abbott, D., Voss, A., and Baumert, M. (2011). Quantification of cardiorespiratory interactions based on joint symbolic dynamics. *Ann. Biomed. Eng.* 39, 264–214.

Malliani, A. (1999). The pattern of sympathovagal balance explored in the frequency domain. *News Physiol. Sci.* 14, 111–117.

Malpas, S. C. (2002). Neural influences on cardiovascular variability: possibilities and pitfalls. *Am. J. Physiol. Heart Circ. Physiol.* 282, H6–H20.

Marinazzo, D., Pellicoro, M., and Stramaglia, S. (2008). Kernel method for nonlinear Granger causality. *Phys. Rev. Lett.* 100, 144103.

Montano, N., Gnecchi Ruscone, T., Porta, A., Lombardi, F., Pagani, M., and Malliani, A. (1994). Power spectrum analysis of heart rate variability to assess the change in sympathovagal balance during graded orthostatic tilt. *Circulation* 90, 1826–1831.

Mullen, T. J., Appel, M. L., Mukkamala, R., Mathias, J. M., and Cohen, R. J. (1997). System identification of closed loop cardiovascular control: effects of posture and autonomic blockade. *Am. J. Physiol.* 272, H448–H461.

Nollo, G., Faes, L., Antolini, R., and Porta, A. (2009). Assessing causality in normal and impaired short-term cardiovascular regulation via nonlinear prediction methods. *Philos. Transact. A Math. Phys. Eng. Sci.* 367, 1423–1440.

Nollo, G., Faes, L., Porta, A., Antolini, R., and Ravelli, F. (2005). Exploring directionality in spontaneous heart period and systolic pressure variability interactions in humans. Implications in baroreflex gain evaluation. *Am. J. Physiol. Heart Circ. Physiol.* 288, H1777–H1785.

Nollo, G., Faes, L., Porta, A., Pellegrini, B., Ravelli, F., Del Greco, M., Disertori, M., and Antolini, R. (2002). Evidence of unbalanced regulatory mechanism of heart rate and systolic pressure after acute myocardial infarction. *Am. J. Physiol. Heart Circ. Physiol.* 283, H1200–H1207.

Palus, M., Stefanovska, A., and Veber, M. (2004). Causality between the amplitude and frequency of cardiac oscillations. *Cardiovasc. Eng.* 4, 127–132.

Pinna, G. D., Maestri, R., La Rovere, M. T., Gobbi, E., and Fanfulla, F. (2006). Effect of paced breathing on ventilatory and cardiovascular variability parameters during short-term investigations of autonomic function. *Am. J. Physiol. Heart Circ. Physiol.* 290, H424–H433.

Pitzalis, M. V., Mastropasqua, F., Massari, F., Passantino, A., Colombo, R., Mannarini, A., Forleo, C., and Rizzon, P. (1998). Effect of respiratory rate on the relationships between RR interval and systolic blood pressure fluctuations: a frequency-dependent phenomenon. *Cardiovasc. Res.* 38, 332–339.

Pompe, B., Blidh, P., Hoyer, D., and Eiselt, M. (1998). Using mutual information to measure coupling in the cardiorespiratory system. *IEEE Eng. Med. Biol. Mag.* 17, 32–39.

Porta, A., Baselli, G., Liberati, D., Montano, N., Cogliati, C., Gnecchi-Ruscone, T., Malliani, A., and Cerutti, S. (1998). C measuring regularity by means of a corrected conditional entropy in sympathetic outflow. *Biol. Cybern.* 78, 71–78.

Porta, A., Baselli, G., Lombardi, F., Montano, N., Malliani, A., and Cerutti, S. (1999). Conditional entropy approach for the evaluation of the coupling strength. *Biol. Cybern.* 81, 119–129.

Porta, A., Baselli, G., Rimoldi, O., Malliani, A., and Pagani, M. (2000a). Assessing baroreflex gain from spontaneous variability in conscious dogs: role of causality and respiration. *Am. J. Physiol.* 279, H2558–H2567.

Porta, A., Guzzetti, S., Montano, N., Pagani, M., Somers, V., Malliani, A., Baselli, G., and Cerutti, S. (2000b). Information domain analysis of cardiovascular variability signals: evaluation of regularity, synchronisation and co-ordination. *Med. Biol. Eng. Comput.* 38, 180–188.

Porta, A., Bassani, T., Bari, V., Tobaldini, E., Takahashi, A. C., Catai, A. M., and Montano, N. (2011a). Model-based assessment of baroreflex and cardiopulmonary couplings during graded head-up tilt. *Comput. Biol. Med.* doi: 10.1016/j.compbiomed.2011.04.019.

Porta, A., Catai, A. M., Takahashi, A. C., Magagnin, V., Bassani, T., Tobaldini, E., van de, B. P., and Montano, N. (2011b). Causal relationships between heart period and systolic arterial pressure during graded head-up tilt. *Am. J. Physiol. Regul. Integr. Comp Physiol.* 300, R378–R386.

Porta, A., Furlan, R., Rimoldi, O., Pagani, M., Malliani, A., and van de Borne, P. (2002). Quantifying the strength of the linear causal coupling in closed loop interacting cardiovascular variability signals. *Biol. Cybern.* 86, 241–251.

Richman, J. S., and Moorman, J. R. (2000). Physiological time-series analysis using approximate entropy and sample entropy. *Am. J. Physiol.* 278, H2039–H2049.

Riedl, M., Suhrbier, A., Stepan, H., Kurths, J., and Wessel, N. (2010). Short-term couplings of the cardiovascular system in pregnant women suffering from pre-eclampsia. *Philos. Transact. A Math. Phys. Eng. Sci.* 368, 2237–2250.

Rosenblum, M. G., Cimponeriu, L., Bezerianos, A., Patzak, A., and Mrowka, R. (2002). Identification of coupling direction: application to cardiorespiratory interaction. *Phys. Rev. E Stat. Nonlin. Soft Matter Phys.* 65, 041909.

Saul, J. P., Berger, R. D., Albrecht, P., Stein, S. P., Hui Chen, M., and Cohen, R. J. (1991). Transfer function analysis of the circulation: unique insights into cardiovascular regulation. *Am. J. Physiol.* 261, H1231–H1245.

Schreiber, T. (2000). Measuring information transfer. *Phys. Rev. Lett.* 85, 461–464.

Small, M. (2005). *Applied Nonlinear Time Series Analysis: Applications in Physics, Physiology and Finance.* Singapore: World Scientific.

Suhrbier, A., Riedl, M., Malberg, H., Penzel, T., Bretthauer, G., Kurths, J., and Wessel, N. (2010). Cardiovascular regulation during sleep quantified by symbolic coupling traces. *Chaos* 20, 045124.

Taylor, J. A., and Eckberg, D. L. (1996). Fundamental relations between short-term RR interval and arterial pressure oscillations in humans. *Circulation* 93, 1527–1532.

Toska, K., and Eriksen, M. (1993). Respiration-synchronous fluctuations in stroke volume, heart rate and arterial pressure in humans. *J. Physiol.* 472, 501–512.

Triedman, J. K., and Saul, J. P. (1994). Blood pressure modulation by central venous pressure and respiration. Buffering effects of the heart rate reflexes. *Circulation* 89, 169–179.

Vakorin, V. A., Krakovska, O. A., and McIntosh, A. R. (2009). Confounding effects of indirect connections on causality estimation. *J. Neurosci. Methods* 184, 152–160.

Wessel, N., Suhrbier, A., Riedl, M., Marwan, N., Malberg, H., Bretthauer, G., Penzel, T., and Kurths, J. (2009). Detection of time-delayed interactions in biosignals using symbolic coupling traces. *Europhys. Lett.* 87, 10004.

Conflict of Interest Statement: The authors declare that the research was conducted in the absence of any commercial or financial relationships that could be construed as a potential conflict of interest.

Received: 15 July 2011; accepted: 15 October 2011; published online: 07 November 2011.

Citation: Faes L, Nollo G and Porta A (2011) Information domain approach to the investigation of cardio-vascular, cardio-pulmonary, and vasculo-pulmonary causal couplings. Front. Physio. ***2****:80. doi: 10.3389/fphys.2011.00080*

This article was submitted to Frontiers in Computational Physiology and Medicine, a specialty of Frontiers in Physiology.

frontiers in
PHYSIOLOGY

ORIGINAL RESEARCH ARTICLE
published: 07 February 2012
doi: 10.3389/fphys.2011.00123

Integrated central-autonomic multifractal complexity in the heart rate variability of healthy humans

D. C. Lin* and A. Sharif

Department of Mechanical and Industrial Engineering, Ryerson University, Toronto, ON, Canada

Edited by:
Riccardo Barbieri, Massachusetts Institute of Technology, USA

Reviewed by:
Van Toi Vo, International University of Vietnam National Universities, Vietnam
Yoshiharu Yamamoto, University of Tokyo, Japan

****Correspondence:***
D. C. Lin, Department of Mechanical and Industrial Engineering, Ryerson University, 350 Victoria Street, Toronto, ON, Canada M5B 2K3.
e-mail: derlin@ryerson.ca

Purpose of Study: The aim of this study was to characterize the central-autonomic interaction underlying the multifractality in heart rate variability (HRV) of healthy humans. **Materials and Methods:** Eleven young healthy subjects participated in two separate ∼40 min experimental sessions, one in supine (SUP) and one in, head-up-tilt (HUT), upright (UPR) body positions. Surface scalp electroencephalography (EEG) and electrocardiogram (ECG) were collected and fractal correlation of brain and heart rate data was analyzed based on the idea of relative multifractality. The fractal correlation was further examined with the EEG, HRV spectral measures using linear regression of two variables and principal component analysis (PCA) to find clues for the physiological processing underlying the central influence in fractal HRV. **Results:** We report evidence of a central-autonomic fractal correlation (CAFC) where the HRV multifractal complexity varies significantly with the fractal correlation between the heart rate and brain data ($P = 0.003$). The linear regression shows significant correlation between CAFC measure and EEG *Beta* band spectral component ($P = 0.01$ for SUP and $P = 0.002$ for UPR positions). There is significant correlation between CAFC measure and HRV LF component in the SUP position ($P = 0.04$), whereas the correlation with the HRV HF component approaches significance ($P = 0.07$). The correlation between CAFC measure and HRV spectral measures in the UPR position is weak. The PCA results confirm these findings and further imply multiple physiological processes underlying CAFC, highlighting the importance of the EEG *Alpha*, *Beta* band, and the HRV LF, HF spectral measures in the supine position. **Discussion and Conclusion:** The findings of this work can be summarized into three points: (i) Similar fractal characteristics exist in the brain and heart rate fluctuation and the change toward stronger fractal correlation implies the change toward more complex HRV multifractality. (ii) CAFC is likely contributed by multiple physiological mechanisms, with its central elements mainly derived from the EEG *Alpha*, *Beta* band dynamics. (iii) The CAFC in SUP and UPR positions is qualitatively different, with a more predominant central influence in the fractal HRV of the UPR position.

Keywords: multifractal HRV, central nervous system, autonomic nervous system, fractal correlation

1. INTRODUCTION

Heart rate regulation in healthy humans is known to exhibit complex variability over an extensive dynamic range. Specifically in the beat-to-beat RR interval (RRi) sequence, the underlying fluctuation is intrinsic (Aoyagi et al., 2000, 2003; Amaral et al., 2001) and exhibit scale-free characteristics of the multifractal type (Ivanov et al., 1999; Sassi et al., 2009). The scale-free component of the heart rate variability (HRV) is of basic importance. Not only is this dynamic feature broadly observed in diverse natural and artificial systems (Task Force of ESC and NASPE, 1996; Gisiger, 2001), it also carry relevant information in the clinical context, where a diminishing fractal HRV was consistently reported in various heart disease processes (Task Force of ESC and NASPE, 1996; Komatsu et al., 1997; Lombardi, 2000; Mahon et al., 2002), and in old age (Makikallio et al., 2001; Kors et al., 2007). Although the HRV scale-free dynamics has been a subject of intense study, its dynamic origin and possible functional correlates remain largely unclear.

The sympathetic (SNS) and parasympathetic (PNS) branches of the autonomic nervous system (ANS) are known to have strong influence on the pace maker cells of the heart (Akselrod et al., 1981; Task Force of ESC and NASPE, 1996; Malliani et al., 1997). However, the complex interaction between SNS and PNS does not provide an immediate characterization of the fractal HRV. For example, via pharmaceutical means, SNS blockade is known to have a minor effect on the multifractal property of HRV, but PNS blockade can dramatically change the HRV scale-free dynamics into one characterized by a much narrower range of scaling exponents (Amaral et al., 2001; Gisiger, 2001). In passive head-up-tilt (HUT), where there is a SNS activation and PNS withdrawal caused by the reduced baroreflex afferent input (Tulppo et al., 2001), the change of the HRV multifractal property may not follow these pharmaceutical effects interpreted separately (Lin and Sharif, 2010). It is thus plausible, at least in passive HUT, that other factors exist to influence the HRV scale-free dynamics.

One potential source that could provide further insights of fractal HRV is the central nervous system (CNS). While fractal fluctuation can emerge from the spontaneous activity of cultured cardiac myocytes (Kucera et al., 2000), the changing fractal HRV properties reported in sleep (Bunde et al., 2000; Brandenberger et al., 2001; Van den Berg et al., 2005; Togo et al., 2006; Pereda and Gonzalez, 2008) and mental exercise (Lucini et al., 1997; Peng et al., 1999; Kubota et al., 2001; Phongsuphap et al., 2008) provide a stronger support for a central-autonomic interaction in the HRV scale-free dynamics. In general, the central influence on cardiac functions is well known (Loewy and Spyer, 1990; Dampney et al., 2002). Despite the brainstem centers that interact with the afferent inputs, "direct" central command can trigger efferent responses to influence heart rate and blood pressure in such events as anticipation of threat (Loewy and Spyer, 1990; Dampney et al., 2002), onset of exercise (Goodwin et al., 1972; Loewy and Spyer, 1990; Dampney et al., 2002). However, specific to the fractal component of HRV, the potential role of CNS, whether anatomical or functional, is mostly unclear.

The objective of the present study is to examine and characterize the central link in fractal HRV. The presence of the central component implies that the fractal properties of the heart rate and brain activity data should be correlated to each other. But fractal correlation of time series should be interpreted differently from the commonly used two-point correlation based on the second order statistics. There are at least two reasons to make such a distinction. First, fractal characterizes the property of a distribution and cannot be fully described using only the second order statistics (Falconer, 1990). For example, the two-point cross correlation of fractal signals is self-similar and qualitatively the same. Secondly, physiological data are not purely fractal signal and can exhibit rhythmic oscillation in a narrow frequency band. Such Fourier modes can lead to a false impression of the two-point cross correlation that has little to do with the fractal component. A novel solution to the fractal correlation problem in general was independently developed by Riedi and Scheuring (1997), and Lévy-Léhel and Vojak (1998). Among others, their main idea implies the scaling exponents of the time series is not sufficient to describe the fractal correlation and the need for a multivariate approach. Indeed, time series can be coupled to exhibit a wide range of fractal correlation without changing the underlying scaling exponents (Lin and Sharif, 2007; Appendix A). It is thus believed that a bi-variate multifractal approach is necessary for the current investigation.

The main goals of the paper are to report evidence of a *central-autonomic fractal correlation* (CAFC) in the heart rate and brain data from the passive head-up-tilt (HUT) experiment. The CAFC was further examined based on the regression with HRV and EEG frequency domain measures. Both linear regression of two variables and principal component analysis (PCA) were employed to gain insights of the physiological processes underlying CAFC.

2. MATERIALS AND METHODS

2.1. SUBJECTS AND EXPERIMENTS

Eleven subjects (eight males and three females; age: 25.72 ± 4.3-year-old; weight: 69.48 ± 12.2 kg; height: 173.83 ± 8.2 cm) without known cardiovascular, pulmonary, and neurological conditions participated in the study. Our experiment is a passive HUT body maneuver, which is sufficient to exert measurable effects on the ANS and the fractal HRV property (Tulppo et al., 2001). All subjects were fully explained about the goal and detail of the test reviewed and approved by the University Ethic Board, and signed an informed consent form.

The pre-test protocol requires the subject to maintain normal daily activity and routine, and have sufficient sleep. Heavy exercise and alcohol consumption were not allowed before the test. The subjects were asked to stay calm and remain steady on a tilt table with foot rest and to keep their eyes open. Moreover, only spontaneous breathing protocol was considered. For the tilt test, subjects were first in the SUP position for 10–20 min before tilted up to a 75° UPR position. The test was conducted in a temperature-controlled and shielded room of slightly dim lighting condition ($\leq$200 lx). No syncope event occurred in the tilt test.

Standard electrocardiogram ECG (five-lead) recording and electroencephalography EEG bipolar measurement (International 10-20 system) were taken simultaneously via a 16-bit ADC ambulatory recorder at a 256 Hz sampling rate (g.MobiLab, GTEC Inc., Austria). The recorder has a hardcoded passband of 0.01–100 Hz for the ECG recording and 0.01–30 Hz for the EEG recording. The R wave in ECG was examined and any skip beat or erroneous detection (due mostly to a significant P wave in ECG) was manually corrected. These problematic beats account for a small portion of the entire record. On average, there are 3,849 uninterrupted RRi in SUP (mean $\pm$ SD: 0.965 ± 0.079 s) and 5,308 RRi in UPR (mean $\pm$ SD: 0.662 ± 0.055 s). All data analyzed below are based on the frontal site recordings (FP1-FC3, FP2-FC4). Neighboring frontal sites (AF3-F3, AF6-F4) were also recorded and showed similar results.

2.2. RELATIVE MULTIFRACTALITY BETWEEN TIME SERIES

The traditional multifractal analysis of a time series is achieved in two technical steps: first, estimate the singularity exponent, α, which quantifies the fluctuation strength from one sample to the next, and, second, calculate the multifractal spectrum, $f(\alpha)$, of the intervals in which α is observed. The value of $f(\alpha)$ is also proportional to the number of intervals that exhibit the fluctuation strength α (Falconer, 1990). Hence, the larger the $f(\alpha)$ is, the more frequent the fluctuation strength α is observed. The width of $f(\alpha)$ is an important indicator for fractal complexity and one of the primary variables used in this work. When the fluctuation is characterized by one single $\alpha = \alpha_0$, such as the fractional Brownian motion, $f(\alpha)$ reduces to a singleton: i.e., $f(\alpha_0) = 1$ at $\alpha = \alpha_0$ and $f(\alpha) = 0$ for $\alpha \neq \alpha_0$ (Falconer, 1990). In this case, the width of $f(\alpha)$ is 0 and the fluctuation is considered relatively simple since it is uniformly "the same." This is to compare to the case where α spans an interval, such as the binomial cascade (Falconer, 1990; Riedi and Scheuring, 1997; Lin and Sharif, 2007 and Appendix A). In this case, $f(\alpha)$ has a finite width and the fluctuation is considered complex since it consists of a mixture of different fluctuation strengths. The width of $f(\alpha)$ can therefore properly measure the fractal complexity of a time series.

Riedi and Scheuring (1997), and Lévy-Léhel and Vojak (1998) made an important extension to the multifractal analysis. These authors introduced the idea of relative multifractality (RM) by

using the fractal property of one time series to measure that of the other. While the technical details remain similar, one now focuses on the relative singularity exponent, denoted as α_{RM}. It is in this setting that the fractal correlation is addressed. In particular, for identical fractal time series, $\alpha_{\mathrm{RM}} = 1$, which simply reflects the same fluctuation of the time series. Having a constant α_{RM} also implies the corresponding $f(\alpha_{\mathrm{RM}})$ is a singleton of zero width. In general, strongly correlated fractal properties imply a small α_{RM} range and a small $f(\alpha_{\mathrm{RM}})$ spectrum width. As the difference of fluctuation in time series widens, in both the α_{RM} value and the interval scale in which α_{RM} is observed, the α_{RM} range increases and $f(\alpha_{\mathrm{RM}})$ attains a finite width (Lévy-Léhel and Vojak, 1998; Lin, 2008; Lin and Sharif, 2010; Lin and Sharif, 2007; Riedi and Scheuring, 1997). Hence, the width of $f(\alpha_{\mathrm{RM}})$ of two time series measures a different property from the width of $f(\alpha)$ of a single time series; namely, a smaller (larger) $f(\alpha_{\mathrm{RM}})$ width implies a stronger (weaker) fractal correlation between the time series.

To employ RM in the present work, we first constructed the aggregated EEG sequence based on the RRi. Let the EEG be $e(t)$, and RRi, and its time stamp be $r(n)$, $t(n) = \Sigma^n r(i)$, respectively. The aggregated EEG sequence is defined by: $y(n) = \Sigma\, e(t')/M_n$ for t' in $[t(n-1),\, t(n)]$, $n = 1,2,\ldots$, where M_n denotes the number of EEG samples in $[t(n-1),\, t(n)]$. To perform RM analysis, the method of joint wavelet transform modulus maxima (JWTMM) was used to determine the relative singularity exponent, denoted as $\alpha_{R/E}$, and the corresponding $f(\alpha_{R/E})$ spectrum (Lin and Sharif, 2007, 2010; Lin, 2008). The JWTMM consists in the following four steps (Appendix B):

(i) Calculate the wavelet transforms of $R(n)$, $E(n)$ where $R(n) = \Sigma^n r(n')$, $E(n) = \Sigma^n y(n')$, and identify the corresponding modulus maxima lines in the time scale plane. The issues of using other wavelets or higher order Gaussian derivative wavelet have been discussed in the past (Lin and Sharif, 2007). We used the first order Gaussian derivative wavelet in this work as it shows more robust scaling [see (1) below].

(ii) Estimate the scaling exponent $\tau(q,\ p)$ in the power law relationship

$$Z(a;\ q,\ p) = \sum C_R(a)^q C_E(a)^p \sim a^{\tau(q,\ p)} \tag{1}$$

where a represents the scale, C_R, C_E are, respectively, the wavelet modulus maxima of $R(n)$, $E(n)$, of the nearest maxima lines.

(iii) Extract the (q_*, p_*) values from the level set $L = \{(q_*, p_*), \tau(q_*, p_*) = 0\}$ and, by considering p_* as a function of q_*, $p_*(q_*)$, calculate

$$\begin{aligned} \alpha_{R/E} &= (d/dq_*)(-p_*(q_*)), \\ f(\alpha_{R/E}) &= q_*\alpha_{R/E} + p_*(q_*) \end{aligned} \tag{2}$$

where the derivative term is approximated using finite difference.

(iv) Estimate the width of $f(\alpha_{R/E})$, $W^{\lambda}_{R/E}$, $\lambda = \mathrm{SUP}$, UPR, for q_* in the interval (Appendix B).

The background of these calculations are rooted in the mathematics of multifractal theory and has a statistical physics analog (Falconer, 1990). It should be noted that the level set extracted in step (iii) above was designed to capture the exact idea of "using the fractal of one time series to measure that of the other" in the RM analysis. We will leave these background and technical details in the references for interested readers (Falconer, 1990; Riedi and Scheuring, 1997; Lévy-Léhel and Vojak, 1998; Lin, 2008; Lin and Sharif, 2007, 2010). In order to distinguish from the traditional multifractal spectrum, $f(\alpha_{R/E})$ will henceforth be called the *RM spectrum*.

The RM spectrum width $W^{\lambda}_{R/E}$ estimated in (iv) above will be used to measure the fractal correlation between the $r(n)$ and $y(n)$ sequences. In addition, the UPR-SUP width-ratio $U_{R/E} = W^{\mathrm{UPR}}_{R/E}/W^{\mathrm{SUP}}_{R/E}$ were calculated to examine the changing fractal correlation in HUT. Thus, $U_{R/E} < 1$ (>1) implies the transition toward a stronger (weaker) fractal correlation in the UPR position. Note, a superscript $\lambda = \mathrm{SUP}$, UPR is added hereafter to the variable when it is necessary to reference the body position. Separately, we also estimated the spectrum width of the RRi sequence and calculated the UPR-SUP width-ratio, U_{RRi}, to address the changing fractal complexity of HRV in HUT. Here, $U_{\mathrm{RRi}} > 1$ (<1) implies the transition toward a more (less) complex RRi fluctuation in the UPR position.

2.3. SURROGATES

Two types of surrogates were generated from the $r(n)$, $y(n)$ sequences to test the fractal correlation result: shuffle and iterated amplitude adjusted Fourier transformed (IAAFT) surrogates. While the shuffle surrogates completely change the original data into uncorrelated random noise, IAAFT surrogates preserve both the 1/*f*-like power spectra and the amplitude distribution (Schreiber and Schmitz, 2000). We followed the algorithms documented in the literature (Schreiber and Schmitz, 2000) and verified these properties. Once the surrogates of $r(n)$, $y(n)$ were generated, their RM spectrum width was estimated and compared to the original data.

2.4. HRV AND EEG SPECTRAL COMPONENTS

Normalized LF (0.04–0.15 Hz) and HF (0.15–0.4 Hz) spectral components (in unit *nu*) of HRV were calculated to characterize the SNS-PNS interaction and PNS activities in the autonomic control of the heart rate (Akselrod et al., 1981; Task Force of ESC and NASPE, 1996; Malliani et al., 1997). To track the changing ANS activities, these calculations were carried out in segments of B heart beats: $K_j = \{r((j-1)\,B+1), \ldots, r(jB)\}$, $j = 1, \ldots, N_B$. For each K_j, the corresponding EEG segment over the time interval of B heart beats was obtained: $Y_j = \{e(m_j\Delta t), \ldots, e(n_j\Delta t)\}$, where Δt denotes the sampling time, $m_j\Delta t = t((j-1)\,B+1)$, $n_j\Delta t = t(jB)$. We then estimated the spectrum based on the segment Y_j in *Theta* (4–7 Hz), *Alpha* (8–13 Hz), and *Beta* (13–30 Hz) bands and the result is normalized by the total EEG spectral power of the segment. Since RRi is unevenly spaced, the Lomb periodogram (Press et al., 2007) was used to estimate the normalized LF, HF components. The spectral measures for each EEG segment Y_j was estimated using the Welch method. Results reported in this work are based on the intervals of $B = 128$ beats with 50% overlap (64-beat). Using $B = 64{,}256$ and/or using non-overlapping segments yield similar results (**Figure A1**).

2.5. REGRESSION ANALYSIS

To examine the underlying physiological processing in fractal correlation, regressions were performed between the RM spectrum width and the HRV, EEG spectral measures. There are a total of six variables of interest:

$$\mathcal{A} = \{ W^{\lambda}_{R/E},\ \mu^{\lambda}_{\mathrm{LF}},\ \mu^{\lambda}_{\mathrm{HF}},\ \mu^{\lambda}_{Theta},\ \mu^{\lambda}_{Alpha},\ \mu^{\lambda}_{Beta} \}\,, \tag{3}$$

where μ^{λ}_{η} for $\eta =$ LF, HF, *Theta*, *Alpha*, *Beta* are, respectively, the mean HRV and EEG spectral measures averaged over all segments in $\lambda =$ SUP, UPR positions.

Two approaches were adopted. The first is a standard linear regression between $W^{\lambda}_{R/E}$ and any one of the remaining five variables in $\mathcal{A}$. Motivated by the possibility of multiple physiological processes influencing fractal HRV, principal component analysis, PCA, was also conducted to achieve a higher dimensional regression (Jolliffe, 2002).

In PCA, we first built a 11×6 data array with the variables in $\mathcal{A}$ arranged from column $i = 1$–6. Hence, each row of this data array contains the subject's response in RM and spectral measures. Conceptually, one could also imagine the data in a six dimensional Euclidean space spanned by the coordinate $\mathcal{X}_1 = W^{\lambda}_{R/E}$, $\mathcal{X}_2 = \mu^{\lambda}_{\mathrm{LF}}, \ldots, \mathcal{X}_6 = \mu^{\lambda}_{Beta}$ (following the order listed in $\mathcal{A}$). We then applied PCA to seek an optimal coordinate transformation of $\mathcal{X}_i$ to best capture the data scattering in the six dimensional space. The transformed axes, denoted as $\mathcal{Z}_i$, $i = 1, \ldots 6$, are known as the principal axes and are given by the linear combination of the $\mathcal{X}_i$'s:

$$\mathcal{Z}_i = \sum_{j=1}^{6} d_{ji} \mathcal{X}_j \tag{4}$$

where d_{ji} are the coefficients that measure the contribution of the coordinate $\mathcal{X}_j$ in the ith principal axis. Each $\mathcal{Z}_i$ is also associated with a principal value, PV_i, that measures the data scattering along the $\mathcal{Z}_i$. Arranging PV_i in descending order, we used the cumulative PV_i

$$\Sigma PV(k) = \sum_{i=1}^{k} PV_i / \sum_{i=1}^{6} PV_i. \tag{5}$$

and report only the first N_P principal axes that satisfy the criterion $\Sigma PV(N_P) < Th$, $Th \sim 1$. The remaining principal axes are of little importance since they capture only a minute fraction of the data scattering. Geometrically, it means the data scatter in almost the perpendicular directions of these remaining principal axes.

2.6. STATISTICS

Standard methods were used to calculate the mean and SD of the EEG, RRi spectral measures. Normal distribution was verified using the Kolmogorov-Smirnov test. Differences between the spectral measures were tested for significance using the, two-tail, paired t-test. Pearson's product moment correlation coefficient was used in the regression analysis between the spectrum width estimates and the HRV, EEG spectral measures.

3. RESULTS

Our results will be given using two sets of variables. The first is the spectrum width. They include the width of the RM spectrum of the $r(n)$, $y(n)$ sequences and the width of the RRi multifractal spectrum. The width-ratios $U_{R/E}$ and U_{RRi} will be used to compare the response between the SUP and UPR positions. The second set of variables are the HRV and EEG spectral measures and their regression results.

3.1. RM AND RRI SPECTRUM WIDTH

Figure 1 shows the RRi, EEG data, the spectral measures, as well as the multifractal property of the $r(n)$, $y(n)$ sequences from two subjects. The power law (1) estimated in the RM analysis is given in **Figure 2A**. Most subjects exhibit robust scalings, ranging from one to two heart beats to about 10^2 heart beats (**Table 1**). This scaling range may be of interest as it could give a rough idea of the time scale associated with the fractal correlation.

The main result of this work is given in **Figure 2B**, which shows the width-ratios $U_{R/E}$ versus U_{RRi}. It is evident that the HUT maneuver stimulates a range of different "fractal reaction" in the subjects. In particular, we identify a subgroup of subjects $\mathcal{G} =$ (S2, S5, S9, S10) that are characterized by $U_{\mathrm{RRi}} > 1$; i.e., these subjects exhibited more complex fractal fluctuation in the UPR position. These subjects are also characterized by a much smaller $U_{R/E} \ll 1$, indicating a stronger fractal correlation in their RRi and EEG sequences. The remaining seven subjects are characterized by $U_{\mathrm{RRi}} < 1$, showing less complex RRi fluctuation in the UPR position.

The overall negative trend is observed in this empirical relationship and it is significant ($P = 0.003$). To this end, it is important to emphasize that the fractal property of the individual sequence does not dictate the outcome of the fractal correlation. As shown in the past, fractal time series can be coupled to result in a wide range of fractal correlation without changing their scaling exponents (Lin and Sharif, 2007; Appendix A). Hence, the empirical relationship between $U_{R/E}$ and U_{RRi} represents a non-trivial result that suggests the change toward a more correlated EEG, RRi fractal fluctuation is associated with the change toward a more complex fractal HRV.

The above result was further examined using shuffle and IAAFT surrogates. The null hypothesis of the shuffle surrogates is to test whether there is any dynamics at all; namely, would the underlying phenomenon be simply reproduced by independent identically distributed random variates. The shuffling serves to achieve this purpose by destroying the temporal correlation of the original data. As a result, shuffle surrogates exhibit completely independent fluctuations, which, in the present context, means weaker fractal correlation, or a large RM spectrum width. The IAAFT surrogate, on the other hand, is to test the null of a linear gaussian process under (static) non-linear transformation, say, from the measurement device (Schreiber and Schmitz, 2000). The surrogate preserves both the amplitude distribution and the second order scaling property of the original sequence, e.g., the power law power spectrum. Hence, a relatively stronger fractal correlation with a smaller RM spectrum width is expected. Our result is based on the ensemble of 80 pairs of such surrogates from the original $r(n)$, $y(n)$ sequences.

The fractal correlation results of the surrogates are consistent to the characteristics described above; i.e., the RM spectrum width of the shuffle surrogate is consistently larger than the IAAFT's and the original data (**Figures 2C,D**). Using the group-mean statistic, the averaged RM spectrum width of the shuffle surrogate is significantly larger than the original sequences' ($P < 1E{-}5$ for both SUP, UPR positions). It implies that destroying the temporal correlation in $r(n)$, $y(n)$ sequences can result in a qualitatively different outcome and suggests the importance of fractal dynamics in the fractal correlation result. For the IAAFT surrogate, the RM spectrum width is seen to lie in a noticeably narrower range compared to the original data. But the group-mean statistic is not significant in the UPR position and only approaches significance in the SUP position ($P = 0.07$). The non-rejection of the

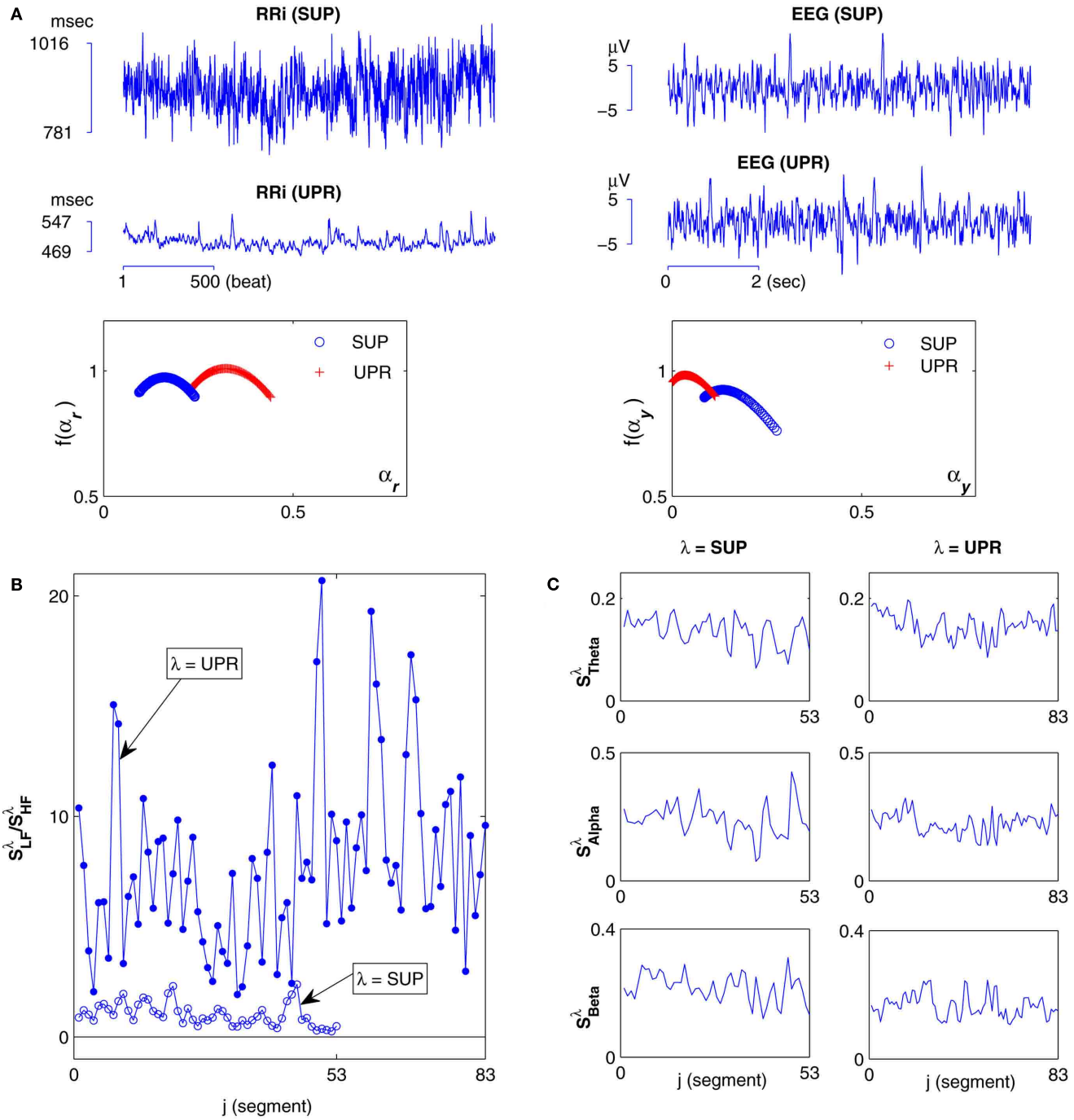

FIGURE 1 | Continued

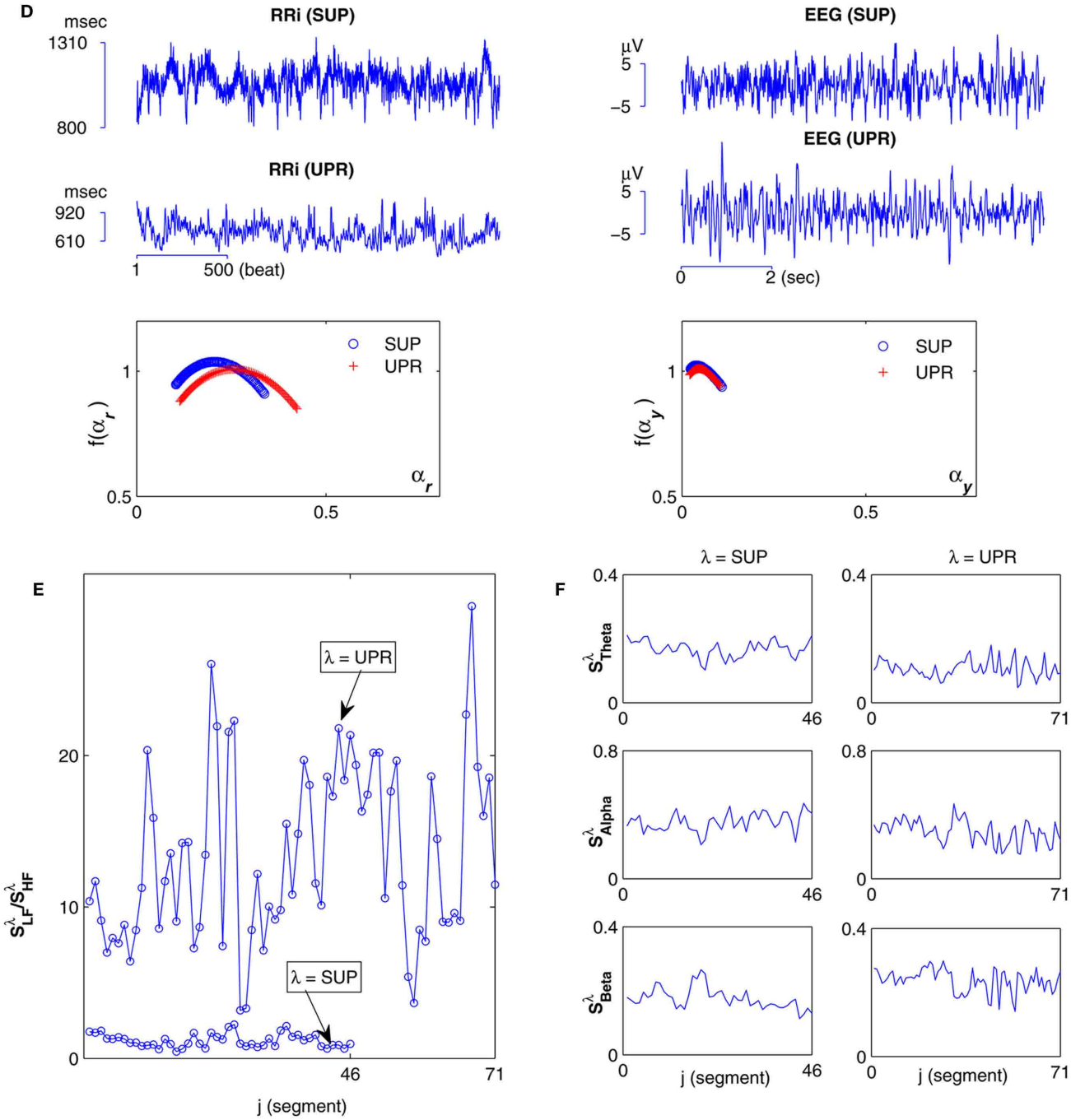

FIGURE 1 | Data segments from a subject (S5) in the group $\mathcal{G}$: (A) Left column: RRi in SUP (top), UPR positions (middle), and their multifractal spectra $f(\alpha_r)$ (bottom). Right column: EEG in SUP (top), UPR positions (middle), and the multifractal spectra of $y(n)$, $f(\alpha_y)$ (bottom). The multifractal spectra were estimated using WTMM with the third Gaussian derivative wavelet and $q \in [-2, 2]$. **(B)** The LF/HF spectral component ratio (sympathovagal index), $\mathcal{S}^{\lambda}_{\mathrm{LF}}(j)/\mathcal{S}^{\lambda}_{\mathrm{HF}}(j)$ in $\lambda = \mathrm{SUP}$ ("$\circ$") and $\lambda = \mathrm{UPR}$ positions ("$\bullet$"). **(C)** Top to bottom rows: normalized EEG spectral components in *Theta*, *Alpha*, *Beta* bands, $\mathcal{S}^{\lambda}_{Theta}(j)$, $\mathcal{S}^{\lambda}_{Alpha}(j)$, $\mathcal{S}^{\lambda}_{Beta}(j)$, respectively, in $\lambda = \mathrm{SUP}$ (left column) and $\lambda = \mathrm{UPR}$ (right column) positions from the same subject. **(D–F)** Show the same set of plots for a different subject (S11).

null hypothesis means, either the width estimate fails to discriminate against the alternative in the data, or the non-linear property in $r(n)$, $y(n)$ may not be essential for CAFC.

3.2. HRV, EEG SPECTRAL MEASURES

Typical segment-to-segment spectral components from two subjects have been shown in **Figure 1**. The expected SNS activation

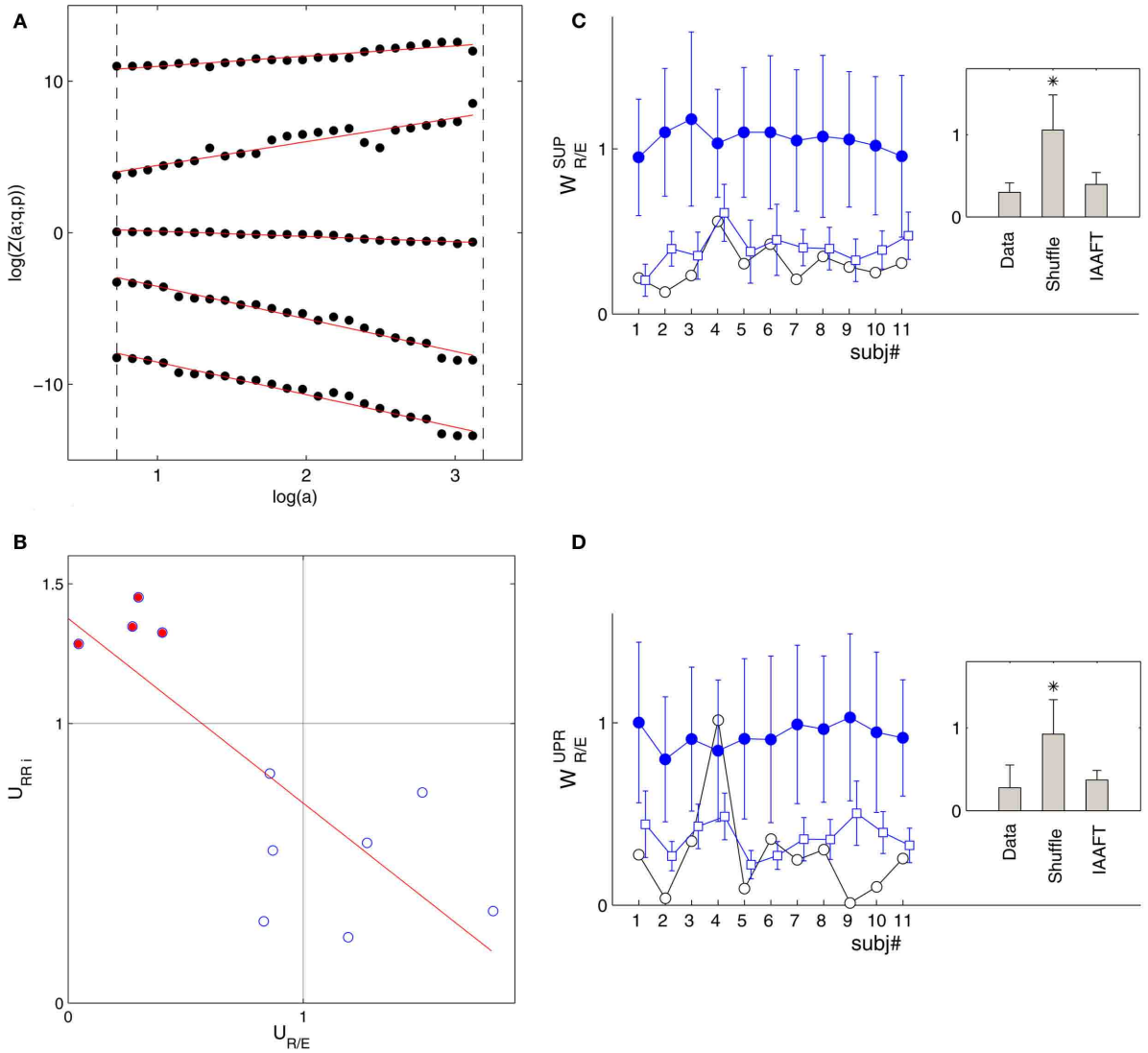

FIGURE 2 | (A) Scaling relationship (1): log $Z(a; q, p)$ versus log(a) in the SUP position from the same subject (S5) shown in **Figure 1A**; (q, p) = (−1.4, −1.4), (2.6, −1.4), (0.6, 0.6), (2.6, 2.6), (−1.4, 2.6) from bottom to top. The curves are separated for clarity purpose. The scaling range is indicated by the vertical long-dash lines. The scaling exponent $\tau(q, p)$ is estimated from the best-fit line shown as the solid line in the figure. **(B)** U_{RRi} versus $U_{R/E}$ relationship. The filled circle indicates the result from the subjects in group $\mathcal{G}$. The solid line is the regression line ($\rho = -0.80$, $P = 0.003$). The spectrum width was calculated for q in [−2, 2] (Appendix B). **(C)** The RM spectrum width of the shuffle surrogates ("•") and IAAFT surrogates ("□") in the SUP position. **(D)** The RM spectrum width of the shuffled surrogates ("•") and IAAFT surrogates ("□") in the UPR position. The width estimates of the original data are also included ("○") for comparison. The error bars represent one SD. The results for the IAAFT surrogates are shifted slightly to the right for clarity. The insets in **(C,D)** show the group-mean RM spectrum width.

and PNS withdrawal due to the reduced baroreflex afferent input in HUT (Tulppo et al., 2001) is indicated by the consistently higher LF and HF spectral components ratio (sympathovagal index) in the UPR position (**Figures 1B,E**). The HRV spectral measures, μ_η^λ, η = LF, HF, along with their EEG counterparts: μ_η^λ, η = *Theta*, *Beta*, *Alpha*, are summarized in **Figure 3**, and are mostly significantly different between the λ = SUP and UPR positions (see also group averaged statistics in **Table 2**).

Table 1 | The mean ± SD of the lower (a_{min}) and upper (a_{max}) scales of the scaling range in (1) (unit: heart beat).

Body position	a_{min}	a_{max}
SUP	6.23 ± 1.70	76.21 ± 11.54
UPR	6.24 ± 1.46	107.10 ± 28.46

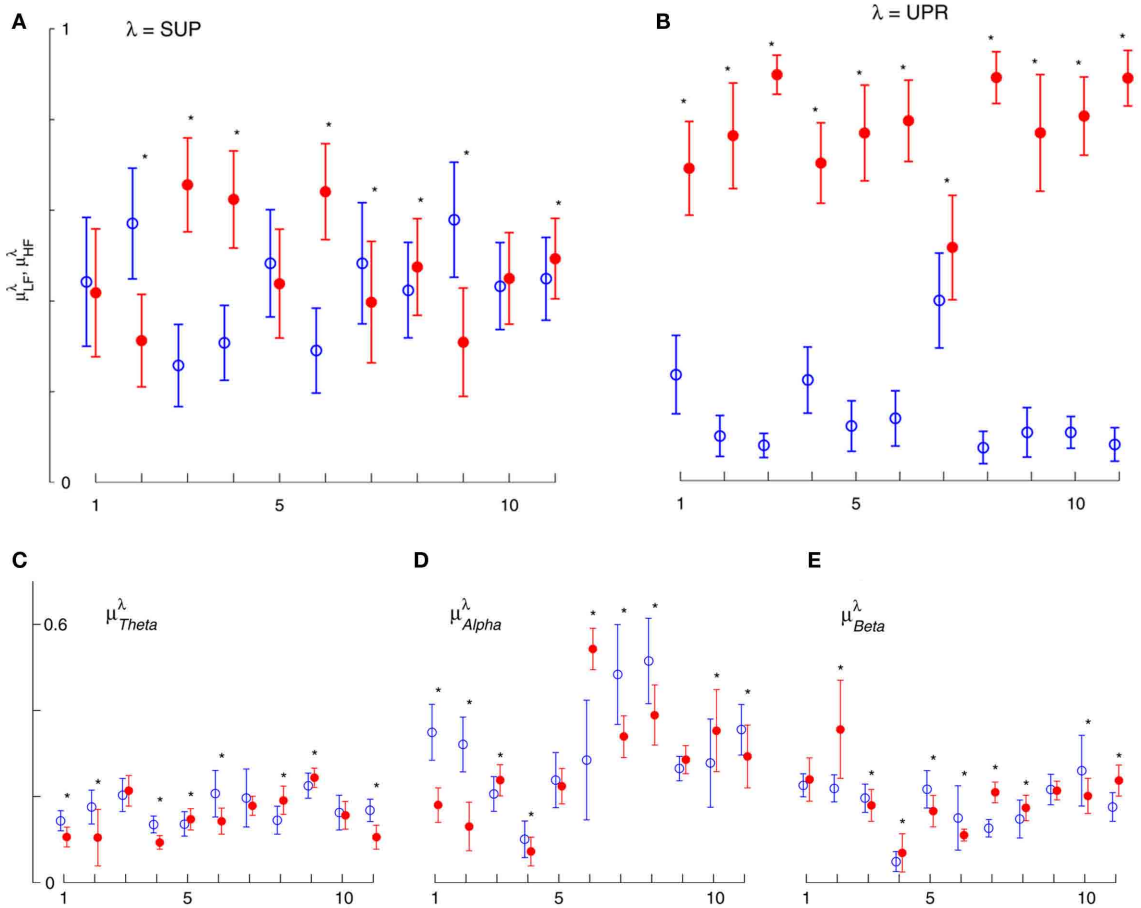

FIGURE 3 | Averaged LF, HF spectral components μ^{λ}_{LF} ("•"), μ^{λ}_{HF} ("∘") in (A) λ = SUP, (B) λ = UPR positions, and the averaged EEG spectral components (C) μ^{λ}_{Theta}, (D) μ^{λ}_{Alpha}, (E) μ^{λ}_{Beta}, λ = SUP ("∘"), UPR ("•"). Significant difference ($P < 0.05$) between the SUP and UPR positions is indicated by the asterisk (*). Note that the HF components in **(A,B)** and the EEG spectral components in the SUP position are shifted slightly to the left for clarity. The error bar represents 1 SD of the segment-to-segment variation of the spectral components.

Table 2 | Group averaged EEG, HRV spectral components: mean ± SD, μ^{λ}_{η}, η = *Theta, Alpha, Beta,* LF, HF, λ = SUP, UPR.

	λ = SUP	λ = UPR
μ^{λ}_{Theta}	0.17 ± 0.03	0.15 ± 0.05
μ^{λ}_{Alpha}	0.31 ± 0.12	0.28 ± 0.13
μ^{λ}_{Beta}	0.18 ± 0.06	0.20 ± 0.07
μ^{λ}_{LF}	0.47 ± 0.12	0.77 ± 0.11*
μ^{λ}_{HF}	0.43 ± 0.11	0.15 ± 0.10*

*$P < 1E{-}5$, SUP versus UPR.

Since their physiological correlates, better understanding of the relation between these spectral measures and the RM spectrum width could shed lights into the physiological processing underlying CAFC. A standard linear regression of two variables and a multivariate PCA were conducted for this purpose. The correlation coefficient (ρ^{λ}) and the associated P value from the linear regression are reported in **Table 3** and described in the next two subsections. The results from the PCA are reported last. To avoid confusion, we shall use the term correlation hereafter to refer to the two-point correlation in the linear regression result. We shall always specify fractal correlation or CAFC wherever necessary.

3.3. LINEAR REGRESSION WITH EEG SPECTRAL MEASURES

Figure 4 shows the scatter plots between the RM spectrum width $W^{\lambda}_{R/E}$ and the EEG μ^{λ}_{Theta}, μ^{λ}_{Alpha}, and μ^{λ}_{Beta} in λ = SUP, UPR positions. It is observed that $W^{\lambda}_{R/E}$ is significantly and negatively correlated with μ^{λ}_{Beta} ($P = 0.01$ for λ = SUP, $P = 0.02$ for λ = UPR), followed by the weaker correlation with μ^{λ}_{Theta} ($P = 0.42$ for λ = SUP, $P = 0.26$ for λ = UPR), and μ^{λ}_{Alpha} ($P = 0.18$ for λ = SUP, $P = 0.40$ for λ = UPR). Further of note is the generally larger μ^{λ}_{Beta} for the subjects in $\mathcal{G}$ (inset of **Figure 4C**).

3.4. LINEAR REGRESSION WITH HRV SPECTRAL MEASURES

Figure 5 shows the scatter plots between RM spectrum width $W^{\lambda}_{R/E}$ and HRV spectral components, μ^{λ}_{LF}, μ^{λ}_{HF}, λ = SUP, UPR. For the

Table 3 | Regression results between averaged EEG, RRi spectral components and $W^{\lambda}_{R/E}$.

	***Theta* band**	***Alpha* band**	***Beta* band**	**LF**	**HF**
ρ^{SUP}, P	−0.27, 0.42	−0.43, 0.18	−0.73, 0.01	0.63, 0.04	−0.56, 0.07
ρ^{UPR}, P	−0.37, 0.26	−0.28, 0.40	−0.70, 0.02	−0.11, 0.74	0.28, 0.40

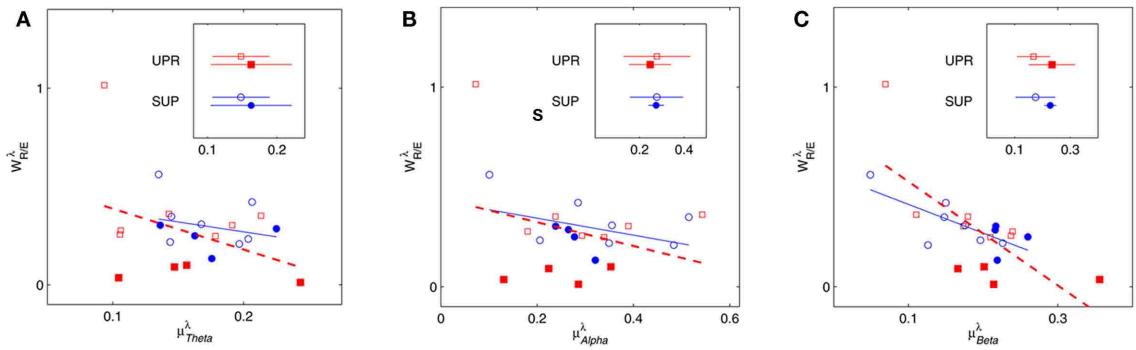

FIGURE 4 | $W^{\lambda}_{R/E}$ versus μ^{λ}_{η} scatter plot for λ = SUP ("∘"), UPR ("□") in the (A) η = *Theta* band, (B) η = *Alpha* band, and (C) η = *Beta*. The regression lines for the SUP (UPR) data are shown as solid (long-dashed) lines. The subgroup of subjects $\mathcal{G}$ are highlighted using filled symbols ("•" for SUP and "■" for UPR data). The inserts show the comparisons of the average of μ^{λ}_{η} between the group $\mathcal{G}$ and the rest. The symbol follow the same description given in **(A–C)**.

SUP position, strong correlations with the LF ($P = 0.04$), HF components ($P = 0.07$) are observed (**Table 3**). In addition, different regression trends are noted: LF component is positively correlated and HF component is negatively correlated. For the UPR position, weak correlation with the LF ($P = 0.74$) and HF components ($P = 0.40$) are observed. Observe also the larger difference of LF, HF components for subjects in $\mathcal{G}$ (insets of **Figures 5A,B**).

3.5. MULTIVARIATE REGRESSION: PRINCIPAL COMPONENT ANALYSIS RESULTS

The PCA results are summarized in **Figure 6**. Using $Th = 0.95$, most of the data scattering can be captured by the first three principal axes (**Figure 6A**). The actual ΣPV value sums up to a Th value of ∼0.97, meaning that 97% of the data scattering is captured by the selected principal axes.

The importance of the coordinate composition of a particular principal axis is determined by the d_{ji} value in (4). We will focus mainly on the ones with a large d_{1i} coefficient since it corresponds to the coordinate associated with $W^{\lambda}_{R/E}$, and thus CAFC. They are $\mathcal{Z}_1$, $\mathcal{Z}_3$ for the SUP position and $\mathcal{Z}_1$ for the UPR position (**Figure 6B**). Two unique features can be found in these principal axes. The first is the relatively comparable d_{ji} values. The only exception is the much smaller d_{4i} related to the EEG *Theta* band spectral measure. These principal axes also share the common characteristic of having significant d_{5i}, d_{6i} coefficients that are associated to the EEG *Alpha*, *Beta* band spectral measures. The second feature is the difference between the SUP, UPR positions. For $\mathcal{Z}_1$, $\mathcal{Z}_3$ of the SUP position and $\mathcal{Z}_1$ of the UPR position, it can be seen the different compositions associated with the HRV spectral measures: those for the SUP position are significantly larger than those for the UPR position. In this regard, the UPR position is qualitatively different in that the HRV spectral measures play a less significant role in CAFC than those in the SUP position.

4. DISCUSSIONS

The main finding of this work is the CAFC in fractal HRV. The surrogate testing quickly confirms that the fractal dynamics in $r(n)$, $y(n)$ sequences are indeed crucial for CAFC. The result from IAAFT surrogates suggests that the non-linear characteristics in $r(n)$, $y(n)$ sequences may not be essential for CAFC, although there is always the possibility that the RM spectrum width does not provide the discriminative statistics necessary to reflect CAFC. Further examination on other surrogate types and alternative statistic should lead to deeper insights. The potential physiological processing underlying CAFC was examined using regression on various spectral measures. These results are discussed below.

4.1. $W^{\lambda}_{R/E}$ AND EEG SPECTRAL MEASURES

In the context of postural change, Cole reported elevated EEG *Beta* band activity in the SUP to UPR transition as a result of a proposed arousal factor (Cole, 1989; see also Nikulin and Brismar, 2004). Consistent to Cole, Schneider and co-workers reported decreased *Beta* band activity in the zero gravity phase of the parabolic flight (Schneider et al., 2008). Lipnicki pointed out a baroreflex induced cortical inhibition contributing to the phenomenon, and further suggested reduced activity in the locus coeruleus noradrenergic system of the brainstem (Lipnicki, 2009). The activation/inhibition of this area of the brain is interesting. Not only does it have widespread projections through out the brain (Berridge and Waterhouse, 2003), neural pathways to the region where preganglionic parasympathetic cardiac neurons are located were also found in the animal study (Ter Horst et al., 1991, 1996). Given the known PNS effect on fractal HRV (Aoyagi et al., 2000,

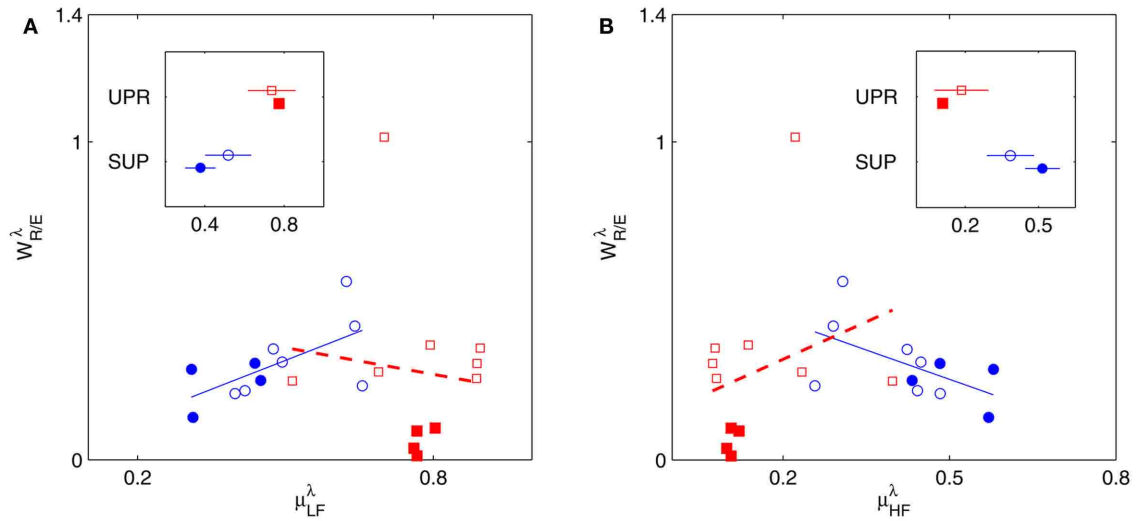

FIGURE 5 | $W^{\lambda}_{R/E}$ **versus** μ^{λ}_{η} **scatter plot for** $\lambda =$ **SUP ("∘"), UPR ("□") and (A)** $\eta =$ **LF, (B)** $\eta =$ **HF.** The regression lines for the SUP (UPR) data are shown as solid (long-dashed) lines. The subgroup of subjects $\mathcal{G}$ are highlighted using filled symbols ("•" for SUP and "■" for UPR data). The inserts show the comparisons of the average of μ^{λ}_{η} between the group $\mathcal{G}$ and the rest. The symbol follow the same description given in **(A,B)**.

2003; Amaral et al., 2001; Makikallio et al., 2005; Heffernan et al., 2008), it is plausible that the link between the EEG *Beta* band activity and HRV scale-free dynamics could exist.

In the current result (**Figure 3E**), we did not observe a consistent *Beta* band elevation in the subjects. The length of the UPR test in the protocol could explain this variation. The UPR test in this work lasted mostly above 40 min and some degree of fatigue in the subject is expected to dampen the effect. But the two-point correlation between μ^{λ}_{Beta} and $W^{\lambda}_{R/E}$ was indeed significant ($P = 0.01$ for $\lambda =$ SUP and $P = 0.02$ for $\lambda =$ UPR; **Table 3**), suggesting the possible link between EEG *Beta* band activity and fractal HRV. However, we were not able to further imply an arousal factor as suggested in the literature. This is because not all subjects exhibited elevated *Beta* band activity, notably the lower μ^{λ}_{Beta} of S5, S10 in the UPR position (**Figure 3E**). The underlying matter is likely more complex due to the multiple processes contributing to CAFC. The PCA result provides the support of this view. In particular, the principal axes with a large $W^{\lambda}_{R/E}$ component all share the similar feature of having, not only a large d_{6i} coefficient related to the *Beta* band spectral measure, but also a relatively large d_{5i} coefficient related to the *Alpha* band spectral measure. If one restricts to the subspace spanned by the coordinates $\mathcal{X}_1$, $\mathcal{X}_5$, $\mathcal{X}_6$ (associated with $W^{\lambda}_{R/E}$, μ^{λ}_{Alpha}, μ^{λ}_{Beta}), i.e., the group with large d_{ji} coefficients in the selected principal axes, the subgroup $\mathcal{G}$ can again be singled out, as it was by using the width-ratios in **Figure 2B**. The same characterization achieved separately by these spectral measures suggests the importance of the EEG *Alpha*, *Beta* dynamics in CAFC.

4.2. $W^{\lambda}_{R/E}$ AND HRV SPECTRAL MEASURES

We will first discuss the results of the SUP position. The linear regression shows strong correlation between $W^{\mathrm{SUP}}_{R/E}$ and the LF, HF HRV spectral measures. The underlying characteristics are consistent to the known SNS, PNS effects on fractal HRV. In particular, concurrent SNS activation and PNS withdrawal were found to lead to relatively simpler HRV fractal pattern (Aoyagi et al., 2000, 2003; Amaral et al., 2001; Makikallio et al., 2005; Heffernan et al., 2008). These past studies and the link between CAFC and the HRV fractal complexity (**Figure 2A**) are consistent to the current finding. In particular, the increase or decrease of the HRV fractal complexity can be separately predicted from the two different sets of variables, one from the known fractal effects based on the changing HRV spectral measures, and one from the empirical relationship between $U_{R/E}$ and U_{RRi}. For example, the HF component is negatively correlated with $W^{\mathrm{SUP}}_{R/E}$, indicating a large HF component enhances CAFC (toward more complex fractal HRV), and the LF component is positively correlated with $W^{\mathrm{SUP}}_{R/E}$, indicating a large LF component weakens CAFC (toward less complex fractal HRV). These results imply that a strong CAFC in the SUP position can in part be attributed to the strength of the PNS activity.

The linear regression result from the UPR position, however, shows quite a different picture. Here, a much weaker correlation between $W^{\mathrm{UPR}}_{R/E}$ and the HRV spectral components are found. In addition, there is a dramatic increase of the P value from the SUP to the UPR positions (**Table 3**). The known autonomic effects on fractal HRV no longer seems to hold (**Figure 2A**). For example, not all subjects exhibit "simpler" fractal HRV pattern with the SNS activation and PNS withdrawal in the UPR position (**Figure 2B**). This is most evident from the subjects in group $\mathcal{G}$, who are characterized by the transition toward more complex HRV fractal pattern ($U_{\mathrm{RRi}} > 1$), stronger CAFC ($U_{R/E} \ll 1$) in the UPR position. We do not have further insights as to why these group exhibit qualitatively different behavior from the rest, except that three of them are trained athletes that participate in the University sport teams. Reports separately on the fractal HRV and EEG spectral powers did indicate that intense exercise can have a marked effect, such as resulting in a smaller scaling exponent in HRV (Tulppo et al., 2003; Karavirta et al., 2009) and higher EEG spectral powers

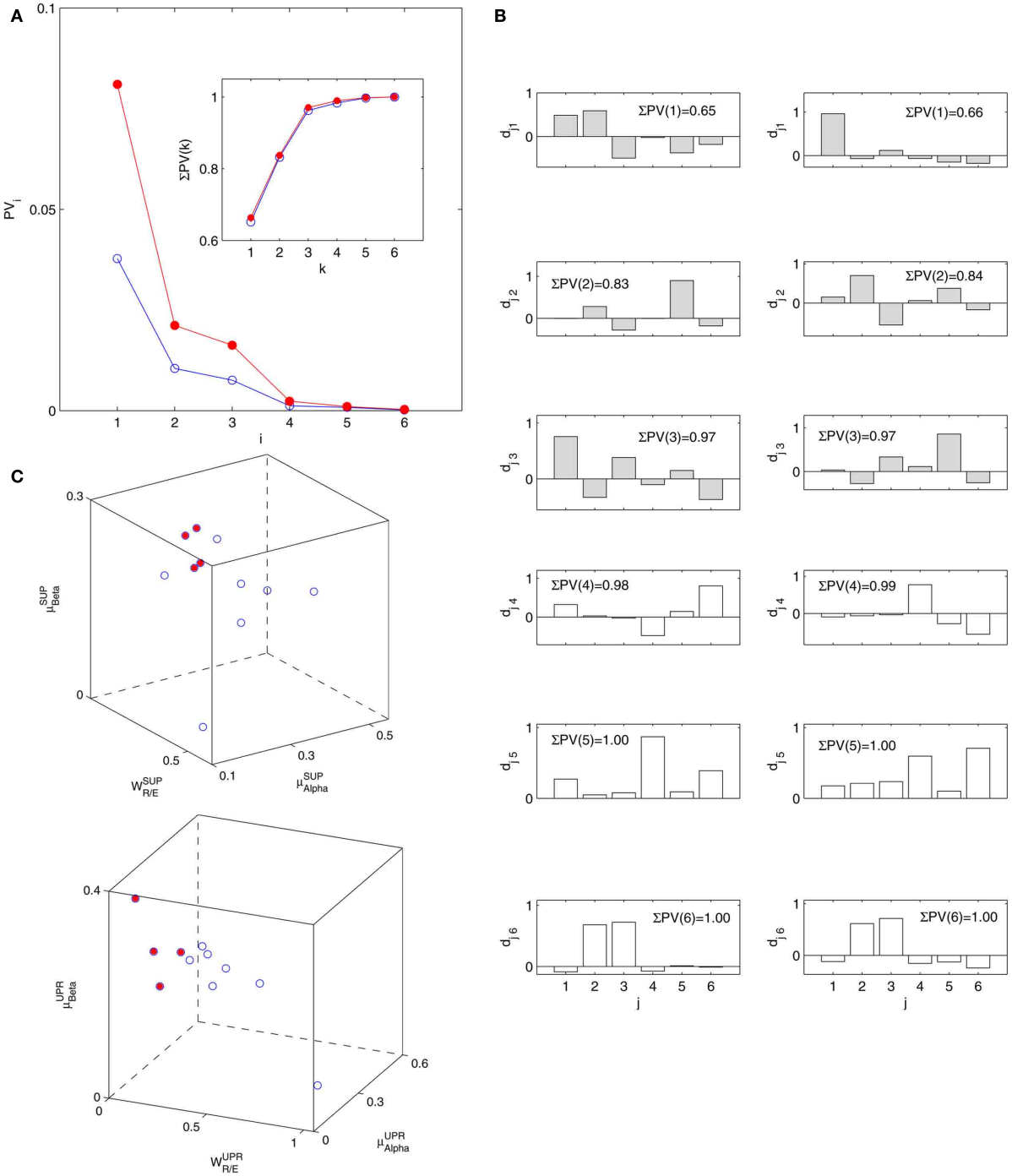

FIGURE 6 | Principal component analysis results. (A) The principal values PV_i in SUP ("∘") and UPR position ("•"). The inset shows the cumulative $\Sigma PV(k)$ as given by (4). **(B)** The principal axis coefficients d_{ji}, $i = 1, \ldots, 6$, (top to bottom) in SUP (left column) and UPR (right column) positions. The x-label, $j = 1,\ldots,6$, specifies the coordinate number associated with $W^{\lambda}_{R/E}$, μ^{λ}_{LF}, μ^{λ}_{HF}, μ^{λ}_{Theta}, μ^{λ}_{Alpha}, and μ^{λ}_{Beta}, respectively. The first three principal axes selected by the criterion $\Sigma PV(3) < 0.97$ are shown with gray bars. **(C)** The projection of the data 11 × 6 data array into the subspace spanned by $W^{\lambda}_{R/E}$, μ^{λ}_{Alpha}, μ^{λ}_{Beta} in SUP (left) and UPR (right) positions. The data correspond to the subgroup of subjects $\mathcal{G}$ are shown as filled circles.

(Lardon and Polich, 1996). However, one of the subjects (S5) in $\mathcal{G}$ does not engage in the same level of exercise as the other three.

The PCA results imply similar interpretations. In particular, considering the principal axes with a large d_{1i} coefficient (related to $W^{\lambda}_{R/E}$), the coefficients d_{2i}, d_{3i} associated with HRV spectral measures are much more significant in the SUP position than in the UPR position (**Figure 6B**). This may be read in parallel to the stronger correlation between the $W^{SUP}_{R/E}$ and the HRV spectral

measures from above, and implies a more substantial central-autonomic interaction contributing to the fractal HRV in the SUP position.

The main implications from the PCA are the multiple physiological processes underlying CAFC and the important roles of the EEG *Alpha*, *Beta* band dynamics. The qualitative difference of the HRV spectral measure composition reported above implies the predominant central influence in CAFC in the UPR position.

LIMIT OF STUDY

The current study is limited by the number of participants and some aspects of the protocol. Particular to the ∼40 min tilt test, it is expected that certain degree of stress and fatigue could develop during the test. However, these factors were not directly measured in this study. We should also remark the intrinsic limit on the methodology, which has affected the protocol used in the study. We held the view that a "free running" of the mind in wakefulness could facilitate the RM analysis, albeit the subject's mental state was influenced by being physically constrained on the tilt table. This is because certain rhythmic patterns can emerge in the more specific brain state, such as the *Alpha* rhythm in meditation or *Theta* rhythm in cognitive processing. Such rhythmic patterns typically manifest into few dominant Fourier modes in the EEG that will inevitably "mask" the underlying fractal pattern (Lin et al., 2006) and limit one's ability to characterize CAFC.

CONCLUSION

Although cardiovascular dynamics has long been a subject of intense interest, the importance and implication of its fractal dynamics are only realized in recent decades. By the general framework of RM and the autonomic perturbation induced by the postural change, we found the empirical support of a central component in fractal HRV, i.e., the CAFC. The regression analysis further implies the importance of the EEG *Alpha*, *Beta* band dynamics in CAFC, and thus fractal HRV. Evidently, such central components introduce additional factors to be included in the fractal HRV analysis. It is thus not surprising to learn the difficulty of finding a consistent "baseline" scaling property in HRV (Tan et al., 2009). The current result may offer a reasonable explanation since other psychophysiological factors may come into play and affect the fractal HRV property.

The PCA results provide us much insight into the potential physiological processing in CAFC. Qualitatively different behaviors between the SUP, UPR position imply the importance of considering central component in fractal HRV. Additional tests on larger ensemble size and demographic differences, as well as with specifically designed protocol to provoke the *Alpha*, *Beta* band activities, are warranted to assess the robustness of these findings. In conclusion, we believe CAFC could play the key role in the manifestation and interpretation of fractal HRV. In application, CAFC may also hold the key for the state of reduced HRV, with further implications on the "simpler" HRV pattern witnessed in certain heart diseased conditions.

ACKNOWLEDGMENTS

This research is supported by the Natural Science and Engineering Research Council of Canada. We are grateful to the valuable comments from the anonymous referees.

REFERENCES

Akselrod, S., Gordon, D., Ubel, F. A., Shannon, D. C., Barger, A. C., and Cohen, R. J. (1981). A quantitative probe of beat to beat cardiovascular control. *Science* 213, 220–222.

Amaral, L. A. N., Ivanov, P. C. H., Aoyagi, N., Hidaka, I., and Tomono S, Goldberger AL, Stanley HE and Yamamoto, Y. (2001). Behavioral-independent features of complex heartbeat dynamics. *Phys. Rev. Lett.* 86, 6027–6029.

Aoyagi, N., Ohashi, K., Tomono, S., and Yamamoto, Y. (2000). Temporal contribution of body movement to very long-term heart rate variability in humans. *Am. J. Physiol. Heart Circ. Physiol.* 278, H1035–H1041.

Aoyagi, N., Ohashi, K., and Yamamoto, Y. (2003). Frequency characteristics of long-term heart rate variability during constant routine protocol. *Am. J. Physiol. Regul. Integr. Comp. Physiol.* 285, R171–R176.

Berridge, C. W., and Waterhouse, B. D. (2003). The locus coeruleus-noradrenergic system: modulation of behavioral state and state-dependent cognitive processes. *Brain Res. Brain Res. Rev.* 42, 33–84.

Brandenberger, G., Ehrhart, J., Piquard, F., and Simon, C. (2001). Inverse coupling between ultradian oscillations in delta wave activity and heart rate variability during sleep. *Clin. Neurophysiol.* 112, 992–996.

Bunde, A., Havlin, S., Kantelhardt, J. W., Penzel, T., Peter, J. H., and Voigt, K. (2000). Correlated and uncorrelated regions in the heart-rate fluctuations during sleep. *Phys. Rev. Lett.* 85, 3736–3739.

Cole, R. J. (1989). Postural baroreflex stimuli may affect EEG arousal and sleep in humans. *J. Appl. Physiol.* 67, 2369–2375.

Dampney, R. A. L., Coleman, J. J., Fontes, M. A. P., Hirooka, Y., Horiuchi, J., Li, Y. W., Polson, J. W., Potts, P. D., and Tagawa, T. (2002). Central mechanisms underlying short- and long-term regulation of the cardiovascular system. *Clin. Exp. Pharmacol. Physiol.* 29, 261–268.

Falconer, K. (1990). *Fractal Geometry: Mathematical Foundations and Applications*. New York: John Wiley and Sons Ltd.

Gisiger, T. (2001). Scale invariance in biology: coincidence or footprint of a universal mechanism? *Biol. Rev. Camb. Philos. Soc.* 76, 161–207.

Goodwin, G. M., McCloskey, D. I., and Mitchell, J. H. (1972). Cardiovascular and respiratory responses to changes in central command during isometric exercise at constant muscle tension. *J Physiol.* 226, 173–190.

Heffernan, K. S., Sosnoff, J. J., Fahs, C. A., Shinsako, K. K., Jae, S. Y., and Fernhall, B. (2008). Fractal scaling properties of heart rate dynamics following resistance exercise training. *J. Appl. Physiol.* 105, 109–113.

Ivanov, P. C. H., Amaral, L. A. N., Goldberger, A. L., Havlin, S., Rosenblum, M. G., Struzik, Z. R., and Stanley, H. E. (1999). Multifractality in human heartbeat dynamics. *Nature* 399, 461–465.

Jolliffe, I. T. (2002). *Principal Component Analysis*, 2nd Edn. New York: Springer-Verlag.

Karavirta, L., Tulppo, M. P., Laaksonen, D. E., Nyman, K., Laukkanen, R. T., Kinnunen, H., and Hakkinen A. Hakkinen, K. (2009). Heart rate dynamics after combined endurance and strength training in older men. *Med. Sci. Sports Exerc.* 41, 1436–1443.

Komatsu, T., Kimura, T., Nishiwaki, K., Fujiwara, Y., Sawada, K., and Shimada, Y (1997). Recovery of heart rate variability profile in patients after coronary artery surgery. *Anesth. Analg.* 85, 713–718.

Kors, J. A., Swenne, C. A., and Greiser, K. H. (2007). Cardiovascular disease, risk factors, and heart rate variability in the general population. *J. Electrocardiol.* 40, S19–S21.

Kubota, Y., Sato, W., Toichi, M., Murai, T., Okada, T., Hayashi, A., and Sengoku, A. (2001). Frontal midline theta rhythm is correlated with cardiac activities during the performance of an attention demanding meditation procedure. *Brain Res. Cogn. Brain Res.* 11, 281–287,

Kucera, J. P., Heuschkel, M. O., Renaud, P., and Rohr, S. (2000). Power-law behavior of beat-rate variability in monolayer cultures of neonatal rat ventricular myocytes. *Circ. Res.* 86, 1140–1145.

Lardon, M. T., and Polich, J. (1996). EEG changes from long-term physical exercise. *Biol. Psychol.* 44, 19–30.

Lévy-Léhel, J., and Vojak, R. (1998). Multifractal analysis of Choquet capacities. *Adv. Appl. Math.* 20, 1–43.

Lin, D. C. (2008). Factorization of joing multifractality. *Physica A* 387, 3461–3470.

Lin, D. C., and Sharif, A. (2007). Wavelet transform modulus maxima based fractal correlation analysis. *Eur. Phys. J. B* 60, 483–491.

Lin, D. C., and Sharif, A. (2010). Common multifractality in the heart rate variability and brain activity of healthy humans. *Chaos* 20, 023121.

Lin, D. C., Sharif, A., and Kwan, H. C. (2006). Scaling and organization of electroencephalographic background activity and alpha rhythm in healthy young adults. *Biol. Cybern.* 95, 401–411.

Lipnicki, D. M. (2009). Baroreceptor activity facilitates cortical inhibition in zero gravity. *Neuroimage* 46, 10–11.

Loewy, A., and Spyer, K. (1990). *Central Regulation of Autonomic Functions.* New York: Oxford University Press.

Lombardi, F. (2000). Chaos theory, heart rate variability, and arrhythmic mortality. *Circulation* 101, 8–10.

Lucini, D., Covacci, G., Milani, R., Mela, G. S., Malliani, A., and Pagani, M. (1997). A controlled study of effects of mental relaxation on autonomic excitatory responses in healthy subjects. *Psychosom. Med.* 59, 541–552.

Mahon, N. G., Hedman, A. E., Padula, M., Gang, Y., Savelieva, I., Waktare, J. E. P., Malik, M. M., Huikuri, H. V., and McKenna, W. J. (2002). Fractal correlation properties of R-R interval dynamics in asymptomatic relatives of patients with dilated cardiomyopathy. *Eur. J. Heart Fail.* 4, 151–158.

Makikallio, T. H., Huikuri, H. V., Makikallio, A., Sourander, L. B., Mitrani, R. D., Castellanos, A., and Myerburg, R. J. (2001). Prediction of sudden cardiac death by fractal analysis of heart rate variability in elderly subjects. *J. Am. Coll. Cardiol.* 37, 1395–1402.

Makikallio, T. H., Huikuri, H. V., Tulppo, M. P., Kiviniemi, A. M., Hautala, A. J., Kallio, M., and Seppanen, T. (2005). Physiological background of the loss of fractal heart rate dynamics. *Circulation* 112, 314–319.

Malliani, A., Montano, N., and Pagani, M. (1997). Physiological background of heart rate variability. *Card. Electrophysiol. Rev.* 3, 343–346.

Nikulin, V. V., and Brismar, T. (2004). Long-range temporal correlations in alpha and beta oscillations: effect of arousal level and test-retest reliability. *Clin. Neurophysiol.* 115, 1896–1908.

Peng, C. K., Mietus, J. E., Liu, Y., Khalsa, G., Douglas, P. S., Benson, H., and Goldberger, A. L. (1999). Exaggerated heart rate oscillations during two meditation techniques. *Int. J. Cardiol.* 70, 101–107.

Pereda, E., and Gonzalez, J. J. (2008). Nonlinear dynamical analysis of the interdependence between central and autonomic nervous system in neonates during sleep. *J. Biol. Phys.* 34, 405–412.

Phongsuphap, S., Pongsupap, Y., Chandanamattha, P., and Lursinsap, C. (2008). Changes in heart rate variability during concentration meditation. *Int. J. Cardiol.* 130, 481–484.

Press, W. H., Teukolsky, S. A., Vetterling, W. T., and Flannery, B. P. (2007). *Numerical Recipes.* New York: Cambridge University Press.

Riedi, R. H., and Scheuring, I. (1997). Conditional and relative multifractal spectra. *Fractals* 5, 153–168.

Sassi, R., Signorini, M. G., and Cerutti, S. (2009). Multifractality and heart rate variability. *Chaos* 19, 028507.

Schneider, S., Brummer, V., Carnahan, H., Dubrowski, A., Askew, C. D., and Struder, H. K. (2008). What happens to the brain in weightlessness? A first approach by EEG tomography. *Neuroimage* 42, 1316–1323.

Schreiber, T., and Schmitz, A. (2000). Surrogate time series. *Physica D* 142, 346–382.

Tan, C. O., Cohen, M. A., Eckberg, D. L., and Taylor, J. A. (2009). Fractal properties of human heart period variability: physiological and methodological implications. *J. Physiol.* 587, 3929–3941.

Task Force of ESC and NASPE. (1996). Heart rate variability, standards of measurement, physiological interpretation, and clinical use. *Circulation* 93, 1043–1065.

Ter Horst, G. J., Hautvast, R. W. M., De Jongste, M. J., and Korf, J. (1996). Neuroanatomy of cardiac activity-regulating circuitry: a transneuronal retrograde viral labelling study in the rat. *Eur. J. Neurosci.* 8, 2029–2041.

Ter Horst, G. J., Toes, G. J., and Van Willigen, J. D. (1991). Locus coeruleus projections to the dorsal motor vagus nucleus in the rate. *Neuroscience* 45, 153–160.

Togo, F., Kiyono, K., Struzik, Z. R., and Yamamoto, Y. (2006). Unique very low-frequency heart rate variability during sleep in humans. *IEEE Trans. Biomed. Eng.* 53, 28–34.

Tulppo, M. P., Hautala, A. J., Makikallio, T. H., Laukkanen, R. T., Nissila, S., Hughson, R. L., and Huikuri, H. (2003). Effects of aerobic training on heart rate dynamics in sedentary subjects. *J. Appl. Physiol.* 95, 364–372.

Tulppo, M. P., Hughson, R. L., Makikallio, T. H., Airaksinen, K. E., Seppanen, T., and Huikuri, H. V. (2001). Effects of exercise and passive head-up tilt on fractal and complexity properties of heart rate dynamics. *Am. J. Physiol. Heart Circ. Physiol.* 280, H1081–H1087.

Van den Berg, J., Neely, G. U., Wiklund, and Landstrom, U. (2005). Heart rate variability during sedentary work and sleep in normal and sleep-deprived states. *Clin. Physiol. Funct. Imaging* 25, 51–57.

Conflict of Interest Statement: The authors declare that the research was conducted in the absence of any commercial or financial relationships that could be construed as a potential conflict of interest.

Received: 04 September 2011; accepted: 28 December 2011; published online: 07 February 2012.

Citation: Lin DC and Sharif A (2012) Integrated central-autonomic multifractal complexity in the heart rate variability of healthy humans. Front. Physio. ***2****:123. doi: 10.3389/fphys.2011.00123*

This article was submitted to Frontiers in Computational Physiology and Medicine, a specialty of Frontiers in Physiology.

APPENDIX A

Fractal time series can be coupled together in various ways, while maintaining the same set of scaling exponents. This has been demonstrated by using binomial cascades (Falconer, 1990). Albeit being a phenomenology model, the binomial cascade is used extensively to simulate multifractal property in many natural processes. It is constructed iteratively from coarse to fine scales. Each iterative step produces a version of the time series according to the scale of resolution. As this process continues ad infinitum, the time series so generated exhibits power law power spectrum and multifractal property (Falconer, 1990), the stylized facts of fractal HRV (Ivanov et al., 1999;Sassi et al., 2009). By coupling two binomial cascades systematically can produce a wide range of fractal correlation property, while maintaining the same set of scaling exponents of the individual cascades. This was shown for the binomial cascade built by using random placement scheme and deterministic weights [equations (10, 16, 17) in Lin and Sharif, 2007]. It is an important fact since it implies the need to adopt a bi-variate approach to analyze the brain-heart fractal interaction.

APPENDIX B

Equation (1) is generally known as the partition function in the literature; (see, e.g. Falconer, 1990). The relative scaling exponent estimated in (2) follows the multifractal formulism using the Legendre transform (Falconer, 1990). In theory, the width estimate of the multifractal spectrum is defined for q in the entire real line $(-\infty, \infty)$. But this requires accurate statistics of the very small and large $\alpha_{R/E}$ exponents, which in turn demands very long time series. For this reason, only a finite interval $q \in [-q_0, q_0]$ could be used to estimate the width since we are limited by the time a HUT test can be performed. The width estimated turns out to be robust in that the ratio $U_{R/E}$ does not vary sensitively with the range of q (Lin et al., 2006).

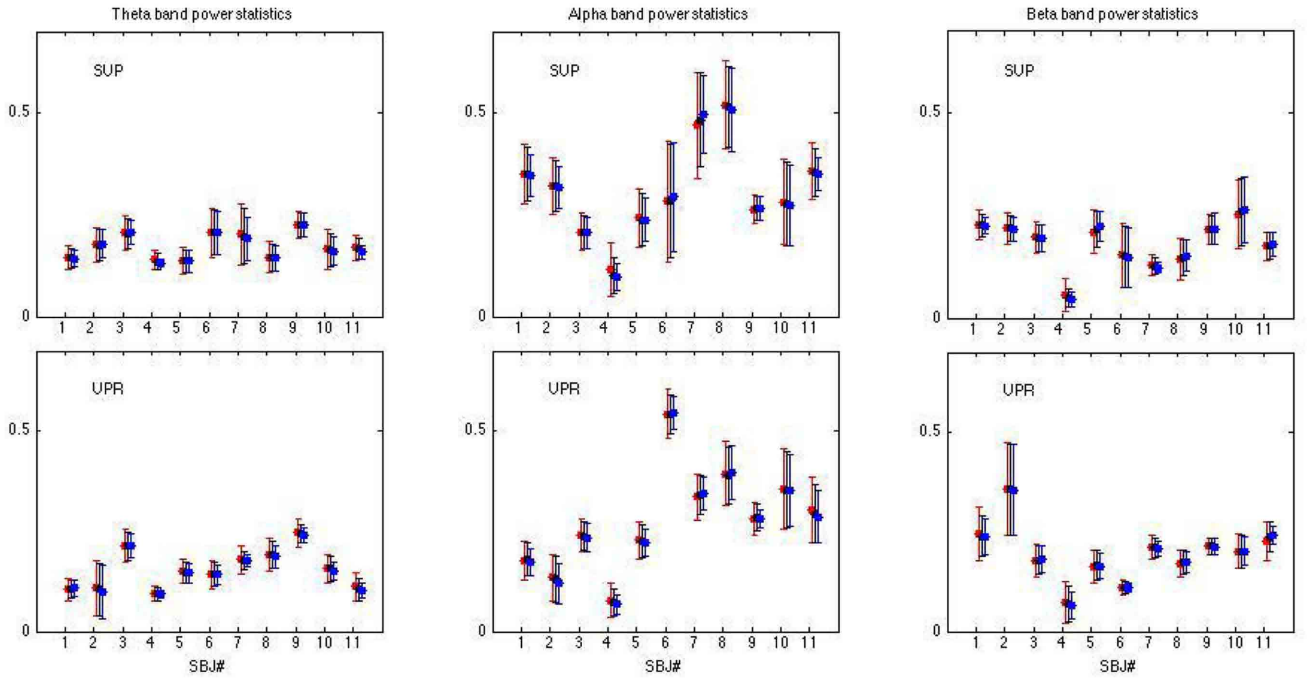

FIGURE A1 | Spectral measures of y(n) using different aggregation: 64 beats (red), 128 beats (black), and 256 beats (blue). The error bar corresponds to 1 SD.

frontiers in
PHYSIOLOGY

ORIGINAL RESEARCH ARTICLE
published: 21 September 2012
doi: 10.3389/fphys.2012.00378

Time scales of autonomic information flow in near-term fetal sheep

M. G. Frasch[1,2]*, B. Frank[3], M. Last[4] and T. Müller[5]

[1] CHU Sainte-Justine Research Centre, Department of Obstetrics and Gynecology, Faculty of Medicine, Université de Montréal, QC, Canada
[2] Centre de recherche en reproduction animale (CRRA), Faculty of Veterinary Medicine, Université de Montréal, QC, Canada
[3] Biomagnetic Centre, Department of Neurology, Friedrich Schiller University, Jena, Germany
[4] School of Medicine, University of California, Davis, CA, USA
[5] Institute of Laboratory Animal Science, Friedrich Schiller University, Jena, Germany

Edited by:
Zhe Chen, Massachusetts Institute of Technology, USA

Reviewed by:
Dirk Hoyer, Jena University Hospital, Germany
Luca Citi, Harvard Medical School, USA

***Correspondence:**
M. G. Frasch, Département d'Obstétrique-Gynécologie, Centre de Recherche du CHU Sainte-Justine, 3175, chemin de la Côte Ste-Catherine, Montréal QC H3T 1C5, Canada.
e-mail: mg.frasch@umontreal.ca

Autonomic information flow (AIF) characterizes fetal heart rate (FHR) variability (fHRV) in the time scale dependent complexity domain and discriminates sleep states [high voltage/low frequency (HV/LF) and low voltage/high frequency (LV/HF) electrocortical activity (ECoG)]. However, the physiologic relationship of AIF time scales to the underlying sympathetic and vagal rhythms is not known. Understanding this relationship will enhance the benefits derived from using fHRV to monitor fetal health non-invasively. We analyzed AIF measured as Kullback–Leibler entropy (KLE) in fetal sheep in late gestation as function of vagal and sympathetic modulation of fHRV, using atropine and propranolol, respectively ($n = 6$), and also analyzed changes in fHRV during sleep states ($n = 12$). Atropine blockade resulted in complexity decrease at 2.5 Hz compared to baseline HV/LF and LV/HF states and at 1.6 Hz compared to LV/HF. Propranolol blockade resulted in complexity increase in the 0.8–1 Hz range compared to LV/HF and in no changes when compared to HV/LF. During LV/HF state activity, fHRV complexity was lower at 2.5 Hz and higher at 0.15–0.19 Hz than during HV/LF. Our findings show that in mature fetuses near term vagal activity contributes to fHRV complexity on a wider range of time scales than sympathetic activity. Related to sleep, during LV/HF we found lower complexity at short-term time scale where complexity is also decreased due to vagal blockade. We conclude that vagal and sympathetic modulations of fHRV show sleep state-dependent and time scale-dependent complexity patterns captured by AIF analysis of fHRV. Specifically, we observed a vagally mediated and sleep state-dependent change in these patterns at a time scale around 2.5 Hz (0.2 s). A paradigm of state-dependent non-linear sympathovagal modulation of fHRV is discussed.

Keywords: fetal heart rate, HRV, autonomic nervous system, permutation entropy, complexity, sleep, atropine, propranolol

INTRODUCTION

Autonomic vagal and sympathetic activities in sheep and human fetuses vary with behavioral states and with the health of the fetus. This has been shown non-invasively in human fetuses and in ovine models of human fetal development by analysis of the fetal heart rate (FHR) variability (fHRV) (Karin et al., 1993; Groome et al., 1994; Metsala et al., 1995; Kimura et al., 1996; Van Leeuwen et al., 2003; Frank et al., 2006a,b; Schneider et al., 2008, 2009; Frasch et al., 2009a,b; Hoyer et al., 2009; Lange et al., 2009; van Laar et al., 2011). In the sheep fetus in late gestation, electrocortical activity (ECoG) is characterized by the alternating high voltage/low frequency (HV/LF) and low voltage/high frequency (LV/HF) states. The HV/LF states are similar to the human 1F state, while the LV/HF states are similar to 2F in the human fetus (Frank et al., 2006a,b; Keen et al., 2011a,b).

FHRV holds promise as a non-invasive, continuous, sensitive, and specific measure that may identify fetuses at risk of adverse outcomes and requiring intervention. Methods assessing linear properties of fHRV to estimate the sympathetic and vagal modulation of fHRV enhanced our knowledge of fetal physiology and pathophysiology (Karin et al., 1993; Groome et al., 1994; Metsala et al., 1995; Kimura et al., 1996; Van Leeuwen et al., 2003; van Laar et al., 2011). However, due to the fundamentally non-linear structure of HRV additional methods are required in order to capture the non-linear fHRV properties, thus overcoming the methodical limitation of the linear HRV analysis (Groome et al., 1999; Frasch et al., 2009a,b; Hoyer et al., 2011).

The origin of the non-linearity of sympathovagal interactions lies in their intrinsic complexity which emerges from interaction of neuronal brainstem networks as weakly coupled non-linear oscillators that are influenced by various afferent signals (Szeto et al., 1992; Fleisher et al., 1997; Lambertz et al., 2000; Vandenhouten et al., 2000). Our knowledge on the impact of the sympathovagal activities on fHRV complexity and non-linearity is still very limited (Hoyer et al., 2005; Frasch et al., 2009a,b; Cysarz et al., 2011; Doret et al., 2011; Hoyer et al., 2011). Specifically, while the influence of the vagal and sympathetic modulations on fHRV properties is non-linear and dependent

on the time scale of observation (Frasch et al., 2009a,b; Hoyer et al., 2011), the time scale-dependent changes in fHRV complexity during physiological electrocortical state activity or under conditions of pharmacological vagal or sympathetic blockade are unknown.

Consequently, our objective was to assess the contribution of vagal and sympathetic activities to *all* time scales of fHRV complexity during HV/LF and LV/HF states in near-term fetus. To this end, we studied fHRV complexity parameters derived from Kullback–Leibler entropy (KLE). KLE has been introduced and validated in human and sheep fetuses (Frank et al., 2006a,b). Briefly, decreasing KLE values correspond to increasing fHRV complexity until they reach zero for noise. KLE's main features are (1) robustness with respect to some noise possibly corrupting the data as is often the case in real life fHRV, and (2) easy computation. Thus, KLE appears to be particularly well suited for fHRV computation offline as well as for potential future development of online fHRV analysis tools (Frasch, 2011). Moreover, in agreement with the non-linear nature of sympathovagal interactions and our objective, computation of KLE over *all* time scales allowed us to make no *a priori* assumptions as to the physiologically relevant "temporal cross sections" through KLE function describing fHRV complexity. We thus captured all potentially relevant fHRV complexity changes dependant on the pharmacological blockades or behavioral ECoG states.

METHODS

SURGICAL PROCEDURE

Experimental procedures were approved by the animal welfare commission of Thuringia. Thirteen Long-Wool Merino × German Blackheaded Mutton cross-bred ewes of known gestational age were acclimated to the animal facilities for at least 5 days before surgery. After food withdrawal for 24 h, surgery was performed under halothane general anesthesia. Following 1 g of ketamine (Ketamin 10, Atarost, Germany) i.m., anaesthesia was induced by 4% halothane (Halothane Liquid 250 ml, Rhodia Organique Fine Ltd., UK) using a face mask. Ewes were intubated and anaesthesia was maintained with 1.0–1.5% halothane in 100% oxygen. Ewes were instrumented with catheters inserted into the common carotid artery for blood sampling and into the external jugular vein for post-operative administration of drugs.

Following hysterotomy, fetuses were instrumented with polyvinyl catheters (Rüschelit, Rüsch, Germany) inserted into the left common carotid artery for arterial blood pressure (ABP) recordings and blood sampling and into the left external jugular vein for drug administration. An additional catheter was placed in the amniotic cavity to record the amniotic pressure in order to permit correction of fetal mean ABP for hydrostatic pressure. Wire electrodes (LIFYY, Metrofunk Kabel-Union, Germany) were implanted into the left suprascapular muscles, muscles of the right shoulder and in the cartilage of the sternum for electrocardiogram (ECG) recording, into the uterine wall to record myometrial activity and into the skull to record electrocorticogram (ECoG) as bihemispherial leads from frontal and parietal regions and fixed with dental cement on the skull bone.

All ewes and fetuses received 0.5 g ampicillin (Ampicillin, Ratiopharm, Germany) intravenously and into the amniotic sac twice a day during the first 3 post-operative days. Metamizol (Arthripur, Atarost, Germany) was administered intravenously to the ewe (30–50 $mg \cdot kg^{-1}$) as an analgesic for at least 3 days. All catheters were maintained patent via a continuous infusion of heparin at 15 $IU \cdot ml^{-1}$ in 0.9% saline delivered at 0.5 $ml \cdot h^{-1}$.

EXPERIMENTAL PROTOCOL

After at least 3 days of post-operative recovery, the experimental protocol started at 09:00 a.m. In seven sheep, at 127 ± 3 days gestational age (dGA, term 150 days) ECG, ECoG, ABP, and uterine EMG were recorded continuously for the duration of the whole experiment. Arterial blood samples were taken daily at 09:00. The samples were analyzed for fetal blood gases, hemoglobin concentration, and oxygen saturation using a blood gas analyzer (ABL600, Radiometer, Denmark; measurements corrected to 39°C). We reported these data to be within physiological range (Frasch et al., 2009a,b).

Five minute ECG epochs were selected in HV/LF and LV/HF ECoG, since at this gestational age sleep state cycling is developed (Frank et al., 2006a,b). Sleep states were determined from ECoG visually and confirmed quantitatively by means of spectral edge frequency analysis of the bifrontal ECoG. This group of fetuses received 2.5 mg atropine-sulfate (Atropinsulfat, B. Braun, Melsungen, Germany) intravenously as a 5 ml bolus to induce vagal blockade and, 24 h later, 2 mg propranolol (Obsidan, Alpharma-Isis, Langenfeld, Germany) as a 2 ml bolus over 60 s to induce a beta-receptor mediated sympathetic blockade according to Yu et al. (Yu and Lumbers, 2000). Starting five minutes after the injections, ECG was analyzed over five minutes.

DATA ACQUISITION

ABP and amniotic pressure were recorded continuously using calibrated pressure transducers (B. Braun, Germany). Myometrial activity was monitored to recognize pressure artifacts during contractures. All biophysical parameters were amplified (Amplifier Model 5900 and 6600, Gould, USA) and digitized using a 16-channel A/D board (DI-400-PGH, DATAQ Instruments, USA) at a sample rate of 1000 s^{-1} for ECG and 100 s^{-1} for blood pressures and uterine EMG and continuously stored on a hard disc of a PC.

ANALYSIS OF PHYSIOLOGICAL VARIABLES

The software package Matlab 6.1, R13, was used to calculate all fHRV measures (The MathWorks, Natick, MA, USA). First, for calculation of FHR and fHRV the individual R peaks were sequentially detected and triggered with a precision of ± 0.49 milliseconds. The fHRV was further processed as described earlier (Frasch et al., 2007a,b, 2009a,b). Briefly, the artifacts were visually controlled for and removed manually. The resulting instantaneous R–R interval sequence was linearly interpolated at a 1000 Hz equidistant sample rate and re-sampled at 10 Hz for further signal analysis.

We reported the behavior of FHR as well as the linear fHRV measures in time and frequency domains (Frasch et al., 2009a,b). Here we aimed to characterize the behavior of the non-linear time scale properties of fHRV under physiological perturbations.

PERMUTATION ENTROPY AND KULLBACK–LEIBLER ENTROPY

Permutation entropy is a complexity measure for time series operating on an ordinal level, i.e., only the ranks of the data in the time series are analyzed, not the distances (metric) of the data. Permutation entropy measures the entropy of sequences of ordinal patterns derived from m-dimensional delay embedding vectors. In the following we briefly summarize the definition of the permutation entropy. A more detailed introduction can be found in the references (Bandt and Pompe, 2002; Cao et al., 2004).

The scalar time series $\{x(t)\}_{t=1}^{T}$ is embedded into an m-dimensional space $X_t = [x(t), x(t+L), \ldots, x(t+(m-1)L]$, where m is called the embedding dimension and L the embedding delay time. For $m = 2$, there are two possible ordinal patterns of X_t, namely $\pi_1 = x(t) < x(t+L)$ and $\pi_2 = x(t+L) < x(t)$. (For this moment we suppose that there are no equal values in X_t, i.e., no tied ranks.) For $m = 3$, X_t can attain one of six different order patterns,

$$\pi_1 = x(t) < x(t+L) < x(t+2L),$$
$$\pi_2 = x(t+L) < x(t) < x(t+2L), \ldots,$$
$$\pi_6 = x(t+2L) < x(t+L) < x(t).$$

In general, there are just $m!$ possible order patterns, which is the number of permutations of the m coordinates in X_t. Now, let $p(\pi)$ denote the relative frequency of order pattern π,

$$p(\pi) = \frac{\#\left\{t|1 \le t \le T-(m-1)L, \text{ where } X_t \text{ has type } \pi\right\}}{T-(m-1)L} \quad (1)$$

Then, for fixed embedding dimensions $m \ge 2$, and fixed delay L, permutation entropy is defined as:

$$H(m; L) = -\sum_{\pi} p(\pi) \log_2 p(\pi), \quad (2)$$

where the sum runs over all $m!$ patterns π.

Equal values in the time series, which can occur because of the limited accuracy of measurement, will be treated as follows. In case, X_t contains two equal values $x_a(t+aL) = x_b(t+bL)$, $a,b = 0, 1, \ldots, (m-1)$, the relative frequency of the permutations which correspond to the cases $x_a < x_b$ and $x_a > x_b$ is increased by $1/2$. For n equal values the respective $n!$ permutations are increased by $1/n!$. Practically this can be done by adding a random number to the data, which is smaller than the accuracy of measurements.

For convenience we normalize $H(m, L)$ by its maximum value $\log_2 m!$

$$0 \le H(m, L)/\log_2(m!) \le 1. \quad (3)$$

Now we introduce the (normalized to 1) [*KLE*, Kullback, 1968]

$$KLE = 1 - H(m, L)/\log_2(m!) \quad (4)$$

which is an information measure for the distance between the probability distribution of the ordinal patterns (permutations) and the uniform distribution. With increasing complexity of the time series, *KLE* decreases until it reaches zero for noise (independent and identically distributed (i.i.d.) process) that corresponds to a uniform distribution of all patterns. Note that due to our handling of tied ranks, a constant series would also provide $KLE = 0$.

We have to choose appropriate values for m and L. The value of m should be at least three; the maximum is limited by the length of time series. For an accurate estimation of *KLE*, the length of the time series must be considerably larger than the factorial of the embedding dimension. This allows for short series around 256 heartbeats only embedding dimensions $m = 3$ and $m = 4$. We tried both values and could not find significant differences in the discriminatory impact of the respective entropy measures (Frank et al., 2006a,b). Thus, based on the shortest length of time series studied, computation rate and memory requirements we chose the embedding dimension $m = 3$ in this paper. It means, in order to predict future heart beats in fHRV, three preceding heart beats from the past are taken as known information which corresponds to ED = 3. The delay time L is varying between 0 and 5 s. KLE of oscillators has its peaks at half the period. Thus, frequency values correspond to the time scales L as:

$$f = 1/(2L). \quad (5)$$

Finally, to get an equidistant time scale, all data were re-sampled with a sampling frequency of 10 Hz.

STATISTICAL ANALYSIS

We used a method to discriminate between ECoG states based on the AIF time scale-dependent function of KLE. To avoid overfitting due to the limited number of subjects available we used a parsimonious model with acceptable discriminatory power. The time scale-dependent variability of KLE between the animals was greater than the variability within one animal across ECoG states. This prevented the formation of global rules, such as "if KLE is above X at time scale Y, then the fetus is in LV/HF state." Instead, we looked for rules that could be used to discriminate ECoG state of the animal when compared to other records of the same animal.

Thus, all physiological parameters were tested for differences between baseline and after drug administration or groups using the Wilcoxon or Mann–Whitney tests, respectively. Baseline LV/HF and HV/LF states were compared to the respective atropine and propranolol treatment fHRV data-set. Hence, Bonferroni–Holm correction for multiple comparisons was used. Data-sets that were 1.8 min long were used to compare the effects of atropine and propranolol blockades with the effects of HV/LF and LV/HF sleep states on fHRV complexity. This data length was chosen to be consistent in comparison of all four data-sets and, consequently, the Mann–Whitney test was used. For analyses of the 12 paired HV/LF and LV/HF data-sets, the Wilcoxon test was applied and data length could be increased to 3.5 min (as was the case in the shortest recording). All results are given as mean ± SEM. P-values < 0.05 were considered significant.

RESULTS

As reported, we found the fetal physiological parameters to be within the norm for the gestational age throughout the study

(Frasch et al., 2009a,b). Mean FHR at baseline during LV/HF ECoG state was 165 ± 5 bpm which was lower than FHR during HV/LF ECoG state at 188 ± 8 bpm. Atropine administration resulted in FHR increase to 237 ± 17 bpm. Propranolol administration lead the FHR to decrease to 151 ± 4 bpm. In all cases the results were statistically significant with the exception of propranolol's effect on FHR compared to the baseline LV/HF ECoG state, which was of borderline significance ($p = 0.052$).

VAGAL AND SYMPATHETIC BLOCKADES

When compared to HV/LF and LV/HF sleep states, atropine blockade resulted in an increase of KLE on the time scale of 0.2 s corresponding to a decrease in fHRV complexity in the 2.5 Hz range (**Figures 1** and **2**). Compared to the LV/HF state, the complexity also decreased at the 0.3 s time scale (1.6 Hz). Propranolol blockade resulted in complexity increase at 0.5–0.6 s time scales (0.8–1 Hz) compared to the LV/HF state

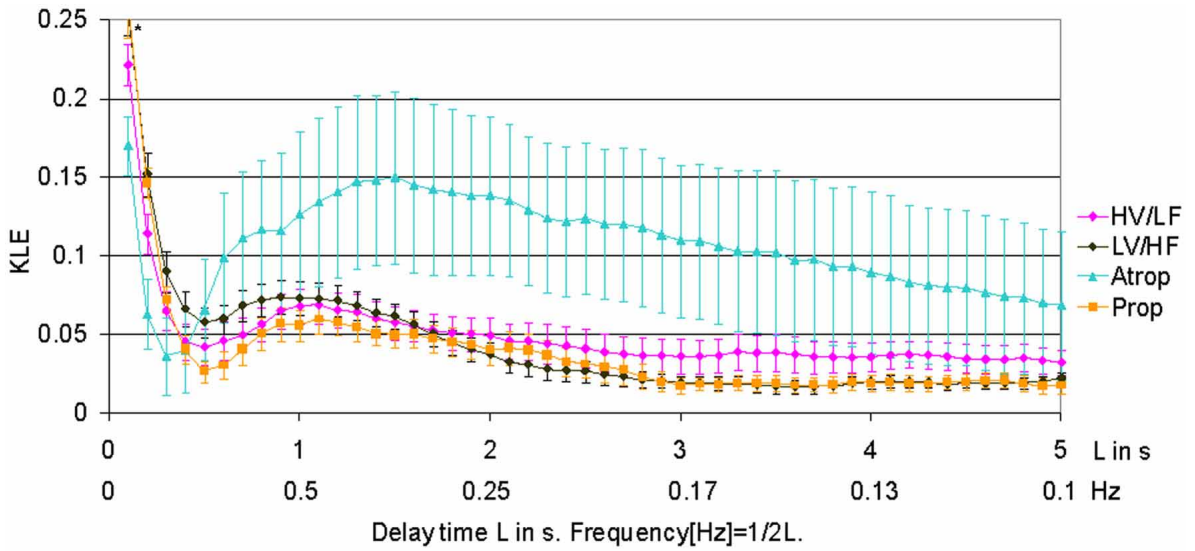

FIGURE 1 | KLE for varying delay time L (in seconds). Increasing complexity corresponds to decreasing KLE values. The whiskers indicate the standard error of the mean. Atropine administration results in profound reduction of complexity on most of the time scales, while propranolol causes a subtle increase in complexity on time scales associated with both vagal and sympathetic modulations of fHRV. The HV/LF curve (lower complexity) lies above the LV/HF curve (higher complexity) within a long-term time scale range. $N = 6$. $^*p < 0.05$.

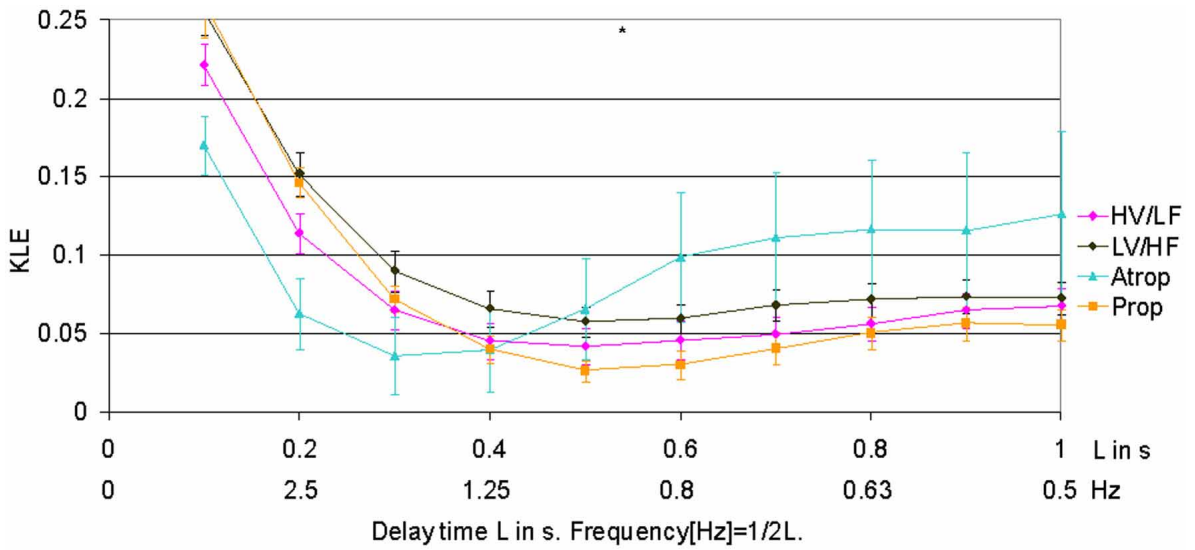

FIGURE 2 | Focus on the short-term time scale KLE segment. This figure demonstrates changes induced by pharmacologic blockades on short-term time scale fHRV complexity measured by KLE. $N = 6$. $^*p < 0.05$.

and no changes compared to the HV/LF state (**Figure 2**). **Figure 1** demonstrates that short (beat-to-beat) and long-term (an integral over 10 heart beats) time scale auto-autonomic information flow (aAIF) approaches to estimate fHRV complexity are relatively crude compared to the millisecond precise dissection of fHRV complexity fluctuations on each time scale that we attempted here with the KLE complexity function (Frasch et al., 2009a,b).

HV/LF AND LV/HF ELECTROCORTICAL STATE ACTIVITY

In 1.8 min long data-sets used to compare effects of atropine/propranolol blockades on fHRV complexity vs. HV/LF and LV/HF sleep states no differences between the sleep states were found. We increased the data-set length to 3.5 min based on the shortest fHRV recording for the analyses of all 12 paired HV/LF and LV/HF data-sets. We found that fHRV complexity in LV/HF vs. HV/LF state in 11 out of 12 fetuses was lower at the time scale of 0.2 s (2.5 Hz) and in 10 out of 12 fetuses higher at the time scale 2.7–3.3 s (Frank et al., 2006a,b) (0.15–0.19 Hz) (**Figures 3** and **4**).

DISCUSSION

Here we show that the variation in fHRV complexity due to changes in sympathovagal activity depends on the time scale used for the analysis. This sympathovagal activity is dependent on behavioral states. It is intriguing that these neural influences can be dissected mathematically using an *a posteriori* approach toward estimating fHRV complexity on physiologically relevant time scales.

VAGAL AND SYMPATHETIC MODULATIONS OF fHRV IMPACT SPECIFIC TIME SCALES OF fHRV

The KLE function allows a more sophisticated detection of state-dependent differences in fHRV complexity. Subtle effects of behavioural states on fHRV time scales retreat and are likely methodically "undersampled" *vis-à-vis* the more pronounced changes induced by the β-receptor-mediated sympathetic blockade and even more so by the vagal blockade. Thus, for the sake of comparing our previous work using aAIF and the current paper we will first focus on the effects of the pharmacological blockades vs. baseline rather than dissecting the baseline into HV/LF or LV/HF ECoG state activities.

Our findings have several implications for understanding near-term fetal sheep physiology of fHRV complexity properties and present possibilities for using fHRV to monitor fetal health.

First, we identified precise time scales of fHRV fluctuations which result from the vagal modulation of fHRV to be 0.2 s (2.5 Hz) and 0.3 s (1.6 Hz). This is in line with previous studies in sheep and human fetuses (Frank et al., 2006a,b; David et al., 2007; Frasch et al., 2007a,b, 2009a,b). These time scales find themselves within the frequency domain equivalent to the upper end of the high frequency spectral power band of fHRV (0.2–2.5 Hz). Of note, atropine blockade of vagal modulation of fHRV resulted in a drop of fHRV complexity at 1.6 Hz and 2.5 Hz compared to the baseline LV/HF ECoG state activity, but not when compared to the HV/LF ECoG state activity. Comparison to the latter rendered a drop in fHRV complexity at 2.5 Hz only, a value high enough to be potentially overlooked by studies designed with certain frequency bands set *a priori*.

Similarly, β-receptor-mediated blockade of the sympathetic modulations of fHRV revealed increases in fHRV complexity at the 0.5–0.6 s time scale (0.8–1 Hz) when compared to LV/HF ECoG state activity, but not when compared to the HV/LF ECoG state activity. While we anticipated the complexity increase following this blockade of sympathetic fHRV modulations based on previous studies (Frasch et al., 2009a,b), the time scale on which we detected this decrease is less intuitive. It may be due to unmasking vagally-mediated fluctuations within fHRV time scales corresponding to a somewhat lower range of high frequency band power spectrum associated with vagal influences on fHRV (Van Leeuwen et al., 2003; Frank et al., 2006a,b; David et al., 2007;

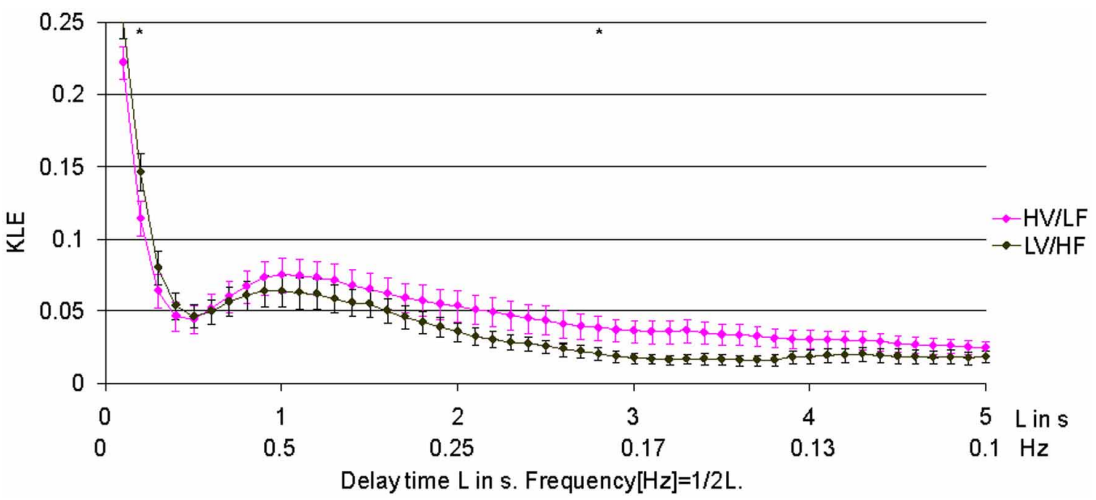

FIGURE 3 | Relationship of HV/LF and LV/HF electrocortical state activities to the time scales of fHRV complexity. KLE complexity of fetal heart rate variability (fHRV) measured during high voltage/low frequency, HV/LF and low voltage/high frequency, LV/HF, electrocortical activites. $N = 12$, mean ± SEM. $^*L = 3$ s; $p < 0.05$; $L = 0.2$ s; $p = 0.05$.

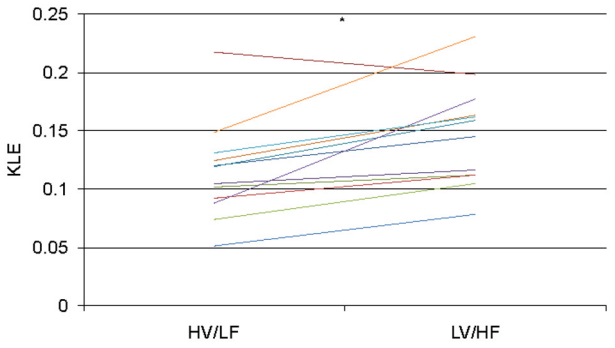

FIGURE 4 | KLE at the time scale of 2.5 Hz (0.2 s) for each animal during HV/LF versus LV/HF state. Each line color represents a different animal. $N = 12$, $^*p = 0.005$.

Frasch et al., 2007a,b, 2009a,b; Van Leeuwen et al., 2007). This may now explain the physiological mechanism behind our earlier finding that propranolol blockade in these fetal sheep resulted in a selective decrease in the nonlinear part of fHRV complexity on the short-term time scale (i.e., beat-to-beat in that case) (Frasch et al., 2009a,b). The mechanism may be as follows: propranolol-blockade results in a relative increase of vagally mediated fluctuations in fHRV, which we measure here as a complexity increase at ∼0.9 Hz. However, measured with aAIF function over all physiologically relevant time scales this sympathetic blockade appears to result in a fHRV complexity decrease—a meaningful finding reflecting an overall reduction in system complexity due to blockade of one of the branches of the autonomic nervous system. Moreover, we showed that vagally mediated fHRV complexity was sufficiently explained by its linear properties (Frasch et al., 2009a,b). In light of this "Gedankenexperiment," it is conceivable that the pinpointed fHRV complexity increase measured by the KLE function due to sympathetic blockade within the vagally mediated time scale corresponds to a complexity decrease in the non-linear part of fHRV complexity, which represents an emergent component that is due to non-linearly superimposed interactions of vagal and sympathetic fluctuations of fHRV.

Second, fetal sheep and human HV/LF and LV/HF ECoG sleep state dynamics are in contrast regarding vagal and sympathetic contributions to FHR and fHRV (Frank et al., 2006a,b). This should be kept in mind when inferences to autonomic nervous system contributions during respective ECoG states are made in this paper with the intent of comparing them to human fetal physiology. With this in mind, the relatively high frequency time scales of vagal fHRV modulations reported in the present study appear to be in contrast with some human fetal studies near-term (Van Leeuwen et al., 2003, 2007). These studies did not account for fetal behavioral states. Accounting for the behavioral states renders similar ranges of state-dependent fHRV fluctuations (Frank et al., 2006a,b).

Hence, for the first section of our discussion we make two key observations: First, fetal behavioral states should be accounted for when effects of treatments or conditions are studied with fHRV. Second, to account for the behavioral state-dependent fluctuations of vagal and sympathetic modulations of fHRV complexity, *a posteriori* study of fHRV time scales appears to be a more encompassing approach to capture all possible time scale dynamics. This challenge is unique to HRV monitoring during the perinatal stage of development when ∼90% of time is spent during HV/LF (NREM) or LV/HF (REM) behavioral states and only ∼10% of time is spent in wakefulness (Richardson and Gagnon, 2008).

CONTRIBUTIONS OF VAGAL AND SYMPATHETIC ACTIVITIES TO ECoG STATE-DEPENDENT CHANGES IN fHRV COMPLEXITY

Our results on ECoG state-dependent differences in fHRV complexity provide several insights into what appears to be a species-specific and time scale-specific behavior in sheep and human perinatal brain development.

First, confirming our previous findings in a different set of fetal sheep of the same gestational age, here we also found higher complexity during LV/HF on long-term time scale of 2.7–3.3 s (0.15–0.19 Hz) (Frank et al., 2006a,b). This time scale region corresponds to fHRV low frequency band spectral power (0.04–0.2 Hz) known in sheep fetuses to contain both sympathetic and vagal influences on fHRV (Frasch et al., 2007a,b, 2009a,b). This finding is in physiological contrast to human mature fetuses of comparable gestational age who show an inverse relationship to behavioral sleep states throughout all physiologically relevant time scales (Frank et al., 2006a,b).

Of note, we did not detect a difference in fHRV complexity at the time scale where the complexity increased due to sympathetic blockade (∼0.5 s or 0.9 Hz). It is possible that sleep state-dependent fluctuations in sympathetic activity on time scales unaffected by β-receptor sympathetic blockade may contribute to the observed lower complexity in the 0.15–0.19 Hz range. We and others have shown that propranolol blockade results in low frequency spectral power decrease of fHRV (0.04–0.2 Hz) (Yu and Lumbers, 2000; Frasch et al., 2009a,b). However, the precise distribution of spectral power was not described. Hence, it seems advantageous for approaches in frequency and multiscale complexity domains of fHRV analysis to report the most complete possible spectra or time horizons (0–5 s appears to be an adequate choice) instead of limiting the results by reporting *a priori* predefined frequency bands or time scales, respectively.

Second, it is intriguing in this context that in the present study we found—in a seeming paradox—lower complexity during LV/HF ECoG state at the same short-term time scale where complexity is also decreased following vagal blockade (at 0.2 s or 2.5 Hz). At first examination, this should mean that lower fHRV complexity during LV/HF ECoG state is due to a relatively lower contribution (i.e., lack of dominance) of vagal activity to modulations of fHRV complexity at this short-term time scale. A closer look suggests two following interpretations.

On one hand, this finding closely resembles the human fetal physiology of fHRV complexity at a comparable gestational age with regard to this specific time scale. This suggests that the species difference may in fact be maturational and not fundamental (Frank et al., 2006a,b). That is, the time scale-specific species difference may be related to the fine tuning of the state-dependent sympathovagal activation/inhibition patterns and their degree of fHRV modulation. It is known that various organ systems, such as

the brain, mature at different speeds in different species (Dobbing and Sands, 1979). In addition, postnatally the autonomic nervous system and cardiovascular controls in lambs appear to behave somewhat similarly to human neonates in relation to sleep states and bivariate heart rate/blood pressure coupling, while the heart rate itself continues to be higher during quiet sleep (∼HV/LF ECoG state) versus active sleep (∼LV/HF ECoG state) in contrast to human neonates (Silvani et al., 2005; Frasch et al., 2007a,b; Booth et al., 2011a,b). Further comparative research is needed to address the sleep state-dependent differences in bivariate and univariate cardiovascular control patterns found in sheep and human species. Such research will render valuable data to better interpret animal research findings in human physiological and clinical contexts, e.g., in the field of Sudden Infant Death Syndrome (SIDS).

On the other hand, our finding of lower fHRV complexity during the LV/HF ECoG state at the 0.2 s time scale where fHRV complexity is also decreased following vagal blockade is in direct contrast with studies also carried out in fetal sheep near-term that showed a dominance of vagal control of cardiovascular system during LV/HF state with lower FHR and blood pressure values versus HV/LF state (Zhu and Szeto, 1987; Jensen et al., 2009). Of note, these studies did not examine higher order properties of fHRV which contain the information about influences of vagal and sympathetic rhythms on fHRV. In a smaller study ($n = 6$) using the same signal analytical approach and comparable gestational age of fetal sheep as presented here, we could not detect differences between ECoG states at this time scale of fHRV complexity (Frank et al., 2006a,b). We cannot exclude that this may be due to a smaller sample size. Similarly, in this study, we could not detect any differences between the ECoG states regarding fHRV complexity at an equally small sample size of $n = 6$.

We believe this paradox can be resolved in the following complementary ways:

(1) In the current study we did not investigate the contribution of non-linearities to the overall complexity as done previously (Frasch et al., 2009a,b). In that study we showed that vagal modulations of fHRV contribute to fHRV linear properties on short-term (beat-to-beat) time scales in near-term sheep, rather than to its non-linear components (Frasch et al., 2009a,b). This means that the vagal blockade-induced fHRV complexity decrease we found here on the same time scale as the fHRV complexity decrease during LV/HF ECoG state vs. HV/LF ECoG state may be due to different contributions of non-linear parts of fHRV complexity to the overall complexity changes we assessed in the present study.
(2) Inferring about contributions of the underlying sympathetic and vagal rhythms from pharmacological blockade-induced fHRV complexity changes to observations made during physiological, unperturbed, ECoG state cycling carries an inherent limitation discussed earlier (Frasch et al., 2009a,b). The limitation is the same that led us to deploy complexity analyses of fHRV in the first place, namely, the non-linear nature of the influences sympathovagal fluctuations have on fHRV. The decreases of overall fHRV complexity following vagal and sympathetic blockades that we reported suggest that both vagal and β-receptor-mediated sympathetic modulations contribute to the complexity of fHRV (Frasch et al., 2009a,b). In agreement with this, the concept of reciprocal vagal or sympathetic activation has been challenged by the evidence of nonreciprocal autonomic modulation of HRV (Guzzetti et al., 2005; Paton et al., 2005), suggesting concomitant vagal and sympathetic activation as in a complex network.

In summary, for the second section of our discussion and to address the apparent "paradox," we suggest that our findings for differences in fHRV complexity during LV/HF vs. HV/LF ECoG states should be seen as reflecting changes in sympathovagal activation patterns as they modulate fHRV, rather than as distinct, independent effects of sympathetic or vagal modulations of fHRV.

IMPLICATIONS FOR HUMAN FHR MONITORING

Our data suggest that relatively short FHR segments of as few as ∼600 heart beats per behavioral state appear to be sufficient to allow for state discrimination based on *a posteriori* time scale fHRV complexity analysis. Moreover, R–R intervals with sampling rates obtainable from regular ultrasound- or scalp-electrode derived FHR read-outs should still permit state discrimination at the time scale of ∼3 s or 0.17 Hz. This is relevant for the prospect of using antepartum FHR monitoring to detect and grade chronic fetal hypoxia. This might be possible because chronic hypoxia disrupts fetal HV/LF and LV/HF ECoG states and may also have a similar effect on the accompanying fHRV dynamics (Keen et al., 2011a,b). Further studies will be needed to investigate these physiologic and pathophysiologic relations.

PERSPECTIVES AND IMPLICATIONS

Vagal and sympathetic modulations of fHRV show sleep state-dependent and time scale-dependent complexity patterns.

The pathophysiologically motivated "fight and flight response" paradigm of the "linearizing," complexity-decreasing effect of sympathetic HRV modulation may be not comprehensive enough to capture the "every day" physiological context. Further studies are needed to enhance this paradigm toward the concept of sympathovagal co-activation, a synergistically occurring physiological pattern of autonomic nervous system activity within the larger multi-organ network. In this context, a unified *a posteriori* multi-scale approach to HRV complexity estimation is required to facilitate cross-study and cross-species comparisons and translation of knowledge into improved HRV monitoring. Ultimately, to more fully account for behavioral state-, time scale- and species-dependent fluctuations in such physiologic patterns, this paradigm should allow for inclusion of multivariate data-sets such as ECoG and blood pressure signals.

ACKNOWLEDGMENTS

The authors thank Holger Friedrich, Petra Dobermann, and Claudia Sommer for technical assistance and Drs. Matthias Schwab and Dirk Hoyer for advice. We acknowledge funding support from Molly Towell Perinatal Research Foundation, CIHR and FRSQ (M. G. Frasch).

REFERENCES

Bandt, C., and Pompe, B. (2002). Permutation entropy: a natural complexity measure for time series. *Phys. Rev. Lett.* 88, 174102.

Booth, L. C., Bennet, L., Guild, S. J., Barrett, C. J., May, C. N., Gunn, A. J., and Malpas, S. C. (2011a). Maturation-related changes in the pattern of renal sympathetic nerve activity from fetal life to adulthood. *Exp. Physiol.* 96, 85–93.

Booth, L. C., Gunn, A. J., Malpas, S. C., Barrett, C. J., Davidson, J. O., Guild, S. J., and Bennet, L. (2011b). Baroreflex control of renal sympathetic nerve activity and heart rate in near-term fetal sheep. *Exp. Physiol.* 96, 736–744.

Cao, Y., Tung, W. W., Gao, J. B., Protopopescu, V. A., and Hively, L. M. (2004). Detecting dynamical changes in time series using the permutation entropy. *Phys. Rev. E Stat. Nonlin. Soft Matter Phys.* 70, 046217.

Cysarz, D., Van Leeuwen, P., Edelhauser, F., Montano, N., and Porta, A. (2011). Binary symbolic dynamics classifies heart rate variability patterns linked to autonomic modulations. *Comput. Biol. Med.* 42, 313–318.

David, M., Hirsch, M., Karin, J., Toledo, E., and Akselrod, S. (2007). An estimate of fetal autonomic state by time-frequency analysis of fetal heart rate variability. *J. Appl. Physiol.* 102, 1057–1064.

Dobbing, J., and Sands, J. (1979). Comparative aspects of the brain growth spurt. *Early Hum. Dev.* 3, 79–83.

Doret, M., Helgason, H., Abry, P., Goncalves, P., Gharib, C., and Gaucherand, P. (2011). Multifractal analysis of fetal heart rate variability in fetuses with and without severe acidosis during labor. *Am. J. Perinatol.* 28, 259–266.

Fleisher, L. A., Dipietro, J. A., Johnson, T. R., and Pincus, S. (1997). Complementary and noncoincident increases in heart rate variability and irregularity during fetal development. *Clin. Sci. (Lond.)* 92, 345–349.

Frank, B., Frasch, M. G., Schneider, U., Roedel, M., Schwab, M., and Hoyer, D. (2006a). Complexity of heart rate fluctuations in near-term fetal sheep during sleep. *Biomed. Tech. (Berl.)* 51, 233–236.

Frank, B., Pompe, B., Schneider, U., and Hoyer, D. (2006b). Permutation entropy improves fetal behavioural state classification based on heart rate analysis from biomagnetic recordings in near term fetuses. *Med. Biol. Eng. Comput.* 44, 179–187.

Frasch, M. G. (2011). Fetal heart rate variability monitoring. Montebello Round Table. Complexity and Variability at the Bedside. September 28 – October 1. Montebello, QC, Canada. *J. Crit. Care* 26, 325–327.

Frasch, M. G., Muller, T., Hoyer, D., Weiss, C., Schubert, H., and Schwab, M. (2009a). Nonlinear properties of vagal and sympathetic modulations of heart rate variability in ovine fetus near term. *Am. J. Physiol. Regul. Integr. Comp. Physiol.* 296, R702–R707.

Frasch, M. G., Muller, T., Weiss, C., Schwab, K., Schubert, H., and Schwab, M. (2009b). Heart rate variability analysis allows early asphyxia detection in ovine fetus. *Reprod. Sci.* 16, 509–517.

Frasch, M. G., Muller, T., Wicher, C., Weiss, C., Lohle, M., Schwab, K., Schubert, H., Nathanielsz, P. W., Witte, O. W., and Schwab, M. (2007a). Fetal body weight and the development of the control of the cardiovascular system in fetal sheep. *J. Physiol.* 579, 893–907.

Frasch, M. G., Zwiener, U., Hoyer, D., and Eiselt, M. (2007b). Autonomic organization of respirocardial function in healthy human neonates in quiet and active sleep. *Early Hum. Dev.* 83, 269–277.

Groome, L. J., Mooney, D. M., Bentz, L. S., and Singh, K. P. (1994). Spectral analysis of heart rate variability during quiet sleep in normal human fetuses between 36 and 40 weeks of gestation. *Early Hum. Dev.* 38, 1–9.

Groome, L. J., Mooney, D. M., Holland, S. B., Smith, L. A., Atterbury, J. L., and Loizou, P. C. (1999). Human fetuses have nonlinear cardiac dynamics. *J. Appl. Physiol.* 87, 530–537.

Guzzetti, S., Borroni, E., Garbelli, P. E., Ceriani, E., Della Bella, P., Montano, N., Cogliati, C., Somers, V. K., Malliani, A., and Porta, A. (2005). Symbolic dynamics of heart rate variability: a probe to investigate cardiac autonomic modulation. *Circulation* 112, 465–470.

Hoyer, D., Pompe, B., Chon, K. H., Hardraht, H., Wicher, C., and Zwiener, U. (2005). Mutual information function assesses autonomic information flow of heart rate dynamics at different time scales. *IEEE Trans. Biomed. Eng.* 52, 584–592.

Hoyer, D., Heinicke, E., Jaekel, S., Tetschke, F., Di Pietro Paolo, D., Haueisen, J., Schleusner, E., and Schneider, U. (2009). Indices of fetal development derived from heart rate patterns. *Early Hum. Dev.* 85, 379–386.

Hoyer, D., Nowack, S., Bauer, S., Tetschke, F., Ludwig, S., Moraru, L., Rudoph, A., Wallwitz, U., Jaenicke, F., Haueisen, J., Schleussner, E., and Schneider, U. (2011). Fetal development assessed by heart rate patterns-Time scales of complex autonomic control. *Comput. Biol. Med.* 42, 335–341.

Jensen, E. C., Bennet, L., Guild, S. J., Booth, L. C., Stewart, J., and Gunn, A. J. (2009). The role of the neural sympathetic and parasympathetic systems in diurnal and sleep state-related cardiovascular rhythms in the late-gestation ovine fetus. *Am. J. Physiol. Regul. Integr. Comp. Physiol.* 297, R998–R1008.

Karin, J., Hirsch, M., and Akselrod, S. (1993). An estimate of fetal autonomic state by spectral analysis of fetal heart rate fluctuations. *Pediatr. Res.* 34, 134–138.

Keen, A. E., Frasch, M. G., Sheehan, M. A., Matushewski, B., and Richardson, B. S. (2011a). Maturational changes and effects of chronic hypoxemia on electrocortical activity in the ovine fetus. *Brain Res.* 1402, 38–45.

Keen, A. E., Frasch, M. G., Sheehan, M. A., Matushewski, B. J., and Richardson, B. S. (2011b). Electrocortical activity in the near-term ovine fetus: automated analysis using amplitude frequency components. *Brain Res.* 1402, 30–37.

Kimura, Y., Okamura, K., Watanabe, T., Murotsuki, J., Suzuki, T., Yano, M., and Yajima, A. (1996). Power spectral analysis for autonomic influences in heart rate and blood pressure variability in fetal lambs. *Am. J. Physiol.* 271, H1333–H1339.

Kullback, S. (1968). *Information Theory and Statistics*. New York, NY: Dover Publications.

Lambertz, M., Vandenhouten, R., Grebe, R., and Langhorst, P. (2000). Phase transitions in the common brainstem and related systems investigated by nonstationary time series analysis. *J. Auton. Nerv. Syst.* 78, 141–157.

Lange, S., Van Leeuwen, P., Schneider, U., Frank, B., Hoyer, D., Geue, D., and Gronemeyer, D. (2009). Heart rate features in fetal behavioural states. *Early Hum. Dev.* 85, 131–135.

Metsala, T., Siimes, A., and Valimaki, I. (1995). The effect of change in sympatho-vagal balance on heart rate and blood pressure variability in the foetal lamb. *Acta Physiol. Scand.* 154, 85–92.

Paton, J. F., Boscan, P., Pickering, A. E., and Nalivaiko, E. (2005). The yin and yang of cardiac autonomic control: vago-sympathetic interactions revisited. *Brain Res. Brain Res. Rev.* 49, 555–565.

Richardson, B., and Gagnon, R. (2008). "Behavioural state activity and fetal health and development," in *Maternal-Fetal Medicine,* eds R. K. Creasy, and R. Resnik (Philadelphia, PA: WB Saunders Co.), 171–179.

Schneider, U., Frank, B., Fiedler, A., Kaehler, C., Hoyer, D., Liehr, M., Haueisen, J., and Schleussner, E. (2008). Human fetal heart rate variability-characteristics of autonomic regulation in the third trimester of gestation. *J. Perinat. Med.* 36, 433–441.

Schneider, U., Schleussner, E., Fiedler, A., Jaekel, S., Liehr, M., Haueisen, J., and Hoyer, D. (2009). Fetal heart rate variability reveals differential dynamics in the intrauterine development of the sympathetic and parasympathetic branches of the autonomic nervous system. *Physiol. Meas.* 30, 215–226.

Silvani, A., Asti, V., Bojic, T., Ferrari, V., Franzini, C., Lenzi, P., Grant, D. A., Walker, A. M., and Zoccoli, G. (2005). Sleep-dependent changes in the coupling between heart period and arterial pressure in newborn lambs. *Pediatr. Res.* 57, 108–114.

Szeto, H. H., Cheng, P. Y., Decena, J. A., Cheng, Y., Wu, D. L., and Dwyer, G. (1992). Fractal properties in fetal breathing dynamics. *Am. J. Physiol.* 263, R141–R147.

Vandenhouten, R., Lambertz, M., Langhorst, P., and Grebe, R. (2000). Nonstationary time-series analysis applied to investigation of brainstem system dynamics. *IEEE Trans. Biomed. Eng.* 47, 729–737.

van Laar, J. O., Peters, C. H., Houterman, S., Wijn, P. F., Kwee, A., and Oei, S. G. (2011). Normalized spectral power of fetal heart rate variability is associated with fetal scalp blood pH. *Early Hum. Dev.* 87, 259–263.

Van Leeuwen, P., Geue, D., Lange, S., Hatzmann, W., and Gronemeyer, D. (2003). Changes in the frequency power spectrum of fetal heart rate in the course of pregnancy. *Prenat. Diagn.* 23, 909–916.

Van Leeuwen, P., Lange, S., Geue, D., and Gronemeyer, D. (2007). Heart rate variability in the fetus: a comparison of measures. *Biomed. Tech. (Berl.)* 52, 61–65.

Yu, Z. Y., and Lumbers, E. R. (2000). Measurement of baroreceptor-mediated effects on heart rate

variability in fetal sheep. *Pediatr. Res.* 47, 233–239.

Zhu, Y. S., and Szeto, H. H. (1987). Cyclic variation in fetal heart rate and sympathetic activity. *Am. J. Obstet. Gynecol.* 156, 1001–1005.

Conflict of Interest Statement: The authors declare that the research was conducted in the absence of any commercial or financial relationships that could be construed as a potential conflict of interest.

Received: 21 May 2012; accepted: 04 September 2012; published online: 21 September 2012.

Citation: Frasch MG, Frank B, Last M and Müller T (2012) Time scales of autonomic information flow in near-term fetal sheep. Front. Physio. ***3****:378. doi: 10.3389/fphys.2012.00378*

This article was submitted to Frontiers in Computational Physiology and Medicine, a specialty of Frontiers in Physiology.